Study of Burning Characteristics of a Porous Combustible Soaked in a Liquid Oxidizer

（液体酸化剤を湿潤させた多孔質固体燃料の燃焼特性に関する研究）

January, 2022

Doctor of Philosophy (Engineering)

Daiki MATSUGI

松木　大輝

Toyohashi University of Technology

Department of Mechanical Engineering	Student ID Number	D153198
Applicant's name	Daiki Matsugi	

Supervisors	Yuji Nakamura Hideki Yanada Akiyoshi Iida

Abstract (Doctor)

Title of Thesis	Study of Burning Characteristics of a Porous Combustible Soaked in a Liquid Oxidizer

Approx. 800 words

With an increasing trend in development of smaller satellites owing to significant progress in microelectronics, and together with an increasing awareness of threats to the environment, a dedicated small launch vehicle for launching the smaller satellites, employing environmentally friendly propellant are becoming highly demanded. To respond this, hybrid rockets have been promising for the launch vehicle and of great interest by many research groups. Although great efforts have been made ever, its practical application as the launch vehicle has been found to be challenging.

In 1997, Nagata et al. proposed a simple propellant consisting of a porous combustible soaked in a liquid oxidizer. They made an experimental investigation of pressure dependency on regression rate of the propellant, and it was found that the propellant could achieve excellent thrusting performance comparable to the existing chemical rocket systems. On the other hand, unwanted burning behaviors, such as an explosion-like burning, were frequently observed in their experiments, and data scattering of the regression rate was measured at random pressure in their experiments. In addition, the burning characteristics have been limited to the pressure dependency on the regression rate since 1997. For guaranteeing safety and reliability of the propellant while leveraging its excellent thrusting performance, it is necessary to obtain comprehensive knowledge of the fundamental burning characteristics of the propellant and clarify the reason for the unwanted burning and the data scattering as fundamental research. In this work, as referred to the previous work by Nagata et al., comprehensive experimental

and numerical investigations on the fundamental burning characteristics of the propellant were conducted.

Comprehensive experimental investigations to obtain the fundamental burning characteristics of the specimen, consisting of a polyethylene foam soaked in enriched hydrogen peroxide, were conducted. To examine the fundamental burning characteristics, such as burning behavior, regression rate, its steadiness, thermal structure during entire burning event, and one-dimensionality of burning process, an experimental setup, testing methodology, and a simple thermal analysis were introduced. Experiments in nitrogen-filled environment were carried out at various pressures (0.1 MPa – 0.35 MPa) and fuel porosities (0.6 – 0.9) to obtain those of the fundamental burning characteristics. It was found that an end-burning at which top surface (burning surface) of the specimen moves downward at reasonably constant rate is successfully achieved under the conditions studied in this work. From results of the direct observation during the burning event and direct temperature measurements by thermocouple, it was revealed that progress of the tested specimen shall be dominated by the premixed-like surface flame established in the vicinity of the top surface. Furthermore, it was proved that the one-dimensionality of the burning process shall be valid by the simple thermal analysis. These facts helped to develop a simple burning model under assumptions; the steady state, premixed combustion, and one-dimensionality.

Based on the experimentally obtained facts, a simple one-dimensional burning model was then developed to numerically investigate the fundamental burning characteristics. The thermal structure and the potential regression rate under various prescribed conditions were predicted using the burning model developed in this work. Separately considering the estimated blow-off limit in the gas-phase over the top surface by CHEMKIN (PREMIX-code), a range needed to achieve successive burning was numerically predicted. The effects of oxidizer type (hydrogen peroxide and liquid oxygen), the fuel porosity, and pressure on the potential regression rate, the thermal structure, and blow-off limit were then discussed. Findings show that the successive burning is widely achievable when hydrogen peroxide is used as the liquid oxidizer, but it is only partially achievable when liquid oxygen is utilized. This fact may support the

data scattering and the behavior observed in the previous work by Nagata et al.

Product gases of the burning specimen at nitrogen-balanced 0.1 MPa ambient to predict thrusting performance of the present specimen were studied. In the experiments, we first measured one-dimensional (1-D) CO_2 and H_2O concentration profiles over the regression surface by a gas chromatography under various fuel porosities 0.77 – 0.84. The concentration profiles exhibited nearly flat, suggesting that chemical equilibrium was reached satisfactory immediately after the regression surface. The equilibrium calculation was then utilized in order to predict optimal combination of pyrolysis gases, oxidizer gases, and their mass fraction, and estimate the other product gases potentially produced and thrusting performance achievable in this burning specimen. Two important facts were noted: (1) the predicted mass fraction of oxygen shall be lower than that of pure H_2O_2 and (2) major pyrolysis gases components were found to be methane (CH_4), ethylene (C_2H_4), and ethane (C_2H_6). Expected specific impulse potentially achievable by the present burning specimen was estimated and found to be in the range of 95 s to106 s, depending on the initial concentration of H_2O_2. This fact implied that using pure H_2O_2 was preferred to achieve the larger specific impulse of the present specimen.

機械工学専攻	学籍番号	D153198
氏名	松木 大輝	

指導教員	中村 祐二 柳田 秀記 飯田 明由

博士論文の要旨(博士)

博士学位論文名	液体酸化剤を湿潤させた多孔質固体燃料の燃焼特性に関する研究

(要旨 1,200 字程度)

小型衛星専用ロケットとして，環境負荷低減を実現でき，固体推進ロケットと液体推進ロケットの両者の利点を有するハイブリッドロケットがこれまで注目されてきた．しかし，推進剤の消費速度（燃料後退速度）が上がりづらいという理由から，実用化の例が極めて少ない．そのため，高い燃料後退速度を実現すべく，世界中でハイブリッドロケットの研究開発が行われている．

1997年，永田らは多孔質固体燃料（発泡体）に液体酸化剤を湿潤させた推進剤を提案し，燃料後退速度の圧力依存性を実験的に調査した結果，固体推進ロケットを凌ぐ燃料後退速度が得られたことを報告した．ところが，爆発のような異常燃焼が頻繁に確認されたこと，得られた燃料後退速度は同圧力にも関わらずデータ散乱が確認されたこと，さらには，どのように燃えるかといった基本的な燃焼特性が明らかとなっていないことから日の目を見ることはなかった．そこで本研究では，本推進剤の基礎燃焼特性（燃料後退速度，その定常性，燃焼挙動，燃焼構造）と永田らの先行研究で観察された異常燃焼とデータ散乱の原因を実験と数値計算を用いて調査することを目的とする．

本研究では，液体酸化剤に濃縮した過酸化水素，多孔質固体燃料にはポリエチレン発泡体を推進剤に用い，燃焼場の可視化と熱電対による温度計測可能な燃焼室を導入した．また燃料後退速度を正しく計測するために画像解析ソフトウェアを導入し，窒素充填場で様々な条件（圧力：0.1 MPa – 0.35 MPa，ポリエチレン発泡体空隙率；0.6 – 0.9）で基礎燃焼特性を調査した．推進剤上端面での強制着火後，すべての実験条件において，上端面が平面形状（一次元）を保ちつつ定常的に後退する“端面燃焼”を確認した．計測された燃料後退速度は1.2 mm/s – 3.2 mm/sであること，可視化と温度計測の結果，本推進剤の燃焼は上端面近傍に形成された予混合火炎に支配されることが明らかとなった．

これらの実験的事実より，定常状態，予混合燃焼，そして一次元を仮定した燃焼モデルを提案した．CHEMKINにより，推進剤上端面の気相の吹き飛び限界を別途与え，酸化剤の種類（液体酸素と過酸化水素），雰囲気圧力，そして燃料空隙率が，燃料後退速度，燃焼構造，そして連続燃焼領域に与える影響について議論した．過酸化水素を用いた場合，広い範囲で連続燃焼が達成できるのに対して，液体酸素を用いた場合では，その領域が狭くなることが明らかとなった．以上より，永田らの先行

研究で観察された異常燃焼やデータ散乱の原因は，液体酸素使用により連続燃焼の持続が困難となるためだと示唆された，
最後に本推進剤の比推力を予測するため，0.1 MPa窒素充填場で燃焼ガス成分をガスクロマトグラフィーにより調査した．実験では，推進剤上端面上方の二酸化炭素と水蒸気の一次元濃度分布を様々な空隙率（0.77 – 0.84）で計測し，化学平衡状態を調査した．結果を踏まえ，化学平衡計算コードを用い，達成しうる比推力を予測した．本推進剤で達成される比推力は，過酸化水素濃度に応じて95sから106sの範囲で変化し，純過酸化水素を用いることでより高い比推力が得られることを示した．

Contents of dissertation

Nomenclature and terminologies

Symbol	Description (English – Japanese)		Unit
A	Pre-exponential factor	頻度因子	[1/s]
b	Pressure exponent	圧力指数	[]
c_p	Specific heat at constant pressure	定圧比熱	[J/kg·K]
D	Mass diffusivity	物質拡散係数	[m^2/s]
d	Diameter	直径	[m]
E_{a_3}	Activation energy	活性化エネルギー	[J/mol]
E_S	Global activation energy	PE 発泡体 活性化エネルギー	[J/mol]
F	Thrust force	推力	[N]
G	Total mass flow rate	全質量流量	[kg/s]
h	Enthalpy	エンタルピー	[J/kg]
h_g	Latent of gasification	固体燃料 ガス化潜熱	[J/kg]
h_v	Latent of vaporization	液体酸化剤 蒸発潜熱	[J/kg]
I_{SP}	Specific impulse	比推力	[s]
k	Specific heat ratio	比熱比	[-]
L	Length of specimen	試験片長さ	[m]
M_C	Average molecular weight	平均分子量	[g/mol]
$\dot{m}$	Total mass flux	全質量流束	[kg/(m^2·s)]
$\dot{m}_O$	Oxidizer Mass flow flux	酸化剤質量流束	[kg/(m^2·s)]
n	Reaction index Number of experimental trials	反応次数 実験回数	[-]
Nu	Nusselt number	ヌッセルト数	[-]

O/F	Oxidizer-to-fuel mass flow rate ratio	酸化剤-燃料 質量流量比	[-]
p	Pressure	圧力	[Pa]
p_e	Pressure at nozzle exit	ノズル出口圧力	[Pa]
p_c	Pressure in combustion chamber	燃焼室内圧力	[Pa]
Δp	Pressure rises	圧力上昇	[Pa/s]
Pr	Prandtl number	プラントル数	[-]
q	Heat generation by chemical reaction	化学反応熱	[J/m^3]
q_r	Thermal radiation	放射熱流束	[W/m^2]
q^*	Non-dimensional heat generation, $= q/[c_{p\_3}(T_\infty - T_0)]$	無次元発熱量	[-]
R	Universal gas constant, $= 8.31$	一般ガス定数	[J/(mol·K)]
Re	Reynolds number	レイノルズ数	[-]
s^2	Unbiased dispersion	不偏分散	
ST	Stanton number	スタントン数	[-]
t	Time or student's t-distribution	時間，t 分布	[s]
T	Temperature	温度	[K]
T_0	Initial temperature	初期温度	[K]
T_L	Boiling temperature	液体酸化剤沸点	[K]
T_S	Gasification temperature	固体燃料 ガス化温度	[K]
T_∞	Adiabatic flame temperature	断熱火炎温度	[K]
u	Velocity	速度	[m/s]
V	Volume of chamber	燃焼室体積	[m^3]
V_f	Regression rate	燃料後退速度	[m/s]
$\overline{V_f}$	Average regression rate	平均燃料後退速度	[m/s]

V_g	Spouting velocity of gas mixture at top-surface	予混合噴出速度	[m/s]
w	Mass consumption rate, (see Eq. 4 - 15)	質量消費率	[Kg/s]
X	Mole-based concentration	モル濃度	[-]
x, x'	Coordinate	座標	[m]
Y	Mass fraction of species	化学種質量分率	[-]

Greek symbol	Description (English – Japanese)		Unit
α	Rosseland means adsorption coefficient	平均吸収係数	[1/m]
β	Zeldovich number, $= E_{a\_3}(T_\infty - T_0)/(RT_\infty^2)$	ゼルドヴィッチ数	[-]
δ	Dried layer thickness	乾燥領域厚み	[m]
ε	Fuel porosity	燃料空隙率	[-]
θ	Non-dimensional temperature	無次元温度	[-]
λ^*	Effective thermal conductivity	有効熱伝導率	[W/m·K]
μ	Viscosity Population means	粘性係数 母平均	[Pa·s]
ν	Kinematic viscosity (chapter 3) stoichiometric coefficient (chapter 4)	動粘性係数 化学両論比	[m^2/s], [-]
Λ	Eigenvalue of total mass flux	質量流束の固有値	[-]
ξ	Non-dimensional coordinate, $= (c_{p\_3}\dot{m}x)/\lambda_3^*$	無次元座標	[-]
ρ_L	Density of liquid oxidizer	液体酸化剤密度	[kg/m^3]
ρ_S	Density of porous combustible	固体燃料密度	[kg/m^3]
ρ_g	Density of gas mixture	予混合ガス密度	[kg/m^3]

σ	Stefan-Boltzmann coefficient, $= 5.67 \times 10^{-8}$	ステファン ボルツマン定数	[W/m^2·K^4]
φ	Equivalence ratio	当量比	[-]

Subscript	Description (English – Japanese)	
1	Wetted layer	湿潤領域
2	Dried layer	乾燥領域
3	Gas-phase layer	気層領域
∞	Infinity	無限方向
F	Fuel	燃料
g	Gaseous phase	ガス
i	Deficient species (chapter 4), *i*th species (chapter 5)	不足化学種 i 番目化学種
L	Liquid phase	液相
O	Oxidizer	酸化剤
S	Solid phase or top surface	固体層 or 上端面
*	Effective	有効

Abbreviation	Description (English – Japanese)	
ABS	Acrylonitrile butadiene styrene	ABS 樹脂
ADN	Ammonium dinitramide	アンモニウム ジニトラミド
Al	Aluminum particles	アルミニウム粒子
AP	Ammonium Perchlorate	過塩素酸 アンモニウム
AN	Ammonium nitrate	硝酸アンモニウム
GAP	Glycidyl azide polymer	グリシジル アジドポリマー
HTPB	Hydroxyl-terminated polybutadiene	末端水酸基 ポリブタジエン
Mg	Magnesium	マグネシウム

Other terminologies

English	Japanese
Anomalous combustion	異常燃焼
Asymptotic analysis	漸近解析
Burning characteristics	燃焼特性（燃料後退速度．その定常性，燃焼挙動，熱構造，一次元性）
Burning behavior	燃焼挙動
Blow off limit	吹き飛び限界
NASA CEA (NASA Chemical Equilibrium with Applications)	化学平衡計算プログラム
Capillary effect	毛細管現象
Chamber	燃焼室
Chemical equilibrium	化学平衡
Combustion	燃焼
Concentration	濃度
Dedicated small launch vehicle	専用打上小型ロケット
Diffusion flame	拡散火炎
Distillation	蒸留
End burning mode	端面燃焼モード
Exothermic reaction	発熱反応
Explosive	火薬，爆薬物
Extinction	消炎
Flame spreading mode	火炎燃え拡がりモード
Forced ignition	強制着火
Fuel porosity	燃料空隙率
Fuel rich, lean	燃料過剰，希薄
Gas chromatography	ガスクロマトグラフィー

Heat flux	熱流束
Hydrocarbon fuel	炭化水素系燃料
Hydrogen peroxide	過酸化水素
Laminar burning velocity	層流燃焼速度
Launch vehicle	打上ロケット
Liquid propellant rocket engine	液体推進ロケット
Molten phase	溶融相
Nozzle theory	ノズル理論
O/*F* variation	酸化剤-燃料質量流量比変動
Payload	ペイロード，荷物
Polymeric solid fuel	高分子固体燃料
Premixed combustion	予混合燃焼
Product gas	燃焼生成物
Propellant	推進剤
Piggyback	ピギーバック，相乗り
Porous combustible	可燃性多孔質固体燃料
Pyrolysis gas	熱分解ガス
Quenching distance	消炎距離
Smallsats (smaller satellites)	小型衛星
Solid propellant rocket motor	固体推進ロケット
Specimen	試験片
Spouting velocity	噴出速度
Successive burning	連続燃焼
Thermal conduction	熱伝導
Thermal convection	対流熱
Thermal pyrolysis	熱分解
Thermal radiation	熱放射（熱輻射）

Thermal structure	熱構造，燃焼構造
Thermocouple	熱電対
Thrust force	推力
Thrusting performance	推力性能
Well-mixed propellant	多孔質固体燃料に液体酸化剤を 湿潤させた推進剤

Acknowledgement

My doctoral program was supported by scholarship program founded by Toyohashi University of Technology, and this research is partially supported by the Nitto cooperation. I would like to extend my sincere gratitude to all of the staff members whom it may concern.

I would like to express my heartfelt thanks for dedicated work and for tremendous time made by Prof. *Hideaki YANADA* (TUT), Prof. *Kentaro Doi* (TUT), and Prof. *Harunori NAGATA* (Hokkaido University) to review my dissertation. They have provided valuable and fruitful comments on my dissertation. Their invaluable comments and hard work to review my dissertation are greatly appreciated.

I would like to express my deepest appreciation and profound gratitude to Prof. *Yuji NAKAMURA* for the dedication that has been made ever to me over the last 6 years of my entire research activities under the supervision from him. He has been committed to sparing his tremendous time to make discussion on my research all the time until finishing writing this doctoral dissertation completely. In addition, he had spent much of time to realize my short stay for ten months in Stuttgart, Germany when I was in 1st year of my master program. At the time, he was spending his time with me to address a bunch of applications, such as scholarship program for the stay (applications, especially for 7th TOBITATE All Japan Young ambassador program and short program at University of Stuttgart). Thanks to his commitment to it, my short stay there was successfully finished with the best quality of the experience, gaining not only the academic skills, but also the international mind. Secondary, he has cared of my health and talked a lot about what is an academic world and even small talks during my student life here and helped to broaden my horizon from various points of view. I'm pretty sure that I wouldn't have gained such a

professional experience if he was not my professor, not only about my (academic) research skills, but also about an internationally minded I have ever gained. I would like to appreciate so much again for the dedication and fruitful advice on professional skills and such the experience.

I would like to convey my sincere gratitude to associate professor, *Tsuneyoshi MATSUOKA* for his hard work made ever to me during my entire student life here. When I was in my master program, he was my supervisor and has been encouraged me at the time. Especially for the period of my master program, significant time and effort were given for me to advise on the experiment and my master thesis. Thanks to the dedicated advice, I could finish my master program and my doctoral program. The hard work and the dedication are greatly appreciated. Besides, I would like to express appreciation for adding me as a co-author to a journal paper entitled "Necessary condition for measurement of heat flux sensor using a thermoelectric module". I had learned a lot, which is valuable for an academic person, during entire period until the paper was publicized.

I would like to thank assistant professor, *Takuya YAMAZAKI*, very much for the technical advice on the doctoral program, how to write papers, etc. With the advice, I could spend my doctoral program very smooth. Especially, without the technical discussion on the experiment for the 2nd paper, I couldn't complete obtaining all the date shown in the paper. The technical advice and assistance made ever to me are greatly appreciated. Secondary, I would like to express my sincere gratitude to Dr. *Ju Xiaoyu* for advising me a lot from his entire researcher life and what an academic life is. He has always told me not only about the small things, but also discussion about my research and dissertation, especially for the discussion on the 2nd paper submitted to Journal of Thermal Science and Technology. The supports and the daily discussion are highly appreciated.

For my laboratory members, I would like to appreciate all of members of the ECE laboratory and alumni. Especially for my colleagues: *Akihiro YOSHIMASA*, *Kanata OGISO*, *Kento KIKUTA*,

Kisuke SATOMI, *Masashi KAMIJO*, *Mikio MIZUNO*, *Satoshi MURAKAMI*, and *Takuma KAJIMOTO*. They had always supported me during the entire period of my student life until we graduated from our master's program and still have got in touch with me to cheer me up to complete the doctoral dissertation. Thank you very much for the supports from them all. Secondary, I would like to express my gratitude to former students in this lab.: *Shoma KAWAMURA* and *Masashi MASUDA*, who all supported me when processed the experimental setup. I could finish all the experiments thanks to their advice. To *Shun SATO*, *Tatsuki KOJIMA*, and *Tatsuya MIGITA*, I cannot say thank you enough for tremendous supports from them. their supports had greatly helped me. Lastly, the experimental supports from *Yosuke HASEBE* are greatly appreciated. I could write completely the 2nd paper for his hard work.

I would like to express my sincerest appreciation to my family; Sakura, Takeshi, Yoshiki, Nanaka, Yukihiko, and Akemi who all have given countless supports all the time during my student life all the time. If there were no help from them all, I have to say that I have not completed my student life without good health. To my mother, *Sakura MATSUGI*, I cannot say thank you enough from her always support and help. I couldn't definitely have completed my entire student life without her supports. Her tremendous supports made ever to me is greatly appreciated in especial. To the late my grandfather, *Yukihiko NAKAYAMA*, he had always given me interesting stories about the space and rocket, and these stories made me realize the interest in the scientific field. It is not too much to say that the reason and the motivation for this challenge in the doctoral program shall be given from him. I have always wanted to say thank you very much. I'd be happy if he were warmly on my side from now on.

To *Reiko MATSUI*, lastly, I would like to express my deepest gratitude for tremendous supports from her. She has helped me all the time. I have to say that if there's no support from her, I have

not completed this dissertation and not done the papers necessary for my graduation. Thank you very much for being at my side all the time. Furthermore, she has taken care of my physical health and mental health in kind ways as possible as she can. The supports she made is the most powerful and made me energetic. I cannot say thank you enough to her for the greatest support.

Chapter 1

1 Introduction

1.1 Introduction and objective of this chapter

With a recent growth in microelectronics' technologies, many research groups have started to develop smaller satellites for space activities. On the other hand, the current launch vehicle is incapable of reducing manufacturing time and cost, so that the launch supply for the smaller satellites' customers is insufficient at this time. In addition to these limitations, it is hard for the small satellites' customers to select their preferable launch timing and orbit, because the launch timing and the destination is pre-determined by the large satellites' customers as primary customers. To respond the trend and accelerate the space activities by the smaller satellites further, a dedicated small launch vehicle, which can reduce manufacturing time and cost and achieve flexible launch timing and orbit selection for smaller satellites' customers, is highly demanded.

In this chapter, we aim to introduce not only the current situation of the space activities with the smaller satellites, but the limitations associated with the current launch vehicles and with the dependence on the demand from the primary customers. Together with these limitations, we also aim to introduce necessary features for the dedicated small launch vehicle in this chapter while introducing chemical rocket systems mainly used for the launch vehicle.

1.2 Current situation on space activities

1.2.1 Smallsats

With the recent dramatical growth and technological progress in microelectronics, materials, and its assembling process, miniaturized artificial satellites, commonly referred to as “smallsats”, have been drawing significant interests by engineers and researchers for the last twenty years [1] [2] [3]. The smallsats are classified into Pico, nano, micro, and minisatellites (they all are hereinafter called “smallsats”), depending on its mass in a range between 1 kg and 250 kg [4] [5], as summarized in Table 1 - 1.

Table 1 - 1 Generally accepted definition of smallsats mass class under 250 kg, cost, and time

	Mass [4]	Cost, Millions of dollars [5]	Time, Years [5]
Minisatellite	100 – 250 kg	75	2
Microsatellites	10 – 100 kg	50	1 – 2
Nanosatellites	1 – 10 kg	1 – 5	1
Picosatellite	< 1 kg	< 0.5	< 1

Examples of the smallsats are shown on the following figure [6] [7]. The satellites are now capable of reducing its scale by the palm of the hand, thanks to the recent progress in the technologies.

Up to present, many research groups in even university laboratories and small-medium companies have started to develop the smallsats by their own capability due to its attractive benefits: more reduced manufacturing time, significantly more cost effective, scale down capability, and easier to manufacture, to name a few [5] [8], in comparison with traditional large satellites. In the future, it is therefore expected that the great efforts made by the research groups will make our life better further, for instance, better remote sensing technologies for the weather forecast based on the Earth and stratosphere observation [9] [10], space communication, even clean energy generation in the space environment (so called “space solar power system”) [11] [12], educational projects (CubeSats projects) [13], disasters management, and more.

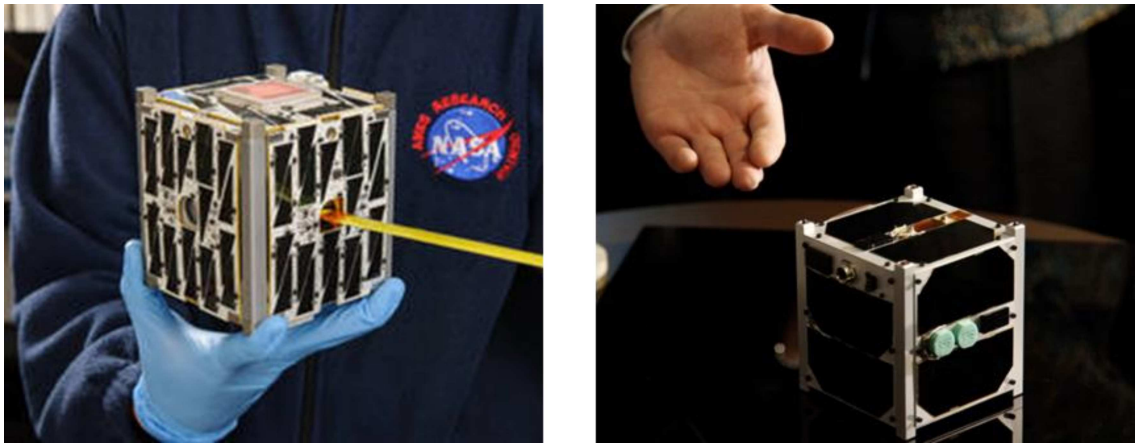

Fig. 1 - 1 Typical examples of hand-sized smallsats [6] [7].

In reality, as shown in Fig. 1 - 2, the weight of the satellites launched already shows a decreasing trend, and the number of the launches for the smallsats under the mass weight of 200 kg a year

has dramatically increased over the last ten years, as shown in Fig. 1 - 3. Therefore, the smallsats will continue to be paid much attention further for the space activities and accelerate owing to the beneficial advantages.

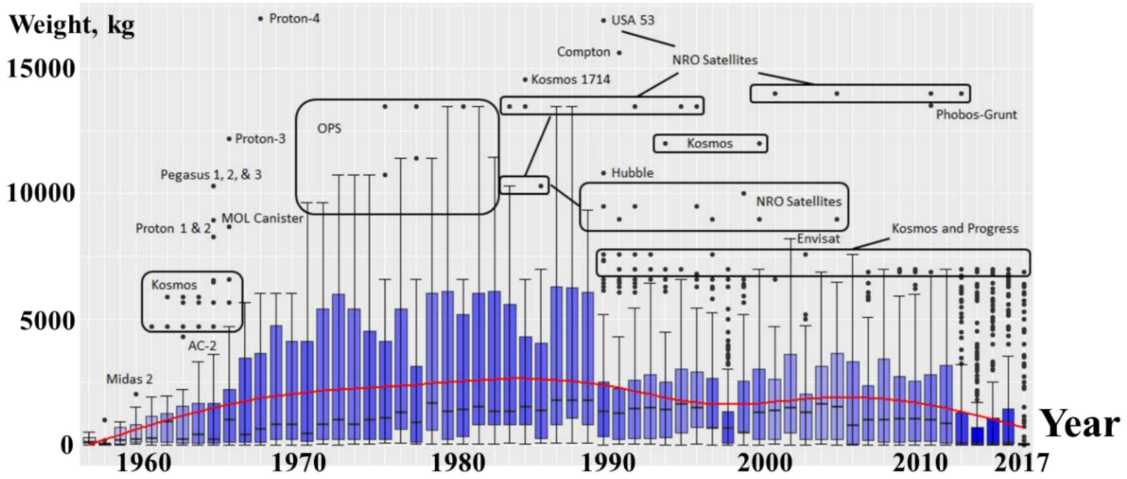

Fig. 1 - 2 World trend of time history of satellite weight [3].

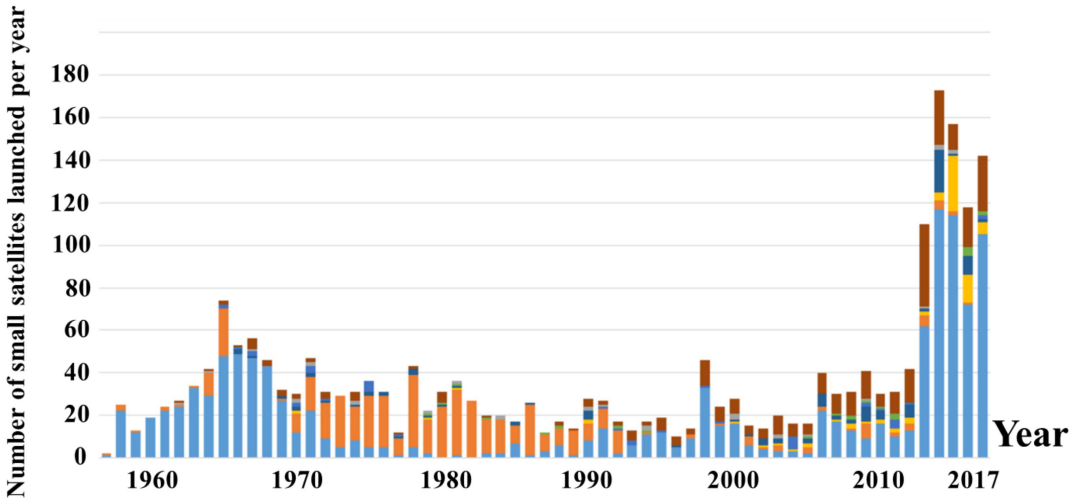

Fig. 1 - 3 World trend of number of small satellite weight (< 200 kg) launched per a year [14].

1.2.2 Current limitations on smallsats' customers

In contrast to the increasing number of the development in the smallsats, the launch service supplies for the smallsats' customers are not provided enough [2]. Currently, only the launch vehicle available for launching the smallsats into the space environment from the ground is the "chemical rocket system". The smallsats are loaded into the launch vehicle, namely the chemical rocket system, as payloads and transported into a designated orbit for respective missions. A set of the large-sized launch vehicle (Fig. 1 - 4), which consists of a combination of the chemical rocket system of a large liquid-propellant rocket engine and composite solid rocket boosters, has been mainly used. Typical examples of the current large-sized launch vehicle, which has ever launched worldwide, is listed in Table 1 - 2. As it is found, the liquid-propellant rocket engine and solid-propellant rocket boosters have been mainly used for the space missions.

Table 1 - 2 Typical examples of large sized rocket system launched ever worldwide.

Name	Country	Operational period	Engines
Arian 4 [15]	Europa (ESA)	1988-2003	Liquid rocket engine
Space shuttle [16]	United states (NASA)	1981-2011	Liquid rocket engine Two solid rocket boosters
H - II [17]	Japan (JAXA)	1994-	Liquid rocket engine Two solid rocket boosters

Basically, the majority of the smallsats are launched by the launch vehicle as secondary payloads, which is so called "*piggyback*" payload that utilizes launch capability of the large-sized launch vehicle, or so called "*cluster launch*". Since the launching timing and the destination of the launch vehicle depends on demands from the primary payloads' customers, the smallsats' customers (secondary payloads' customers) do not have a priority to select the launching timing and the destination, and they have to contend with the orbit pre-determined by the primary payload customer [2]. Thus, they do not have much choice not only for the launch timing but the selection of their orbit, as the destination is pre-determined by the primary payload customer. In addition to the limitation related to the secondary payload, the current large-sized launch vehicles are not capable of reducing manufacturing cost and time owing to several reasons (will be mentioned in next section).

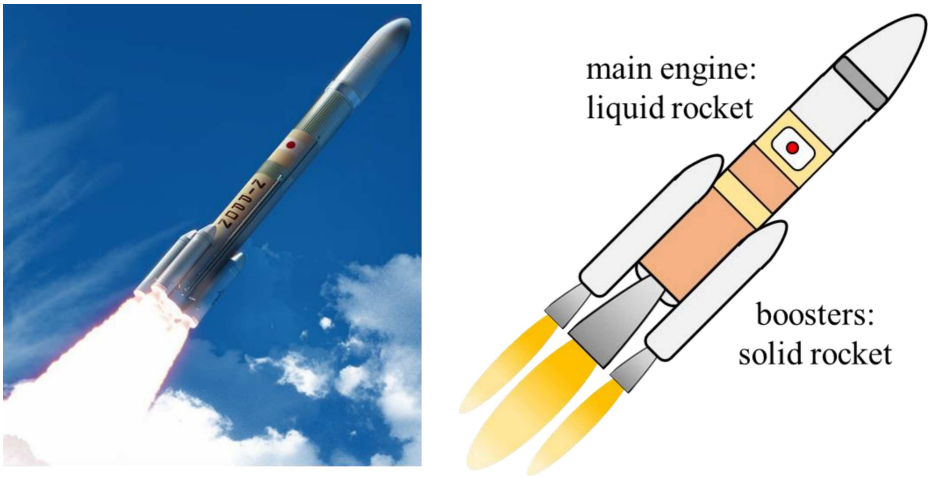

Fig. 1 - 4 Current large launch vehicle consisting of liquid-propellant rocket engine and solid-propellant rocket boosters [18].

With this respect, launch supplies to the smallsats' customers have been further limited because of the limitations associated with the dependence on the demands from the primary customer and associated with the cost and size of the current launch vehicle.

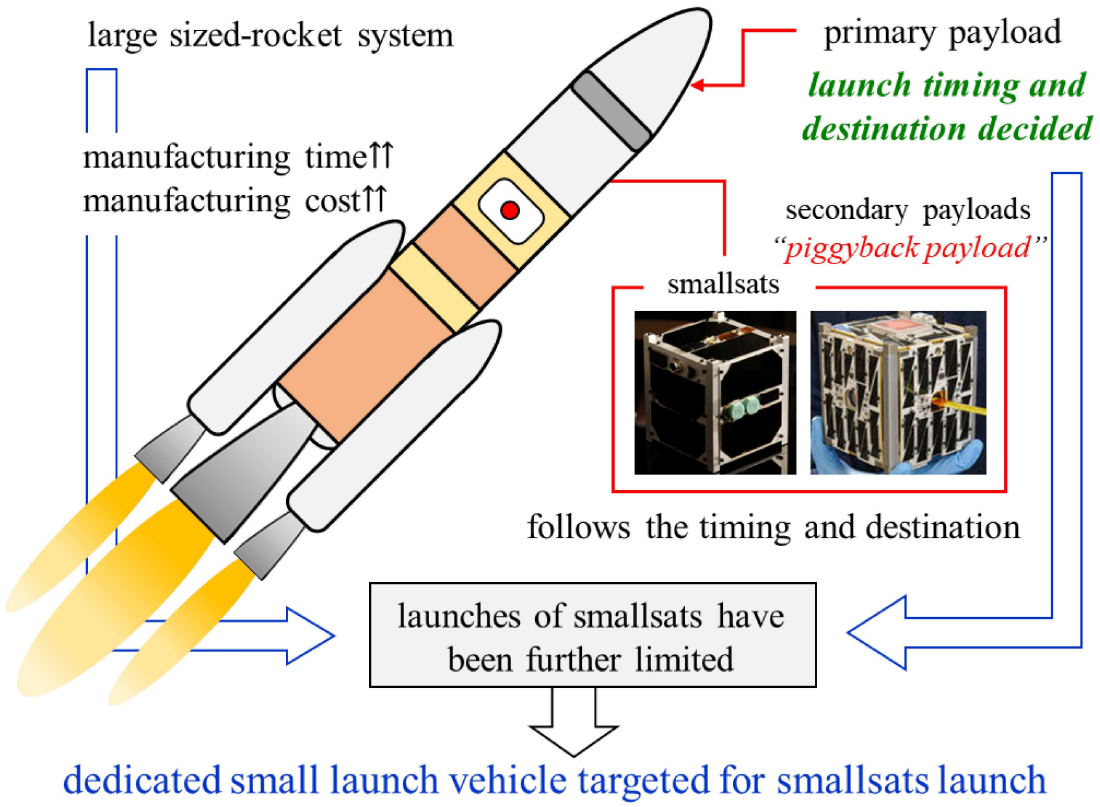

Fig. 1 - 5 Schematic explanation of a series of limitations associated with current launch vehicle and dependence on demand from primary customers.

In especial for the research groups in the universities and small-medium companies, the reduced cost for launching their smallsats is highly demanded. For the aforementioned reasons, a "*dedicated small launch vehicle*" mainly targeted for the smallsats as the main payloads (primary

payloads), which can realize the flexible launch timing, the flexible orbit selection, the reduced manufacturing time, and reduced cost, is now highly demanded to provide enough opportunities to the smallsats' customers [19]. The aforesaid limitations related to the current launch vehicle are schematically summarized in Fig. 1 - 5.

1.2.3 Necessary features for dedicated small launch vehicle

In order to reduce the effect of the intrinsic limitations on the smallsats' customers, the features necessary for the dedicated small launch vehicle mainly targeted for the smallsats as the primary payloads are summarized in Fig. 1 - 6.

Fig. 1 - 6 Features demanded for dedicated small launch vehicle mainly targeted for launching smallsats.

More importantly, to transport the smallsats to the space environment, comparable thrusting performance to the existing launch vehicle shall be required for the practical uses. In the following, we will touch ways to meet the necessary features (summarized in Fig. 1 - 6) for the dedicated small launch vehicle by using the current launch vehicle while introducing features, advantages, and disadvantages of the chemical rocket system used for the current launch vehicles.

1.3 Chemical rocket systems

When the launch vehicle goes upward toward the space environment from the ground, 9.8 m/s of the velocity per a second is reduced due to the gravitational acceleration. The only launch vehicle that can overcome the effect of the gravimetric acceleration, while ascending, is “chemical rocket system” because of the excellent thrusting performance. As altitude of the chemical rocket system is higher, the ambient air (oxygen) is less, and therefore the chemical rocket system are necessary to have both the oxidizer and fuel in itself. In addition, they all are systems that converts thermal energy generated by chemical reaction in combustion chamber (where the propellant burns) into kinetic energy via a rocket nozzle attached downstream.

The chemical rocket systems are specifically broken up into three systems, depending on its phase of the fuel and the oxidizer used for the propellant: liquid-propellant rocket engine and solid-propellant rocket motor. Although the practical application has been limited, hybrid-propellant rocket motor is well known and has been of a significant interest for rocket community. The features, advantages, disadvantages, and the schematic illustrations for each chemical rocket system, together with the reason for the limitations stemmed from each chemical rocket system mentioned above will be touched. Plus, the ways to meet the necessary features shown in Fig. 1 - 6 for the dedicated small launch vehicle are discussed for each chemical rocket system here.

1.3.1 Liquid-propellant rocket engines

The liquid-propellant rocket engines (hereinafter called “liquid rocket”) have been widely used as the most launch vehicles for the main engine since 1920’s [20]. The schematic illustration of the liquid rocket is drawn in Fig. 1 - 7. The liquid fuel and liquid oxidizer are physically separated in each tank, and premixed-gas mixture that is made at the premixed chamber is injected into the combustion chamber, occurring continuous combustion. Thrust force, as the thrusting performance, that is power of the chemical rocket system is then generated by ejecting high-temperature and high-pressure gas generated in the combustion chamber through the nozzle to the atmospheric environment. The advantages of the liquid rocket are the highest specific impulse (the terminology will be mentioned later), its flexible controllability of thrust force, re-ignition, and re-start capability, and a wider range availability of fuel-oxidizer combination can be available. Also, propellant combination of hydrogen and oxygen is quite environmentally friendly to the atmospheric environment. On the other hand, the liquid rocket is composed of a set of complex system composed of fuel and oxidizer feeding system, cooling units of the liquid oxidizer and fuel, pumps to pressurize the oxidizer and fuel, turbines, and more, so that reduced rocket size and reduced manufacturing cost would be hard to be achieved, hence, the liquid rocket is found that it may not be suitable for the dedicated small launch vehicle, owing to its structural

complexity. The longer manufacturing time and higher amount of the cost are firstly addressed in the liquid rocket for the dedicated small launch vehicle; however, current technologies would be incapable of achieving these issues, and the liquid rocket has not been found not to be promising for the dedicated small launch vehicle.

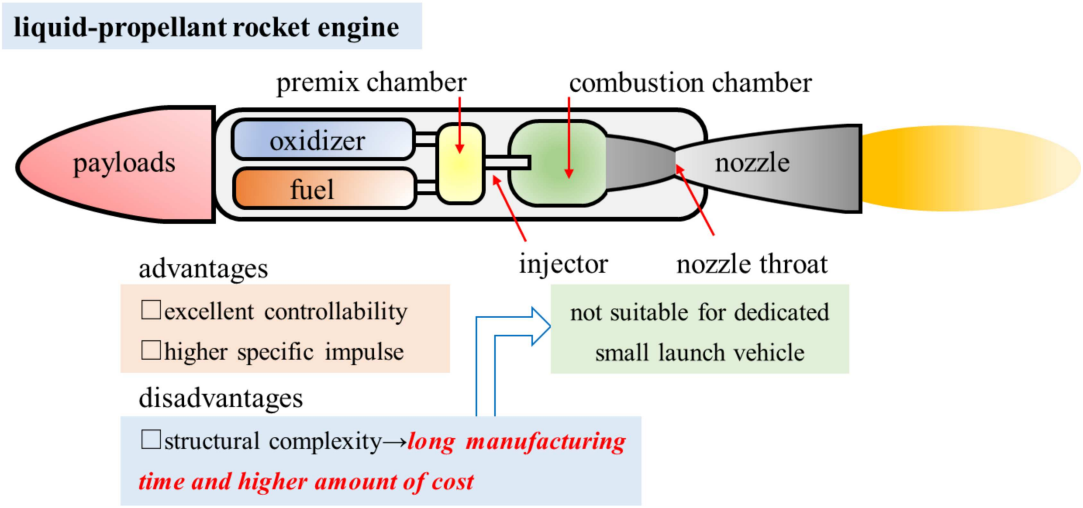

Fig. 1 - 7 Schematic illustration of configuration of liquid-propellant rocket engine, and advantages and disadvantages found in liquid propellant rocket engine, together with reason for not suitable for dedicated small launch vehicle.

1.3.2 Solid-propellant rocket motors

The solid-propellant rocket motors (we call “solid rocket” hereafter) have also widely used, for instance, for the launcher boosters as illustrated in Fig. 1 - 4, tactical and strategical missiles, as well as a small-sized launch vehicles alone for several decades [21] [22]. The schematic illustration, the advantages, and disadvantages of the solid rocket employing general composite solid propellant is shown in Fig. 1 - 8. They have been drawing attractive advantages: structural simplicity, higher reliability in operation than liquid rocket, excellent thrusting performance, and a relatively simple manufacturing process [23] [24].

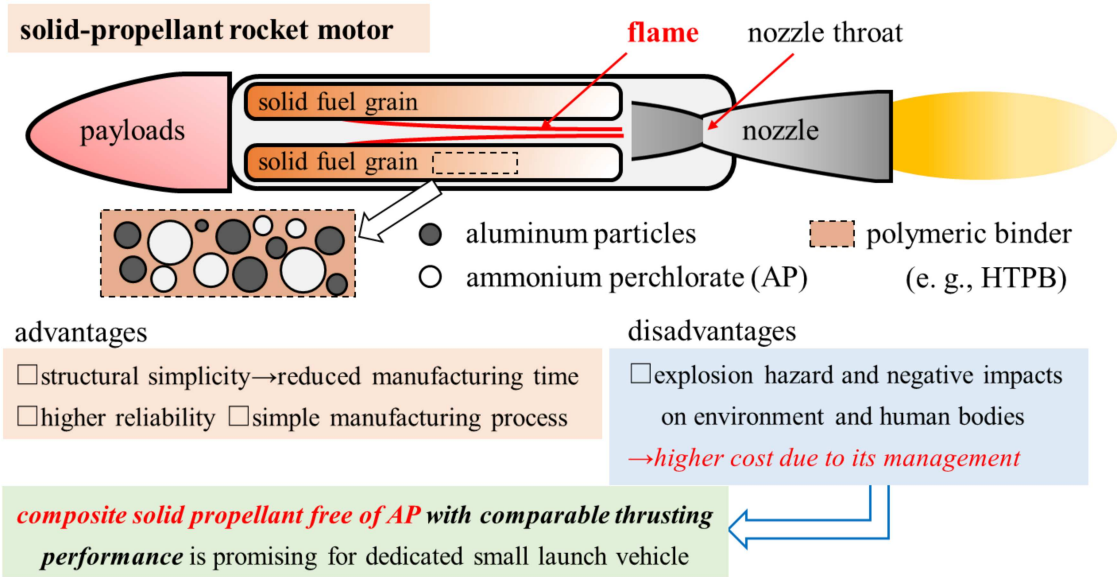

Fig. 1 - 8 Schematic illustration of configuration of composite solid propellant based on ammonium perchlorate as solid oxidizer, aluminum particles as energetic additive, and HTPB as fuel binder, and advantages and disadvantages found in solid-propellant rocket motor, together with feasibility to dedicated small launch vehicle.

The general composite solid propellant consists of lots of ammonium perchlorate (AP, chlorine-based oxidizer) as a solid oxidizer, aluminum particles (Al) as an energetic additive, and HTPB (hydroxyl-terminated polybutadiene) as a polymeric binder to condensate all the components together. This composite solid propellant is frequently called “AP-based composite solid propellant”. Although the AP-based composite solid propellants have been drawing the attractive advantages, however, AP behaves as an explosive [25], so that it is carefully handled to ensure our safety from explosion, when manufacturing, transporting, storage, and its operation of the propellant. Therefore, high amount of management cost associated with the management of AP is inevitable. According to a literature, the total costs stemmed from the management of AP account for important percentage for the solid rocket [26]. In addition, it has been pointed out that the AP-based solid propellants release gaseous hydrogen chloride (HCl) and have given negative impacts on the environment and our health, for instance, ozone layer depletion, acid rain, and atmospheric contamination [27] [28]. According to the European and international agendas, the environmentally friendly launch vehicle, which can reduce those negative impacts on the environment and human bodies, have become a top priority for sustainable developments and future use [29].

For aforementioned reasons, a composite solid propellant using environmentally friendly solid

oxidizer (not AP) sounds good for the dedicated small launch vehicle. With this respect, the reduced amount of management cost can be achieved. The rest of the features necessary for the dedicated small launch vehicle with AP-free composite solid propellant is to guarantee the comparable thrusting performance to the existing launch vehicles.

1.4 Traditional hybrid-propellant rocket motors

The chemical rocket system, which uses a cylindrical polymeric solid fuel and liquid/gaseous oxidizer, is called “hybrid propellant rocket motor” (hereinafter called “hybrid rocket”). The schematic illustration of the traditional hybrid rocket is presented to Fig. 1 - 9. The history of the development in the traditional hybrid rocket is by no means old and can be dated back to 1930s. The traditional hybrid rockets have paid much attention by many research groups (i.e., [30] [31] [32] [33] [34] [35]) for a long time because of its excellent advantages; less-explosion hazard, flexible throttle ability, re-ignition, and re-start capability [36] [37]. The advantages and disadvantages of the traditional hybrid rocket are firstly drawn in Fig. 1 - 9. Combustion is taken place inner the cylindrical solid fuel surface continuously reacted with the pyrolysis gas and the injected oxidizer gas. As the combustion progresses, the diameter of the cylindrical solid fuel is enlarging during the burning event. Since both the oxidizer and fuel are physically and chemically

separated, and the explosive such AP is not employed under a concept of the traditional hybrid rocket, reduced explosion hazard in comparison with the liquid rocket and solid rocket can be emphasized on [38] [39], leading to lower management cost.

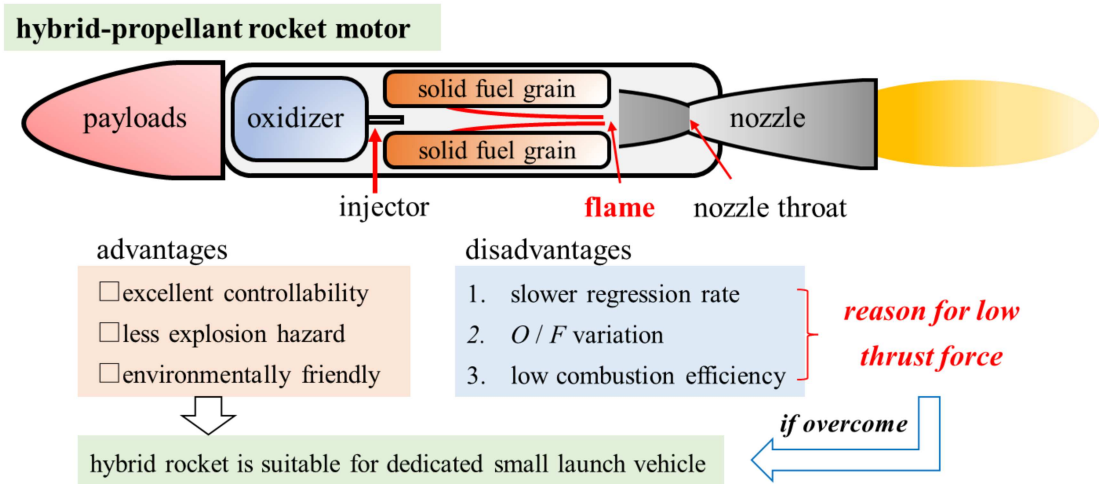

Fig. 1 - 9 Schematic illustration of hybrid-propellant rocket motor, advantages and disadvantages found in hybrid-propellant rocket motor, together with feasibility to dedicated small launch vehicle.

Moreover, the hybrid rocket can be considered as an environmentally friendly propellant [31] [40] because a polymeric solid fuel (e.g., hydroxyl-terminated polybutadiene (HTPB), polyethylene (PE), etc.) is usually selected as the solid fuel. In the hybrid rocket, a wide range of fuel-oxidizer combination is available (oxidizers i.e., gaseous or liquid oxygen, nitrous oxide N_2O, hydrogen peroxide H_2O_2, etc. [41]). The structural complexity can be also avoided because of the relatively simple structure in comparison with the liquid rocket [42], as the only needs to be

equipped with one feeding system for the traditional hybrid rocket. For this reason, the hybrid rocket is the rocket system that has the excellent advantages of the solid rocket and liquid rocket.

On the one hand, despite of those attractive advantages, the practical application has been quite limited as compared with those chemical rocket systems because of the disadvantage of lower thrusting performance of the hybrid rocket. In particular, it is said that the main shortcoming of the lower thrusting performance is attributed to the slower regression rate (rate at which the diameter recedes) of the solid fuel [41] [43]. Other than the slower regression rate, variation of the oxidizer-to-fuel mass flow rate ratio (O/F) during the burning event and lower combustion efficiency due to poor mixing and diffusion at the solid fuel surface are the reason for the lower thrusting performance. For these reasons, many research groups have been made significant effort to upgrade the thrusting performance of the traditional hybrid rocket so far. If these intrinsic disadvantages of the lower thrusting performance in the traditional hybrid rocket are improved, and it sounds very attractive for the dedicated small launch vehicle due to its excellent advantages. The advantages and disadvantages in the traditional hybrid rocket as compared with the existing liquid rocket and the solid rocket are lastly listed in Table 1 – 3 as follows.

Table 1 - 3 Advantages and disadvantages of hybrid rocket vs liquid rocket and solid rocket

	Solid rocket	Liquid rocket	Hybrid rocket
Structure	Simple	Complex	Relatively simple
Controllability[*1]	Difficult	Easy	Easy
Explosion hazard	High	Medium[*2]	Low
Thrust force	Large	Large	Small
Burned gas	Harmful	Harmful-less	Harmful-less
Specific impulse	-250[*3]	-400[*4]	-300[*5]

*1. Thrust control, re-ignition, and re-start capability

*2. Potential explosion hazard once the liquid fuel is leaked. Especially for a case when liquid hydrogen is employed as liquid fuel, careful management and storage are necessary in operation to avoid leakage and explosion accident.

*3. Fuel combination is aluminum (18 %), ammonium perchlorate (68 %) and HTPB (14 %) [44]

*4. When fuel combination is liquid oxygen and liquid hydrogen [44]

*5. When fuel combination is liquid oxygen and HTPB [44]

1.5 Feasibility of chemical rocket for dedicated small launch vehicle

The ways that shall be introduced for each chemical rocket system, necessary to meet the features for the dedicated small launch vehicle shown in Fig. 1 - 6, are schematically summarized in Fig. 1 - 10. As we have already stated, the liquid rocket would be incapable of achieving the reduced manufacturing time and reduced cost, owing to its structural complexity. Therefore, the liquid rocket may not be suitable for the dedicated small launch vehicle. The composite solid propellant sounds promising for the dedicated small launch vehicle, in terms of the reduced

manufacturing time from the benefit of the structural simplicity. However, high amount of the management cost associated with the handling of the explosive (AP) and negative impacts on the environment and human bodies should be unavoidable. The solution is to use environmentally friendly solid oxidizer (not AP), while achieving the comparable thrusting performance to the existing AP-based solid propellant.

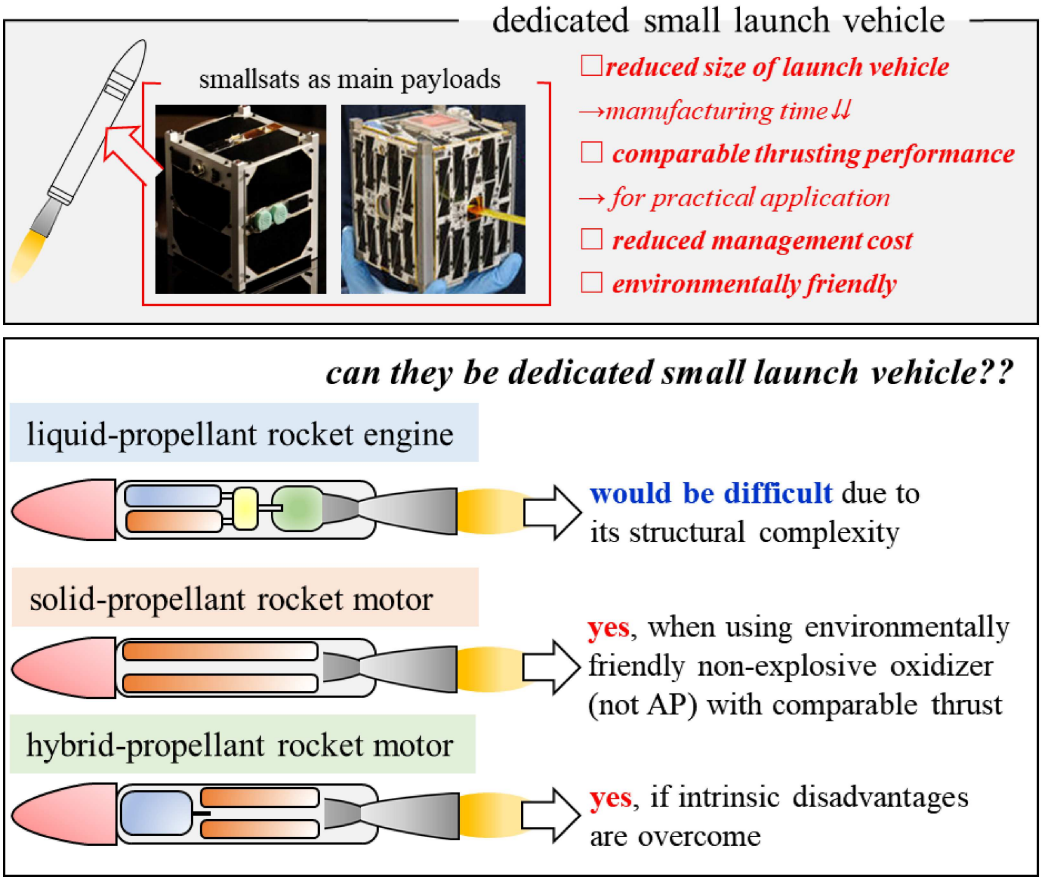

Fig. 1 - 10 Necessary features for the dedicated small launch vehicle and ways that should be introduced for each chemical rocket system.

The hybrid rocket can achieve the reduced manufacturing time and reduced cost due to the use of environmentally friendly solid fuel and oxidizer and relatively simple structure, whereas the technical and challenging tasks to improve the lower thrusting performance, due to slower regression rate, *O*/*F* variation, and lower combustion efficiency, still remain. Thus, if these intrinsic disadvantages are overcome, the hybrid rocket sounds attractive to the dedicated small launch vehicle.

For the abovesaid reasons against each chemical rocket system, the composite solid propellant, which is free of the explosive (AP), and the hybrid rockets have been of significant interests by many research groups all over the world for the dedicated small launch vehicles. In the next chapter, a literature review on great efforts by many research groups, to realize the dedicated small launch vehicle by the AP-free composite solid propellant and the hybrid rocket, will be made.

1.6 Concluding remarks in this chapter

The current situation of the space activities with smallsats and the limitations related to the current launch vehicles and to the dependence from the primary payloads' customers were stated. We have also touched the chemical rocket systems used for the space activities: the liquid rocket, the solid rocket, and the hybrid rocket, and the configuration, advantages, and disadvantages of the chemical rocket systems were summarized. In addition, to reduce the effect of the limitations, it was stated that the dedicated small launch vehicle for the smallsats has been highly demanded. It was summarized that the features necessary for the dedicated small launch vehicle were the reduced manufacturing time, reduced cost, environmentally friendly, and together with the comparable thrusting performance to the existing launch vehicle. It was found that the liquid rocket would be hard to become the dedicated small launch vehicle because of the disadvantages associated with the structural complexity, and the AP-based composite solid propellant is not promising to become the dedicated small launch vehicle, due to the higher amount of management cost and negative impacts on the environment and human bodies. For this reason, it was concluded that the composite solid propellant free of the explosive such as AP, and the hybrid rocket, which can guarantee the comparable thrusting performance to the existing launch vehicle, were found to be promising for the dedicated small launch vehicle.

Chapter 2

2 Literature review, motivations, and objectives

2.1 Introduction and objective of this chapter

In this chapter, we aim firstly to introduce equations to describe the thrusting performance of the composite solid propellant and the hybrid rocket and to discuss methodologies to increase the thrusting performance of those propellants, since many research groups have been upgrading the AP-free composite solid propellant and various type of the hybrid rockets, which are based on the methodologies. The literature review of the significant effort made by many research groups, concerning various type of the composite solid propellants and the hybrid rockets to increase their thrusting performance will be then made here. Based on the literature review, the motivations and objective of the present dissertation will be stated in the last of this chapter.

2.2 Thrusting performance evaluation

It was mentioned that the comparable thrusting performance to the existing launch vehicles is of great importance for the replacement into the dedicated small launch vehicle. First of all, brief explanation for evaluating the thrusting performance on the hybrid rocket and the AP-free

composite solid propellant is made here. The following figure can be referred to for good readability of the following discussion.

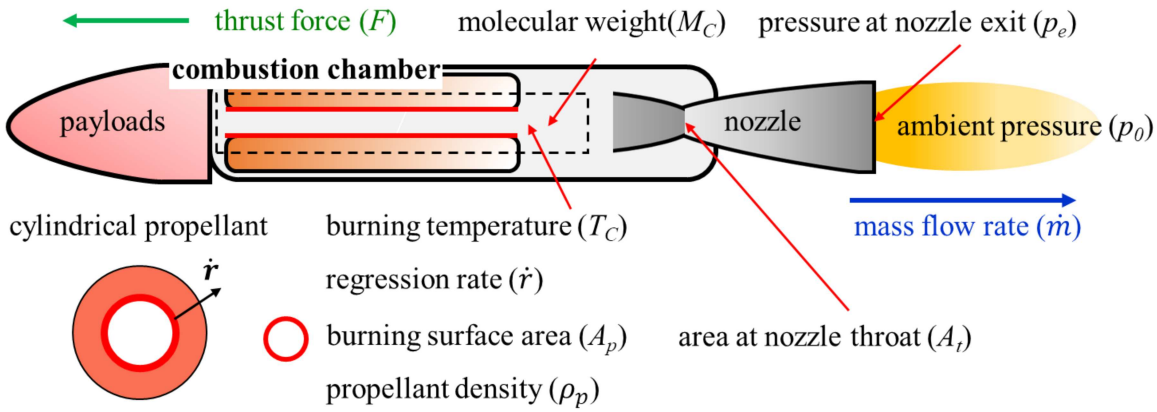

Fig. 2 - 1 Schematic illustration of location of each physical properties and explanation used for evaluating thrusting performance.

2.2.1 – Mass flow rate $\dot{m}$–

Since the chemical rocket system is a system that converts the thermal energy generated by chemical reaction into the kinetic energy, it should be paid attention to know how large amount of the propellant is burned and ejected from the propellant through the rocket nozzle into the atmospheric environment. The indictor to exhibit “how large amount of the propellant is burned” is a mass flow rate. The mass flow rate denotes a unit mass burned at the burning surface of the propellant per a second, $\dot{m}$ [kg/s] and is defined as the following equation. The equation is divided

into two cases, and the former equation and the latter equation are expressed as the mass flow rates for the composite solid propellant and hybrid rocket, respectively.

$$\dot{m} = \rho_P V_f A_P \text{ or } \dot{m} = \rho_S V_f A_P + \dot{m}_O \qquad \text{Eq. 2 - 1}$$

where ρ_P [kg/m^3] is the average density of the propellant, V_f [m/s] is the regression rate (the rate at which the propellant is consumed), and A_P [m^2] is the burning surface area of the propellant, ρ_S [kg/m^3] is the density of the solid fuel, and $\dot{m}_O$ [kg/s] is the oxidizer mass flow rate injected into the solid fuel port, respectively. As is expressed, the large amount of the mass of the propellant can be released for the case of (1) higher density of the propellant or the solid fuel (ρ_P, ρ_S), (2) faster regression rate (V_f), and (3) larger burning surface area (A_P). In the hybrid rocket, it is also important to inject higher amount of the oxidizer mass flow rate ($\dot{m}_O$).

2.2.2 – Specific impulse I_{SP} –

Next, the specific impulse is introduced here. The specific impulse denotes the thrust force produced per unit rate of the consumption of the propellant, thus the specific impulse shows a propellant efficiency. The specific impulse (unit: second), which is defined as the following relation derived from so called the “nozzle theory” [44], is frequently used for performance

evaluation of the chemical rocket system.

$$I_{SP} = \frac{1}{g_0}\sqrt{\frac{2k}{k-1}\frac{R}{M_C}T_C\left\{1-\left(\frac{p_e}{p_C}\right)\right\}^{\frac{k-1}{k}}} \qquad \text{Eq. 2 - 2}$$

where I_{SP} [s] is the specific impulse, g_0 [m/s^2] is the gravimetric acceleration at the sea level, k [-] is the specific heat ratio of the burned gas, R [J/mol·K] is the universal gas constant, M_C [kg/mol] is the average gas molecular weight of the burned gas, T_C [K] is the burning temperature of the burned gas, p_e [Pa] is pressure at the nozzle exit, and p_C [Pa] is pressure in the combustion chamber. The specific impulse is helpful to know the efficiency of the propellant. It is seen that obtaining the lower average molecular weight (M_C) and the higher burning temperature (T_C) plays vital role in obtaining the higher efficiency of the propellant. On the one hand, the burning temperature and the average molecular weight of the burned gas are essentially pre-determined, depending on the oxidizer and fuel combination employed for the propellant, its oxidizer-to-fuel mass flow ratio (*O*/*F*), etc. Therefore, the specific impulse is essentially design value.

2.2.3 – Thrust force *F* –

The higher value of the specific impulse is a helpful indicator to know not only the propellant

efficiency but how fast burned gas is ejected from the rocket nozzle. The velocity ejected from the nozzle (v_e) is quite important since the rocket system goes upward according to the action and reaction by the Newton's third law. The velocity at the nozzle exit can be estimated with the following relation by using the specific impulse.

$$v_e = g_0 I_{SP} \qquad \text{Eq. 2 - 3}$$

With using the velocity, the thrust force (F) is estimated by the following equation.

$$F = \dot{m} v_e + A_e(p_e - p_0) \qquad \text{Eq. 2 - 4}$$

where F [N] is the thrust force, v_e [m/s] is the exit velocity ($I_{SP} \times g_0$), A_e [m^2] is the area at the nozzle exit, and p_0 [Pa] is the ambient pressure. The former term and latter term are so called "momentum thrust force" and "pressure thrust force", respectively. From a series of explanation, it can be understood that increase in the specific impulse (I_{SP}), mass flow rate of the propellant ($\dot{m}$), and pressure in combustion chamber (p_C), and pressure at the nozzle exit (p_e) plays very important role in the larger thrust force.

The ways to increase thrust force in the composite solid propellant and hybrid rocket mentioned above are summarized in Table 2 - 1. Based on this fact, most of the research in the composite solid propellant and the hybrid rocket has been focusing on increasing the ***"mass flow rate ($\dot{m}$)***

or *regression rate (V_f)"* and the ***"burning surface area (A_P)"*** of the propellant.

Table 2 - 1 Methodologies to increase thrust force in solid rocket and hybrid rocket.

Regression rate (V_f)	Faster
Burning surface are (A_P)	Larger
Burning temperature (T_C)	Higher (pre-determined)
Average molecular weight (M_C)	Lower (pre-determined)
Pressure (P_C)	Higher

2.3 Regression rate enhancement

Having stated that the key parameters to obtain the large thrust force was the faster regression rate as we have introduced from the last section, we will discuss the method to increase the regression rate with a following schematic illustration. The general expression to describe the regression rate (V_f) is shown as follows [45] [46] [47].

$$V_f \propto \frac{dT}{dx} \qquad \text{Eq. 2 - 5}$$

where dT/dx [K/m] is the temperature gradient between the flame and the top surface of the solid fuel. Therefore, it is fact that the regression rate enhancement can be possible by making the temperature gradient close to the top surface of the solid fuel steeper. In order to achieve this, it is well-known that, as shown in the case (1) on the figure, the higher burning temperature (T_C)

and employing the solid fuel having lower melting temperature (T_S) of the solid fuel make the temperature gradient steeper, resulting in the faster regression rate. With this regard, achieving the higher burning temperature helps not only to increase the specific impulse, but also to enhance the regression rate, simultaneously.

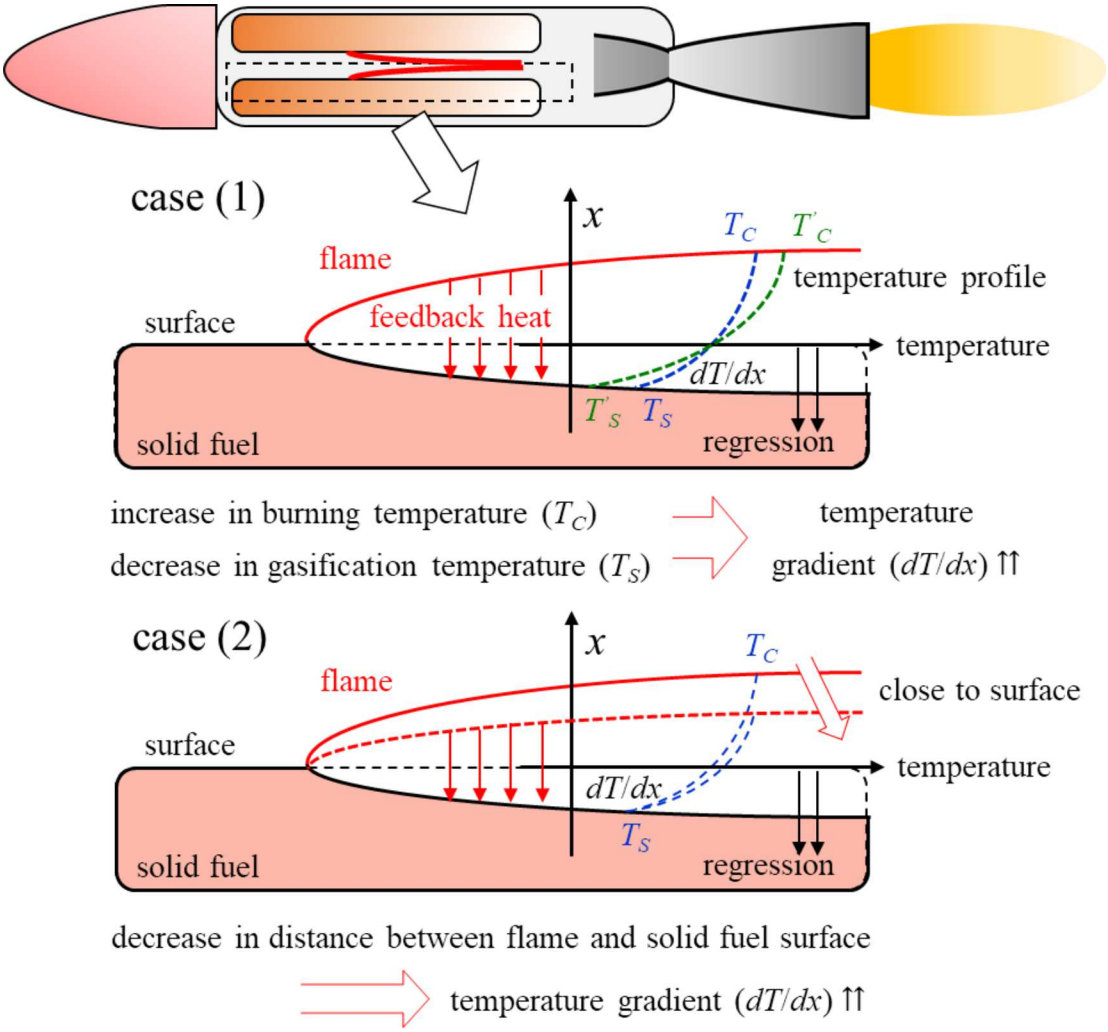

Fig. 2 - 2 Schematic explanation of ways to enhance regression rate: (case 1) increase in burning temperature (T_C) and decrease in gasification temperature (T_S) at solid fuel and (case 2) decrease in distance between flame and solid fuel surface to increase temperature gradient (dT/dx).

In addition to that, case (2) shows another methodology to increase the temperature gradient. It is also possible to enhance the regression rate by making the flame established closer to the top surface of the solid fuel. In reality, development in the composite solid propellant free of AP and the hybrid rocket has been focused on the methodologies based on Table 2 - 1 and Fig. 2 - 2. From the next section, we will make a literature review on the past research and the recent research and development concerning the composite solid propellant free of AP and the hybrid rocket.

2.4 Trend of research and development in composite solid propellants

In this section, we will review the previous works and recent works made ever for replacing the AP-free composite solid propellant into the dedicated small launch vehicle. Up to now, it has been extensively reported that various type of the composite solid propellants using environmentally friendly new solid oxidizer has been proposed all over the world. First, the AP-based composite solid propellant is reviewed.

2.4.1 Composite solid propellant with ammonium perchlorate (AP)

Ammonium perchlorate ("AP", NH_4ClO_4) has exhibited excellent performance, and the thrusting performance of the AP-based composite solid propellant can be tailored by its physical parameters [48]. The combustion of the AP-based composite solid propellant is firstly initiated by thermal decomposition of AP. Although the thermal decomposition of AP differs from its decomposing temperature, the typical processes of the thermal decomposition for AP above 573 K are governed by Eq. 2 – 6 [49].

$$2NH_4ClO_4 = Cl_2 + 2N_2O + O_2 + 4H_2O \qquad \text{Eq. 2 – 6}$$

As can be seen from the thermal decomposition process, chlorine (Cl_2) is released as the

decomposed product. The burning mechanism in the AP-based composite solid propellant at the propellant surface is schematically illustrated from a viewpoint of flame structure as presented to Fig. 2 - 3 [50].

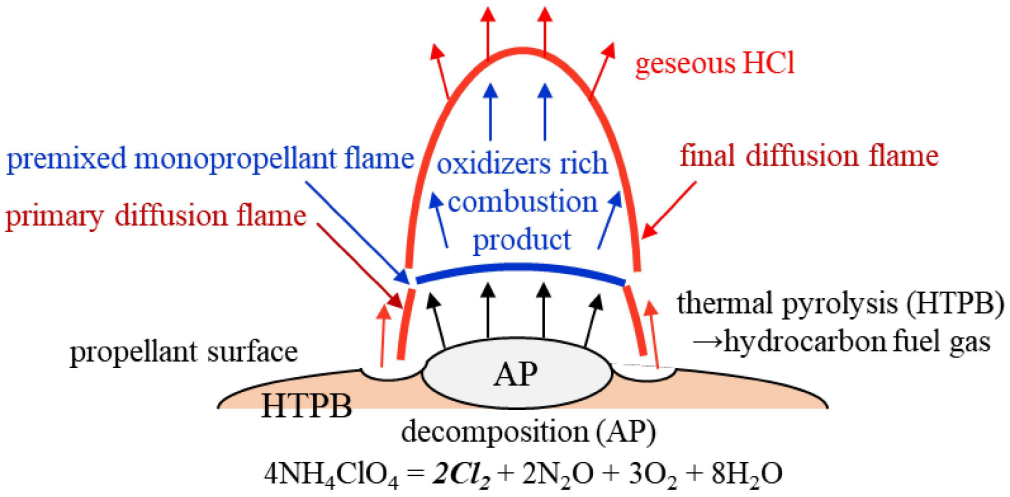

Fig. 2 - 3 Schematic illustration of flame structure and decomposition process of AP.

More importantly, chlorin (Cl_2) generated by the thermal decomposition process then combines with hydrogen component generated from the same thermal decomposition process and the combustion products to form gaseous hydrogen chloride (HCl), releasing to the atmospheric environment. As the gaseous HCl has decomposing nature of the ozone layer (O_3), it has been considered negative impacts on environment and human bodies, by releasing the combustion gas from the AP-based solid propellant. According to the literature [51], in the space shuttle boosters employing AP (containing around 503 tons of its propellant), each of booster produces on an

average of 100 tons of the gaseous HCl during its flight. In addition, in the European space launcher Arian-5 and the Vega launcher, 476 and 122 tons of the propellant produced 270 and 71 tons of the gaseous HCl, respectively, resulting in that more than half of the gaseous HCl was produced from the initial mass of the propellant during the flight. The amount of the emission of the gaseous HCl from the abovementioned launch vehicles is summarized in the following table.

Table 2 - 2 Propellant mass and amount of emission of gaseous HCl from launch vehicles.

Launch vehicle	Propellant mass	HCl emission
Space shuttle booster	503 x 10^3 kg	100 x 10^3 kg
Arian 5 booster	476 x 10^3 kg	270 x 10^3 kg
Vega launcher	122 x 10^3 kg	71 x 10^3 kg

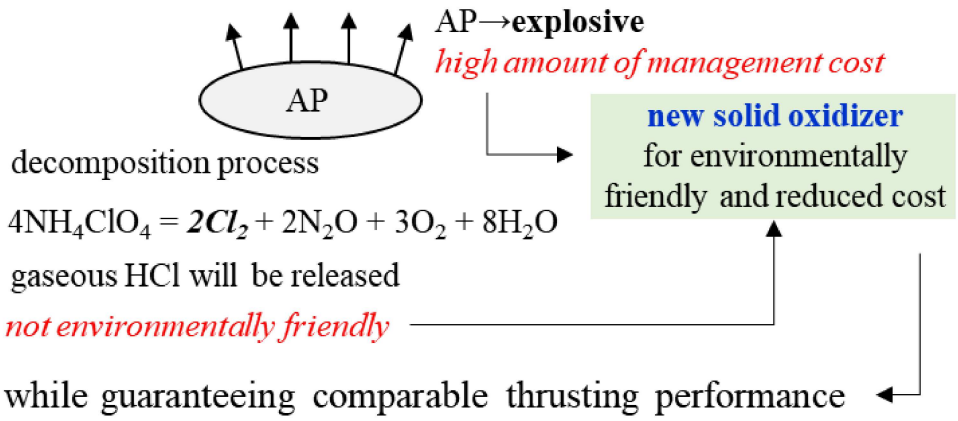

Fig. 2 - 4 Schematic illustration of decomposition process of ammonium perchlorate and reason for demand in new solid oxidizer.

Therefore, in the AP-based composite solid propellant, it has been a key word to achieve the reduced gaseous HCl so as not to give the negative impacts on the environment and human bodies. Also, AP is the explosive, so the replacement of AP into the environmentally friendly new (non-explosive) solid oxidizer and reduced management cost is required, as presented to Fig. 2 - 4.

2.4.2 Composite solid propellant with magnalium particles

As one of the ways to reduce the amount of the gaseous HCl, a composite solid propellant employing mixture of two kinds of metal particles consisting of aluminum and magnesium (so called “magnalium”), as the energetic additive, has been found to be promising [52] [53]. When the magnesium (Mg) particles burn together with the gaseous HCl, the gaseous HCl will be then transformed into the liquid phase, namely, magnesium chloride ($MgCl_2$) under the following chemical reaction is produced.

$$Mg + 2HCl \rightarrow MgCl_2 \text{ (liquid)} + H_2 \text{ (gas)} \qquad \text{Eq. 2 – 7}$$

With this way, the gaseous HCl is transformed into the liquid phase, and it has been highly expected to reduce the amount of the gaseous HCl released into the atmospheric environment. Belal et al. investigated the regression rate characteristics and its pressure dependency using a

propellant consisting of HTPB (14 wt.%), AP (71 wt.%), and magnalium (15 wt.%, Al: Mg = 1: 1). It was found that the regression rate of the propellant employing magnalium was measured at the rate of 9.9 mm/s (at 5 MPa) [52], and its mass flux can be calculated as 18.3 kg/(m^2·s). Habu et al. carried out firing experiments using a propellant composed of HTPB (15 wt.%), AP (65 wt. %), and magnalium (20 wt. %, Al: Mg = 1: 1) to examine its pressure dependency on the regression rate [53]. The regression rate obtained in their experiments was reported as about 8.5 mm/s at 5 MPa, and the corresponding mass flux can be calculated as 15.7 kg/(m^2·s). For a comparison purpose of the performance among the two cases and the conventional AP-based composite solid propellant, the corresponding mass fluxes for each propellant using the neat aluminum and magnalium are summarized as the following table.

Table 2 - 3 Regression rate and mass flux for AP-based composite solid propellant and composite solid propellant with magnalium corresponding to its oxidizer/fuel combination at 5 MPa.

Oxidizer/Fuel combination	Mass, %	Density, 10^3 kg/m^3	Regression rate, mm/s	Mass flux, kg/(m^2·s)
AP/Al/HTPB [54]	68/18/14	1.77	5.30 (5 MPa)	9.38
AP/Mg-Al/HTPB [52]	71/7.5-7.5/14	1.85	9.9 (5 MPa)	18.3
AP/Mg-Al/HTPB [53]	65/10-10/15	1.85	8.5 (5 MPa)	15.7

As it is seen from the table, the regression rate and the corresponding mass flux are dramatically increased in both the cases when the magnalium is employed as the energetic additive. Although the composite solid propellant based on magnalium sounds attractive for the dedicated small launch vehicle from viewpoints of the excellent thrusting performance and reduced negative impacts on the environment and the human bodies, however, it is reported that the gaseous HCl is not completely reduced with this manner, and this propellant still uses AP, therefore, the high amount of the management cost associated with AP shall be inevitable in this manner. The problems raised here about the use of the AP-based composite solid propellant with magnalium are summarized in Table 2 - 4.

Table 2 - 4 Feasibility of composite solid propellant with magnalium for dedicated small launch vehicle.

Features	Feasibility
Reduced rocket size	Achievable
Comparable thrusting performance	Achievable
Reduced management cost	Not achievable
Environmentally friendly	Achievable

2.4.3 Composite solid propellant with ammonium nitrate (AN)

The replacement of AP into ammonium nitrate (AN, NH_4NO_3) as the environmentally friendly solid oxidizer is found to be promising. The thermal decomposition is governed by Eq. 2 – 8 [27].

$$6NH_4NO_3 = N_2O + 2NO_2 + NH_4NO_3 + 10H_2O + 3N_2 \qquad \text{Eq. 2 – 8}$$

It can be seen that the thermal decomposition process is free of chlorine (Cl_2). To know its thrusting performance of AN-based composite solid propellant, Levi et al. investigated its pressure dependency on the regression rate characteristics of a propellant consisting of AN (68 wt.%) as the solid oxidizer, Al particles (18 wt.%) as the energetic additive, and HTPB (14 wt.%) as the polymeric binder, under a pressure-controlled environment [55]. They reported that 3.5 mm/s of the regression rate at 5 MPa was successfully measured in their experiment. The corresponding mass flux is found to be 5.88 kg/(m^2·s). So, the AN-based composite solid propellant has the great potential to reduce the negative impacts on the environment and human bodies. However, it was found that achieving the comparable thrusting performance to the AP-based composite solid propellant is challenging with this propellant (Table 2 – 5), because of its slower regression rate and the lower mass flux than these of the AP-based composite solid propellant. Additionally, AN is also the explosive, so that it is hard to achieve the reduced

management cost.

The comparison between the regression rate of the AP-based composite solid propellant and AN-based composite solid propellant is summarized above, and the feasibility of the AN-based composite solid propellant for the dedicated small launch vehicle is evaluated in Table 2 - 6.

Table 2 - 5 Regression rate and mass flux performance for AP-based composite solid propellant and ammonium nitrate (AN) with its oxidizer/fuel combination.

Oxidizer/Fuel combination	Mass, %	Density, 10^3 kg/m^3	Regression rate, mm/s	Mass flux, kg/(m^2·s)
AP/Al/HTPB [54]	68/18/14	1.77	5.30 (5 MPa)	9.38
AN/Al/HTPB [55]	68/18/14	1.68	3.50 (5 MPa)	5.88

Table 2 - 6 Feasibility of composite solid propellant with ammonium nitrate (AN) for dedicated small launch vehicle.

Features	Feasibility
Reduced rocket size	Achievable
Comparable thrusting performance	Not achievable
Reduced management cost	Not achievable
Environmentally friendly	Achievable

2.4.4 Composite solid propellant with ammonium dinitramide (ADN)

Ammonium dinitramide (ADN, $H_4N_4O_4$) has also paid an attention as the environmentally friendly solid oxidizer. ADN is a chlorine free oxidizer that has been considered a possible AP

replacement for the last 20 years [54]. One of the pathways of the thermal decomposition process of ADN is governed as follows.

$$NH_4N(NO_2)_2 = NH_3 + N_2O + HNO_3 \qquad \text{Eq. 2 – 9}$$

As can be clearly seen, ADN does not release any hazardous chemicals such as chlorin.

Larsson and Wingborg reported the regression rate characteristics with a propellant composed of ADN (70 wt.%) and glycidyl azido polymer (GAP, 30 wt.%) and its pressure dependency. They successfully achieved about 18 mm/s of the regression rate at 5 MPa, and the corresponding mass flux can be calculated as 29.0 kg/(m^2·s). This value is three-times higher than that of the AP-based composite solid propellant, indicating more the excellent thrusting performance than AP-based composite solid propellant. However, the pressure dependency on the regression rate in the ADN-based solid propellant is much stronger than that of the AP-based composite solid propellant. It has been pointed out that the regression rate of ADN-based solid propellant is too fast to apply this propellant to the solid rocket. Although the excellent thrusting performance shall be promised, the practical application of the ADN-based solid propellant has not been made so far. Moreover, ADN is also the explosive, thus, the reduced management cost shall be difficult to be achieved with this manner. The comparison between the regression rate of the AP-based composite solid propellant and ADN-based solid propellant is listed in Table 2 - 7, and the feasibility of the ADN-

based solid propellant is shown in Table 2 - 8.

Table 2 - 7 Regression rate and mass flux for AP-based composite solid propellant and ADN-based solid propellant corresponding to its oxidizer/fuel combination.

Oxidizer/Fuel combination	Mass, %	Density, 10^3 kg/m^3	Regression rate, mm/s	Mass flux, kg/(m^2·s)
AP/Al/HTPB [54]	68/18/14	1.77	5.30 (5 MPa)	9.38
ADN/GAP [54]	70/30	1.61	18.0 (5 MPa)	29.0

Table 2 - 8 Feasibility of composite solid propellant with ammonium dinitramide (ADN) for dedicated small launch vehicle.

Features	Feasibility
Reduced rocket size	Achievable
Comparable thrusting performance	Achievable
Reduced management cost	Not achievable

The result of the comprehensive survey on the composite solid propellant using magnalium, AN, or ADN is schematically explained in Fig. 2 - 5, with advantages (in blue) and disadvantages (in red) for each composite solid propellant. As can be seen in Fig. 2 - 5, all the new solid oxidizers considered to be environmentally friendly are found to be the explosive, so that it may be hard to achieve the reduced amount of cost associated with its management for all the cases made ever.

At a first glance, the use of ADN looks like promising for the dedicated small launch vehicle in terms of the excellent thrusting performance and environmentally friendly propellant, however,

it is reported that ADN is difficult to use because of the strong pressure dependency on the regression rate. Even though technologies to inhibit the pressure dependency have been growing, it is now under investigation. For this reason, another series of the propellant to realize the dedicated small launch vehicle, which does not use such the explosive, has to be sought. Especially, the management cost related to the explosive is so high that propellant free of the explosive is better to achieve the reduced management cost.

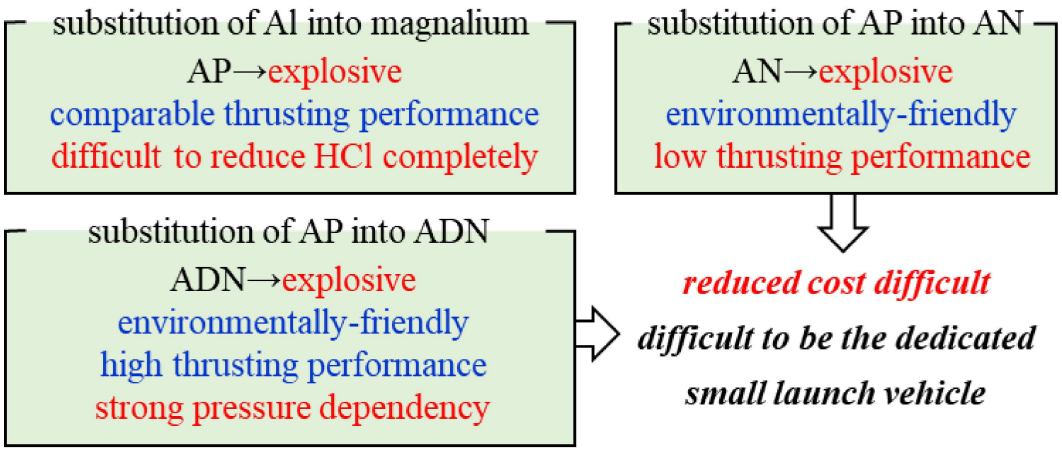

Fig. 2 - 5 Feasibility of various type of composite solid propellants free of ammonium perchlorate for dedicated small launch vehicle.

2.5 Traditional hybrid rocket and boundary layer combustion theory

The traditional hybrid rockets do not use such the explosive in the solid fuel, the management cost is dramatically reduced accordingly. If the intrinsic disadvantage of the low thrusting performance, which is mainly attributed to the slower regression, is overcome, the traditional hybrid rocket has the potential to realize the dedicated small launch vehicle. In this section, the reason for the lower thrusting performance will be discussed with a well-known theory, and the ways to improve the thrusting performance will be reviewed.

The burning process of the traditional hybrid rocket is quite complicated, but by the great effort made by Marxman and Gilbert [56], the well-known theory to predict the regression rate and the theoretical burning model widely accepted have been provided. The schematic illustration of the burning model is presented in Fig. 2 - 6. Under some assumptions that thickness of thermal boundary layer is identical to velocity boundary layer, and Reynolds' analogy can be adopted, the following relation between the regression rate and other physical parameters has been provided.

$$\rho_S V_f = 0.03G\left(\frac{Gx}{\mu}\right)^{-0,2}\left(\frac{St}{St_0}\right)\left(\frac{u_e}{u_b}\right)\left(\frac{\Delta h}{h_v}\right)+\frac{q_r}{h} \qquad \text{Eq. 2 – 10}$$

where ρ_S [kg/m^3], V_f [m/s], G [kg/(m^2·s)], x [m], μ [Pa·s], (St/St_0), u_e [m/s], u_b [m/s], Δh [J/kg], h_v [J/kg] and q_r [W/m^2] are the density of solid fuel, the regression rate, the total mass

flux of the gaseous oxidizer and the gaseous fuel gasified at the solid fuel surface, the coordinate of flow direction, the viscosity, the ratio of the Stanton number with/without gasification of the solid fuel at the solid fuel surface, the velocity at the main stream, the velocity at the flame, the total enthalpy difference between the flame and the solid fuel surface, the enthalpy of the gasification of the solid fuel, and the radiative heat flux from the diffusion flame sheet. The first term shows convective heat transfer rate, and the second term is expressed as radiative heat transfer rate.

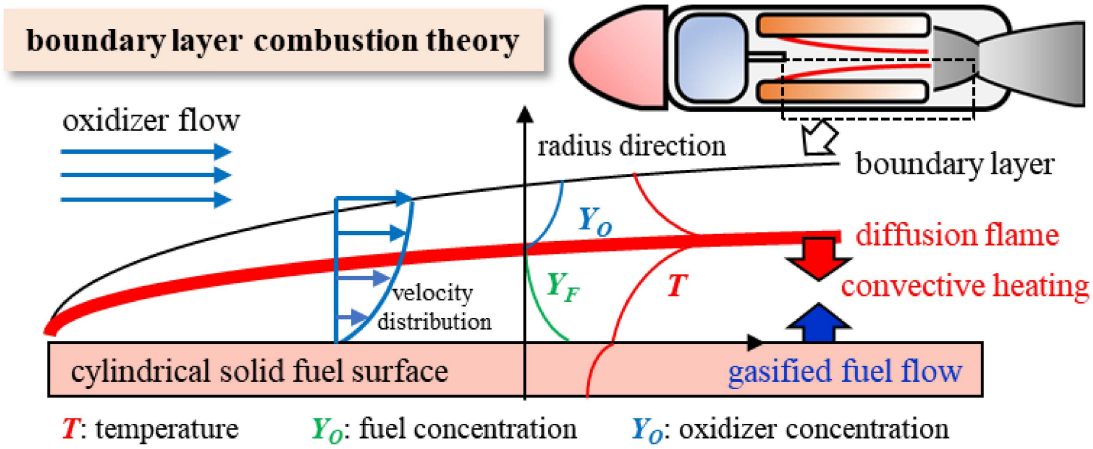

Fig. 2 - 6 Schematic illustration of turbulent boundary layer combustion theory proposed by Marxman and Gilbert [56] applicable to traditional hybrid rocket combustion.

Although it is seen that the regression rate tends to be increased with the increase in the injected amount of the oxidizer mass flux because the diffusion flame is established closer to the solid fuel, the Stanton number (*St*) decreases simultaneously with the increase in the oxidizer mass flux. This

is because “hot” fuel mass flux gasified (hot pyrolysis gas) at the solid fuel surface increases, leading to thicker thermal boundary layer and poor convective heat transfer exposed onto the solid fuel surface. Therefore, it is understood that the limiting effect on the regression rate appears when the oxidizer mass flux is increased to obtain the faster regression rate in the traditional hybrid rocket, as found in the Marxman’s theory. This is so called “blocking effect” [57]. This series of the explanation is drawn in Fig. 2 - 7.

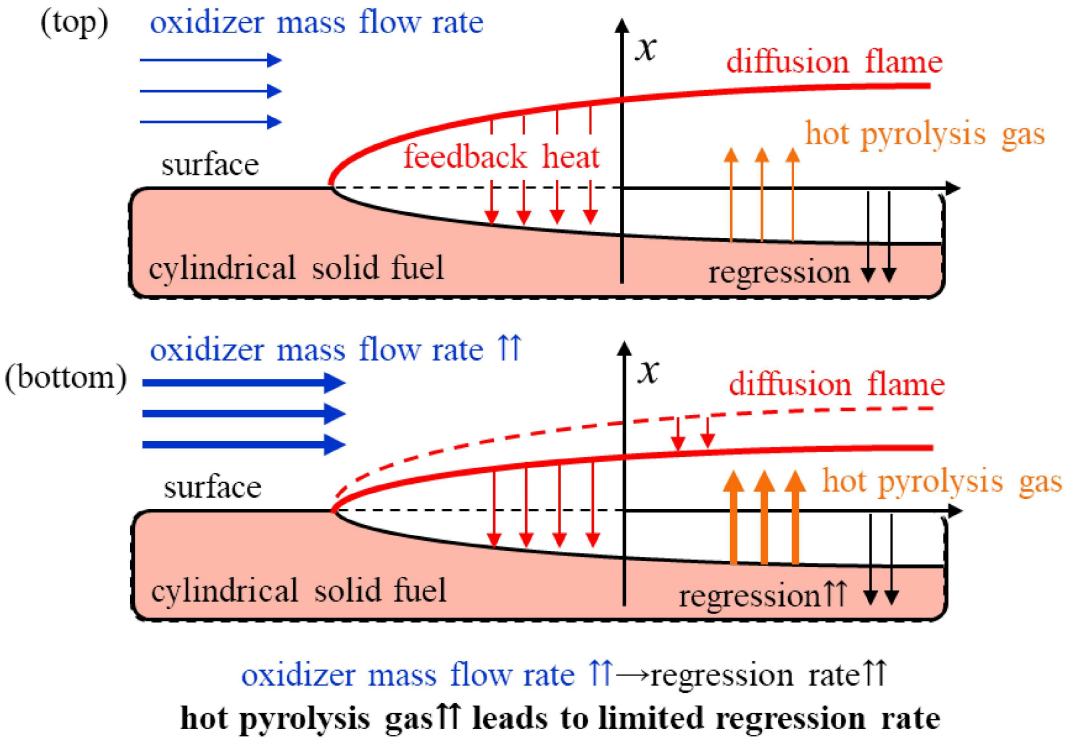

Fig. 2 - 7 Schematic illustration of blocking effect in traditional hybrid rocket.

This effect results in physical separation between the diffusion flame and the solid fuel surface, leading to the reduced heat flux exposed onto the solid fuel surface further [30]. For this reason, the regression rate achievable in the traditional hybrid rocket has been limited. Fig. 2 - 8 shows a typical result of the average regression rate as a function of the oxidizer mass flux with various type of the solid fuels (HTPB, PMMA, and high-density polyethylene (HDPE)) and oxygen [58].

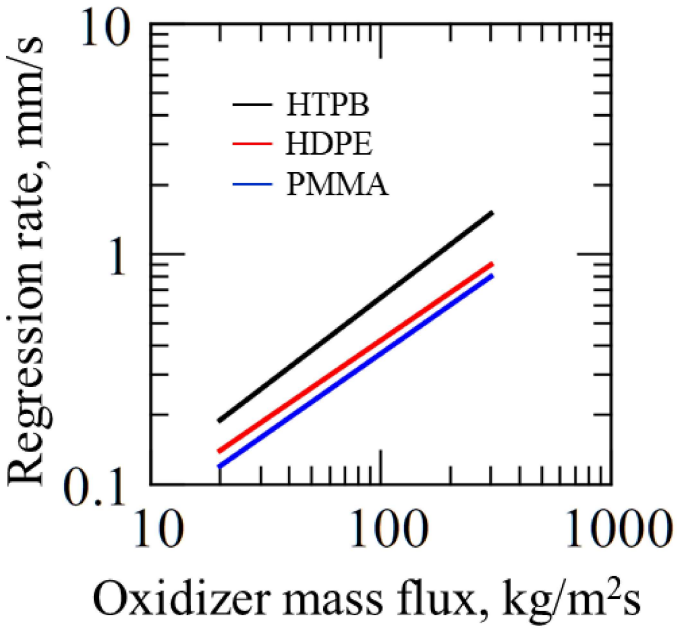

Fig. 2 - 8 Typical result of regression rate characteristics as a function of oxidizer mass flux with various type of polymetric materials and oxygen [58].

As it is clearly seen, the regression rate is increased in one order of magnitude with the increase in the oxidizer mass flux for all the cases. In the conditions reported in the literature, a maximum regression rate was obtained as 1.5 mm/s at 300 kg/(m^2·s) in the case when HTPB is employed.

The corresponding fuel mass flux can be estimated as 1.37 kg/(m^2·s). Taking into the account the regression rate and its mass flux in the conventional AP-based composite solid propellant (5.3 mm/s, 11 kg/(m^2·s) at 5 MPa), it is well-understood that the reason for the less practical application is attributed to its slower regression rate. With this regard, it is found that enhancing the regression rate and its mass flux further in the traditional hybrid rocket is quite important but is found to be challenging.

To overcome the intrinsic disadvantage of the lower thrusting performance owing to the slower regression rate in the traditional hybrid rocket, various type of hybrid rockets has been proposed and updated ever with significant effort made by many research groups. In particular, two aspects: (1) the large burning surface area (A_P) and (2) improvement of the convective heat transfer onto the solid fuel surface have been focused on. The literature review on the various type of the hybrid rockets will be made hereafter. Please note that the terminology of the traditional hybrid rocket is to use the combination of the gaseous/liquid oxidizer and the “cylindrical” polymeric solid fuel having the “single port”. The hybrid rocket which will be touched from next section is different from the concept of the traditional hybrid rocket.

2.6 Trend of research and development of various type of hybrid rockets

2.6.1 To enlarge burning surface area

The new ideas applicable to the hybrid rockets have been extensively proposed by many research groups (e. g., [59] [60] [61]). The basic idea shown here at first is to enlarge the burning surface area. It is reported so far that employing a polymeric solid fuel having multi ports or an intricate fuel port for the traditional hybrid rockets is found to be attractive. Some examples of the unique geometries of the solid fuels are shown in Fig. 2 - 9.

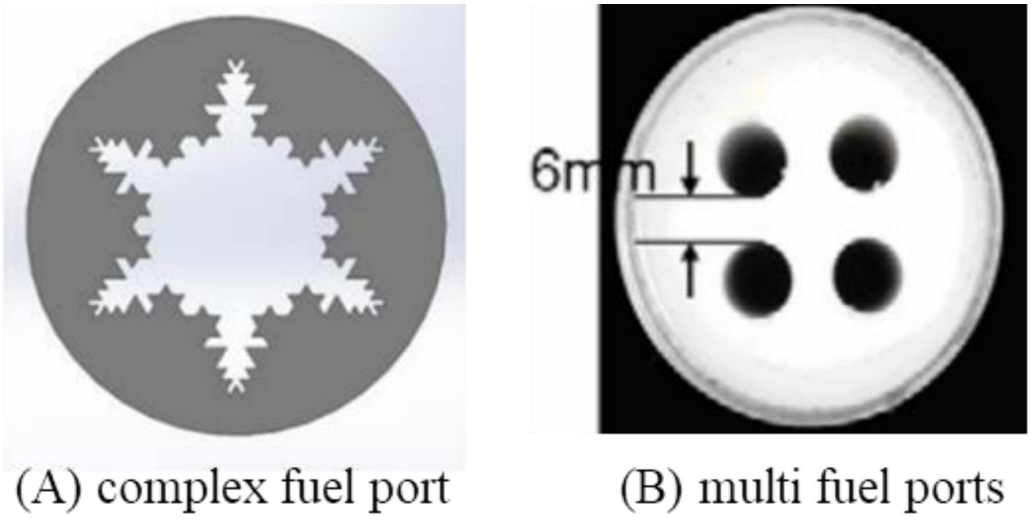

Fig. 2 - 9 Solid fuel having unique geometry used for hybrid rocket: (A) fractal star fuel port [60] and (B) multiport solid fuel [61].

Funami et al. conducted firing experiments using a cylindrical acrylonitrile butadiene styrene (ABS) having a star fractal fuel port, as shown in Fig. 2 - 9 (A) [60], with nitrous oxide (N_2O). It was revealed that they achieved the large burning surface area as compared to that of the

traditional hybrid rocket, and 1.7 mm/s of the regression rate at 140 kg/(m^2·s) of the oxidizer mass flux was obtained in a range where they tested. Kim et al. conducted firing experiments with a propellant employing polymethyl methacrylate (PMMA), which has four ports arranged around the center as shown in Fig. 2 - 9 (B), and gaseous oxygen [61]. It was reported that the achieved regression rate was 0.55 mm/s at the oxidizer mass flux of 120 kg/(m^2·s), whereas approximately 0.5 mm/s of the regression rate at the same oxidizer mass flux for the case of HDPE and PMMA in the traditional hybrid rocket was measured. With this respect, the solid fuel having multiport is capable of achieving not only the slightly higher regression rate than that of the HDPE and PMMA used in the traditional hybrid rocket, but also the larger burning surface area, at the same oxidizer mass flux. However, although these methodologies sound attractive for the dedicated small transport vehicle, the thrusting performance remains low for the practical application level.

2.6.2 To enhance convective heat transfer in hybrid rocket

According to the beforementioned Marxman's turbulent boundary combustion theory, it was explained that the regression rate is enhanced by improving the poor convective heat transfer rate from the diffusion flame exposed onto the solid fuel surface. Hence, there has been extensive research on challenging improvement in the convective heat transfer rate further by adding a change in the gas flow field (e. g., [33] [35] [34] [57] [62] [63] [64] [65] [66] [67] [68]).

Karabeyoglu carried out firing experiments using a paraffin-based solid fuel and the gaseous oxygen to improve the convective heat transfer rate by taking advantage of lower melting temperature of the solid fuel than that of the solid fuel, such as polyethylene, HTPB, PMMA, etc. [35] [40] [57]. As shown in the following burning model, the solid fuel starts to melt at the lower temperature and is then liquified to numerous droplets at the vicinity of the solid fuel surface, generating entrainment phenomena of the droplets into the diffusion flame by shearing force induced by the oxidizer flow. The blocking effect occurred in the traditional hybrid rocket shall be overcome by adopting the paraffin-based solid fuel. This is due to the formation of the droplets fuel near the solid fuel surface, and higher thermal conductivity of the droplet than that of the fuel gases.

In Fig. 2 - 10 (B), a result of the regression rate characteristics for two types of the solid fuels

(paraffin base and HTPB) with oxygen are presented with the oxidizer mass flux controlled for comparison purpose. It is clear that, at the mass flux of 200 kg/(m^2·s) three-times faster regression rate than that of HTPB typically used for the traditional hybrid rocket can be achievable for the case when the paraffin or wax based solid fuel is employed.

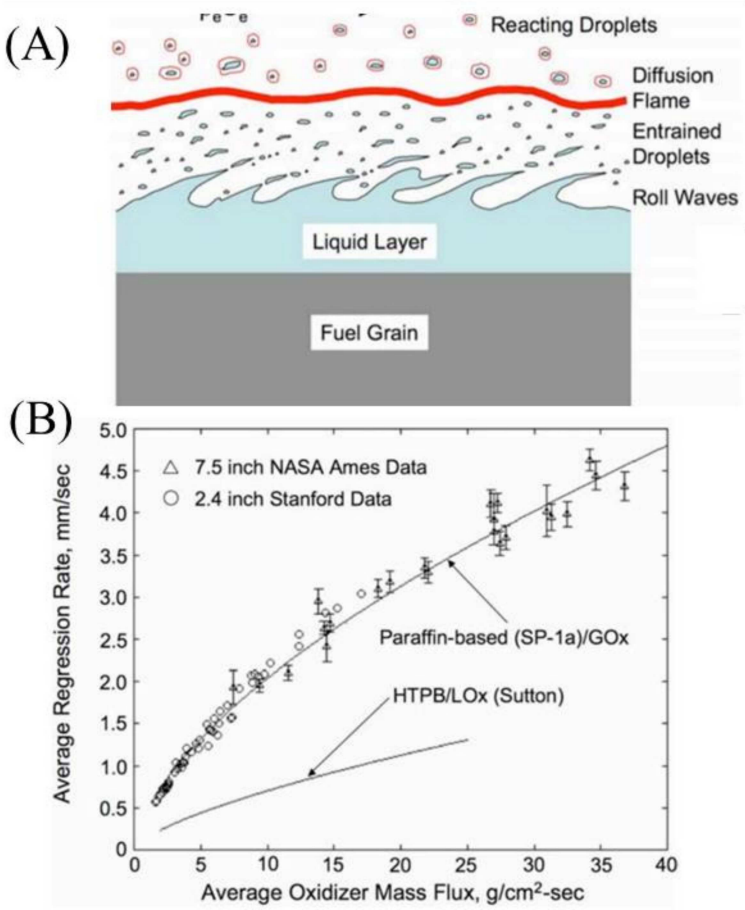

Fig. 2 - 10 (A) Schematic illustration of burning model proposed by Karabeyoglu and (B) testing results of the paraffin based solid fuel and the traditional solid fuel in hybrid rocket [40].

Nagata et al. proposed a quite unique idea of the gas flow field in the hybrid rocket, named the cascaded multistage impinging-jet (CAMUI) hybrid rocket, to enhance the convective heat

transfer further [33]. A schematic illustration of the CAMUI hybrid rocket and its burning process are presented to Fig. 2 - 11. In the CAMUI hybrid rocket, solid fuel blocks having two holes drilled around the center are arrange in a row, and each solid fuel block is arranged at 90 degrees out of the phase. The oxidizer and burned gas are injected onto each solid block's surface as impinging jet flow. By taking advantage of the impinging jet flows and the larger burning surface area, the convective heat transfer and the total heat exposed onto the solid fuel are dramatically intensified. Even though such the intricate geometry in the CAMUI hybrid rocket is quite hard to compare the regression rate between the traditional hybrid rocket and the CAMUI hybrid rocket, it is reported that the average regression rate in the CAMUI hybrid rocket is increased up to three times as compared with the traditional hybrid rocket [69].

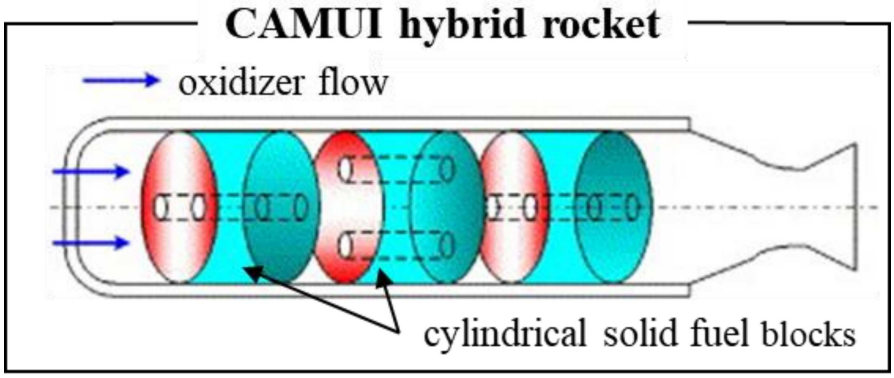

Fig. 2 - 11 Schematic illustration of CAMUI hybrid rocket proposed by Nagata [33].

Swirling jet flow type hybrid rockets have been paid attention as the research interest by many research groups worldwide [34] [63] [64] [65] [67] [68] [70]. Great effort by Shimada et al. in the

Japan aerospace exploration agency (JAXA) is one of the well-known examples of the development in the swirling jet flow type hybrid rocket. A schematic illustration of the swirling jet flow type hybrid rocket is drawn in Fig. 2 - 12 [70].

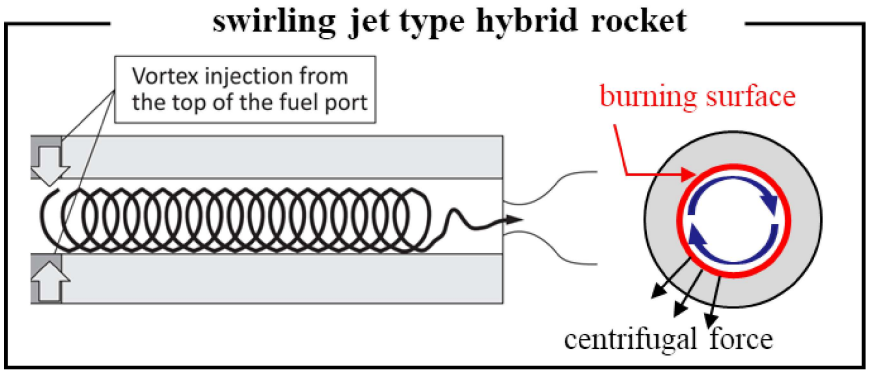

Fig. 2 - 12 Schematic illustration of burning mechanism of swirling jet type hybrid rocket proposed by Shimada in JAXA, burning surface location, and schematic illustration of centrifugal force generated in solid fuel [70].

The oxidizer and the burned gas are flown along the radius direction while enhancing its mixing effect between the oxidizer and the fuel gas. The centrifugal force generated by the swirling flow pushes the oxidizer and the burned gas onto the solid fuel surface further, making the thermal boundary layer thinner and the temperature gradient steeper. With this methodology, it is expected to improve not only the poor convective heat transfer rate, but also the low combustion efficiency that are pointed out as the disadvantages of the traditional hybrid rocket. As expected, it was reported that they successfully achieved from two to three-times faster regression rate than that of the traditional hybrid rocket.

For comparison purpose, the regression rates and its corresponding "fuel" mass fluxes at almost the same oxidizer mass flux (120 – 140 kg/(m^2·s)) achieved in the various type of the hybrid rockets are summarized in the following table.

Table 2 - 9 Regression rate and fuel mass flux at almost same oxidizer mass flux (120 – 140 kg/(m^2·s)) for six hybrid rockets: traditional hybrid rocket (Traditional), hybrid rocket employing the intricate geometry (Intricate), the hybrid rocket employing the multi ports (Multi ports), the swirling jet flow type hybrid rocket (Swirling), and the CAMUI hybrid rocket (CAMUI).

Type	Fuel/Oxidizer	Regression rate, mm/s	Fuel density, kg/m^3	Fuel mass flux, kg/(m^2·s)
Traditional	HTPB/O_2	0.9 at 140 kg/(m^2·s)	0.902 x 10^3	0.812
Intricate	ABS/N_2O	1.7 at 140 kg/(m^2·s)	1.05 x 10^3	1.79
Multi ports	PMMA/O_2	0.55 at 120 kg/(m^2·s)	1.18 x 10^3	2.60 (four ports)
Paraffin	Paraffin base/O_2	2.5 at 140 kg/(m^2·s)	920 [35]	2.3
Paraffin	Paraffin based composite/O_2	0.88 at 60 kg/(m^2·s)	984	0.87
Swirling	PMMA/O_2	1.4 at 140 kg/(m^2·s)	1.18 x 10^3	1.65
CAMUI	HDPE/O_2	3.0 [69] at 140 kg/(m^2·s)	950	2.85

In the table, the combination of the oxidizer and the solid fuel, together with the density of the solid fuel, are summarized. As it is clearly seen, more excellent thrusting performance of the abovementioned hybrid rockets, in terms of the regression rate and the mass flux as compared with those of the traditional hybrid rocket, is demonstrated. On the other hand, even though the

significant efforts by many research groups have been made ever as summarized in the table, the practical application of these hybrid rocket for the dedicated small launch vehicle, which can be applicable to the launch of the smallsats, has not been made so far. Therefore, it is suggested that further update on the hybrid rocket should be required.

A flowchart is lastly created here in order to recall the series of the abovesaid explanation about the various type of the hybrid rockets and the composite solid propellant free of AP as follows.

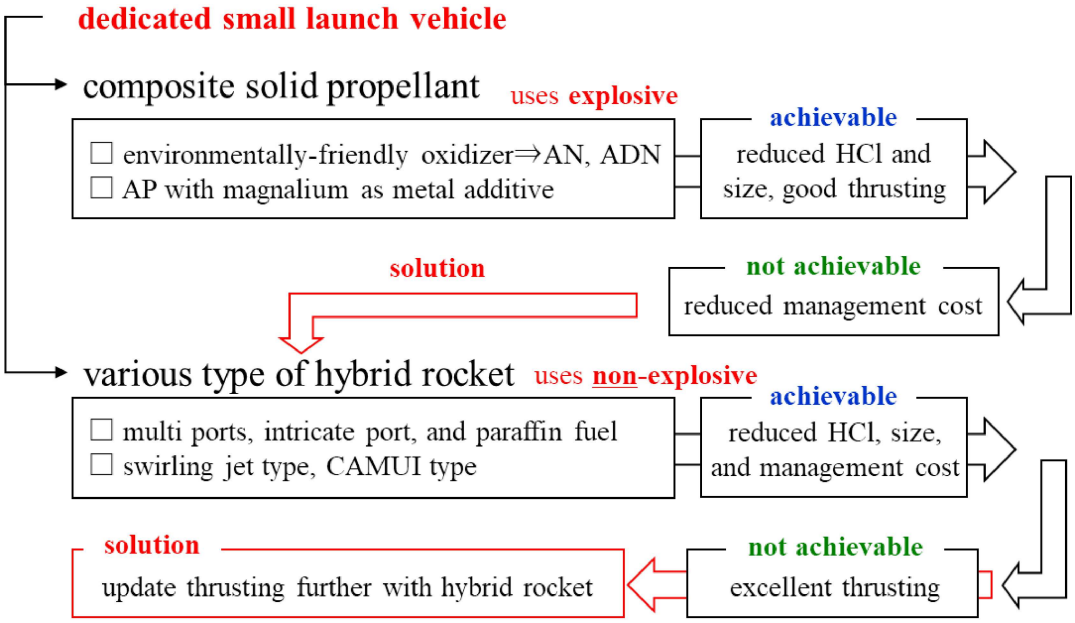

Fig. 2 - 13 Flowchart of a series of explanation of development in various type of hybrid rockets and composite solid propellant using magnalium as energetic additive or AN or ADN as environmentally friendly solid oxidizer.

2.7 Thrust force achieved ever hybrid rockets and challenging in update

It is interesting to note the thrust force achieved ever in various type of the hybrid rockets to evaluate its thrusting performance. The launch year since 1990 and the thrust force achieved in the various type of hybrid rockets, including static experiments, is presented to Fig. 2 - 14, together with the thrust force of the Epsilon rocket consisting of the three stages of the AP-based composite solid propellant based on AP [71] for comparison purpose. The horizontal and the vertical axes are launch year and logscale thrust force in kilonewton, respectively. It is found that the thrust force achieved in the various type of hybrid rockets shows an increasing trend towards the launch year. As found, the thrusting performance in the hybrid rocket is becoming higher as a year basis. To the author's best literature review, the research group in Stuttgart University (Germany) has achieved the highest performance in terms of the thrust force in 2016. Although the great efforts by many research groups to upgrade its thrusting performance of the hybrid rocket are demonstrated ever, however, it can be seen that the thrusting performance in the hybrid rockets has not been reached to applicable level of the AP-based composite solid propellant (1^{st} stage, 2^{nd} stage, and 3^{rd} stage) used for the Epsilon rocket used for the space missions. The difference is still one order of magnitude or more. This fact proves that the upgrading its thrusting performance of the hybrid rockets is quite challenging, as mentioned earlier. For this reason, many research

groups have been making continuous great effort for increasing the regression rate further. The data plotted on the figure are also summarized in the following table.

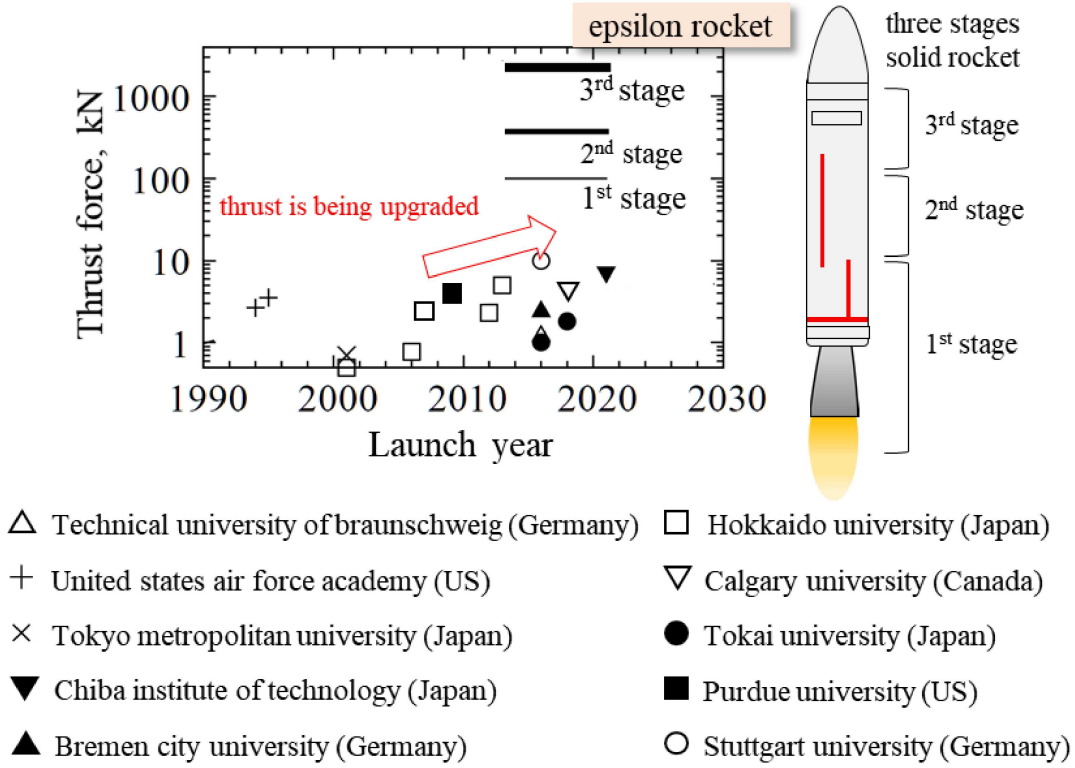

Fig. 2 - 14 Thrust force achieved ever in various type of hybrid rockets, launch year, research groups, and thrust force of three stages solid rocket for Epsilon rocket developed by JAXA for comparison purpose [71].

Table 2 - 10 Thrust force achieved in hybrid rocket and its launch year.

Research group	Year	Thrust force, N	Altitude, m
United states air force academy [72]	1994	2670	3,000
United states air force academy [72]	1995	3570	4,600
Tokyo metropolitan institute of technology [73]	2001	700	600
Hokkaido university	2001	500	Static experiment
Hokkaido university	2006	780	780
Hokkaido university	2007	2450	2450
Purdue university [74]	2009	4000	1859
Hokkaido university [75]	2012	2310	2310
Hokkaido university [76]	2013	5000	8,300
Stuttgart university [77]	2016	10000	32,300
Tokai university [78]	2016	1000	1,900
Technische universität braunschweig [79]	2016	1250	5,400
Bremen city university [80]	2016	2500	6,500
Tokai university [78]	2018	1800	6,200
Calgary university [81]	2018	4400	Static experiment
Chiba institute of technology [82]	2021	6900	Static experiment

2.8 Well-mixed propellants for further update

As it is noticed, the thrusting performance of the hybrid rocket should be more updated to achieve the practical use level. For the further update, there has been great interests in a methodology to increase dramatically not only the burning surface area, but also the heat transfer and mass transfer, resulting in the higher regression rate. The methodology is to utilize a “well-mixed propellant” whose employs a porous combustible or metallic particles with liquid oxidizer. Schematic illustration of two examples of the well-mixed propellant is shown Fig. 2 - 15 and Fig. 2 - 16. As can be understood from comparison between the well mixed propellant and the composite solid propellant illustrated in Fig. 1 - 8, the well-mixed propellants resemble the composite solid propellant. Different point is that the porous combustible or the metallic particles, and the liquid oxidizer are initially separated before the ignition, and both can be quickly mixed, whereas the composite solid propellant shall take time to manufacture more than the well-mixed propellant. Clearly, although this combination of the liquid oxidizer and the solid fuel is the same as one configurated in the hybrid rocket, please note that the burning process is similar to the composite solid propellant rather than the hybrid rocket. In combustion of the well-mixed propellant, once the ignition is made, the gasified fuel and oxidizer are pre-mixed quickly each other in gas-phase layer in the vicinity of the burning surface. It is therefore expected to establish

a flame close to the burning surface and thus increase the regression rate further with this manner. In addition, the explosive is not used for these propellants, with this respect, the inherent explosive hazard and costs associated with the management, which is regarded as one of the disadvantages of the AP-based composite solid propellant, can be avoided. Based on the abovesaid advantages, research groups have proposed various type of the well-mixed propellants and reported its regression rate characteristics of the well-mixed propellant so far (e. g., [83] [84] [85] [86] [87]). We will now touch three typical examples of the well-mixed propellant

2.8.1 Metal particle group soaked in liquid oxidizer

Sabourin et al. carried out a series of experiments using a mixture of 32 wt.% hydrogen peroxide as the liquid oxidizer and numerous aluminum particles (38 nm in diameter) under ambient pressure-controlled environments [84], as illustrated in Fig. 2 - 15. The mixture was well-mixed before the experiments and then inserted into a vertically oriented transparent quartz tube for good visibility. The regression rates were measured by tracking the top surface of the mixture from recorded video, and they reported that 55 kg/m^{2}s (five-times larger than that of the composite solid propellant) of the mass flux at 3.65 MPa were successfully achieved.

As another work on the well-mixed propellant, Sundaram and Yang predicted pressure

dependency on the regression rate characteristics of a mixture consisting of the aluminum particles and hydrogen peroxide, by developing a burning model. The mixture is almost the same as one shown in Fig. 2 - 15. It is reported that about 13 mm/s of the regression rate at 5 MPa with the mixture consisting of 20 μm aluminum particles and 90 wt. % hydrogen peroxide under the condition studied in their work is predicted. The corresponding mass flux was introduced as 29.2 kg/(m^2·s), and it is found that this value is much higher than that of the hybrid rocket and about 2.5 times higher than that of the AP-based composite solid propellant.

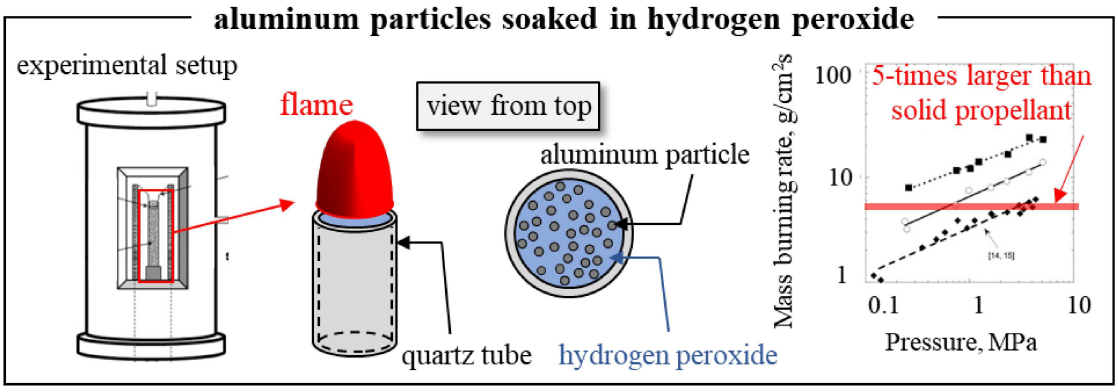

Fig. 2 - 15 Schematic illustration of well-mixed propellant consisting of numerous aluminum particles initially well-soaked in 32 wt.% hydrogen peroxide and its mass flux obtained in previous work by Sabourin et al [84].

2.8.2 Porous combustible soaked in liquid oxidizer

In 1997, Nagata et.al investigated the pressure dependency on the regression rate of the well-mixed propellant, consisting of a fibrous polyamide (the porous combustible) soaked in liquid oxygen (LOX) under pressure-controlled environment, as they illustrated in Fig. 2 - 16 (top) [85]. The fibrous polyamide is soaked into LOX tank cooled by liquid nitrogen (LN_2), and then the propellant is set in the chamber, and forced ignition is made at the top surface of the propellant in a pressure-controlled environment.

As reported, the regression rates were measured by signals from three fuses initially embedded into the propellant before experiments. The obtained relationship between regression rate and pressure is provided as shown in Fig. 2 - 16 (bottom). As it was expected, the regression rate was dramatically improved and measured at the rate of 20 mm/s at 0.3 MPa in their experiments. The corresponding mass flux can be calculated as 24 kg/(m^2·s), and it is found that this value is also two times higher than that of the AP-based composite solid propellant (of course, much higher than that of the hybrid rocket). As proved by the three examples of the well-mixed propellant, even though the explosive is not used for the well-mixed propellant, the thrusting performance of the well-mixed propellant, in terms of the regression rate and the mass flux, is found to be promising. Moreover, as can be stated, the well-mixed propellant can be scale down and

environmentally friendly propellant and achieve the reduced management cost and the reduced manufacturing time. Therefore, it is apparent that the well-mixed propellant can meet the necessary features for the dedicated small launch vehicle.

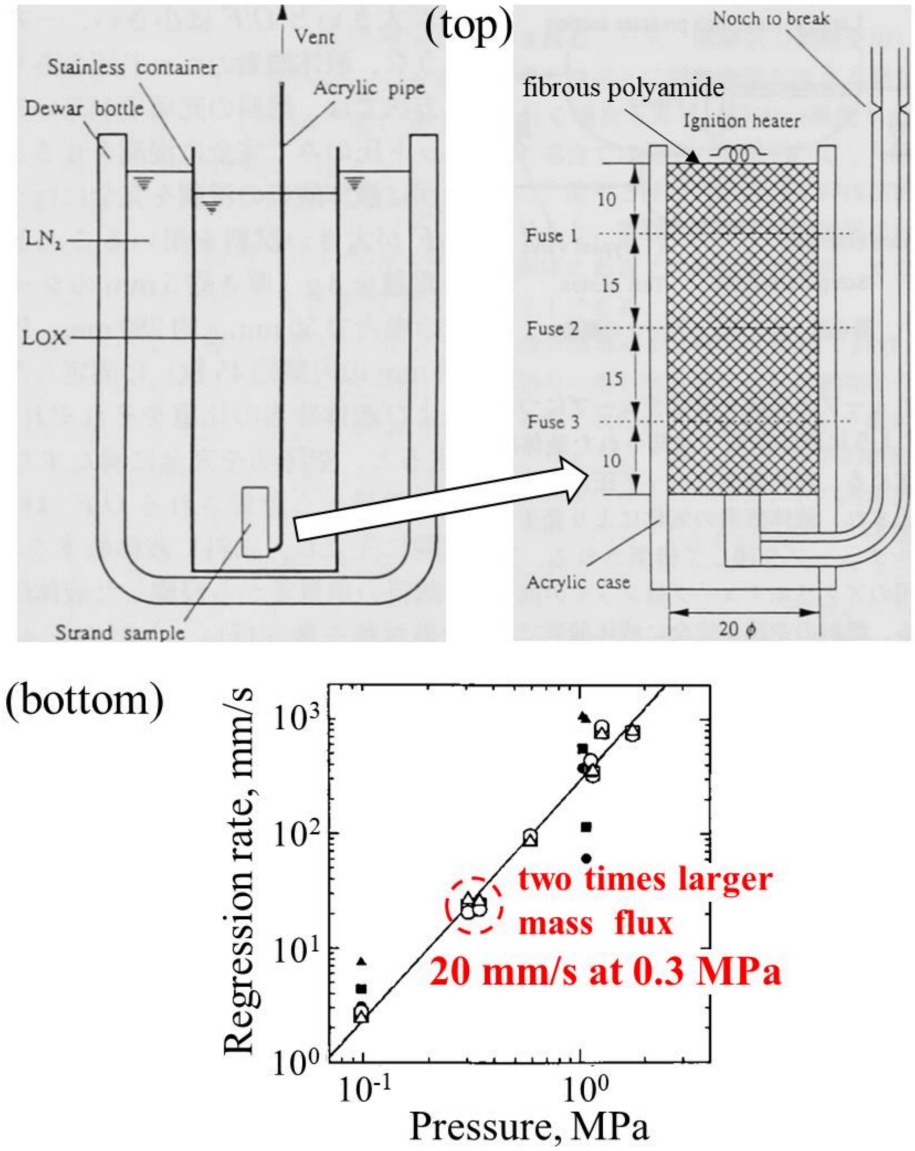

Fig. 2 - 16 (A) Schematic illustration of well-mixed propellant consisting of a fibrous polyamide (porous combustible) initially well-soaked in liquid oxygen (liquid oxidizer), proposed by Nagata et al.in 1997 and reported pressure dependency on measured regression rate [85].

2.8.3 Uncontrollable burning behavior in well-mixed propellants

Although the excellent thrusting performance in the well-mixed propellants was demonstrated by the previous works by Sabourin et al., Sundaram et al., and Nagata et al., however, uncontrollable burning behaviors were frequently observed in the three works. For instance, anomalous burning behavior (acceleration of the burning surface) during the burning event was observed (Sabourin et al. [84]), leading to a rupture of the quartz tube as presented to Fig. 2 - 17.

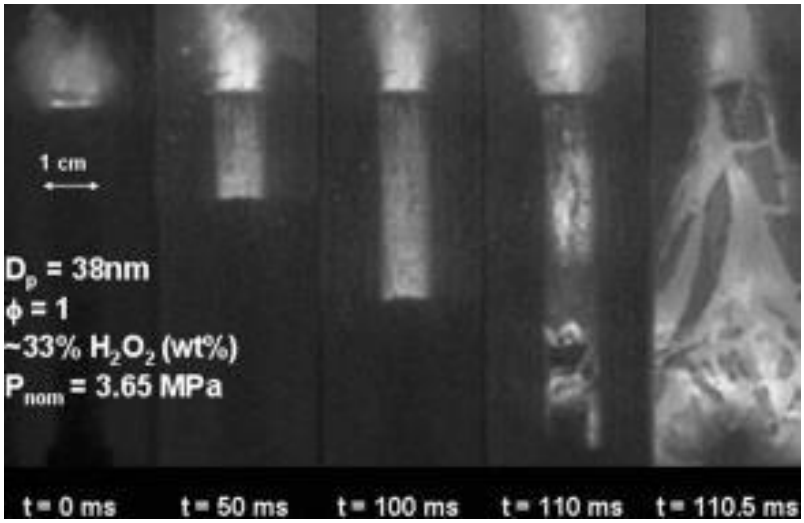

Fig. 2 - 17 System instability: anomalous burning behavior leads to rupture of quartz tube [84].

An unwanted burning behavior such as an explosion-like burning was also observed (Nagata et al. [85]). Therefore, these facts have shown that a system stability to achieve steady burning was not promised in the well-mixed propellant. Unfortunately, the reason for the unwanted burning behavior was not discussed in detail in their papers. In addition, as shown in Fig. 2 - 16

(B), it is clearly seen that the observed data of the regression rate were scattered at random pressure environment even in the standard pressure. The reason was not also discussed in detail in the paper. In Nagata's experiments, as the use of LOX needs a cooling system so as not to prevent LOX from vaporizing before the experiment, they were probably forced to do their experiments with a very complex experimental setup. For this experimental limitation, direct observation during the burning event was not made in their work. Moreover, the experimental data was only limited to the signals from the fuses embedded into the propellant. This fuse-based method allows to measure just "average regression rate", and it is unclear whether the regression rates plotted on the figure exhibit steady burning or not. Therefore, even fundamental burning characteristics, such as the burning behavior, steadiness of the regression rate, have been missing since Nagata's work due to its limitations on the experimental setup and the methodology.

To leverage its excellent features of the good thrusting, the structural simplicity, the reduced management cost (not use the explosive), and the less harmful combustion gas, it is necessary to understand the fundamental burning characteristics of the well-mixed propellant in a precise manner as a first step. Furthermore, knowing the possible reason for the data scattering and the explosion-like burning behavior plays pivotal role in the safety use and reliability of the propellant. To do so, re-designing the testing methodologies, including the whole experimental setup and the

design of the propellant is highly recommended. A summary of this series of the explanation is presented to Fig. 2 - 18.

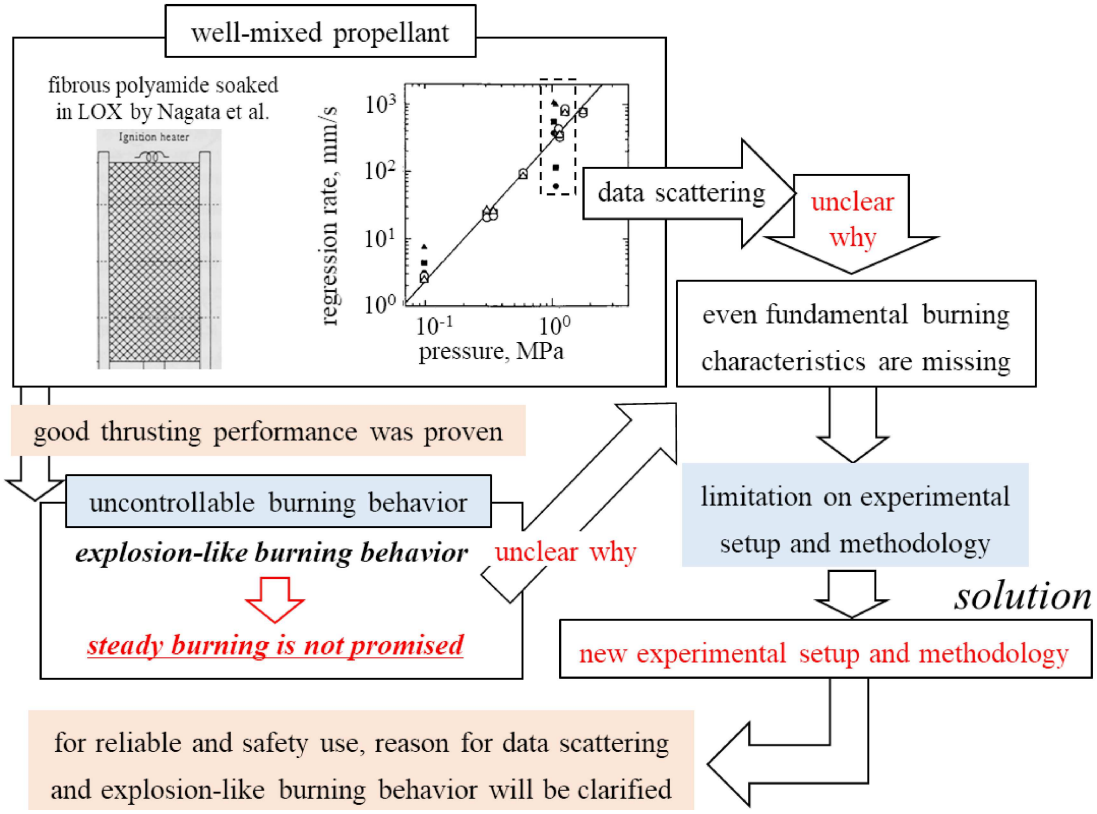

Fig. 2 - 18 Summary of raised issues and solutions on well-mixed propellant by Nagata et al.

2.9 Approach, motivation, and objective of this dissertation

2.9.1 Approach of the dissertation

To know the reasons of such the unwanted burning behavior and the data scattering, first it is necessary to investigate “what was happened inside/outside the propellant” and “what triggered such the phenomena” in a precise manner. For this purpose, visualization of the burning behavior

during the entire burning event and investigation on thermal structure inside/outside the propellant are necessary to be examined as a first place.

From the previous work by Sabourin et al., the visualization can be done easily by adopting hydrogen peroxide (not LOX). Hydrogen peroxide is in a liquid phase at room temperature, and hence complex experimental setup to keep the temperature very low is not required. In addition, from the previous work by Nagata et al., it is found that the temperature measurement could be conducted with the porous combustible made of "foam", whereas it would be difficult when the aluminum particles are used as the porous combustible since the aluminum particles moves upward very fast. With the use of the "foam" type solid fuel as the porous combustible, a contact type thermometer such as thermocouples can be inserted into the porous combustible for the temperature measurement. However, in the case when the contact type thermometer is inserted, it should be noted that we only obtain time history of the temperature as illustrated in Fig. 2 - 19.

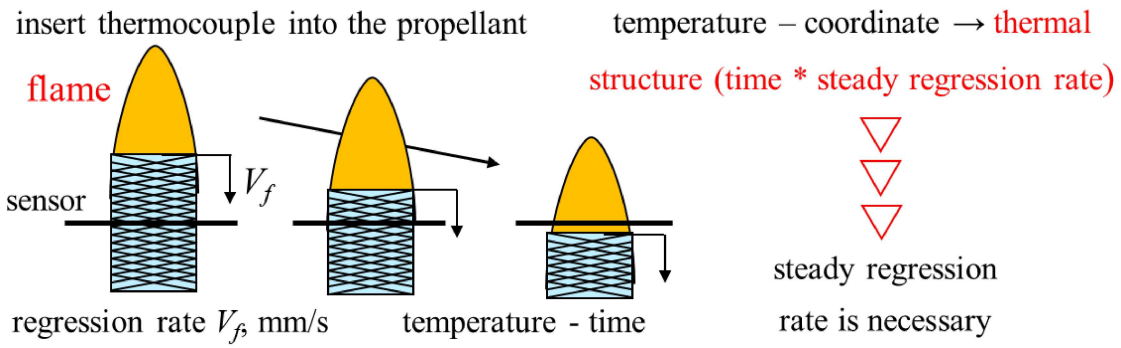

Fig. 2 - 19 Methodology to obtain thermal structure by direct measurement with thermocouple.

As the aim is to obtain the thermal structure (temperature vs coordinate), to convert the time history temperature profile into the thermal structure, the elapsed time should be multiplied by the steady (constant) regression rate. For this reason, a system that achieves the steady burning process is necessary to be established.

For the abovesaid reason, the propellant is replaced from the research by Nagata et al. and Sabourin et al. as follows. A polyethylene foam is used as the porous combustible, whereas enriched hydrogen peroxide (not liquid oxygen) is employed as the liquid oxidizer. Following this replacement, a simple experimental setup which is equipped with a pair of quartz windows is configurated so as to enable us to conduct the direct temperature measurement by the inserted thermocouple and to visualize the entire burning behavior. Then, a methodology to trace the instantaneous location of the burning surface to measure the regression rate by using image processing software is introduced. With this approach, the regression rate, steadiness of the regression rate, the burning behavior, the thermal structure, and its effect of physical parameters on these burning characteristics will be examined in detail in a precise manner.

2.9.2 Motivation and objective of the dissertation

The organization (flowchart) of this dessertation, based on the abovesaid explnation, is presented to Fig. 2 - 20.

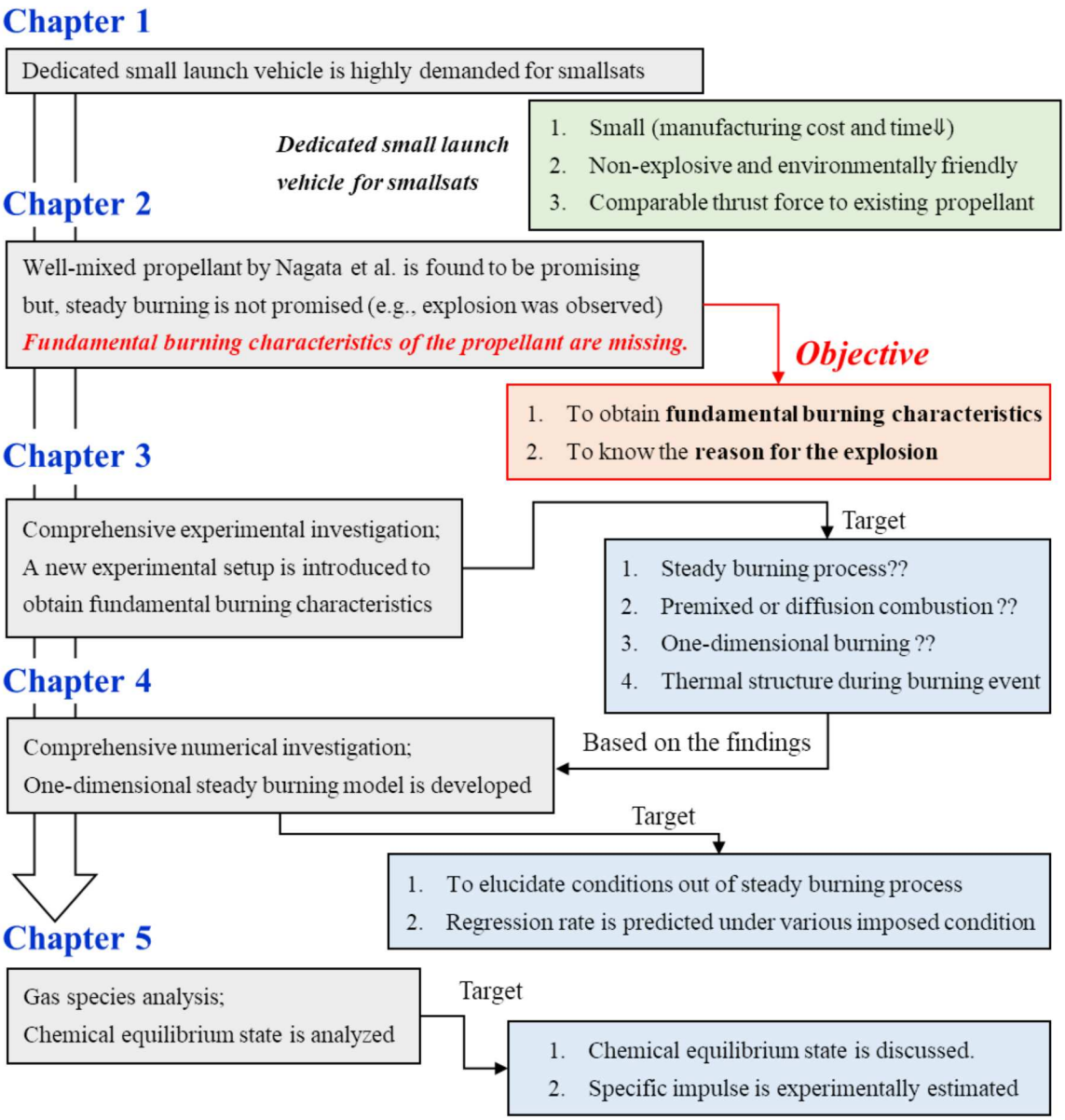

Fig. 2 - 20 Organization (flowchart) of this dissertation.

Motivation of this dissertation

Specifically speaking, the motivation of this dissertation is that the fundamental burning characteristics of the well-mixed propellant consisting of the porous combustible soaked in the liquid oxidizer, have not been well investigated in detail in the previous work, due to the limitations associated with the experimental setup and methodology. In addition, the reason for the data scattering and the explosion were not clearly discussed in the previous work. This work is motivated to address these issues.

Objective of this dissertation

In this work, the fundamental burning characteristics of the well-mixed propellant consisting of the porous combustible soaked in the liquid oxidizer, developed in accordance with the previous work by Nagata et al., are experimentally and numerically investigated.

With the replaced propellant and the experimental setup, the steadiness of the regression rate, the burning behavior during the entire burning event, thermal structure inside/outside the propellant are then experimentally investigated under various fuel porosities at various pressure environment.

In theoretical modeling, based on the experimental findings, a simple one-dimensional burning

model is developed, and its validity is evaluated by the experimental results. Effects of the type of liquid oxidizer (hydrogen peroxide and liquid oxygen), fuel porosity of the porous combustible, and ambient pressure on the potential regression rate, on the thermal structure, and on the pressure exponents are examined. Considering blow off criteria given by CHEMKIN premix code, the blow off criteria under the imposed conditions is examined accordingly. With this manner, the possible reason of the data scattering and the explosion-like burning, observed in the previous works are discussed to aid optimal design of the well-mixed propellant for future use.

In addition to the obtained burning characteristics, our interest is to evaluate thrusting performance of the present propellant. To evaluate the thrusting performance, product gases of the propellant at 0.1 MPa ambient are studied. In the experiments, we first measure one-dimensional (1-D) concentration profiles over the regression surface by a gas chromatography under various fuel porosities. The achievable thrusting performance of the present propellant is then obtained from the experiment and chemical equilibrium calculation by CEA (NASA (Chemical equilibrium with Applications).

2.10 Concluding remarks of this chapter

In this chapter, the equations to describe the thrusting performance of the composite solid propellant and the hybrid rockets and the methodologies to enhance the thrusting performance were introduced. The comprehensive literature review concerning the various type of the composite solid propellants and the hybrid rockets to increase the thrusting performance, based on the methodologies, was then made. Based on the literature review, the well-mixed propellant, consisting of the porous combustible or metal particles soaked in the liquid oxidizer was found to be promising for the dedicated small launch vehicle, in terms of the excellent thrusting performance, whereas it was reported that the steady burning process is not promised in the well-mixed propellant. To obtain the fundamental burning characteristics which have been missing since the previous work by Nagata et al., and to seek the potential reason for the explosion-like burning and the data scattering observed in the previous work by Nagata et al., the approach, the motivation, and the objective of the present dissertation were stated in this chapter.

Chapter 3

3 Comprehensive experimental investigation

3.1 Introduction and objective of this chapter

In the previous work initially conducted by Nagata et al., the fundamental burning characteristics of the well-mixed propellant consisting of the fibrous polyamide soaked in liquid oxygen were not fully understood, owing to its limitations associated with experimental setup and methodologies (i.e., the difficulty in the use of LOX and the measurement method). To leverage its excellent thrusting performance of the well-mixed propellant, it is necessary to know fundamental burning characteristics, such as the whole burning behavior, parameter dependency on the regression rate, its steadiness, thermal structure, etc., as a first step. This chapter therefore aims to make comprehensive experimental investigations to clarify those fundamental burning characteristics of the porous combustible soaked in the liquid oxidizer, as referred to the previous work by Nagata et al. in 1997 [85]. The experimental setup, including the design of the propellant (hereinafter called “specimen”) and its measurement methodology of the regression rate, is firstly replaced into a following. A polyethylene foam (PE foam) for the porous combustible and enriched hydrogen peroxide for the liquid oxidizer for easy to handle at room temperature are

used in this work. Following the replaced specimen, a large volume chamber, which simply equips with a pair of transparent quartz window to allow direct observation, is newly introduced. With the replaced specimen and the chamber, the fundamental burning characteristics of the specimen and its effect of ambient pressure (0.1 MPa – 0.35 MPa) and fuel porosity (0.6 – 0.9) of the PE foam are experimentally examined in this work. Additionally, direct temperature measurement trials using an R-type thermocouple initially embedded into the specimen are conducted to know a thermal structure inside/outside the specimen during the burning event. Taking advantage of results of the temperature measurement trials, a global activation energy of the specimen is obtained by plotting relation between top surface temperature (burning surface temperature) and the regression rate. By comparing the global activation energy obtained in this work and global activation energies of the polymeric material reported by other research groups, its reliability of the results of the temperature measurement trials is discussed. Lastly, with the careful observation of the burning behavior during the burning event and with a simple thermal analysis, discussion of an applicability of the one-dimensional burning model in the present specimen is made.

3.2 Experiment

3.2.1 Experimental setup and tested specimen

Fig. 3 - 1 (A) and (B) show schematic diagrams of the whole experimental setup and an enlarged view of the tested specimen used in this work, respectively. All experiments are carried out in the large volume chamber (300 mm × 300 mm × 400 mm) which is equipped with a pair of quartz windows to allow direct observation during the entire burning event. The tested specimen is composed of the polyethylene (PE) foam (Sakai Chemical Industry Co., Ltd.; 99 % PE composition, 185 kg/m^3 apparent density), which measures 18 mm in diameter and 60 mm in height, and it is fully soaked in enriched hydrogen peroxide, H_2O_2 (Mitsubishi Gas Chemical Company, Inc.; solvent of 60 wt.% H_2O_2 concentration from an original product) as the liquid oxidizer. Ideally the solvent is enriched up to 100 wt.% by distillation. The tested specimen is then inserted into the vertically oriented transparent quartz tube for good visibility, which measures 18 mm in inner diameter and 50 mm in height, and one end of the quartz tube is closed off. As shown in Fig. 3 - 1 (B), about 10 mm of the PE foam is placed over the top edge of the quartz tube for ease of forced ignition. In the temperature measurement trials, the R-type thermocouple, TC (The Nilaco Cooperation, 0.1 mm in diameter and about 0.2 mm of junction size in diameter) is embedded into the center of the specimen in radius direction at the distance

of 25 mm below from the top edge with an inclined angle of about 30° as shown in the figure. The TC is tensioned moderately not to be dragged by force, such as viscosity of melted PE foam, from the original position, during the entire burning event.

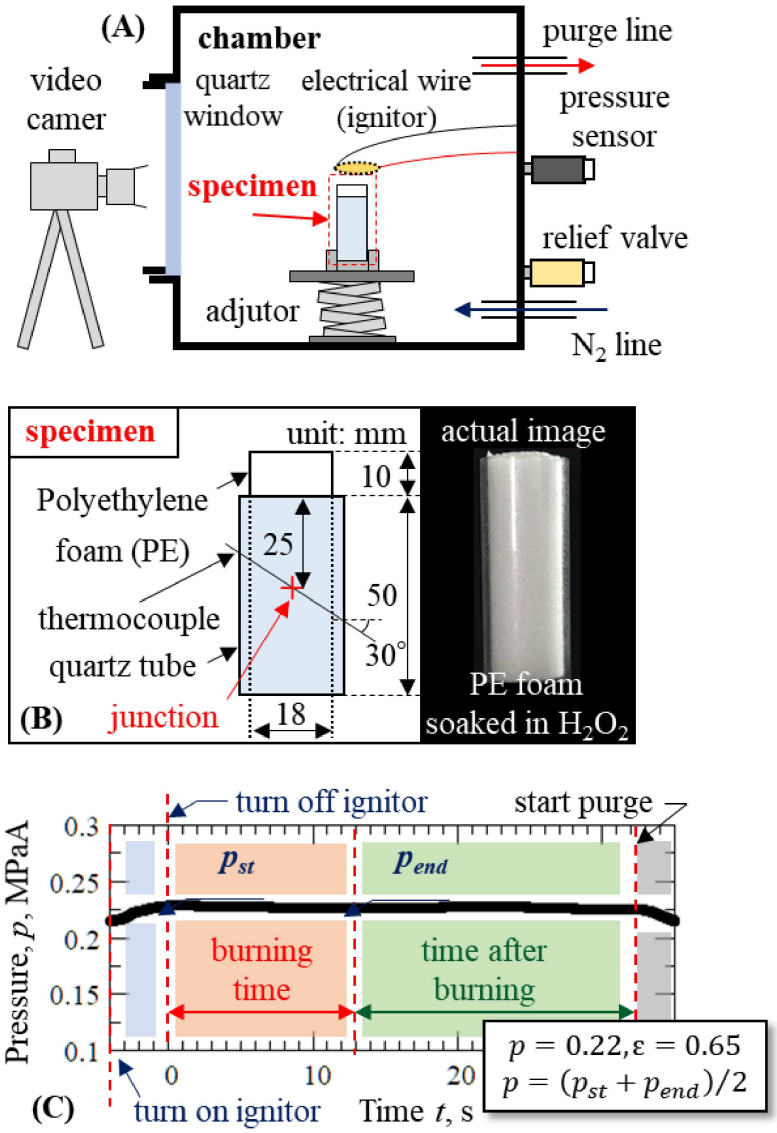

Fig. 3 - 1 Schematic diagram of (A) whole experimental setup and (B) enlarged view of tested specimen and (C) typical time history of pressure (p = 0.22 MPa) inside the chamber measured by the pressure sensor.

The forced ignition is induced by a U-shaped nickel–chrome wire (ignitor) that measures 0.8 mm in diameter. Once the specimen is set in the chamber, the U-shaped ignitor is set to be attached to the top surface of the specimen, and pressurization by nitrogen gas is initiated. The oxygen component in the air would affect the burning characteristics, so that nitrogen environment is adopted to investigate the burning characteristics of the present specimen itself. Only for the experiment at p = 0.1 MPa in absolute, the nitrogen and the purge lines remain open during its experiment to supply nitrogen gas into the chamber to make a nitrogen environment. Except for p = 0.1 MPa, the purge line is closed off to make high pressure environment, and the pressurization is done by manual operation. In this work, since the pressurization with nitrogen gas is started from when air (21 % oxygen concentration in vol.) is contained in the chamber before the pressurization, it is considered that the inside the chamber is not fully filled with pure nitrogen for all the cases. Pressure inside the chamber during entire the experiment is then measured by a pressure sensor (Valcom Co., LTD, VPRT (F), rated capacity: 1 MPa) which is connected to a wall of the chamber. Temporal signals from the pressure sensor and the TC are recorded by a data logger (GRAPHTEC midi LOGGER GL900) at a 100 Hz sampling rate. After completing pressurization up to a desired value, 210 W power is applied to the ignitor for 5 – 10 s to achieve successful ignition. The ignitor is then removed from the top of the specimen to prevent any

disturbance by the ignitor on the burning event. The whole burning behavior is recorded by a digital video camera (Canon iVIS HF G20; 60 fps frame rate, 1/250 shutter speed, 18 dB gain, 2.8 F number) through the view window. The moving burning surface is traced using an image processing software ImageJ [88]. The experiments are conducted at an initial pressure range from p = 0.1 MPa to p = 0.35 MPa in absolute and a fuel porosity range from 0.6 to 0.9. As a typical example of the pressure during the entire experiment, Fig. 3 - 1 (C) shows overall time history of the pressure inside the chamber when the averaged pressure is set as p = 0.22 MPa in absolute. An initial time when confirming the ignition at the top surface is adjusted to t = 0. Four periods are then shown; a period while the ignitor is turned on and off, a period during the burning event, and a period after burning event, and a period during the purge event, respectively. An averaged pressure at the two points of the initial pressure P_{st} (when we confirm the ignition) and the final pressure P_{end} (when the burning event finishes (flame quenches)) is employed in this work (see Fig. 3 - 1 (C)). We confirmed that all the experiments are conducted under almost the constant pressure environment as denoted on the figure (C), thus granting quasi-steady burning conditions. The reason for the slight fluctuation of the pressure in the burning time is due to the manual operation to achieve the desired pressure. After confirming that the burning event is completed, the purge line opens, and burned gas is exhausted outside the chamber.

3.2.2 Large volume chamber

In this work, the self-made large volume chamber which measures 300 mm in length, 300 mm in width, and 400 mm in height is used. When the specimen is burned in a pressurized environment (in the chamber), it may affect the pressure inside the chamber. Furthermore, if the dimension of the specimen is large, large amount of burned gas from the specimen is ejected. These may lead to deviation from the initial pressure and affecting the overall burning characteristics. Therefore, it is necessary to design the chamber large enough, together with considering the specimen dimension, so as not to be deviated from the initial pressure and affect the burning characteristics during the entire burning event. Here, the reason for determination of the dimension of both the chamber and the specimen, and its validity will be stated by considering simple calculation.

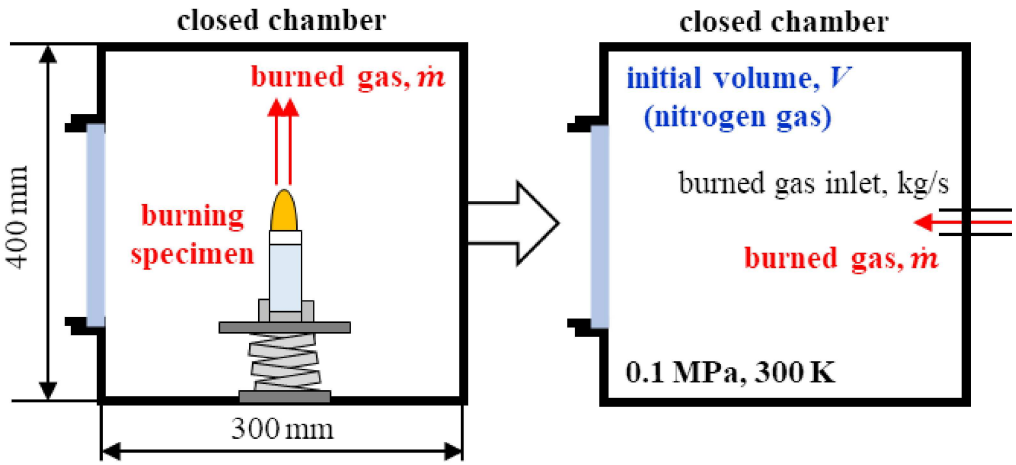

Fig. 3 - 2 Explanation of validity for large volume chamber dimension.

An explanation, with a schematic illustration, of the determination and its validity for the chamber dimension is presented to Fig. 3 - 2. Let us consider the situation in the right figure where the burned gas at the rate of kg/s is injected from the “burned gas inlet” into the chamber in which pure nitrogen (300 K, 0.1 MPa in absolute) is initially filled. Assuming that the top surface of the specimen moves downward at the rate of 2 mm/s (V_f), the mass flow rate of the burned gas ($\dot{m}$) injected into the chamber is calculated as follows (Eq. 2 - 1).

$$\dot{m} = \rho_P V_f A_P$$

The apparent density of the specimen (ρ_P) of 1344 kg/m^3 and the burning surface area (A_P) of 0.254 x 10^3 m^2 (calculated based on 18 mm in diameter) are used for the calculation of the mass flow rate. Thus, the burned gas ($\dot{m}$) is injected into the chamber at the rate of 0.684 x 10^{-3} kg/s. Considering that an ideal gas and rapid diffusion of the burned gas in the entire volume (V) in the chamber are assumed, pressure rise (Δp) per second, Pa/s, can be estimated by the combined gas law (Boyle-Charle’s law).

$$\Delta p = \frac{\dot{m}}{V}\frac{R}{M}T \qquad \text{Eq. 3 - 1}$$

where R [J/(mol·K)] is the universal gas constant, M [kg/mol] is the average molecular weight of the gas in the chamber, and T [K] is the average temperature of the gas in the chamber. The

"average" means average values of the mixed gas (the burned gas and nitrogen). Let us assume that the PE foam is a polymer of ethylene (C_2H_4), and pyrolysis gas is pure ethylene. The following overall chemical reaction can be considered.

$$C_2H_4 + 6H_2O_2 = 2CO_2 + 8H_2O \qquad \text{Eq. 3 - 2}$$

Hence, the molecular weight of 23.2 x 10^{-3} kg/mol for the burned gas is introduced, and the average molecular weight (M) of 25.6 x 10^{-3} kg/mol can be finally estimated by assuming that the average molecular weight is the average value of the burned gas and nitrogen gas for simple purpose. Hence, the pressure rise (Δp) is estimated as 6.17 x T [Pa/s]. The initial volume (V) is much larger than the total volume of the burned gas, thus, the average temperature is considered as much as low ≈ 300 K. Therefore, the pressure rise can be estimated as 1851 Pa/s and negligible (small enough), judging that the effect of the burned gas on the pressure rise and the burning characteristics is negligible. For this reason, we can say that the dimension is valid, and the size of the present specimen is enough so as not to occur the pressure deviation after finishing the combustion.

3.2.3 Thermocouple tensioner and methodology of tension and inclination

As already mentioned, the TC is moderately tensioned and inclined about 30 degrees toward the horizontal direction. The methodology to make the tension and the inclination is schematically illustrated in Fig. 3 - 3. Each metal wire of the TC is fixed by the compensated wires, and the compensated wires are fixed at the tensioner and allowed to move the horizontal direction by the mover. One of the metal wires for the TC is located upper than another TC to make the inclination about 30 degrees toward the horizontal direction.

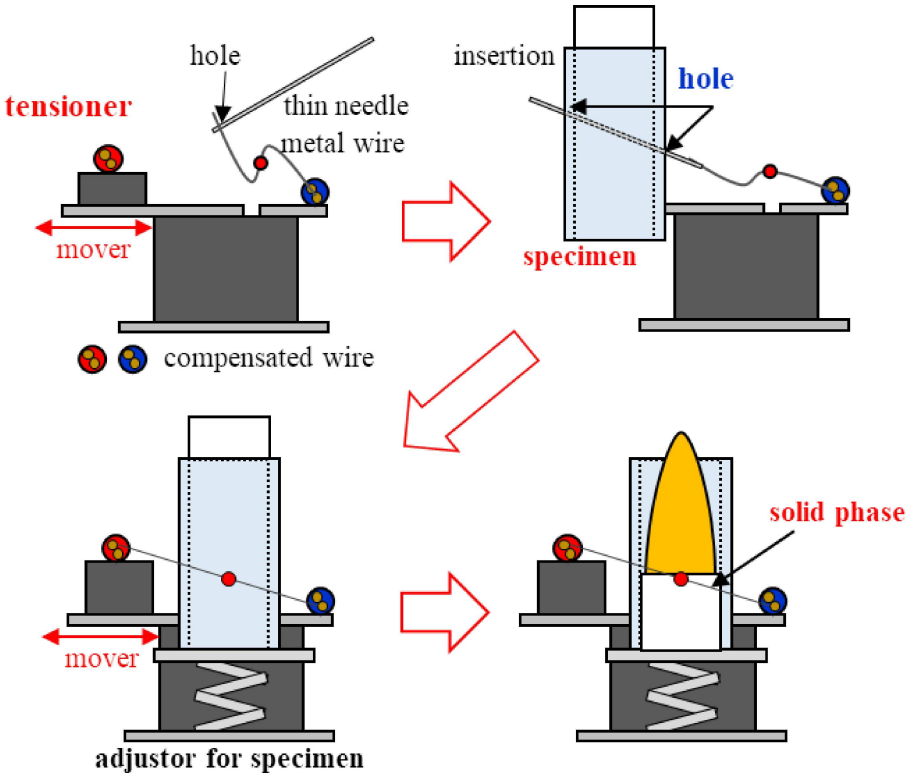

Fig. 3 - 3 Methodology of tension and inclination with thermocouple tensioner.

After making the junction of the TC by a burner, one of the metal wires is fixed at the compensated wire, and then the junction of the TC is inserted into the specimen by using the thin needle, which has a hole to pass through. Two holes are drilled at the side of the quartz tube to insert. After inserting the junction and the other side of the metal wire is fixed to the other side of the compensated wire, the setup is finished. It was found in the preliminary experiment that the melted PE foam dragged the TC downward when the TC is set horizontally as shown in Fig. 3 – 4 (left). Holding the TC inclined 30 degrees as shown in the right figure, although the left side of the TC (not junction) is passing through the flame, the right side of the TC remains in solid phase. With this respect, it is reasonable that the TC is inclined at 30 degrees to hold at the original location even during the burning event.

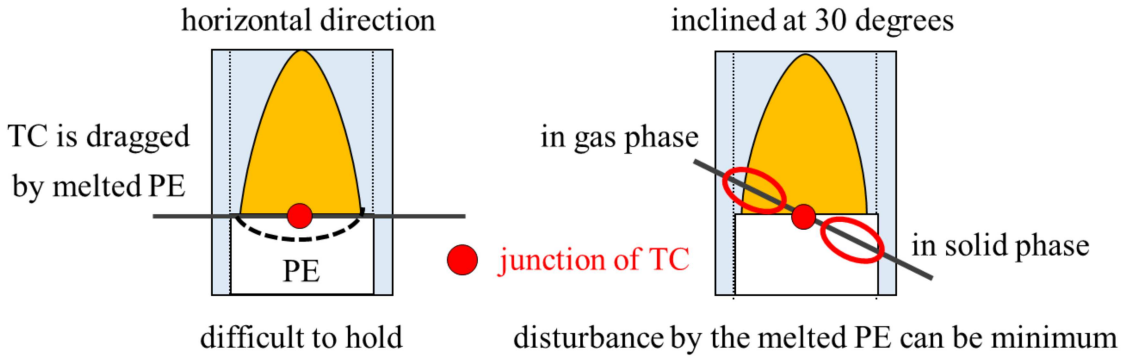

Fig. 3 - 4 Methodology of tension and inclination with thermocouple tensioner.

3.2.4 Distilling process of hydrogen peroxide

As have stated previously, the concetnration of the original solvent of hydrogen peroxide (comercially-available product) is 60 wt.%, and the rest is purified water. When pure hydrogen peroxide is heated and reached to its boiling temperature, molecular oxygen and water are generated while releasing much of heat by an exthothermic decompoition reaction. Fig. 3 - 5 and Fig. 3 - 6 show the relationship between oxygen liberation capacity and the H_2O_2 concentration and the relationship between the latent heat (vaporization and decomposition) and the H_2O_2 concentration.

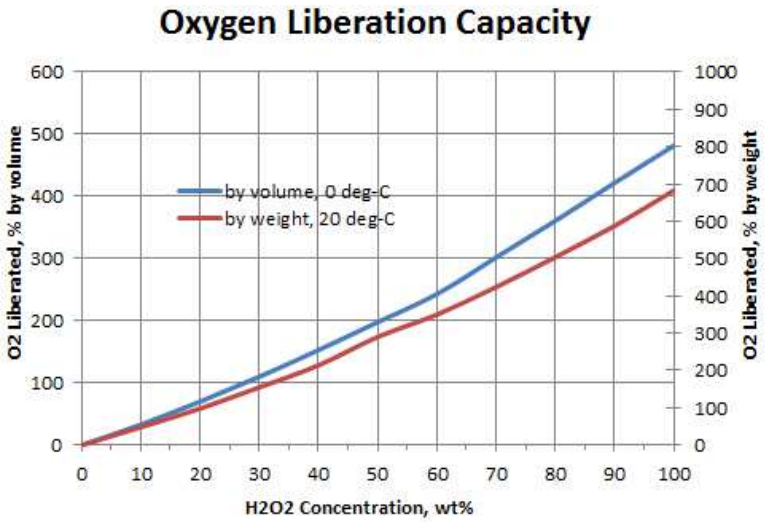

Fig. 3 - 5 Relationship of oxygen liberation capacity and H_2O_2 concentration [89].

In Fig. 3 - 5, higher ammount of the molecular oxygen shall be liberated in the case when the H_2O_2 concentration is enriched. More importantly from Fig. 3 - 6, the exothermic reaction shall

be intensified for the case of the higher H_2O_2 concentration. For this reason, the original product of hydrogen peroxide is enriched in order to obtain a lot of heat in this work. .

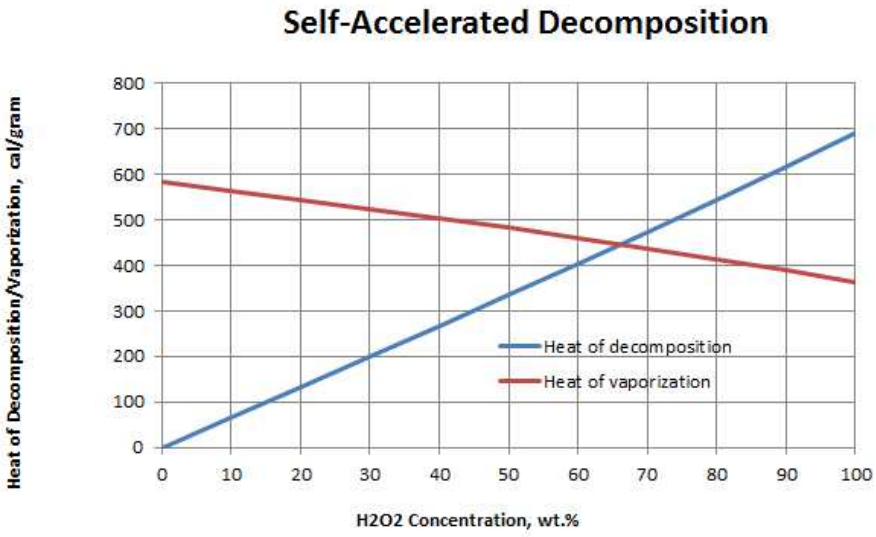

Fig. 3 - 6 Relationship of heat of vaporization and decomposition of hydrogen peroxide and H_2O_2 concentration [90].

A following distilling procedure is adopted to enrich the H_2O_2 concentration. Firstly, a spirit lamp, thermocouple (CHINO CORPORATION, 0.5 mm sheeth-type (K-type)), the data logger, and the original product of 40 mL pored into a beaker are prepared. As shwon in Fig. 3 - 7, the beaker is heated by the spirit lamp, and its temprature is monitored by the data logger to keep the boiling point of water (373 K).

Assuming that only water component in the solevnt and no hydrogen peroxide component are vaporized at the boiling temperature, the mass-based concentration (wt.%) is determined as

follows.

$$(\text{wt.}\%) = \frac{\alpha_{in} m}{\alpha_{in} m + [(1 - \alpha_{in}) m - \rho_{H2O} y]} \qquad \text{Eq. 3 - 3}$$

where α_{in} [wt.%] is the initial H_2O_2 concentration (60 wt.%), m [kg] is the initial mass of the original product (water-dilluted hydrogen peroxide) poured into the beaker, ρ_{H2O} [kg/m^3] is the density of water, and y [m^3] is the water volume necessary to be reduced. Therefore, as soon as the initial mass of the original solvent poured into the beaker is determined, the concentration corresponding the reduced water volume (y) is determined accordingly. The electronic balance (Shimadzu Corporation, UW820S) is used for measuring the initial mass of the original solvent. Ideally, to obtain 100 wt. % at the left hand side of Eq. 3 - 3, it can be calculated that 16 mL of the water volume should be reduced from the original solvent (initial volume: 40 mL) left at the boiling temperature of the water all the time. The detailed characteristics of hydrogen peroxide are summarized in the Appendixes (B – 3 – 2).

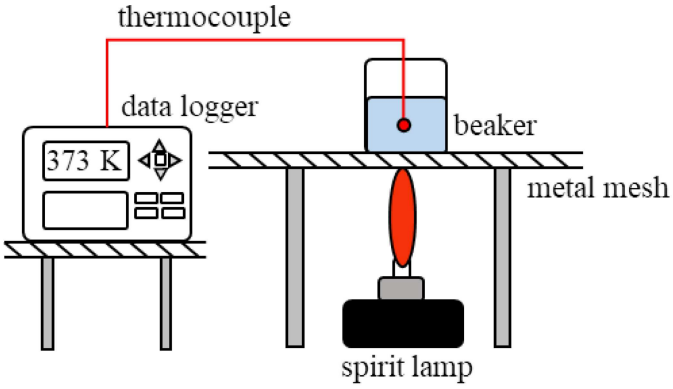

Fig. 3 - 7 Whole experimental setup to enrich original product of hydrogen peroxide.

3.2.5 Image processing

To track the instantaneous location of the top surface of the specimen and measure the regression rate, the top surface of the specimen during the entire burning event is firstly detected by using the image processing software (Image J). Procedure of the image processing to obtain the top surface is shown in the following flowchart. Firstly, the video during the burning event, recorded at 60 fps, is split into 10 frames. Typical example of sequential flame shapes at an interval of 2 seconds under an experimental condition (p = 0.1 MPa in absolute and ε = 0.72) is presented to Fig. 3 - 8 (top). Scale image taken beforehand is inserted into image J to determine the relationship between the scale (mm) and pixel. The split images shown on Fig. 3 - 8 (top) are then converted into 8-bit images, and binarized images shown on Fig. 3 - 8 (bottom) are produced. As it is seen, luminosity of the flame shapes is varied depending on time and experimental conditions, hence, the most suitable method, which can detect the top surface clearly, by comparing 16 types of the methods built-in the image J, was adopted in this work. The “Otsu” method is adopted in this work. From the binarized images (bottom), the white areas show the flame shapes detected by the image processing, and it is considered that the lowest point of the white area is the flame tip. In this work, the top surface of the specimen is defined as the lowest

point of the white area for convenient purpose. The top surface location obtained with this manner is then saved into CSV file.

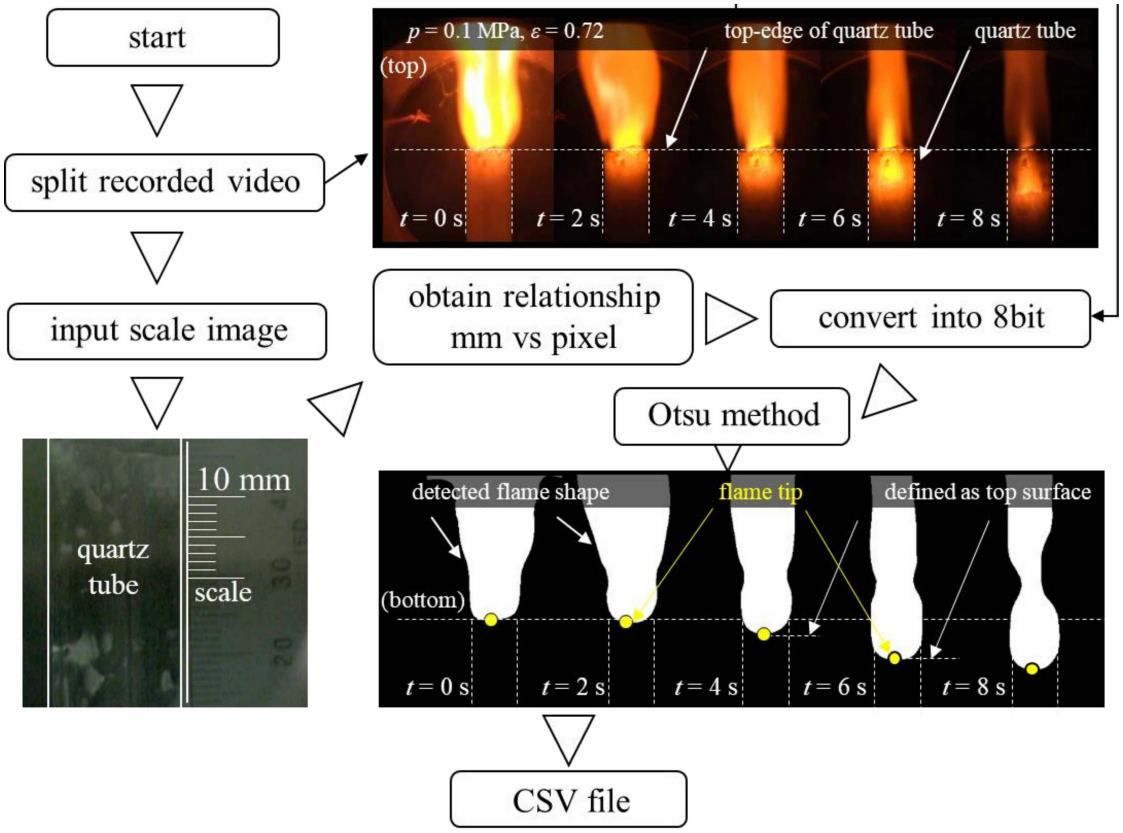

Fig. 3 - 8 Procedure of image processing and typical example of the image processing: (top) sequential flame shapes during burning event and (bottom) binarized images of sequential flame shapes (p = 0.1 MPa in absolute and ε = 0.72).

3.2.6 Statistical analysis

After measuring the regression rate by the image processing, the repeatability of the regression rate will be confirmed by applying a statistical analysis. In practice, we rarely know the true values of experimentally obtained data, because a lot of considered errors are included in the data, so that the experimental data is always different even though the experimental procedure and the conditions are the same. However, it is possible to estimate the true values based on the experimentally obtained data by adopting the 95 % confidence interval using the student's *t*-distribution. The definition of the 95 % confidence interval of the regression rate is "a range of the regression rate so defined that there is a specified probability (95 %) that the regression rate lies within it". We will obtain the 95 % confidence interval (so called "error bars") from student's *t*-distribution and show the error bars on the experimental results. The student's *t*-distribution is used instead of the normal distribution when the experimental trials are limited (small number of experimental trials).

An example of the explanation of the student's *t*-distribution is schematically illustrated in Fig. 3 - 9. In the figure, the example of the regression rate and the average regression rate ($\overline{V_f}$) are displayed. The true value of the regression rate based on the example values of the regression rate on the table can be calculated with the following manner. First, *t*-distribution formula is expressed

by Eq. 3 - 4, and the right-hand side of Eq. 3 - 4 is calculated.

$$t = \frac{\bar{V}_f - \mu}{\sqrt{\frac{s^2}{n}}} \qquad \text{Eq. 3 - 4}$$

$$s^2 = \frac{1}{n-1}\sum_{i=1}^{n}\left(V_{f\_i} - \bar{V}_f\right)^2 \qquad \text{Eq. 3 - 5}$$

where t is the values of the t-distribution, $\bar{V}_f$ is the average regression rate obtained in nth-runs experiments, μ is the population mean of the regression rate, and s^2 is the unbiased dispersion.

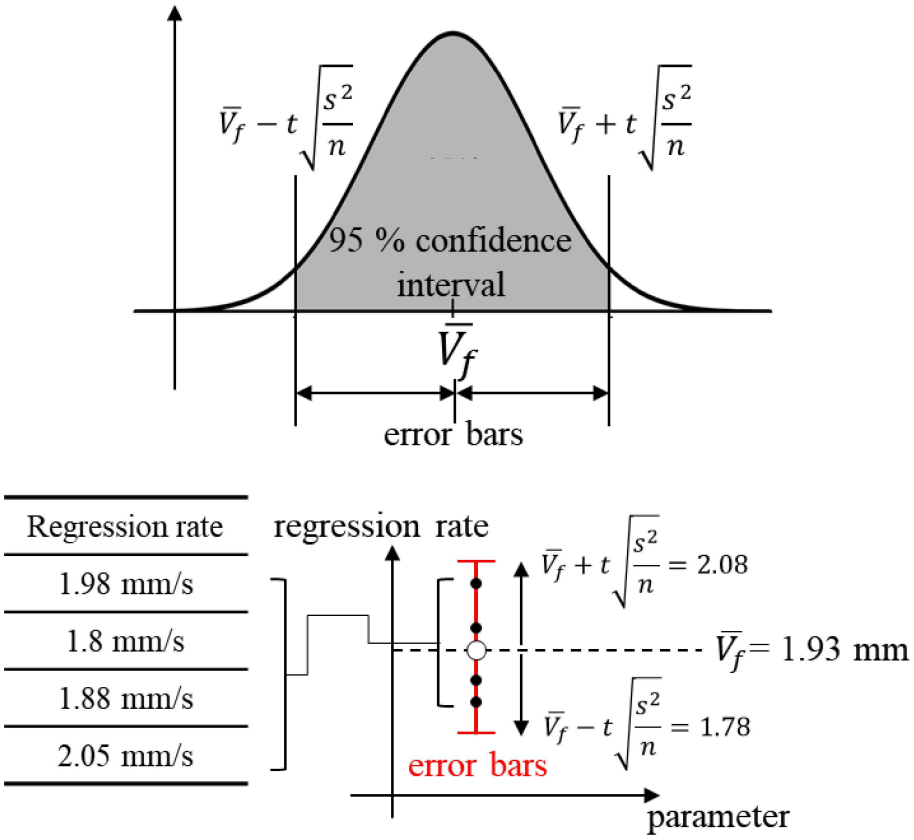

Fig. 3 - 9 Schematic illustration of error bars obtained from student's t-distribution and example of calculation of error bars.

In this work, four-runs measurement (n = 4) of the regression rate at the same experimental conditions will be carried out, and the 95 % confidence interval is estimated based on the results of the four-runs experiments. t value (t) shown in Eq. 3 - 4, is then derived from the t-table. In the case of the 95 % confidence interval and four-runs experiments (n = 4), t value of 2.776 can be used. Hence, the true value of the regression rate (μ) based on the experimentally obtained regression rate is finally estimated as follows. The left-hand side and the right-hand side of the following relation show the error bar.

$$\overline{V_f} - t\sqrt{\frac{s^2}{n}} < \mu < \overline{V_f} + t\sqrt{\frac{s^2}{n}} \qquad \text{Eq. 3 - 6}$$

The obtained range, estimated by Eq. 3 - 6, is between $1.78 < \mu < 2.08$ mm/s from the example of the regression rate. This indicates that the true value of the regression rate (μ) is within the obtained range. This analysis methodology will be affected to the experimental results in this chapter.

3.2.7 Definition of global equivalence ratio depending on fuel porosity

The fuel porosity of the PE foam is one of the fuel properties that affect the burning characteristics. In the present work, the experiment will be conducted under various fuel porosities to examine its effect. The definition of the fuel porosity is given as follows

$$\varepsilon = \frac{V_L}{V} = \frac{\frac{m_L}{\rho_L}}{\frac{m_L}{\rho_L} + \frac{m_S}{\rho_S}} \qquad \text{Eq. 3 - 7}$$

where ε [-] is the fuel porosity of the PE foam, V_L [m^3] is the total pores' volume of the PE foam, V [m^3] is the total volume of the H_2O_2-soaked PE foam, m_L [kg] is the initial mass of H_2O_2 contained in the PE foam, m_S [kg] is the initial mass of the PE foam, ρ_S [kg/m^3] is the density of the PE foam, and ρ_L [kg/m^3] is the density of H_2O_2, respectively. The fuel porosity of the PE foam can be adjusted by making each mass (m_L and m_S) control from the original product (PE foam) by uniformly drilling along vertical direction with a very thin drill (0.1 mm in diameter). m_L and m_S are measured by electronic balance (Shimadzu Corporation, UW820S), and the fuel porosity can be determined accordingly. We made our best to fully soak H_2O_2 into the pores of the PE foam for every experiment. In case when H_2O_2 is completely soaked in all the pores, and assuming that the steady burning process is achieved, an oxidizer-to-fuel mass ratio (namely, *O/F*) is introduced

as a following relation with using the fuel porosity (ε) or each mass (m_L and m_S). Thus, global equivalence ratio (φ) is given as follows with the fuel porosity expression.

$$\left(\frac{O}{F}\right)_{ex} = \frac{\varepsilon\rho_L}{(1-\varepsilon)\rho_S} = \frac{m_L}{m_S} \qquad \text{Eq. 3 - 8}$$

$$\varphi = \frac{\left(\frac{O}{F}\right)_{th}}{\left(\frac{O}{F}\right)_{ex}} = \frac{\left(\frac{O}{F}\right)_{th}}{\frac{\varepsilon\rho_L}{(1-\varepsilon)\rho_S}} \qquad \text{Eq. 3 - 9}$$

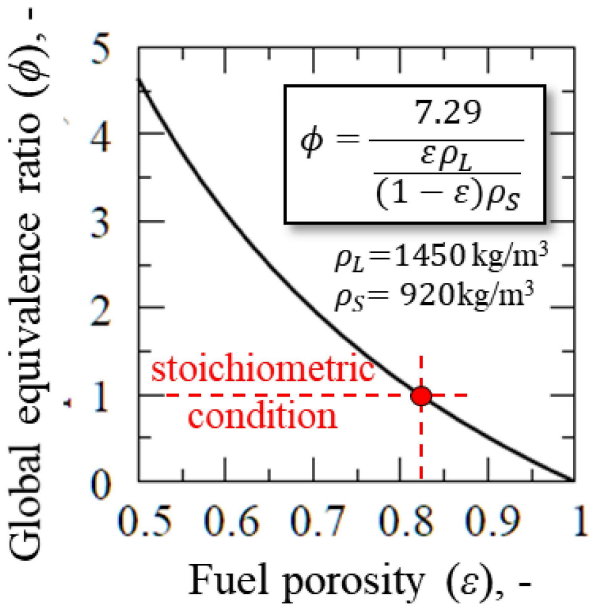

Fig. 3 - 10 Relation of global equivalence ratio (φ) and fuel porosity (ε) determined by Eq. 3 - 9.

Assuming that one-step overall reaction (Fuel + v Oxidizer → (1 + v) Product, v is the stoichiometric coefficient based on a mass) is adopted, and pyrolysis gas of the PE foam mainly

consists of ethylene (C_2H_4), a stoichiometric oxidizer-to-fuel mass ratio $(O/F)_{th}$ shall be 7.29 as calculated using the molecular weights (C_2H_4: 28 g/mol and H_2O_2: 34 g/mol) from overall chemical reaction shown in Eq. 3 - 2. By giving the densities (ρ_L ; 1450 kg/m^3 and ρ_S ; 920 kg/m^3), the relation between the global equivalence ratio and the fuel porosity is obtained in Fig. 3 - 10, and the fuel porosity to achieve the stoichiometric condition is determined as ε = 0.82.

3.3 Experimental results and discussion

3.3.1 Effect of pressure on flame shapes and location of surface flame

Fig. 3 - 11 shows the effect of pressure (A) p = 0.1 MPa, (B) p = 0.22 MPa, and (C) p = 0.29 MPa in absolute with almost the constant fuel porosity ε = 0.65 on the typical sequential flame shapes during the burning event. The origin of the x' coordinate $(x' = 0)$ is fitted to the top edge of the quartz tube. The global equivalence ratio that corresponds to ε = 0.65 is φ = 2.5, calculated based on Eq. 3 - 9. Therefore, combustion for all the cases here is taken place under the fuel-rich condition. After the successful ignition at the top surface of the specimen, it is confirmed that the top surface of the specimen moves downward for all the cases. In addition, it is identified that two distinctive flames are established. One is an elongated diffusion flame (an outer flame), the other is a surface flame (a brighter flame) around the exposed surface, as illustrated in Fig. 3 - 11 (D). For this type of combustion, thermal pyrolysis (gasification) of the PE foam gradually occurs at the location beneath the top surface, and vaporization of the H_2O_2 is expected to occur deeper than the location where the thermal pyrolysis is initiated. Taking into the account this fact, the premixed-gas mixture (mixture of the gasified fuel and the vaporized oxidizer) is formed inside the PE foam and will be supplied into the flame, establishing the premixed-like surface flame near the top surface. The outer flame is then established because the premixed-gas mixture which does

not consume at the surface flame reacts again with the oxygen slightly containing in the ambient gas. Hence, if nitrogen gas is fully filled in the chamber, it is expected that the outer flame does not appear. Additionally, it is also identified that the luminosity of the surface flame increases as pressure increases. As pressure increases, in general, adiabatic flame temperature and soot formation are increased [91]. These may contribute to the change in the flame brightness.

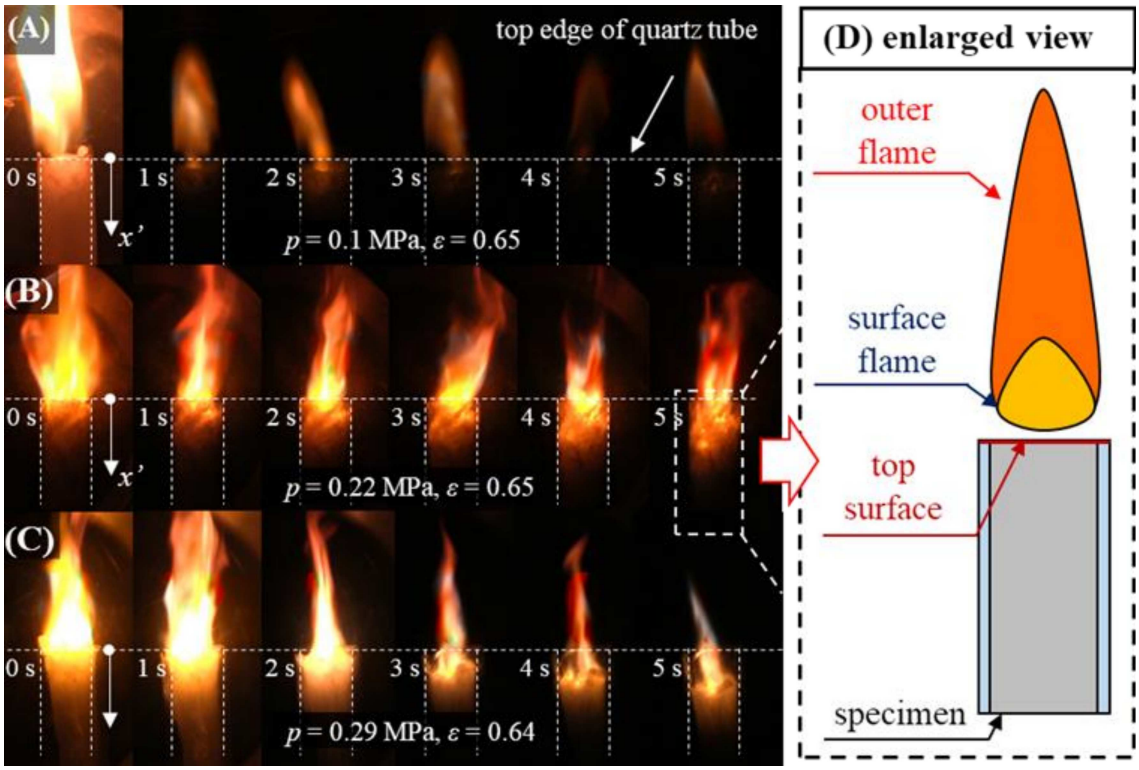

Fig. 3 - 11 Typical sequential flame shapes after forced ignition at top surface of specimen with $\varepsilon = 0.65$ of fuel porosity at (A) $p = 0.1$ MPa, (B) $p = 0.22$ MPa, and (C) $p = 0.29$ MPa in absolute, and (D) schematic diagram of surface flame and outer flame.

In order to quantitatively evaluate the regression rates for the conditions of (A) p = 0.1 MPa, (B) p = 0.22 MPa, and (C) p = 0.29 MPa, time histories of locations of the surface flame attached to the top surface are plotted in Fig. 3 - 12, by adopting the image processing software. In the figure, lines obtained from the least squared method for each condition are shown together. The gradient of the lines shows the linear regression rate (in this chapter, called "overall regression rate" hereafter). It is obvious that the surface flame moves downward with reasonably constant rates of (A) 1.6 mm/s (R^2: 0.9655), (B) 2.4 mm/s (R^2: 0.9897), and (C) 2.9 mm/s (R^2: 0.9762), respectively, with satisfactory R^2 (coefficient of determination) values. For the sake of convenience, the burning event when obtaining overall regression rate with more than 0.96 R^2 value are dealt with as "steady burning" in this work.

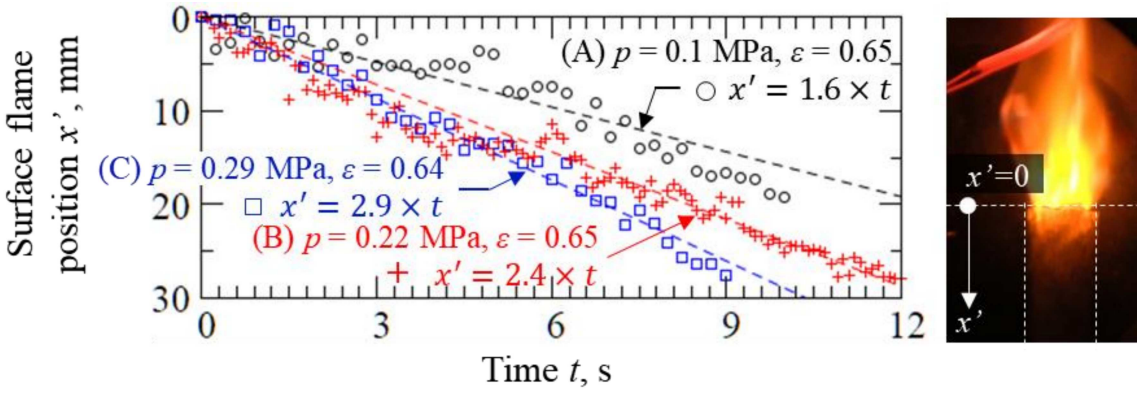

Fig. 3 - 12 Time history of locations of surface flame obtained from image processing software under (A) p = 0.1 MPa, (B) p = 0.22 MPa, and (C) p = 0.29 MPa in absolute with almost the constant fuel porosity ε = 0.65.

3.3.2 Effect of fuel porosity on flame shapes and location of surface flame

Fig. 3 - 13 shows the effect of the fuel porosity (A) $\varepsilon = 0.65$, (B) $\varepsilon = 0.72$, and (C) $\varepsilon = 0.80$ on the burning behavior during the burning event at standard pressure ($p = 0.1$ MPa in absolute), respectively. The global equivalence ratios that correspond to those fuel porosities are (A) $\varphi = 2.5$ ($\varepsilon = 0.65$), (B) $\varphi = 1.8$ ($\varepsilon = 0.72$), and (C) $\varphi = 1.2$ ($\varepsilon = 0.80$), respectively. Therefore, combustion in (A) and (B) is taken place under fuel-rich condition, and combustion in (C) is taken place under almost the stoichiometric condition. For all the cases, the outer flame and the surface flame as described in the previous section are identified. As mentioned, it is considered that inside the chamber is not completely full of nitrogen gas, so that the outer flames are pronounced. In comparison with all the conditions, as the fuel porosity approaches to the stoichiometric condition ($\varepsilon = 0.8$), the luminosity of the two flames is increased. This is attributed to an increase in the flame temperature when the fuel porosity approaches to the stoichiometric condition. Moreover, it is seen that the outer flame elongates when the fuel porosity approaches to the stoichiometric conditions. Especially for when the fuel porosity approaches to the stoichiometric condition from such a fuel-rich condition, the regression of the specimen is promoted, and the amount of the (fuel rich) premixed-gas mixture which does not consume at the surface flame is increased. This leads to that the outer flame elongates.

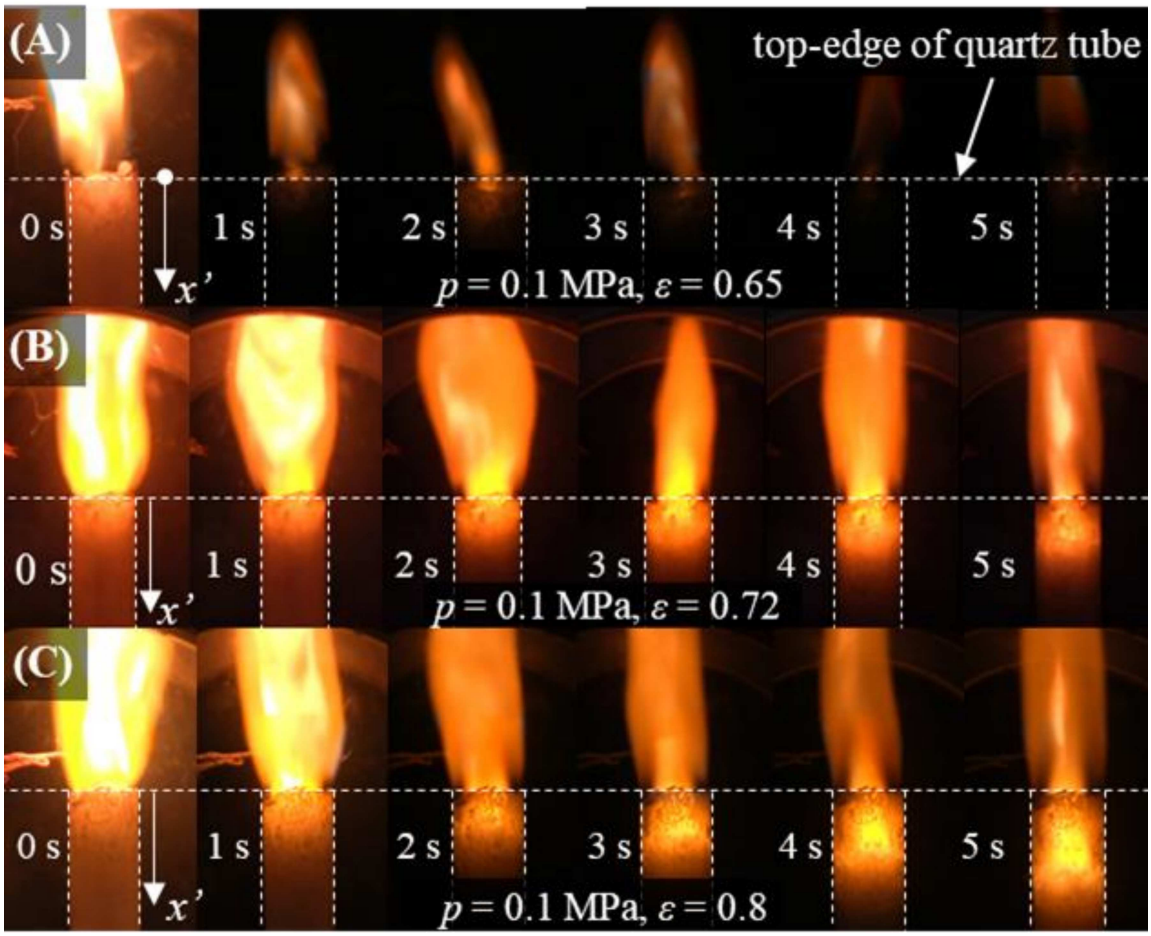

Fig. 3 - 13 Typical sequential flame shape after forced ignition at top surface of specimen around p = 0.1 MPa in nitrogen environment with fuel porosity (A) ε = 0.65, (B) ε = 0.72, and (C) ε = 0.8.

Again, the time histories of the locations of the surface flame are plotted in Fig. 3 - 14 for (A) ε = 0.65, (B) ε = 0.72, and (C) ε = 0.8 at p = 0.1 MPa in absolute, together with the lines obtained from the least squared method. It is obvious that the surface flame moves downward with reasonably constant at the rate of (A) 1.6 mm/s (R^2: 0.9655), (B) 1.8 mm/s (R^2: 0.9932), and (C)

2.7 mm/s (R^2: 0.9950), respectively with satisfactory R^2 value as well. By these facts, we may safely say that the present specimen can achieve steady burning event experimentally in the conditions studied. On the other hand, it is seen that slight fluctuations of the locations of the flame surface are plotted in both the figures (Fig. 3 - 12 and Fig. 3 - 14). This is attributed to formation of molten PE adhered to the inner wall of the quartz tube during the burning event. Although this makes it difficult to visualize the exact location of the surface flame, it does not hinder the experimental computation of the overall regression rate in this system.

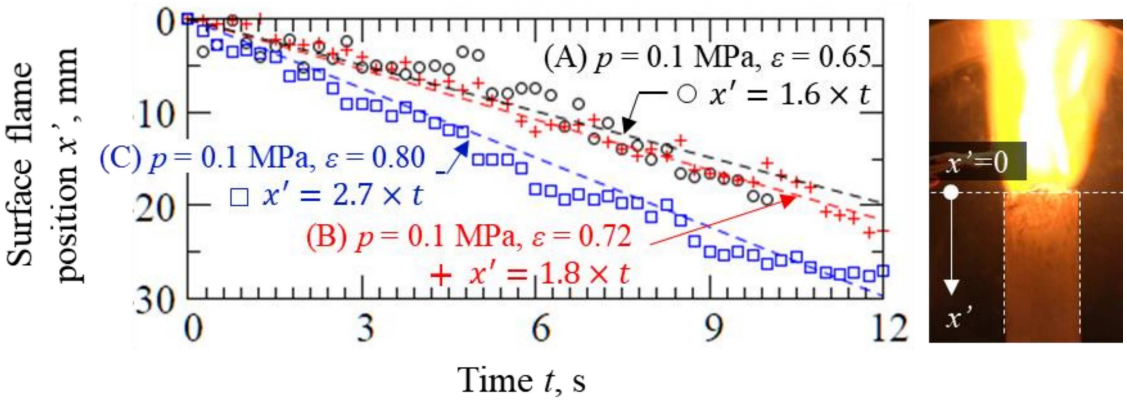

Fig. 3 - 14 Time history of location of surface flame obtained from image processing software at p = 0.1 MPa in absolute with (A) ε = 0.65, (B) ε = 0.72, and (C) ε = 0.8, together with lines obtained from least squared method.

In all the experimental conditions, it was found that the surface flames were attached to the top surface of the specimen all the time. At least, we did not observe phenomenon such as flame spreading mode under studied conditions. The direct observation reveals that the burning event

occurs at which the top surface moves downward constantly and indicating that combustion in this specimen occurs as an end burning mode.

3.3.3 Effect of fuel porosity and pressure on overall regression rate

In this section, we would like to summarize the overall regression rates obtained under various pressures and the fuel porosities. Fig. 3 - 15 (A) shows the overall regression rate versus the fuel porosity for p = 0.1 MPa, 0.15 MPa, 0.2 MPa, 0.25 MPa, 0.3 MPa in absolute. The global equivalence ratios corresponding to the fuel porosities are shown on the second horizontal axis. Four-runs experiments for each porosity and pressure are carried out for reproducibility. The error bars shown in the figure are calculated by 95 % confidence interval, based on Eq. 3 - 6. It is clearly seen that the overall regression rate varies depending on the fuel porosity and pressure. The reproducibility (the error bars) is found to be less than 1 mm/s for all the cases. In this work, the overall regression rates are obtained with a wider range of the fuel porosity (ε = 0.6 - 0.9) at p = 0.1 MPa, and it is found that the overall regression rates vary from 1.4 mm/s to 2 mm/s, depending on the fuel porosity. The maximum overall regression rate is measured with ε = 0.8. The reason for the trend of the overall regression rate obtained for the fuel porosity is because, as mentioned, the combustion follows the fuel porosity as shown in Fig. 3 - 10. This increasing or

decreasing trends of the regression rate versus the fuel porosity at p = 0.1 MPa, across the stoichiometric condition are essentially similar to the trend of the laminar burning velocity of premixed-gas mixture versus the equivalence ratio. Looking at the result at p = 0.1 MPa, it is, therefore, expected that the overall regression rate is influenced by the (premixed-like) surface flame, and premixed burning model is found to be valid. However, the experiments in a wide range of the fuel porosity are limited only at p = 0.1 MPa, further experiments with various fuel porosity under high pressure environments are needed to support this expectation.

Fig. 3 - 15 (B) summarizes the overall regression rate (V_f) versus pressure (p) with the fuel porosity $\varepsilon = 0.65 \pm 0.05$ and $\varepsilon = 0.75 \pm 0.05$. The logarithmic display for both the axes is adopted. It is seen that the overall regression rates span from 1 mm/s to 3.2 mm/s under the conditions studied, and that the overall regression rate increases as pressure increases and has pressure dependency. This increasing trend of the regression rate with the increase in pressure is qualitatively consistent with one found in the AP-based composite solid propellant [92] and the previous work by Nagata et al. [85].

As the abovementioned results, we could successfully obtain those fundamental burning characteristics of the tested specimen (i. e., the pressure and the fuel porosity dependency on the overall regression rate, its steadiness, and the burning behavior, which the data have been missed

since the previous work by Nagata et al. (1997) [85]. In this work, it made us possible to develop the simple experimental setup to investigate those burning characteristics by adopting H_2O_2 (not LOX). For this reason, adopting H_2O_2 is suitable to employ as the liquid oxidizer as a first place for the deep understandings of the well-mixing specimen.

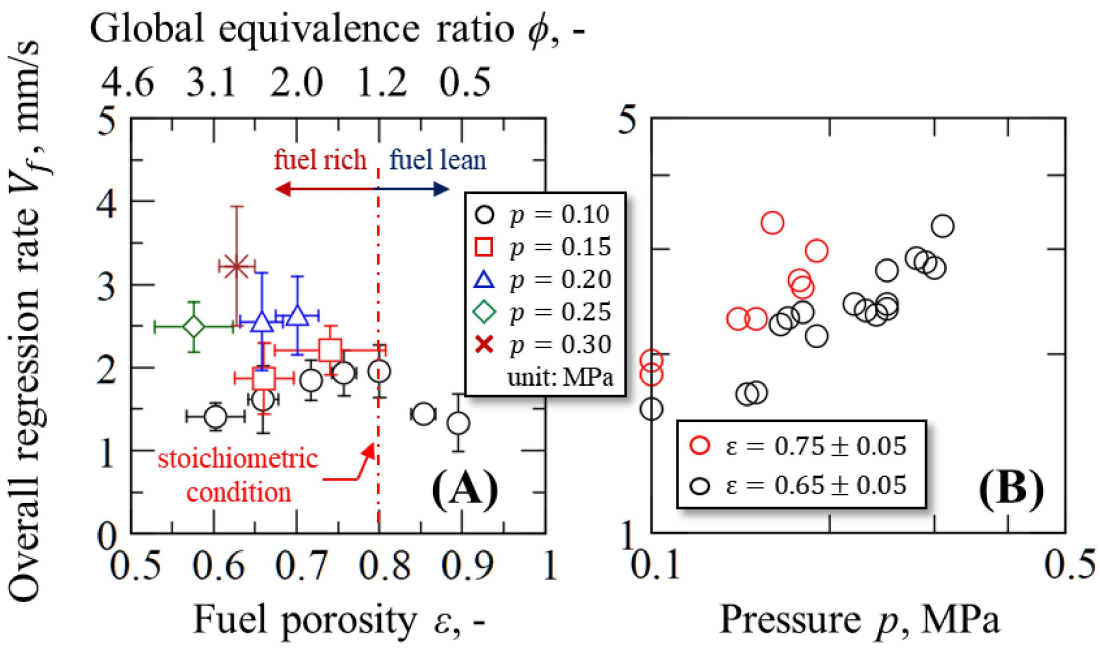

Fig. 3 - 15 (A) Overall regression rate vs fuel porosity under various pressure (p = 0.1 MPa, 0.15 MPa, 0.2 MPa, 0.25 MPa, 0.3 MPa) and (B) regression rate vs pressure with ε = 0.65 ± 0.05 and 0.75 ± 0.05.

3.3.4 Effect of pressure on thermal structure

Assuming that a dominant heat flux from the flames to the specimen is thermal conduction through the gas-phase layer between the surface flame and the top surface of the specimen,

examining thermal structure (e.g., profiles of temperature, temperature gradient, and top surface temperature) is of significant importance to know the reason for the increasing or decreasing trend of the regression rate as found in Fig. 3 - 15. In the AP-based composite solid propellant, the methods to tailor the regression rate have been discussed from a viewpoint of the thermal structure. In order to examine the thermal structure in the AP-based composite solid propellant, many research groups have made a significant effort to measure the thermal structure by various type of methodologies. Especially, temperature measurements using a fine thermocouple have been widely conducted (e. g, [93] [94] [95] [96] [97]).

To know the thermal structure in the present specimen, additional experiments for temperature measurements using the R-type thermocouple (junction size: 200 μm) are carried out. Before presenting results of the temperature measurement, we would like to show the location of the top surface of the specimen, the location of thermocouple, and its corresponding temperature signal measured by the thermocouple as schematically illustrated in Fig. 3 - 16 for easier understanding of the temperature measurement. As shown in Fig. 3 - 16, after when the ignition at the top surface is made, the temperature signal measured by the thermocouple will increase by the boiling temperature (T_L) of H_2O_2 (top). A few second later, the burning surface (the top surface of the specimen) will move downward, and finally reach the liquid surface where H_2O_2 vaporizes and

decomposes into the oxygen molecular and the water vapor (left). The thermocouple will then reach the top surface of the PE foam and passes through the gas-phase layer finally. Since the steady burning is achieved as well in the experiments of the temperature measurement, the time history of the temperature profile obtained can be converted into profiles of the x coordinate versus temperature by multiplying elapsed time by the overall regression rate.

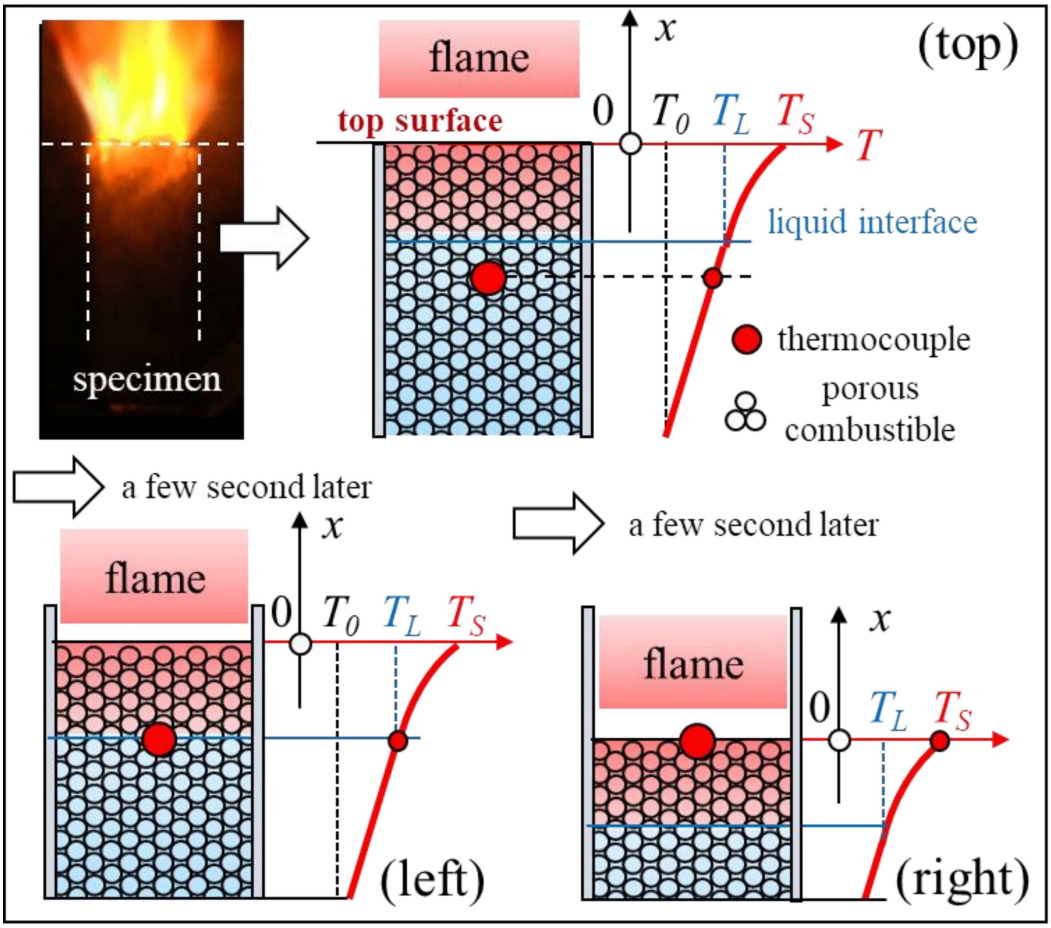

Fig. 3 - 16 Schematic illustration of location of moving top surface, location of thermocouple, and corresponding temperature signals measured by thermocouple.

The obtained results of the temperature measurement for p = 0.1 MPa, 0.17 MPa, and 0.24 MPa (absolute pressure) with a constant fuel porosity (around ε = 0.7) is presented to Fig. 3 - 17 (A).

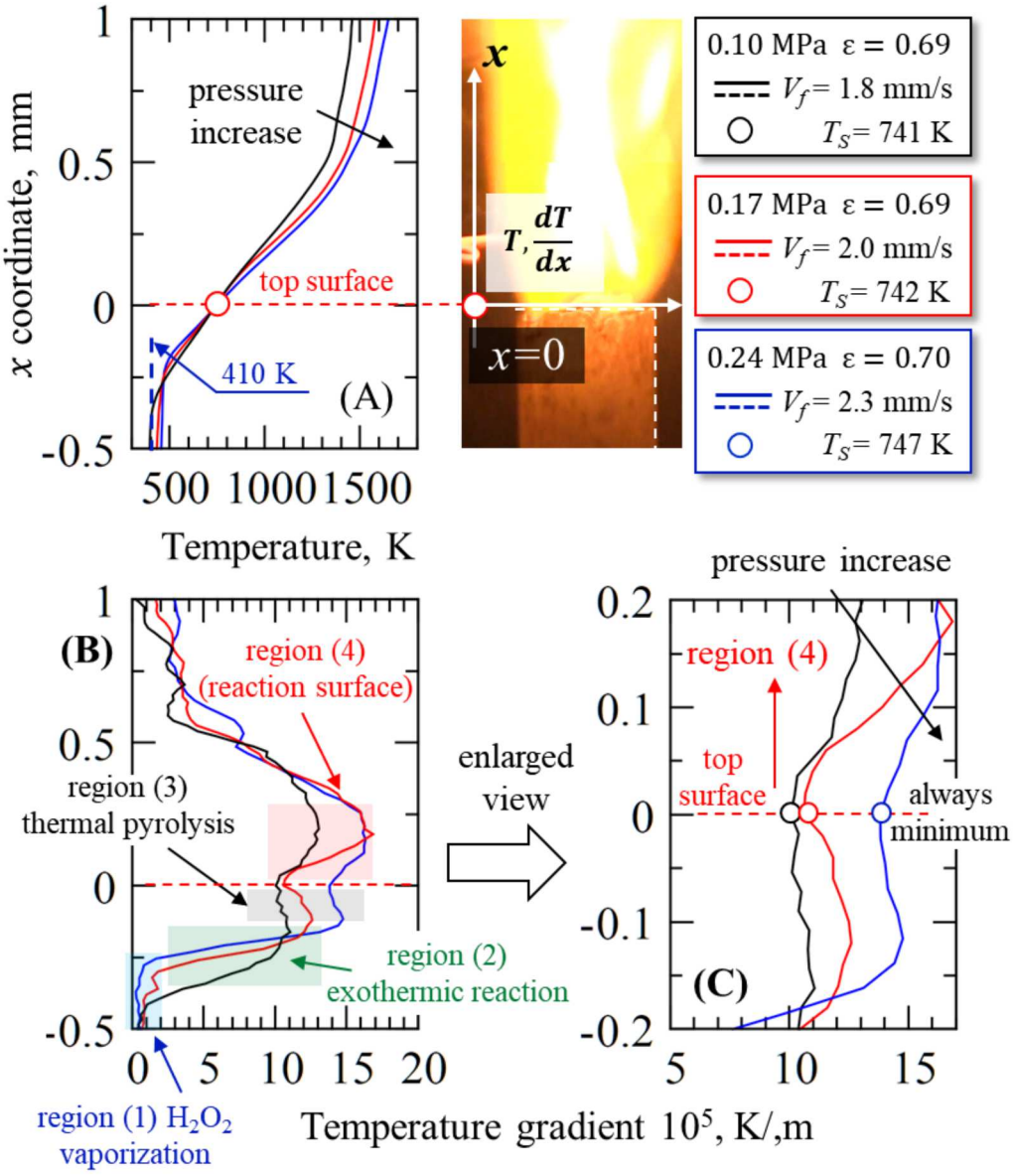

Fig. 3 - 17 Profiles of (A) temperature and (B) temperature gradient obtained from direct temperature measurement trials using R-type thermocouple during the entire burning event for p = 0.1 MPa, 0.17 MPa, and 0.24 MPa with a constant fuel porosity ε = 0.7, and (C) enlarged view of regions (3) and (4) with values of top surface temperature.

The horizontal and vertical axes show measured temperature and the coordinate, respectively. The overall regression rate (V_f) and the top surface temperature (T_S), obtained for each condition are denoted on the figure. $x = 0$ is adjusted to the top surface temperature, and the definition of the top surface temperature will be explained hereafter. All the axes are adjusted to the same for better visibility. As it is seen in Fig. 3 - 17 (A), the TC passes through certain distance around the vaporization temperature of H_2O_2 (410 K, 0.1 MPa in absolute), and then temperature increases monotonically up to maximum temperature about 1450 K ($p = 0.1$ MPa), 1550 K ($p = 0.17$ MPa), and 1600 K ($p = 0.24$ MPa), respectively. It is found that the temperature profiles converge to the maximum temperature beyond the distance of 1 mm from the location of the top surface temperature. It is suggested that a reaction surface, which may act as “main” heating source to promote the regression of the specimen, namely, the surface flame, is located within the distance of 1 mm. Furthermore, quenching distance between the top surface and the surface flame is found to be less than 1 mm. However, only with this temperature profiles, it would be hard to precisely identify an exact thermal structure (i.e., a gas-phase (the surface flame)) layer and a solid-phase layer)

The temperature profiles are then converted into profiles of temperature gradients (dT/dx), in order to know the exact thermal structure. The temperature gradients are presented in Fig. 3 - 17

(B) for the same experimental conditions, and an enlarged view of Fig. 3 - 17 (B) is shown in Fig. 3 - 17 (C) for better visibility. In Fig. 3 - 17 (B), it is seen that the peak of the temperature gradients increases from 13 x 10^5 K/m (p = 0.1 MPa) up to 17 x 10^5 K/m (p = 0.24 MPa), as pressure increases. With careful observation of the temperature gradients, four regions can be identified: (1) a region where the temperature gradients are almost the constant under about 500 K (blue-colored region). (2) a region where the temperature gradients increase sharply between about 500 K and a point below from x = 0 (green-colored region), (3) a region where the temperature gradients slightly decrease or be flat (gray-colored region), and (4) a region where the temperature gradients increase sharply again (red-colored region).

In the region (1), the vaporization of H_2O_2 is initiated, and the heat is absorbed continuously to vaporize H_2O_2. The reason for the certain distance around the vaporization point may be because the boiling H_2O_2 is pushed upward through capillary effect. In this region, it is expected that input heat, which affects the temperature gradients, is a constant net heat of thermal conduction from the top surface of the specimen and the heat adsorption by the latent heat of the vaporization, so that the constant temperature gradients are obtained in the region (1). Then, it is considered that the profiles of region (2) may be attributed to peculiar reaction phenomenon of H_2O_2, namely, the exothermic reaction processes. As mentioned, H_2O_2 is vaporized (decomposed) around 410 K (p

= 0.1 MPa in absolute) into the vapor, and the vapor will then decompose into the water vapor and the molecular oxygen while releasing a lot of heat by the exothermic reaction process until around 760 K [98]. Based on the fact, it is considered that this region receives the thermal conduction and the heat by the exothermic reaction process. Therefore, the temperature gradients increase sharply accordingly. In the region (3), it can be seen that the decrease or flat trend of the temperature gradients are measured. This may be affected by continuous heat adsorption due to the thermal pyrolysis of the PE foam. In the region (4), it is measured that the temperature gradients are sharply increased. Thus, the region (4) is considered as the gas-phase layer where the premixed-gas mixture evolved from the top surface is reacted. In this work, there is always the minimum temperature gradient around the regions (3) and (4) before the sharp increase as shown in Fig. 3 - 17 (C). With this respect, we defined the point where the temperature gradient becomes minimum around the regions (3) and (4) as the top surface temperature of the specimen. The abovementioned thermal structure inside/outside the specimen is depicted in Fig. 3 - 18. Although the diameter of the used thermocouple is large, namely, the spatial resolution is not well enough, the temperature profiles are very smooth, hence, we can safely say that the thermal structure obtained in this work could be clarified qualitatively.

As mentioned, the dominant heat flux is determined by the temperature gradient near the top surface in the gas-phase layer. It is seen that the peak value of the temperature gradients increase as pressure increases, hence, the heat flux exposed onto the top surface increases, leading to the increasing trend of the overall regression rate as shown in Fig. 3 - 17. Additionally, after the TC passes at x = 0.5 mm, the temperature gradients (in the outer flame) are much lower than that of the surface flame. Therefore, it is found that the outer flame does not affect the overall regression rates, rather, the dominant heating source shall be the surface flame. This fact supports our expectation mentioned in this section.

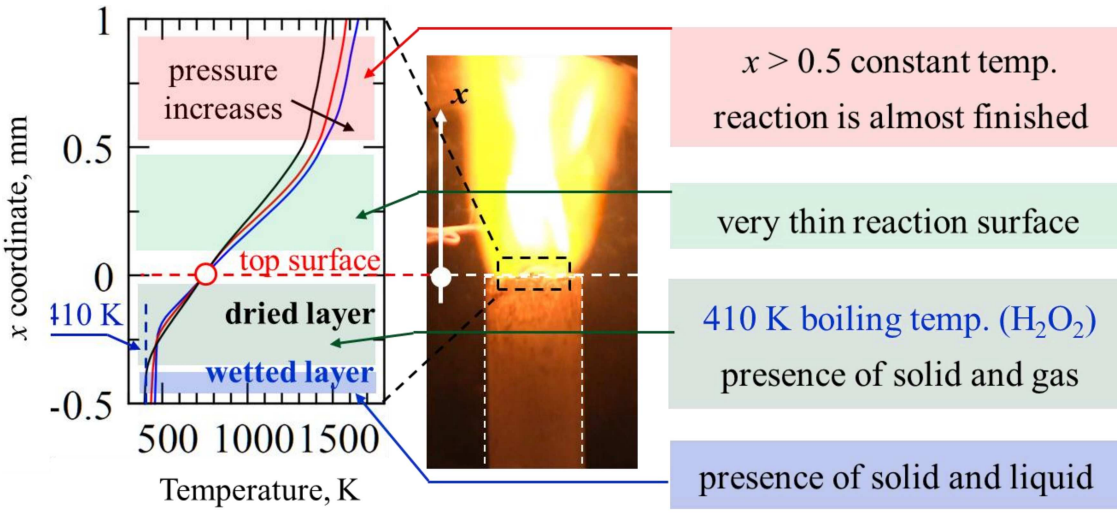

Fig. 3 - 18 Profiles of temperature during the entire burning event for p = 0.1 MPa, 0.17 MPa, and 0.24 MPa with a constant fuel porosity ε = 0.7, together with locations of wetted, dried and gas-phase layers (reaction surface).

3.4 Effect of pressure on top surface temperature and activation energy

In this section, reliability of the temperature measurement results is confirmed by obtaining a global activation energy of the present specimen and comparing the obtained global activation energy with the activation energy of the polymeric solid fuel reported by other research groups. The global activation energy can be obtained with use of the top surface temperature and the regression rate by adopting the Arrhenius pyrolysis law [99] as follows.

$$V_f \propto exp\left[-\frac{E_S}{RT_S}\right] \qquad \text{Eq. 3 - 10}$$

where E_S [J/mol] is the global activation energy at the top surface temperature, which is characteristic of the family of chemicals that the propellant belongs to [46], R [J/(mol·K)] is the universal gas constant, and T_S [K] is the top surface temperature of the specimen, respectively. Many research groups have ever tried to obtain the global activation energy of polymeric fuels used for the AP-based composite solid propellant by means of the same methodology adopted in this work [93] [94] [95] [96] [97] [99] [100]. Since the top surface temperature shall be varied depending on pressure and heating rate [93] [96], the pressure dependency on the top surface temperature and the overall regression rate are first measured, and then the global activation energy is obtained by plotting the regression rate and the top surface temperature.

Fig. 3 - 19 (A) displays the pressure dependency on the top surface temperature and the overall burning rate. The horizontal axis, the vertical axis, and the second vertical axis are denoted as pressure, the top surface temperature, and the overall burning rate measured in the temperature measurement at the same time. The dashed lines obtained by the least squared method are depicted together. It is found that the top surface temperature is in a range between 740 K (p = 0.1 MPa) and 750 K (p = 0.24 MPa), and the overall burning rates are increased accordingly. As expected, the top surface temperature is varied, depending on pressure and increases as pressure increases. In addition, it is seen that the top surface temperature increases with the increase in the overall burning rate, and these trends are the same as one obtained in the previous works [99] [100].

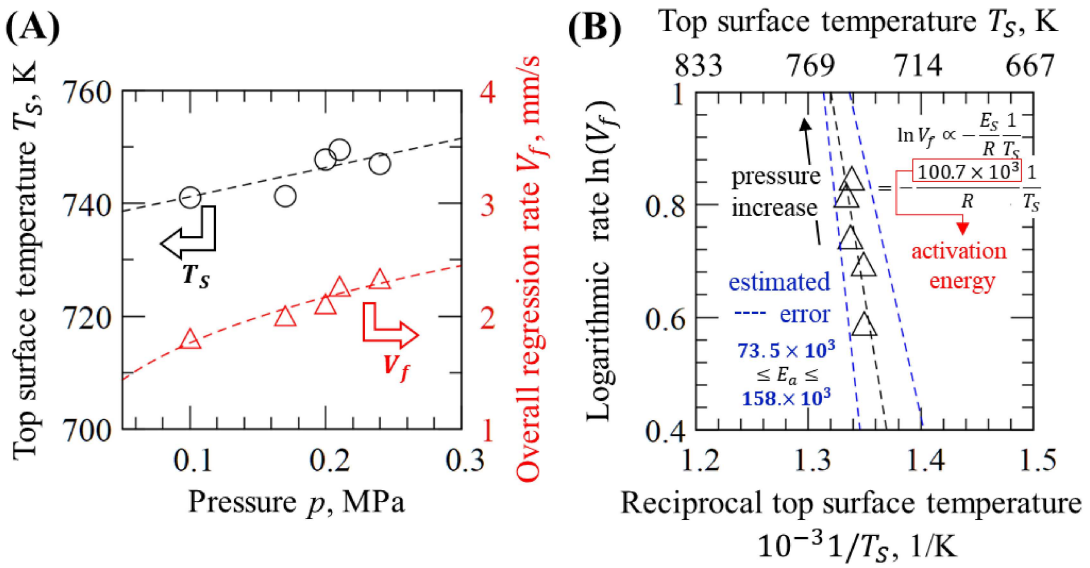

Fig. 3 - 19 (A) Obtained top surface temperature by thermocouple and overall regression rate (V_f) as a function of pressure and (B) relationship between log natural V_f (ln (V_f)) and reciprocal top surface temperature ($1/T_S$), together with global activation energy (E_S) with the estimated errors.

By taking a logarithmic expression of Eq. 3 - 10, the global activation energy at the top surface temperature can be derived from a gradient of the log natural burning rate ($\ln V_f$) and a reciprocal top surface temperature ($1/T_S$). Fig. 3 - 19 (B) shows the relationship between ($\ln V_f$) and ($10^{-3}/T_S$). The horizontal axis, the vertical axis, and the second horizontal axis are shown as the reciprocal top surface temperature ($10^{-3}/T_S$), the log natural burning rate ($\ln V_f$), and the corresponding top surface temperature (T_S). The obtained data are then fitted with a relation denoted on the figure. This result reveals that the global activation energy at the top surface temperature is determined as 100.7 kJ/mol. It is reported that the conventional values of the global activation energies of the polymeric solid fuels, such as PMMA and HTPB, were in a range between 70 kJ/mol and 200 kJ/mol [97] [101] [102]. Especially for the PE foam, an article has revealed that the global activation energy was derived as 119 kJ/mol [103]. Therefore, the obtained global activation energy exhibits the same order as the polymeric fuels and fairly good agreement with the previous work by Park et al.. Additionally, the global activation energy obtained in this work is not pressure dependent and is rather determined as an eigenvalue of the present system [99] [100]. For aforementioned facts, our methodology for the temperature measurement is found to be sufficient. On the other hand, however, as it is seen in Fig. 3 - 15 (A) and Fig. 3 - 19 (A), the overall burning rate varies about 1 mm/s at maximum (ε = 0.63, p = 0.3

MPa), and the top surface temperature varies about 5 K from the dashed line at maximum (p = 0.17 MPa) in the present work. Taking into the account the fact, the global activation energy shall vary in a range between 75.5 kJ/mol and 153.7 kJ/mol within the measurements conducted in this present work. In any cases, the global activation energy obtained in this work shows quantitatively good agreement with one reported by the previous work, and thus the reliability of the temperature measurement results is considered to be sufficient.

3.5 Applicability of one-dimensional burning model

As found from the previous section, the steady end-burning at which the top surface moves downward was confirmed, and the regression of the top surface of the specimen is found to be dominated by the surface flame, which is established close to the top surface. If we can know its one-dimensionality of the burning process, a further investigation on those of the fundamental burning characteristics of the specimen shall be possible by developing a “simple” burning model under the assumptions: the steady end-burning, premixed combustion, and one-dimensional burning. Therefore, the applicability of the one-dimensional burning mode in the present specimen will be examined in this section using a simple thermal analysis. In this work, the one-dimensionality of the burning process is confirmed by comparing heat losses to wall of the quartz

tube with total enthalpy of the burned gas. Namely, if the heat losses to the wall of the quartz tube is negligible as compared to the total enthalpy of the burned gas, the applicability of the one-dimensionality to the present specimen shall be valid. For understandable purpose of this explanation, Fig. 3 - 20 shows an actual image recorded during the burning event, a schematic illustration depicting the total enthalpy of the burned gas and the heat losses, and together with its directions and size of the present specimen.

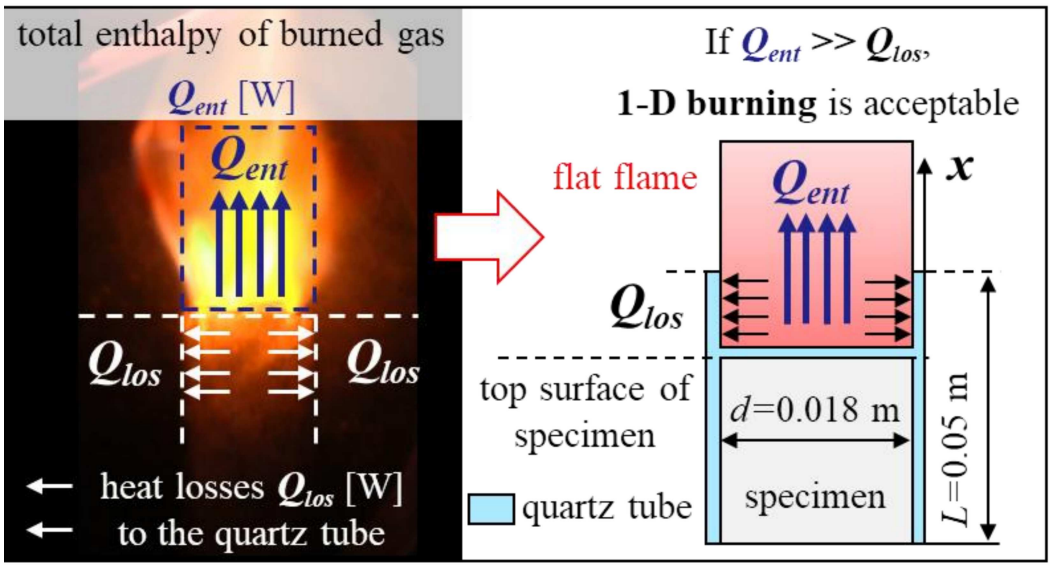

Fig. 3 - 20 Actual image (left) during burning event and schematic illustration (right) of heat loss direction to wall of quartz tube and total enthalpy of burned gas.

To estimate both the heat losses to the wall (Q_{los}) and the total enthalpy of the burned gas (Q_{lent}), following equations are adopted in this work.

Total enthalpy of burned gas

$$Q_{ent} = \dot{m} c_p T_\infty A \qquad \text{Eq. 3 - 11}$$

Heat losses to wall

$$Q_{los} = h A_S \int_0^L (T(x) - T_0) dx \qquad \text{Eq. 3 - 12}$$

where Q_{ent} [W] is the total enthalpy, c_p [J/(kg·K)] is the specific heat of the burned gas at constant pressure, T_∞ [K] is the burning (flame) temperature, A [m^2] is the burning surface area ($\pi d^2/4$), d [m] is the diameter of the specimen, Q_{los} [W] is the heat losses to the wall of the quartz tube, h [W/(m^2·K)] is the heat transfer coefficient between the wall and the burned gas, A_s [m] is πd (π: *pi*), L [m] is the length of the quartz tube, T (x) [K] is the temperature of the burned gas with respect to x coordinate, and T_0 [K] is the surface temperature of the wall. Under some assumptions, such as, the constant surface temperature (T_0), laminar flow in circular tube, hydrodynamically developed flow, thermally developed flow, and short pipe ($L/d < 60$). the heat transfer coefficient (h) is assumed to follow the Hausen's empirical correlation, referred from [104].

The Hausen's empirical correlation

$$Nu = \frac{hd}{\lambda} = 3.66 + \frac{0.104 \times \left(Re \times Pr \times \frac{d}{L}\right)}{1 + 0.016 \times \left(Re \times Pr \times \frac{d}{L}\right)^{0.8}} \qquad \text{Eq. 3 - 13}$$

$$Re = \frac{ud}{v} \qquad \text{Eq. 3 - 14}$$

where Nu [-] is the Nusselt number, λ [W/(m·K)] is the thermal conductivity, Re [-] is the Reynolds number, Pr [-] is the Prandtl number, u [m/s] is the velocity of the burned gas, and v [m^2/s] is the kinematic viscosity. To estimate the heat transfer coefficient (h) from Eq. 3 - 13, the velocity of the burned gas (u), the kinematic viscosity (v), and the Prandtl number (Pr) should be firstly known. In this simple thermal analysis, the velocity of the burned gas can be estimated from the mass continuity at the burning surface of the specimen (the top surface) and assumed to be constant velocity towards the gas flow direction.

$$\dot{m} = \rho_g u = V_f[(1-\varepsilon)\rho_S + \varepsilon\rho_L] \qquad \text{Eq. 3 - 15}$$

where ρ_g [kg/m^3] is the density of the burned gas, V_f [m/s] is the regression rate, ε [-] is the fuel porosity, ρ_S [kg/m^3] is the density of the solid fuel, and ρ_L [kg/m^3] is the density of the liquid oxidizer, respectively. The regression rate (V_f) and the fuel porosity (ε) are referred from the experiments, and the others (ρ_g, Pr, v) are calculated by NASA CEA calculation under almost the same conditions of the conducted experiment. The typical values used for the thermal analysis are listed in Table 3 – 1, together with the specific heat of the burned gas (c_p), the flame temperature (T_∞), and the Prandtl number

The calculated Reynolds number (*Re*), the Nusselt number (*Nu*), the heat transfer coefficient (*h*), the total enthalpy of burned gas (Q_{ent}), the heat losses (Q_{los}) to the wall of the quartz tube, and its ratio (Q_{ent}/Q_{los}) are listed as the following table. Looking at the table, it is found that the heat losses to the wall is small in comparison with the total enthalpy of the burned gas ($(Q_{los}/Q_{ent}) < 17.2$ %). Hence, we judged that the applicability of one-dimensional burning process in the present specimen shall be valid.

Table 3 - 1 Typical physical properties used in the simple thermal analysis.

Name	Symbol	Value	Unit
Diameter	d	18	mm
Length	L	50	mm
Density of polyethylene	ρ_S	920	kg/m^3
Density of hydrogen peroxide	ρ_L	1.45 x 10^3	kg/m^3
Fuel porosity	ε	0.65	-
Global equivalence ratio	φ	2.49	-
Regression rate	V_f	1.65	mm/s
Total mass flux	$\dot{m}$	2.09	Kg/(m^2·s)
Velocity of burned gas	u	23.5	m/s
Kinematic viscosity	v	8.77 x 10^{-4}	m^2/s
Density of burned gas	ρ_g	8.89 x 10^{-2}	kg/m^3
Prandtl number	Pr	0.607	-
Specific heat	c_p	3.22 x 10^3	J/(kg·K)
Thermal conductivity	λ	0.304	W/(m·K)
Flame temperature	T_∞	2.34 x 10^3	K

Table 3 - 2 Values calculated by thermal analysis.

Name	Symbol	Value	Unit
Reynolds number	Re	482	-
Nusselt number	Nu	10.24	-
Heat transfer coefficient	h	173	W/(m^2·K)
Total enthalpy of burned gas	Q_{ent}	4.96 x 10^3	W
Heat losses to wall	Q_{los}	0.853 x 10^3	W
Ratio of Q_{los} to Q_{ent}	Q_{los}/Q_{ent}	0.172	-

3.6 Concluding remarks of this chapter

The comprehensive experimental investigations to gain the fundamental burning characteristics of the polyethylene foam soaked in the enriched hydrogen peroxide were made in this chapter. The experiments were carried out at the initial pressure range from 0.1 MPa to 0.35 MPa in absolute pressures and the fuel porosities range from 0.6 to 0.9 under nitrogen-balanced environment. The direct temperature measurements inside/outside the specimen during the entire burning event using the R-type thermocouple embedded into the specimen were carried out to examine the thermal structure and global activation energy of the specimen. Lastly, the simple thermal analysis was performed in order to confirm the applicability of the one-dimensional burning process in the present specimen. The following findings were obtained in this experiment work:

The burning behavior in the present tested specimen was considered to be the end-burning mode at which the top surface of the tested specimen moves downward.

The reasonably constant regression rates (steady burning), ranging from 1.2 mm/s and 3.2 mm/s under the conditions conducted in this work were measured.

With the careful observation of the flame, it was found that the distinctive two flames were identified; one is the surface flame exposed onto the top surface that is considered to be premixed

flame, the other is the outer flame that is established far away from the top surface of the specimen that is considered to be diffusion flame.

The thermal structure (temperature 0 coordinate) inside/outside the specimen was successfully obtained by the signal from the thermocouple (time history of temperature) and the steady regression rate.

The global activation energy of the specimen obtained in this work was 117 kJ/mol. This value shows quantitatively good agreement with the typical value for the polymeric solid fuel. From these facts, the reliability of our methodology for the temperature measurement was considered to be sufficient.

Chapter 4

4 Theoretical modeling

4.1 Introduction and objective of this chapter

In this chapter, the fundamental burning characteristics of the tested specimen out of the range of the experimental conditions, together with the reason for the data scattering and the explosion-like burning, observed in the previous work by Nagata et al., is numerically investigated. To do so, a simple burning model is firstly developed, based on the experimental findings in Chapter 3. Using the simple burning model, further investigations on the fundamental burning characteristics of the specimen under various prescribed conditions are made. In this work, not only hydrogen peroxide (hereinafter described "H_2O_2") but also liquid oxygen (hereinafter described "LOX") is used for a target of this numerical investigation, in order to examine the possible reasons for the data scattering and the explosion-like burning, observed in the previous work. The effect of the fuel porosity, ambient pressure, and type of the liquid oxidizer on the fundamental burning characteristics of the present specimen is examined accordingly. In addition, considering the nature of the premixed combustion in the specimen, it is fact that there must be a critical condition to achieve the steady burning process. Therefore, separately taking into the account a criterion of

blow-off limits of the premixed combustion given by CHEMKIN (PREMIX-code), the range needed to achieve the steady burning process is predicted. Not only the effect of the imposed condition on the fundamental burning characteristics of the specimen, but on the blow-off criteria are discussed in this chapter. Based on findings, the possible reasons for the data scattering and the explosion-like burning will be examined.

4.2 Model description

The one-dimensional universal burning model applied in this work is shown in Fig. 4 - 1. The burning model is developed with the assumptions of the premixed combustion, the steady state, and the one-dimension, as reported in the previous chapter.

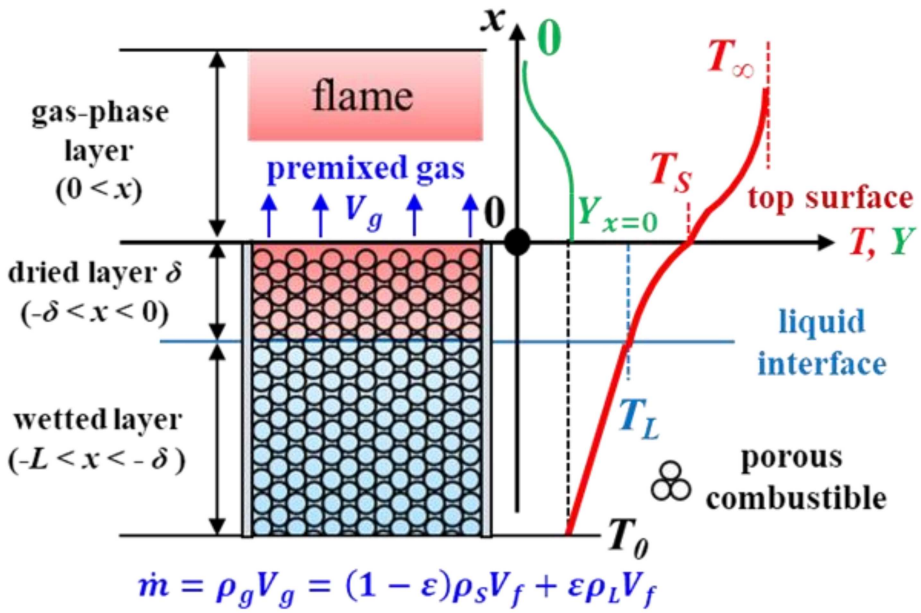

Fig. 4 - 1 One-dimensional burning model considered in this work.

To make the problem simple, boiling (gasification) temperature of the liquid oxidizer (T_L) is assumed to be lower than the pyrolysis temperature of the porous combustible (T_S). Further, we assume that the porous combustible does not melt during the burning event, namely, the fuel porosity of the porous combustible stays as constant [105]. Based on those assumptions, the entire domain is divided into the three layers as shown in the figure. Since steady burning is assumed,

the burning surface (top surface) as well as the boiling surface (liquid interface) moves at a constant rate (namely, the regression rate, V_f). For convenient purpose, the origin is fixed at the top of the specimen accordingly.

The upper part of the porous combustible, whose temperature is higher than the boiling temperature of the liquid oxidizer (T_L), shall be called as the "dried" layer, whereas the lower part is the "wetted" layer, where the porous combustible is fully soaked in the liquid oxidizer. The oxidizer is fully vaporized above the liquid interface, whereas the porous combustible is fully gasified at the top surface of the porous combustible. Above the top surface of the specimen, the premixed-gas mixture of the gasified fuel gas and the oxidizer is evolved at the rate of V_g (calculated from the total mass flux $\dot{m}$ [kg/(m^2·s)]), which is consumed by the premixed flame in the gas-phase layer. With this respect, when the steady burning is achieved, V_g shall be the same as the laminar burning velocity (V_{th}). Then, the regression rate of the specimen V_f is given as a function of the total mass flux $\dot{m}$. The temperature at the top surface is assumed to be constant at the pyrolysis temperature (T_S), and we limit the pyrolysis to only occur at the top surface (nevertheless, the pyrolysis rate shall vary). In reality, pyrolysis may occur in the dried layer (not limited to the surface), and the top surface temperature shall vary depending on the local thermal balance, as reported in the chapter 3. Nevertheless, the pyrolysis rate increases sharply around T_S,

the use of a constant pyrolysis temperature as first model assumption shall be acceptable.

The following assumptions are also made in the following analysis.

1 The overall reaction of pyrolysis gas (fuel) in gas-phase, F (fuel) + O (oxidizer) → P (product), and its rate shall be expressed as an Arrhenius law (see Eq. 4 - 15).

2 The solid part and the gaseous part in the dried layer, and the solid part and the liquid part in the wetted layer are in local thermal equilibrium.

3 The gaseous mixture can be considered as an ideal gas.

4 Changes in density and specific heat in the dried and wetted layers are negligible.

5 The boiling temperature of the liquid oxidizer varies by imposed pressure following the Clausius–Clapeyron equation.

6 The pyrolysis gas is assumed to be pure C_2H_4 [106].

7 The spouting velocity of premixed gas mixture is ejected from the top surface as the initial velocity (V_0), and the spouting velocity is assumed to be constant with respect to the x coordinate ($V_0 = V_g$)

8 A species conservation equation in the gas-phase layer uses a deficient species and is separately used, depending on the equivalence ratio, namely, the mass fraction of the fuel gas Y_F for $\varphi < 1$, the mass fraction of the oxidizer gas Y_O for $\varphi < 1$.

9 The Lewis number (*Le*) of the fuel gas, the oxidizer gas, and the premixed-gas mixture are unity, and the mass diffusion coefficient (*D*) of each gas are the same.

In the meantime, it is well-known that the exothermic reaction is taken place when H_2O_2 decomposes into the molecular oxygen and water vapor, as we have already mentioned. The effect of the heat release is neglected in the present burning model, however, the heat release rate due to the decomposition is found to be at most 6 % of the total heat transfer rate in the dried and the gas-phase layers. Hence, the effect of the exothermic reaction is negligible, and this assumption shall be acceptable.

4.2.1 Equations in each layer

Under the aforementioned assumptions, the following simplified equations in terms of energy conservation, species conservation, and boundary conditions are introduced. The wetted, dried, and gas-phase layers are denoted by subscripts of "1", "2", and "3", respectively.

1. Wetted layer (energy)

$$\dot{m} c_{p\_1} \frac{dT_1}{dx} = \lambda_1^* \frac{d^2 T_1}{dx^2} \qquad \text{Eq. 4 - 1}$$

$$x = -\delta \qquad T = T_L \qquad \text{Eq. 4 - 2}$$

$$x = -\infty \qquad T = T_0 \qquad \text{Eq. 4 - 3}$$

where $\dot{m}$ [kg/(m^2·s)] is the total mass flux; c_{p_1} [J/(kg·K)] is the effective specific heat, defined by $(1-\varepsilon)c_{p\_S} + \varepsilon c_{p\_L}$; ε [-] is the fuel porosity of the porous combustible; c_{p_S} [J/kg·K] is the specific heat of the porous combustible; c_{p_L} [J/kg·K] is the specific heat of the liquid oxidizer; T [K] is the temperature; λ_1^* [W/m·K] is the effective thermal conductivity, defined by $(1-\varepsilon)\lambda_S + \varepsilon\lambda_L$; λ_S [W/m·K] is the thermal conductivity of the porous combustible; λ_L [W/m·K] is the thermal conductivity of the liquid oxidizer; T_0 [K] is the initial temperature; and δ [m] is the dried layer thickness.

2. Dried layer (energy)

$$\dot{m}c_{p\_2}\frac{dT_2}{dx} = \lambda_2^*\frac{d^2T_2}{dx^2} \qquad \text{Eq. 4 - 4}$$

$$x = 0 \qquad T = T_S \qquad \text{Eq. 4 - 5}$$

$$x = -\delta \qquad T = T_L \qquad \text{Eq. 4 - 6}$$

where c_{p_2} [J/(kg·K)] is the effective specific heat; defined by $(1-\varepsilon)c_{p\_S} + \varepsilon c_{p\_g}$; c_{p_g} [J/(kg·K)] is the specific heat of the gaseous oxidizer; λ_2^* [W/(m·K)] is the effective thermal conductivity in the dried layer, defined by $(1-\varepsilon)\lambda_S + \varepsilon\lambda_{L\_g} + 16\sigma T_m^3/3a$ [107]; λ_{L_g} [W/(m·K)] is the thermal conductivity of the gaseous oxidizer; σ [W/m^2·K^4] is the Stefan–

Boltzmann coefficient; T_m [K] is the mean temperature in the dried layer; and α [1/m] is the Rosseland mean absorption coefficient. The thickness of δ is determined by the following thermal balance (interfacial matching condition).

$$\lambda_2^* \frac{dT_3}{dx} = \lambda_1^* \frac{dT_1}{dx} + \dot{m} h_v + \dot{m} c_{p\_1} Y_O T_L \qquad \text{Eq. 4 - 7}$$

where h_v [J/kg] is the latent heat of vaporization for the liquid oxidizer.

3. Gas-phase layer (energy)

$$\dot{m} c_{p\_3} \frac{dT_3}{dx} = \lambda_3^* \frac{d^2 T_3}{dx^2} + \frac{qw}{\nu_i}, (i = F, O) \qquad \text{Eq. 4 - 8}$$

$x = \infty$ $$T = T_\infty \qquad \text{Eq. 4 - 9}$$

$x = 0$ $$\lambda_3^* \frac{dT_3}{dx} = \lambda_2^* \frac{dT_2}{dx} + (1 - \varepsilon) \rho_S V_f h_g + Y_F c_{p\_2} \dot{m} T_S \qquad \text{Eq. 4 - 10}$$

$$\dot{m} = \rho_g V_g = (1 - \varepsilon) \rho_S V_f + \varepsilon \rho_L V_f \qquad \text{Eq. 4 - 11}$$

3. Gas-phase layer (species)

$$\dot{m} \frac{dY_i}{dx} = \rho_g D_i \frac{d^2 Y_i}{dx^2} - \nu_i w, (i = F, O) \qquad \text{Eq. 4 - 12}$$

$x = 0$ $$Y_{i,x=0} \dot{m} = Y_i \dot{m} + \rho_g D_i \frac{dY_i}{dx} \qquad \text{Eq. 4 - 13}$$

$$Y_{i,x=0} = \frac{Y_i}{Y_O + Y_F} \qquad \text{Eq. 4 - 14}$$

$$w = A_3 (\rho_g Y_i)^n \exp(-\frac{E_{a\_3}}{R T_3}) \qquad \text{Eq. 4 - 15}$$

where c_{p_3} [J/kg·K] is the specific heat in the gas-phase layer; q [J/m^3] is the combustion heat by the chemical reaction; w [kg/m^3·s] is the mass consumption rate; v_i [-] is the stoichiometric coefficient based on a mass basis, namely, $v_F = 1$ and $v_O = v$; T_∞ [K] is the adiabatic flame temperature; h_g [J/kg] is the latent heat of gasification; ρ_g [kg/m^3] is the density of the gas mixture; v_g [m/s] is the spouting velocity of the premixed-gas mixture from the top surface; D_i [m^2/s] is the *i*th species mass diffusion coefficient ; A_3 [1/s] is pre-exponential factor of the premixed-gas mixture; E_{a_3} [J/mol] is the activation energy of the gas mixture. The mass consumption rate (w) is assumed to be proportional to the *n*th power of the mass fraction of the reactant Y_i [-]. and the density of the gas mixture (ρ_g). $Y_{i,x=0}$ [-] given in Eq. 4 - 16 is the initial mass fraction of *i*th species reactant at the top surface (x = 0). Again, oxidizer-to-fuel mass ratio (O/F) is recalled as;

$$Y_{i,x=0} = \frac{Y_i}{Y_F + Y_O} = \frac{\frac{Y_i}{Y_F}}{1 + \frac{Y_O}{Y_F}} \qquad \text{Eq. 4 - 16}$$

$$\frac{\frac{Y_i}{Y_F}}{1 + \frac{Y_O}{Y_F}} = \begin{cases} \dfrac{1}{1 + \frac{Y_O}{Y_F}} & (\varphi < 1, i = F) \\ \dfrac{\frac{\varepsilon\rho_L}{(1-\varepsilon)\rho_S}}{1 + \frac{\varepsilon\rho_L}{(1-\varepsilon)\rho_S}} & (\varphi \geq 1, i = O) \end{cases}$$

$$\frac{O}{F} = \frac{\varepsilon\rho_L}{(1-\varepsilon)\rho_S} \qquad \text{Eq. 4 - 17}$$

The specific heat (c_{p_3}), adiabatic flame temperature (T_∞), thermal conductivity (λ_3^*), and density of the gas mixture (ρ_g), for the gas-phase layer, are obtained from Chemical Equilibrium with Applications (CEA) codes [108]. Interfacial boundary conditions are adopted between the wetted and dried layers and between the gas-phase and dried layers to connect each layer.

4.2.2 Obtaining the regression rate

The mathematical formulations provided in the previous section indicate that the incoming total mass flux ($\dot{m}$) must be known at first. Because the gas-phase layer is the same as the premixed laminar flame structure, we employ a theoretical approach [109] [110] to obtain the total mass flux ($\dot{m}$). Then, the thermal structure of the entire domain is determined accordingly.

For $i = F$, transforming Eq. 4 - 8 and Eq. 4 - 12 into non-dimensional forms with the following non-dimensional variables: non-dimensional temperature (θ) non-dimensional coordinate (ξ), non-dimensional heat generation (q^*), and Zeldovich number (β). Under the assumption of the fast reaction (i.e., β is large enough), it is possible to find $\dot{m}$ as eigenvalue of the system.

$$\theta = \frac{(T - T_0)}{(T_\infty - T_0)} \qquad \xi = \frac{(c_{p\_3}\dot{m}x)}{\lambda_3^*} \qquad q^* = \frac{q}{c_{p\_3}(T_\infty - T_0)} \qquad \beta = \frac{E_{a\_3}(T_\infty - T_0)}{(RT_\infty^2)}$$

$$\frac{d\theta_3}{d\xi} = \frac{d^2\theta_3}{d\xi^2} + q^* \Lambda {Y_F}^n \exp[-\beta(1-\theta_3)] \quad \text{Eq. 4 - 18}$$

$$\frac{dY_F}{d\xi} = \frac{d^2Y_F}{d\xi^2} - \Lambda {Y_F}^n \exp[-\beta(1-\theta_3)] \quad \text{Eq. 4 - 19}$$

where Λ [-] is the eigenvalue of the total mass flux of this system and is defined as the following:

$$\Lambda = \frac{\rho_g^n \lambda_3^* A_3}{\dot{m}^2 c_{p\_3}} \exp\left(-\frac{E_{a\_3}}{RT_\infty}\right) \quad \text{Eq. 4 - 20}$$

With the addition of $q^* \times$ Eq. 4 - 19 from Eq. 4 - 21, the following relation is introduced:

$$\frac{d\theta_3}{d\xi} + q^* \frac{dY_F}{d\xi} = \frac{d^2\theta_3}{d\xi^2} + q^* \frac{d^2Y_F}{d\xi^2} \quad \text{Eq. 4 - 21}$$

In this work, since the Lewis number (Le) is assumed to be unity, temperature distribution $(\theta_3(\xi))$ and mass fraction distribution $(Y_F(\xi))$ in the gas-phase layer shall be similar. For this reason, Eq. 4 - 21 is necessary to meet the following relation at $\xi = \infty$:

$$\theta_3 + q^* Y_F = Const \quad \text{Eq. 4 - 22}$$

Solving Eq. 4 - 22 with the boundary conditions ($\xi = \infty$, $\theta_3 = 1$, $Y_F = 0$), the following relation on the mass fraction of the reactant Y_F and non-dimensional temperature θ_3 can be obtained:

$$Y_F = \frac{1}{q^*}(1-\theta_3) \quad \text{Eq. 4 - 23}$$

The following non-dimensional conservation equation corresponding to the gas-phase layer can be obtained by substituting Eq. 4 - 23 into Eq. 4 - 18:

$$\frac{d\theta_3}{d\xi} = \frac{d^2\theta_3}{d\xi^2} + \Lambda(q^*)^{1-n}(1-\theta_3)^n \exp[-\beta(1-\theta_3)] \qquad \text{Eq. 4 - 24}$$

The non-dimensional conservation equation is also transformed into the following form by introducing new independent variables, namely, $p = d\theta_3/d\xi$, $dp/d\theta_3 = d^2\theta_3/d\xi^2$, and $t = \beta(1-\theta_3)$. The first term on the left side and the first term and the second term on the right side are denoted as the convection, diffusion, and chemical reaction terms, respectively.

$$p = p\frac{dp}{d\theta_3} + \Lambda(q^*)^{1-n}\left(\frac{t}{\beta}\right)^n \exp[-t] \qquad \text{Eq. 4 - 25}$$

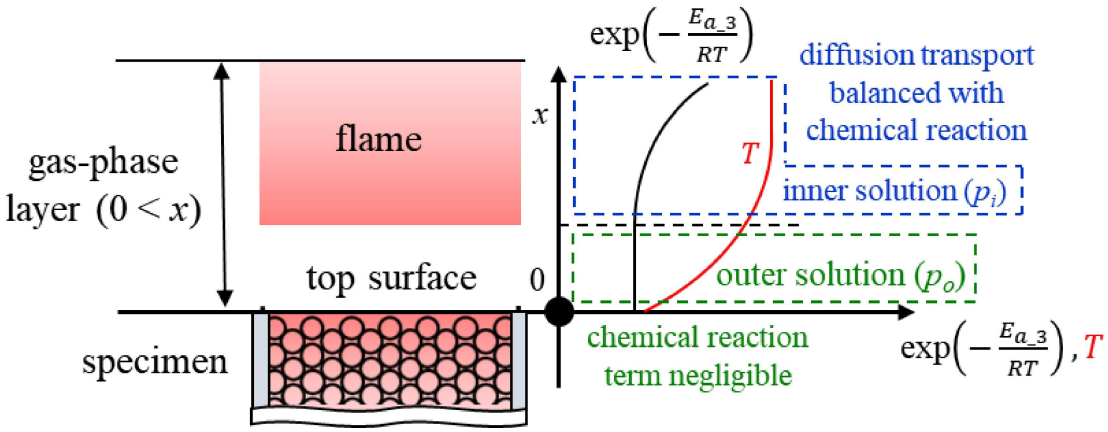

Fig. 4 - 2 Two layers in gas-phase layer: a layer where convective transport term is balanced with diffusion transport term (negligible chemical reaction term), a layer where chemical reaction term is balanced with diffusion transport term.

Two layers in the gas-phase layer are then introduced as illustrated in Fig. 4 - 2. In a layer where convective transport term is balanced with diffusion transport term, the chemical reaction term shall be negligible and can be omitted. The following outer solution (called "p_O") is introduced:

$$p_o = \frac{d\theta_3}{d\xi} = \theta_3 + C \qquad \text{Eq. 4 - 26}$$

C is a constant of integration. In order to determine the constant of integration *C*, the boundary condition Eq. 4 - 10 at $\xi = 0$ is transformed into the following non-dimensional equation:

$$\xi = 0 \qquad \frac{d\theta_3}{d\xi} = \frac{c_{p\_2}}{c_{p\_3}}\frac{d\theta_2}{d\xi} + \frac{(1-\varepsilon)\rho_S V_f h_g}{\dot{m} c_{p\_3}(T_\infty - T_0)} + \frac{c_{p\_2} T_S Y_F}{c_{p\_3}(T_\infty - T_0)} \qquad \text{Eq. 4 - 27}$$

In addition, with solving Eq. 4 - 4 with the boundary condition Eq. 4 - 5, the following relation at $\xi = 0$ can be obtained:

$$\xi = 0 \qquad \frac{d\theta_2}{d\xi} = \theta_S = \frac{T_S - T_0}{T_\infty - T_0} \qquad \text{Eq. 4 - 28}$$

With Eq. 4 - 26, Eq. 4 - 27, and Eq. 4 - 28, the following outer solution (p_O) can be given by determining the constant of integration *C*:

$$p_o = \frac{d\theta_3}{d\xi} = \theta_3 + \left(\frac{c_{p\_2}}{c_{p\_3}} - 1\right)\theta_S + \frac{(1-\varepsilon)\rho_S V_f h_g}{\dot{m} c_{p\_3}(T_\infty - T_0)} + \frac{c_{p\_2} T_S Y_F}{c_{p\_3}(T_\infty - T_0)} \qquad \text{Eq. 4 - 29}$$

Next, in a layer where the diffusion transport term is balanced with the chemical reaction term,

the convective transfer term shall be negligible and can be omitted. Thus, the following equation shall be solved to obtain the inner solution (called p_i):

$$\beta p_i \frac{dp_i}{dt} = \Lambda (q^*)^{1-n} \left(\frac{t}{\beta}\right)^n \exp[-t] \qquad \text{Eq. 4 - 30}$$

With solving Eq. 4 - 30 with the variable separation method in an integration range of *t* between 0 and *t*, the following relation is introduced:

$$p_i = \sqrt{\frac{2(q^*)^{1-n}\Lambda}{\beta^{n+1}}\Gamma(n+1)}\sqrt{\left[1 - \frac{\Gamma[n+1,t]}{\Gamma(n+1)}\right]} \qquad \text{Eq. 4 - 31}$$

where $\Gamma(n+1)$ and $\Gamma(n+1,t)$ are the Gamma function and incomplete gamma function. Since the two solutions p_O and p_i share the same boundary interface, namely, $t \sim \infty$ and $\theta_3 \sim 1$ a perfect matching is required at the interface for each solution. By this perfect matching, the eigenvalue of the total mass flux (Λ) can be introduced as follows with an assumption of $n = 1$:

$$\Lambda \sim \gamma \left[1 + \left(\frac{c_{p\_2}}{c_{p\_3}} - 1\right)\theta_S + \frac{(1-\varepsilon)\rho_S V_f h_g}{\dot{m} c_{p\_3}(T_\infty - T_0)} + \frac{c_{p\_2} T_S Y_F}{c_{p\_3}(T_\infty - T_0)}\right]^2 \qquad \text{Eq. 4 - 32}$$

$$\gamma = \begin{cases} \dfrac{\beta^{n+1}}{2(q^*)^{1-n} n!} & (\varphi < 1, i = F) \\ \dfrac{\beta^{n+1}}{2(q^*)^{1-n} \nu_O^{2n-1} n!} & (\varphi \geq 1, i = O) \end{cases}$$

By obtaining the eigenvalue (Λ) using Eq. 4 - 32, depending on the equivalence ratio, the

incoming total mass flux ($\dot{m}$) and then the regression rate (V_f) are derived with Eq. 4 - 20 accordingly. Using the solved total mass flux ($\dot{m}$), all dependent variables in solid phase are solved.

4.3 Definition of blow-off

Recalling that the analysis above assumes the fast reaction (β is large enough), the blow off criteria (blow-off, steady burning, or successive burning) is not properly predicted. In order to find the blow-off criteria, we separately employ the software CHEMKIN v. 18 (with GRI-Mech 3.0) to obtain the laminar burning velocity (V_{th}). The laminar burning velocity is calculated using temperature at the top surface (T_S) as a function of ambient pressure and equivalence ratio (φ). Comparing with the spouting velocity of the premixed-gas mixture (V_g; dashed lines) calculated by the analysis above and the laminar burning velocity (V_{th}; solid lines) calculated by CHEMKIN, blow-off condition is identified as $V_g > V_{th}$. In Fig. 4 - 3, an example using LOX (pure oxygen) as the oxidizer is shown.

As is understood, at the condition at $V_g = V_{th}$, steady burning can be achieved. In case of $V_g < V_{th}$, flame can stay above the top surface and the regression rate may increase by time. We call this condition as “successive burning”, denoting that blow-off is not occurred yet the burning of the specimen can continue. When the difference between V_g and V_{th} gets larger ($V_{th} \gg V_g$),

accelerating the regression of the tested specimen shall be pronounced.

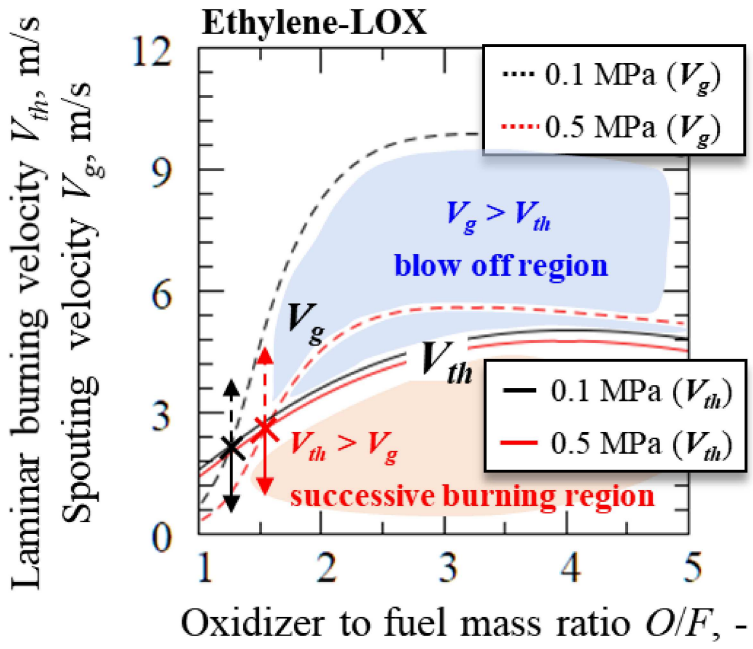

Fig. 4 - 3 Laminar burning velocity (V_{th}) and spouting velocity of premixed-gas mixture (V_g) as a function of mass ratio (O/F) and pressure for ethylene-liquid oxidizer combustion (V_g).

4.4 Results and discussion

4.4.1 Validation of numerically predicted temperature profile

Firstly, the validity of the present burning model is evaluated by comparing the temperature profiles measured in the chapter 3 with numerically predicted temperature profile. The measured temperature profiles used in this validation are obtained at pressure of 0.1 MPa in absolute under the fuel porosity around 0.7. This is the same as the conditions found in Fig. 3 - 17. All the temperature profiles obtained by four runs measurements are summarized in Fig. 4 - 4. The experimental results and predicted result are depicted in the circles and the solid lines (in red), respectively.

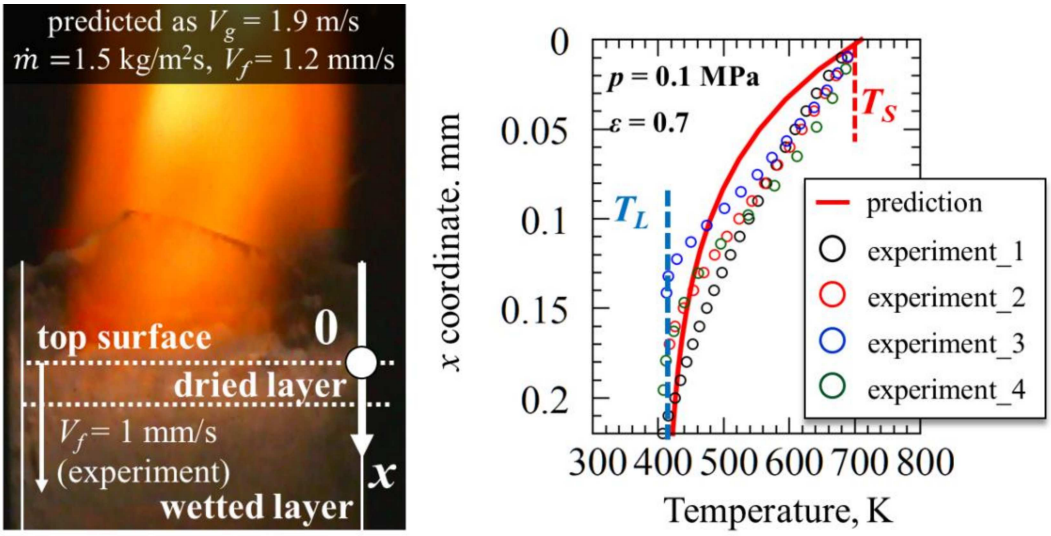

Fig. 4 - 4 Temperature profiles obtained from TC and prediction, including spouting velocity of premixed-gas mixture and total mass flux predicted by one-dimensional burning model for fuel porosity (0.7) and ambient pressure (0.1 MPa).

It is found that the numerically predicted profile shows a good agreement with measured profiles. A difference in the thickness of the dried layer between the measured and the numerically predicted values would be caused by several reasons. For example, it may be attributed to that the liquid interface is pushed up by the capillary effect due to the vaporization of H_2O_2. Moreover, it is obvious that all the measured temperature profiles are gentle slope. This is attributed to the spatial resolution of the thermocouple. Nevertheless, it can be judged that the validity of the presently adopted one-dimensional burning model is satisfactory.

4.4.2 Predicted one-dimensional flame structures under various conditions

The thermal structure of the tested specimen is predicted with developed burning model. As typical examples of the prediction results of the thermal structure, one-dimensional profiles of the temperature (T), the mass fraction of the deficient species (Y_i), and the mass consumption rate (w) over the burning surface (the top surface) under various ambient pressures and the fuel porosities are compared in Fig. 4 - 5 and Fig. 4 - 6. The horizontal axis and the vertical axis are temperature (T) and the x coordinate over the top surface, respectively. The mass consumption rate (w) and the mass fraction of the deficient species are also shown on the second vertical axis and third vertical axis, respectively. Their scales for the three cases shown below are adjusted for better

visibility. H_2O_2 (not LOX) as liquid oxidizer is employed in this prediction. The typical values used in this prediction are summarized in Table 1. The total mass flux ($\dot{m}$) predicted for each case is shown on the prediction results. Again, we assume that density and mass fraction dependent index n is unity [110] in this prediction for all cases.

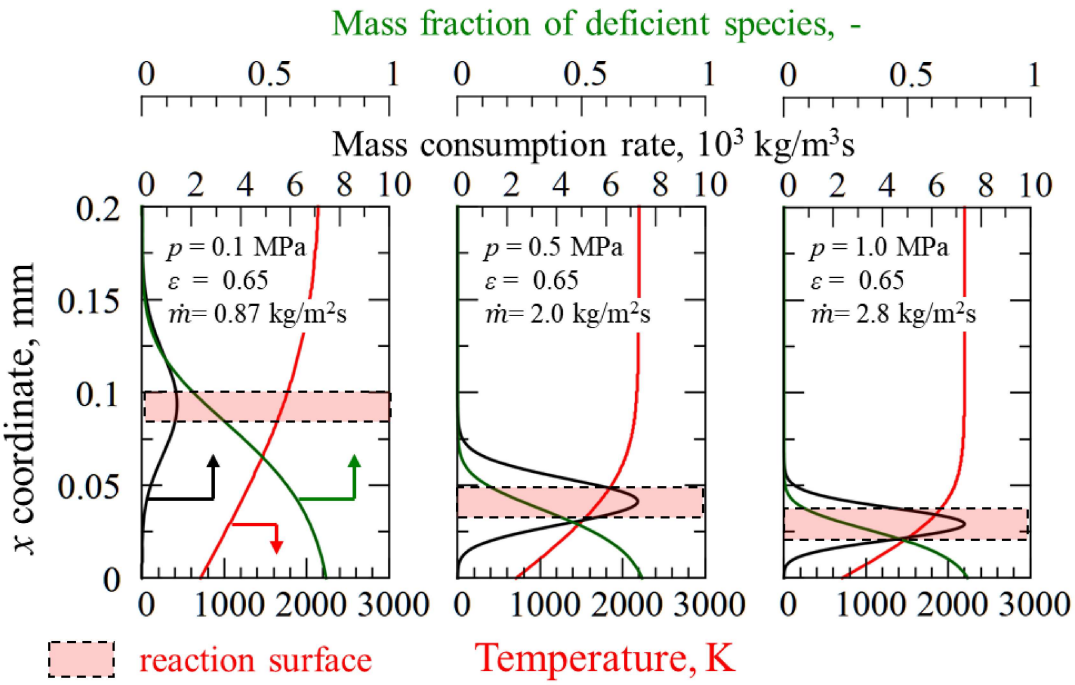

Fig. 4 - 5 Prediction of profiles of temperature (T), mass fraction of reactant (Y), and mass consumption rate (w) in gas layer as functions of pressure: (a) p = 0.1 MPa, ε = 0.65, and $\dot{m}$ = 0.87 kg/(m^2·s); (b) p = 0.5 MPa, ε = 0.65, and $\dot{m}$ = 2.0 kg/(m^2·s); (c) p = 1 MPa, ε = 0.65, and $\dot{m}$ = 2.8 kg/(m^2·s).

Fig. 4 - 5 shows the effect of ambient pressures (p; 0.1 MPa, 0.5 MPa, 1.0 MPa) on the one-dimensional profiles with the constant fuel porosity (ε) 0.65. As it is seen, when pressure increases, the reaction surface, which is defined as the location where mass consumption rate (w) becomes

maximum, approaches to the top surface, and it is found that the mass consumption rate (w) is enhanced. More importantly, this reaction surface shall be a “main heating surface” to promote the regression of the specimen, leading to the increase in the total mass flux accordingly, when pressure increases. Additionally, the adiabatic flame temperature slightly increases from 2189 K (0.1 MPa) to 2201 K (1.0 MPa). These facts make the thermal conduction through the gas-phase layer exposed into the top surface higher, and the pressure dependency on the overall regression rate, obtained in Chapter 3, can explained by these one-dimensional profiles.

Next, the effect of the fuel porosities (ε = 0.65, 0.8, and 0.9) at 0.1 MPa on the one-dimensional profiles is given in Fig. 4 - 6 as well. Findings reveals that, as the fuel porosity approaches to 0.8 from the fuel-rich side (ε = 0.65) or the fuel-lean side (ε = 0.9), the location of the reaction surface approaches to the top surface of the specimen, and it is found that the mass consumption rate (w) and the total mass flux ($\dot{m}$) are increased accordingly. As have already mentioned earlier, the fuel porosity for achieving the complete combustion (namely, equivalence ratio φ = 1) in the present specimen is around 0.82 – 0.85 (optimal value) for H_2O_2 case as the liquid oxidizer, so that the adiabatic flame temperature tends to be increased, and thus the total mass flux increases accordingly as the fuel porosity approaches to the optimal value from fuel-rich side or fuel-lean side. The dependency of the fuel porosity on the regression rate, found in Chapter 3, can be also

explained from a viewpoint of this one-dimensional profile.

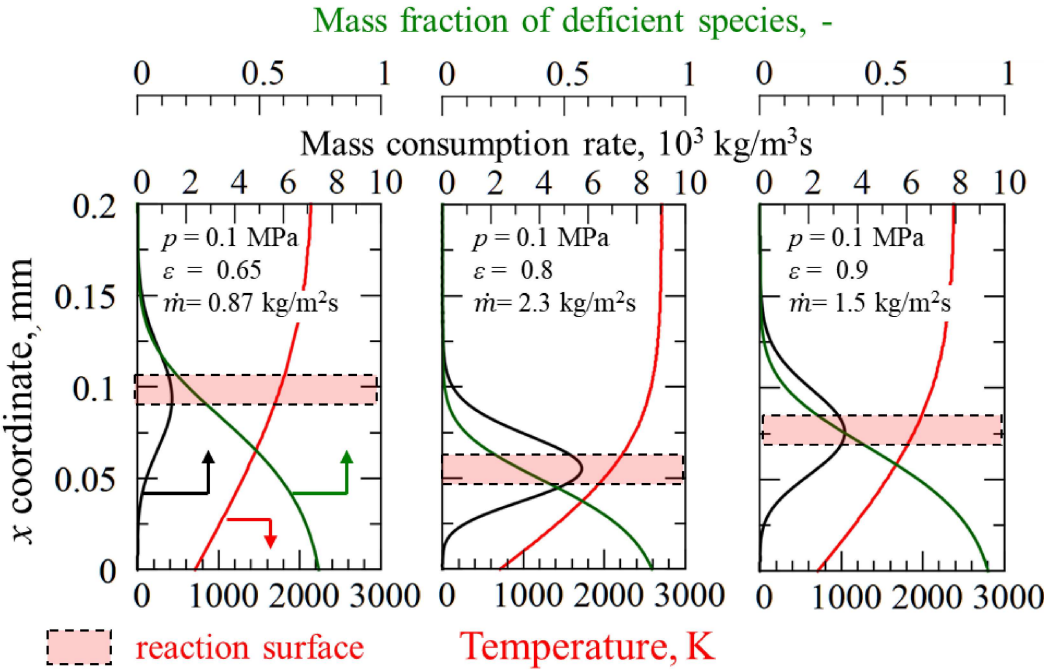

Fig. 4 - 6 Prediction of profiles of temperature (T), mass fraction of reactant (Y), and mass consumption rate (w) in gas layer and temperature profiles in dried and wetted layers as functions of pressure: (a) p = 0.1 MPa, ε = 0.65, and $\dot{m}$ = 0.87 kg/(m^2·s); (b) p = 0.5 MPa, ε = 0.8, and $\dot{m}$ = 2.3 kg/(m^2·s); (c) p = 1 MPa, ε = 0.9, and $\dot{m}$ = 1.5 kg/(m^2·s).

Table 4 - 1 Physical properties used in this prediction.

Name (oxidizer)	Symbol	Value (H_2O_2, LOX)	Unit
Density (liquid)	ρ_L	1.45×10^3, 1.15×10^3	kg/m^3
Specific heat (liquid)	c_{p_L}	2.62, 1.70	kJ/(kg·K)
Specific heat (gas)	c_{p_g}	2.39, 0.920	kJ/(kg·K)
Thermal conductivity (liquid)	λ_L	0.682, 0.152	W/(m·K)
Thermal conductivity (gas)	λ_{L_g}	0.140, 0.0295	W/(m·K)
Heat of vaporization	h_v	1.93×10^3, 2.13×10^2	kJ/kg
Boiling temperature	T_L	410, 90.0 (0.1 MPa)	K
Name (PE)			
Density	ρ_S	920	kg/m^3
Specific heat	c_{p_S}	2.30	kJ/(kg·K)
Thermal conductivity	λ_S	0.340	W/(m·K)
Heat of gasification	h_g	2.25×10^3	kJ/kg
Pyrolysis temperature	T_S	710	K
Initial temperature	T_0	298	K
Name (others)			
Mass diffusivity	$D_F = D_O = D_g$	$= (\lambda_g)/(\rho_g c_{P\_3})$, $(Le = 1)$	m^2/s
Rosseland mean absorption coefficient	a	1800	1/m
Stefan-Boltzmann coefficient	σ	5.67×10^{-8}	W/(m^2·K^4)
Pre-exponential factor	A_3	$10.5 \times 10^9 \times \rho_g$ [111]	1/s
Activation energy	E_{a_3}	$39.2RT_0$ [111]	J/mol
Universal gas constant	R	8.314	J/(mol·K)
Mass-based stoichiometric coefficient	v	7.29 (H_2O_2), 3.43 (LOX)	-

4.5 Discussion with numerical prediction

4.5.1 Effect of pressure and fuel porosity on laminar burning velocity (V_{th})

Like the assumption made in this work, the present specimen is fully controlled by the premixed-type combustion as modeled, hence, there must be a suitable range to achieve successive combustion (i.e., without causing any blow-off). As described in Fig. 4 - 3, there must be critical conditions, i.e., boundaries between the steady-solution (successive burning) region and the blow-off region. In the following, the effect of the kind of oxidizer (H_2O_2 and LOX), the fuel porosity, and ambient pressure on the range of the successive burning is numerically studied using the developed prediction model.

First, the effects of the laminar burning velocity (V_{th}) for the (a) C_2H_4–LOX mixture and the (b) C_2H_4–H_2O_2 mixture under various pressures on the imposed fuel porosity and temperature at the top surface (T_S) are plotted in Fig. 4 - 7. Again, the fuel porosity (ε) and O/F (or equivalence ratio, φ) are varied according to Eq. 4 - 17. For better visibility, the corresponding equivalence ratios (φ) are indicated in the figure. This result is obtained by the software CHEMKIN with the PREMIX code (namely, purely gaseous one-dimensional premixed flame problem is solved). Findings show that the laminar burning velocity (V_{th}) decreases as the pressure increases. The sensitivity of the laminar burning velocity to the applied pressure in the case of LOX as oxidizer

is less than that in the case of H_2O_2 as oxidizer. The maximum peak of the predicted laminar burning velocity is insensitive to the adopted pressure; its value is around 0.75 of the fuel porosity for LOX as oxidizer, and 0.82 of the fuel porosity for H_2O_2 as oxidizer.

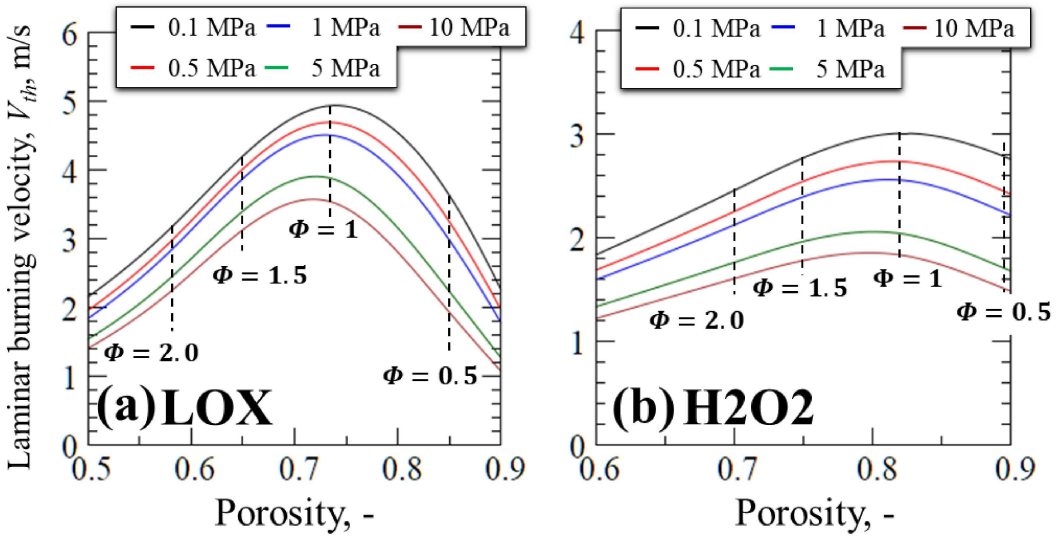

Fig. 4 - 7 Laminar burning velocity under various pressure on the imposed fuel porosity and temperature at the top surface (T_S) for (a) C_2H_4–LOX and (b) C_2H_4–H_2O_2 combustion with constant equivalence ratio lines.

This predicted trend is somehow opposite to what we observe in our specimen. According to Fig. 4 - 5, the total mass flux (or the regression rate) increases with increase in ambient pressure since the gaseous flame, which acts as the main heating source to promote the regression of the porous combustible, is formed close to the top surface. The expectation is that, as the pressure increases, the regression rate is promoted and the spouting velocity of the premixed-gas mixture

from the top surface increases. To achieve a steady solution in this specimen, the spouting velocity of the premixed-gas mixture (V_g) must be *balanced* with the laminar burning velocity (V_{th}) of the mixture as modeled. Given that the laminar burning velocity decreases as the pressure increases, the balance needed to achieve a steady solution (namely, $V_g = V_{th}$) may fail under certain conditions, resulting in blow-off. In the following section, we will study this issue and discuss the potential range of achievable solutions under a wide range of imposed conditions.

4.5.2 Effect of pressure and fuel porosity on blow-off limits

The spouting velocity of the premixed-gas mixture (V_g) is calculated based on the obtained total mass flux ($\dot{m}$) and compared with the laminar burning velocity (V_{th}) to elucidate the critical conditions of the blow off. Examples of their relation are presented in Fig. 4 - 8 for the cases of (a) LOX and (b) H_2O_2 as the liquid oxidizers. In the figure, the solid and dashed lines indicate the laminar burning velocity (V_{th}) and the spouting velocity of the premixed-gas mixture (V_g), respectively. The successive burning condition, including the steady burning is the range needed to meet $V_{th} \geq V_g$.

This figure shows a high probability of blow-off in the case of LOX as the liquid oxidizer, whereas such chance is rather low in the case of H_2O_2 as the liquid oxidizer. In this sense, using

H_2O_2 seems more reasonable; however, the achieved V_g is rather limited. The successive burning range is summarized in Fig. 4 - 9.

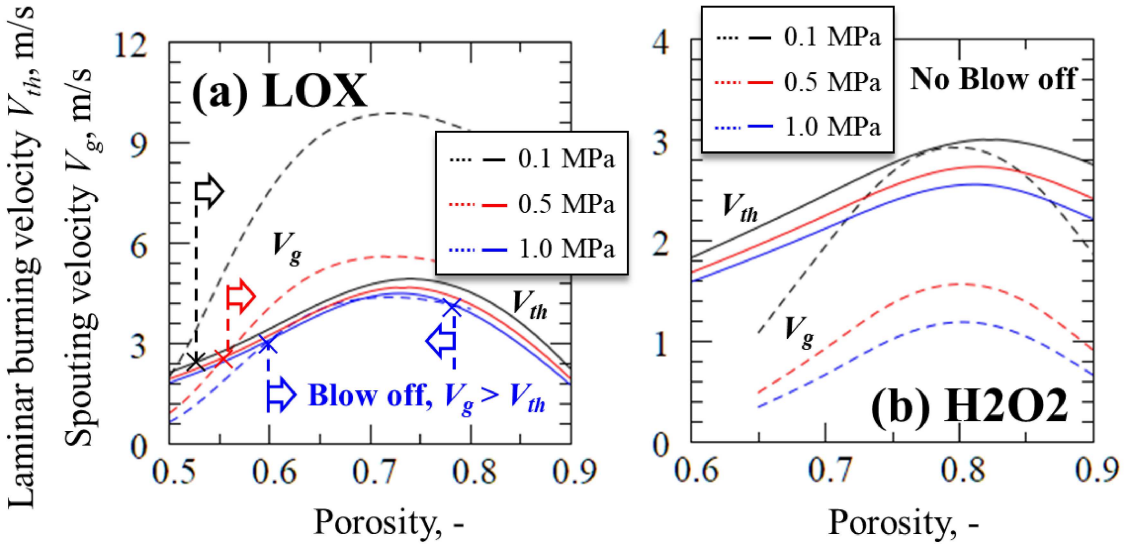

Fig. 4 - 8 Relation between laminar burning velocity (V_{th}) and spouting velocity of premixed-gas mixture (V_g) at top surface as function of fuel porosity and pressure for (a) LOX and (b) H_2O_2 as oxidizer and blow-off limits (blow-off region: $V_g > V_{th}$).

In Fig. 4 - 9, the horizontal and vertical axes are the ambient pressure and the fuel porosity, respectively. The corresponding equivalence ratio is also shown on the second vertical axis. The achievable regression rates (V_f) with successive-burning region are shown in color contour, and the white area is the blow-off region. It is found that the regression rate and the spouting velocity of the premixed-gas mixture increase when the fuel porosity approaches 0.7 and 0.8 for the case of LOX and H_2O_2, respectively. Assuming complete combustion (i.e., the equivalence ratio is

unity) of C_2H_4–LOX and C_2H_4–H_2O_2, the optimal *O*/*F* values for complete combustion are about 3.4 and 7.3, respectively. Thus, the corresponding fuel porosity for complete combustion can be given as 0.73 and 0.82 from the relation of Eq. 3 - 9, and the maximum regression rate can be derived at the optimal fuel porosity of 0.73 (LOX) and 0.82 (H_2O_2).

For (a) (LOX case), a relatively large blow-off region is identified, especially at lower pressures and around the optimal fuel porosity (0.7). At lower pressures (< 0.5 MPa), a lower fuel porosity (< 0.55) is suitable for achieving the successive burning. In addition, a high-pressure environment is also a suitable operating condition for achieving the successive burning at high regression rates, especially > 5 MPa, and high fuel porosity (around 0.7). This is because the density of the gas mixture increases with the pressure, and blow-off is inhibited as the pressure increases. Between 0.1 MPa and 10 MPa of pressure, the maximum regression rate could be over 90 mm/s (around 10 MPa and 0.7 in the fuel porosity). By contrast, the successive burning condition for (b) (H_2O_2 case) can be achieved in a wide range of ambient pressures, namely, between 0.1 MPa and 10 MPa. Although when the pressure is reduced below 0.1 MPa, a small blow-off region is predicted. At 0.1 MPa and fuel-rich condition, steady solution can be predicted, which might be the case we have observed in our experiment.

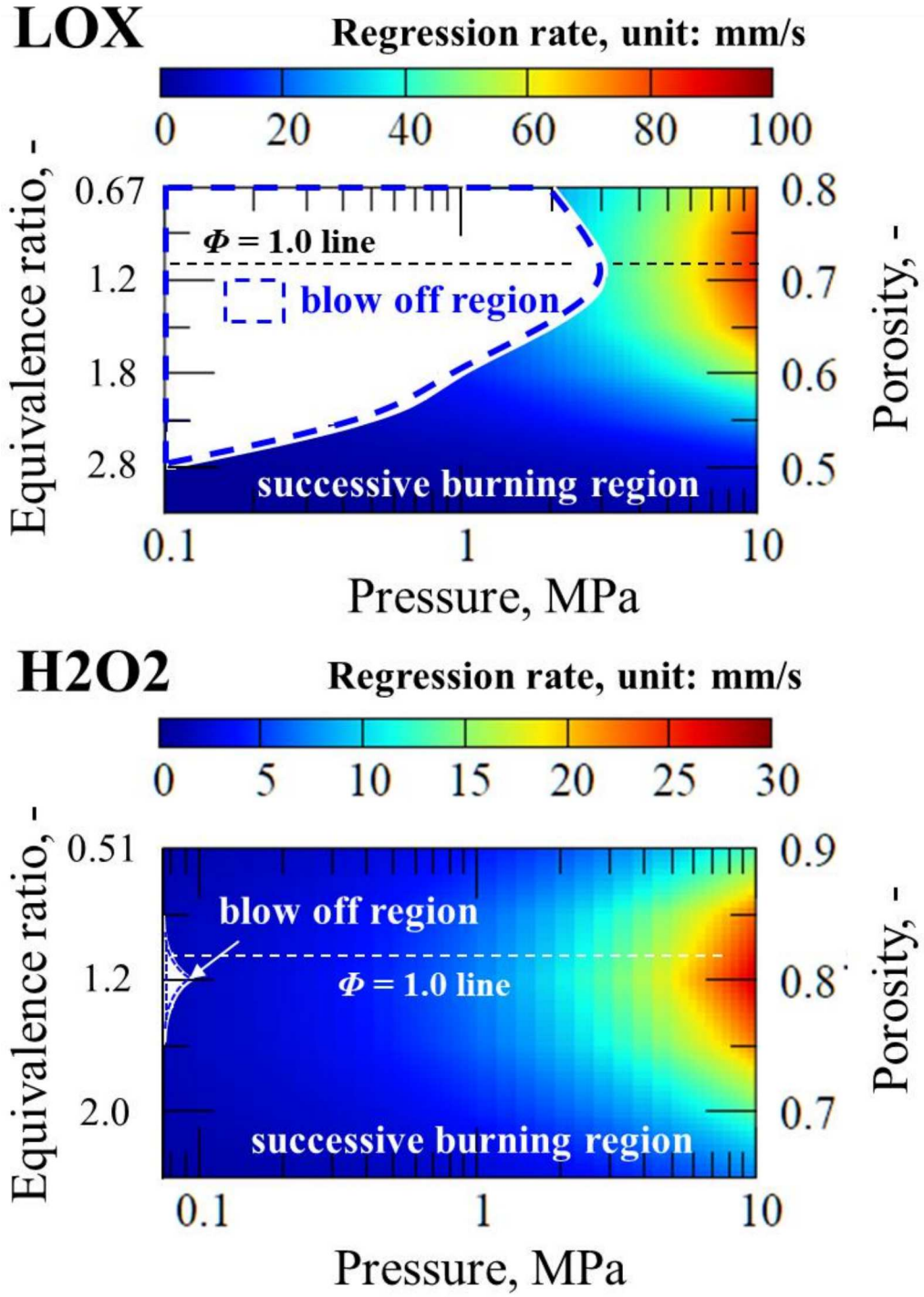

Fig. 4 - 9 Successive burning range as function of ambient pressure and fuel porosity for (a) LOX and (b) H_2O_2 as liquid oxidizer.

More importantly, the large data scattering in the regression rate and frequently observed explosion-like burning, reported by Nagata et al. [85], might be explained by this predicted mapping. Although the different porous combustibles (they used fibrous polyamide and LOX) were used, their tested range might have been partially in the blow-off region, as shown in Fig. 4 - 9 (a). Hence, in the blow-off region, local extinction (blow-off) and re-ignition may occur. This would lead to the data scattering and the explosion-like behavior. In the case when LOX is used, either very rich or lean condition needed to be selected to have the successive burning to avoid any blow-off-driven fluctuation. We are planning to work on high-pressure burning test with LOX in order to understand the direct burning behavior measurement to prove our prediction.

4.5.3 Effect of pressure and fuel porosity on pressure exponent and regression rate

Lastly, the potential regression rate as a function of the ambient pressure and the fuel porosity and the potential pressure exponent (b) of this specimen are discussed. The potential regression rate, as a function of the ambient pressure and the fuel porosity, together with the pressure exponent (b) is given in Fig. 4 - 10 for (a) LOX and (b) H_2O_2, respectively. Please note that the following results are obtained when the reaction index is unity (n = 1). In the figure, the blow off

region and the successive-burning region are depicted in blue and red, respectively, together with the potential regression rate mass that can achieve the comparable mass flux (11 kg/m^{2}s at 5 MPa) of the existing composite solid propellant employing HTPB, Al particles, and ammonium perchlorate.

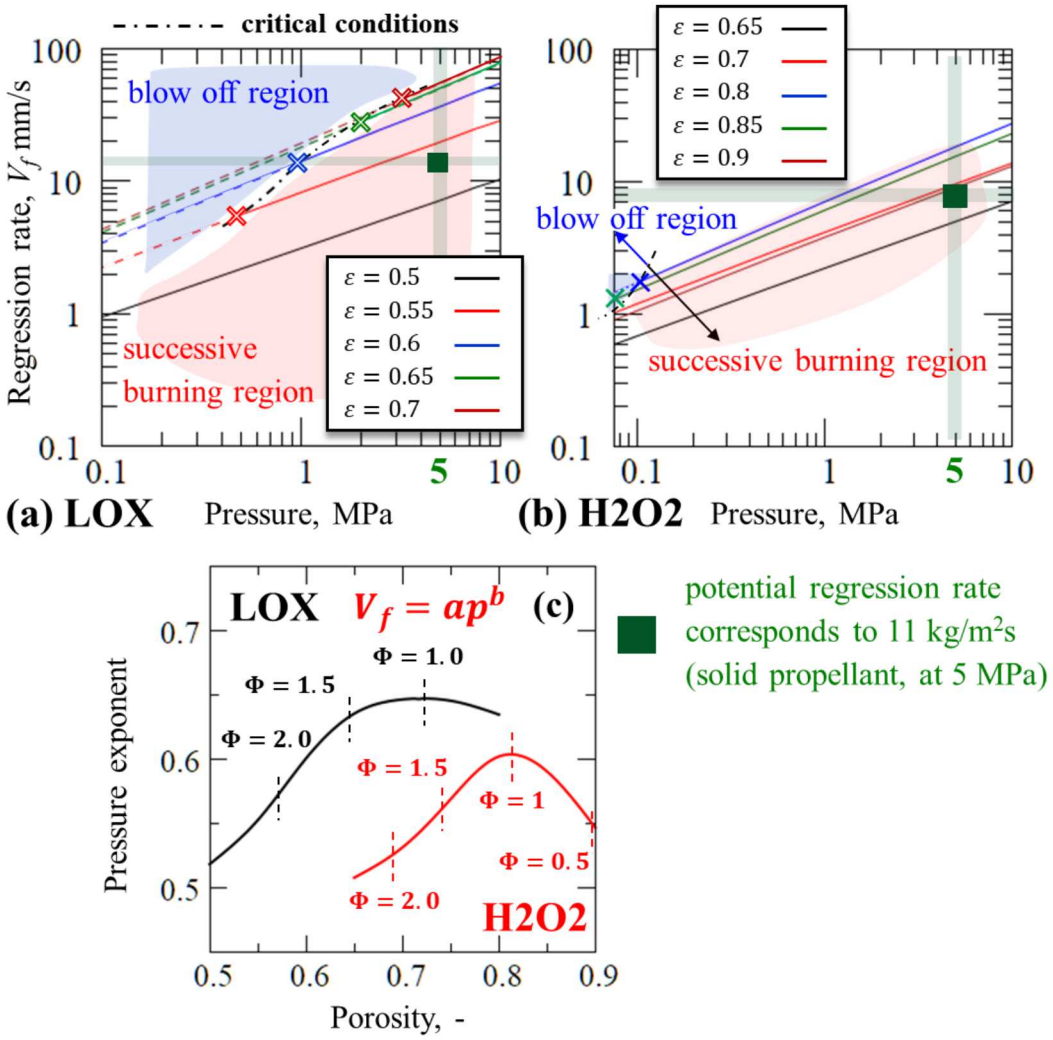

Fig. 4 - 10 Potential regression rate determined as function of pressure and fuel porosity for (a) LOX and (b) H_2O_2 (successive burning region: solid lines; blow-off region: dashed lines) together with (c) pressure exponent.

In (a) and (b), it is found that the comparable mass flux (green quadrangle) can be achievable for both the cases by adjusting the fuel porosity properly. It is interesting to note that the comparable mass flux can be achieved even using hydrogen peroxide.

In (c), the pressure exponent (b) is derived based on a well-known formula, which is denoted on the figure, used for solid propellant [92] (a is the empirical constant) as a function of the fuel porosity. The pressure exponent varies depending on the fuel porosity, and the maximum pressure exponent is obtained around the optimal fuel porosity (0.7 for the LOX case, 0.8 for the H_2O_2 case). The pressure exponent (b), in general, is between 0.3 and 0.6 for general propellant [92]. It could be in the range of 0.4 – 0.5 in the composite solid propellants, especially the AP-based composite solid propellant employing HTPB, Al particles, and ammonium perchlorate (AP) [112]. The pressure exponent in this specimen is predicted to be between 0.51 and 0.65, depending on the fuel porosity and the type of liquid oxidizer. Thus, it is found that this specimen is more pressure sensitive as compared with those of composite solid propellants. For this reason, it is clear that precaution to inhibit the vibration associated with pressure and exothermic reaction by the combustion shall be more necessary in the present specimen than that of the existing composite solid propellant.

4.6 Concluding remarks of this chapter

In this chapter, the comprehensive numerical investigations of the fundamental burning characteristics of the porous combustible soaked in the liquid oxidizer were made. Based on the experimentally obtained findings in the Chapter 3, a steady simple one-dimensional burning model was developed, and the validity of the burning model was confirmed by the experimental results. The thermal structure and the potential regression rate under the various imposed (prescribed) conditions were predicted in this work. Separately considering the estimated blow-off limit in the gas-phase layer, the range needed to achieve successive burning was predicted. Based on the blow-off criteria introduced by the CHEMIKIN premix code, it was found that the achieving successive burning is strongly depended on the adopted oxidizer, the adopted fuel porosity, and the ambient pressure. When LOX (liquid oxygen) is used as the liquid oxidizer, the blow-off can be found in wider range, suggesting that the successive burning is hardly achieved. This finding suggested that possible reason for the data scattering and explosion-like burning, observed in the previous work by Nagata et al., was attributed to the blow off and re-ignition phenomena. By contrast, the successive burning condition for H_2O_2 case can be achieved in a wide range of ambient pressures and fuel porosities. Lastly, this chapter reveals that the potential regression rate is found to be comparable to the existing composite solid propellant even using

hydrogen peroxide, and the pressure exponent of the present specimen is predicted to be more sensitive compared with those of the existing AP-based composite solid propellants. For this reason, the precaution to inhibit the vibration associated by pressure and exothermic reaction by the combustion shall be necessary than that of the composite solid propellant.

Chapter 5

5 Product gas analysis and thrust performance

5.1 Introduction and objective of this chapter

As we have reported, the fundamental burning characteristics of the tested specimen consisting of polyethylene foam soaked in hydrogen peroxide were experimentally and numerically obtained. Now our interest is to predict the achievable specific impulse (thrusting performance), I_{sp}, brought by this present specimen.

To evaluate I_{sp}, first we must know the exact end gas components in a precise manner. Because the solid fuel in the present burning specimen is a polymeric material, its products would be quite complicated [113] [114] and difficult to measure all directly in a precise manner. Suppose that the adopted specimen could reach the equilibrium state, it is possible to identify the major species of the end gas components by direct measurement and the other minor species would be identified through the equilibrium calculation.

In the chapter, firstly we shall experimentally measure distribution of the product gas species over the burning specimen by a gas chromatography to confirm that the present specimen could reach the chemical equilibrium state. Then we shall predict the whole components of the end-

gases assisted by CEA (NASA Chemical Equilibrium with Applications) code [108] in order to evaluate the achievable specific impulse by this burning specimen.).

5.2 Experimental setup and gas species analysis methodology

5.2.1 Experimental setup and tested conditions

A schematic diagram of the whole experimental setup and the tested specimen used in this work is illustrated in Fig. 5 - 1. Basically, the setup is similar to the Chapter 3 so that brief description is made here.

Experiments are carried out under nitrogen-balanced 0.1 MPa environment under various fuel porosities of the polyethylene (PE) foam, ranging from 0.765 and 0.84. A forced ignition using the U-shaped Nickel-chrome wire (stated ignitor in Fig. 5 - 1 (A)) at top surface of the specimen. PE foam is commercially-available (Sakai Chemical Industry Co., Ltd.; 99 % PE composition, 185 kg/m^3 apparent density), which is 18 mm in diameter and 60 mm in height. The PE form is soaked in enriched hydrogen peroxide (H_2O_2), distilled the original solvent (Mitsubishi Gas Chemical Company, Inc 60 wt.% H_2O_2). Distilling procedure is to maintain the solvent at boiling temperature of the water at 0.1 MPa. Ideally, the distilled solvent shall reach 100 wt.% H_2O_2, however, it is not easy to have pure material. It is well-known that H_2O_2 is decomposed into water

vapor and molecular oxygen by heating or a catalyst [115], and the mass fraction of the decomposed water vapor and oxygen depends on H_2O_2 concentration, temperature, pressure, etc. [115] [116] [117] [118]. Because the accurate control of the mass fractions of the decomposed water vapor and oxygen is difficult, we have no way to know "enrich" condition in advance, rather, we shall predict through the product analyses.

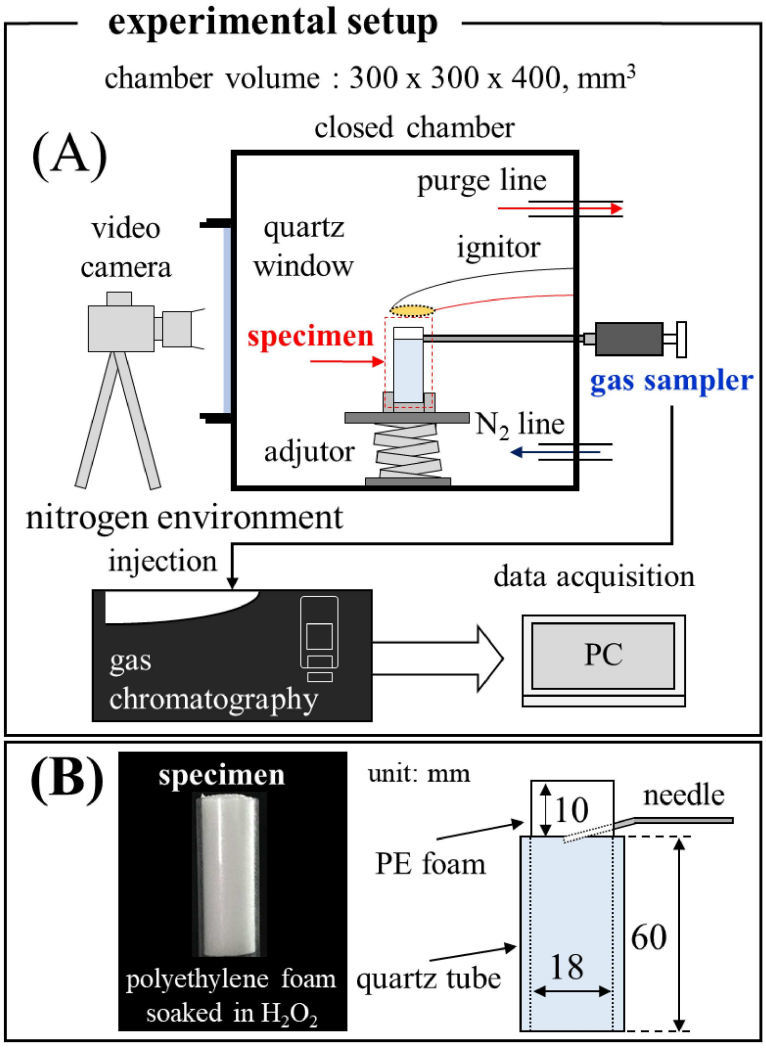

Fig. 5 - 1 (A) Schematic diagram of whole experimental setup and (B) tested specimen used in this work.

The enriched H_2O_2-soaked specimen is inserted into the vertically-oriented transparent quartz tube. Entire burning event after the ignition is recorded by the video camera (Canon iVIS HF G20; 60 fps frame rate, 1/250 shutter speed, 18 dB gain, 2.8 F number) through the quartz window attached to the chamber. The product gas is collected by the gas sampler and analyzed by the gas chromatography (call GC hereafter, GC2030, Shimadzu Corporation). The top surface of the specimen is detected by Image J. In this work, the experimentally obtained results are organized by range of the fuel porosities; case (A) 0.809 – 0.84 and case (B) 0.765 – 0.792.

5.2.2 Product gas measurement

Fig. 5 - 2 (A) shows the gas sampler used in this work. The gas sampler consists of the syringe and the thin needle which measures 0.6/0.3 mm in outer/inner diameter, respectively. The concentration of the product gas species is measured at various location above the burning surface. We call the location as "gas collection distance" (h), and h is defined as the distance between the needle location and the top surface location of the specimen as shown in Fig. 5 - 2 (B). During the experiment, 25 mL of the product gas is sampled taking one second. Note that the sampling volume rate (25 mL/s) is at most 0.5 % of the total product gas released from the burning specimen, so that the sampling procedure should not affect burning event itself.

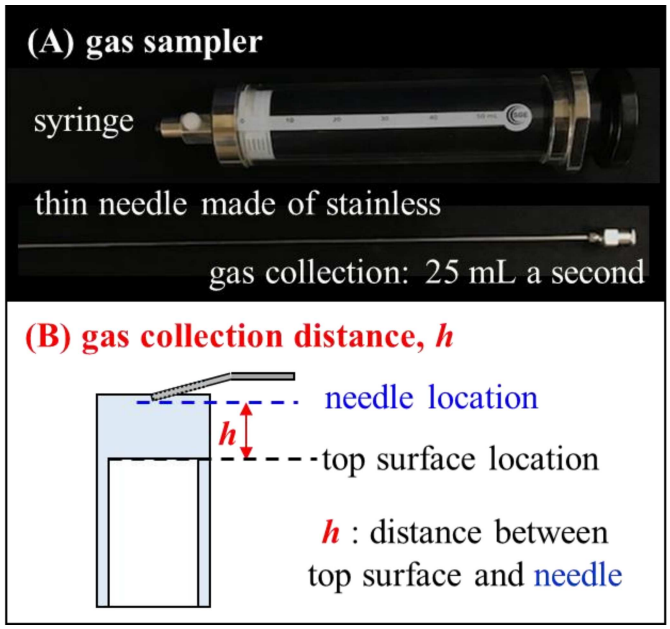

Fig. 5 - 2 (A) Gas sampler used in this work and (B) gas collection distance between needle location and top surface location.

5.2.3 Gas measurement and identification

The product gas species are measured and identified by GC. A typical signal of GC is shown in Fig. 5 - 3 where fuel porosity and the gas collection distance are 0.828 and h = 21.5 mm. The horizontal axis and the vertical axis represent elapsed time and sensitivity, respectively. In Fig. 5 - 3 (A), the detected major product gas species are found to be a mixture gas of nitrogen, oxygen, and carbon monoxide (N_2 + O_2 + CO), and carbon dioxide (CO_2), ethylene (C_2H_4), and acetylene (C_2H_2), respectively. The concentration of each gas species is defined as volume fraction "X_i". Fig. 5 - 3 reveals that N_2 is detected due to the ambient gas present in the chamber, however, volume fraction of N_2 is eliminated in this work in calculation of the concentration.

Fig. 5 - 3 (B) shows an enlarged graph of Fig. 5 - 3 (A). In Fig. 5 - 3 (B), a noise can be confirmed after 8 of the horizontal axis. Taking into the account complete combustion of the hydrocarbon fuel and H_2O_2, water vapor (H_2O) shall be released as the product gas species. Nevertheless, H_2O cannot be detected by the present GC so that we assumed that the noise is affected by H_2O present in the product gas, and that its concentration of H_2O (X_{H2O}) can be estimated as follows.

$$X_{H_2O} = 1 - \left(\sum X_i\right), i = CO, CO_2, O_2, C_2H_2, C_2H_4, N_2 \qquad \text{Eq. 5 - 1}$$

where X_i represents the concentration of each product gas species. Hence, the product gas species

to be analyzed are decided as CO, CO_2, H_2O, O_2, C_2H_2, and C_2H_4.

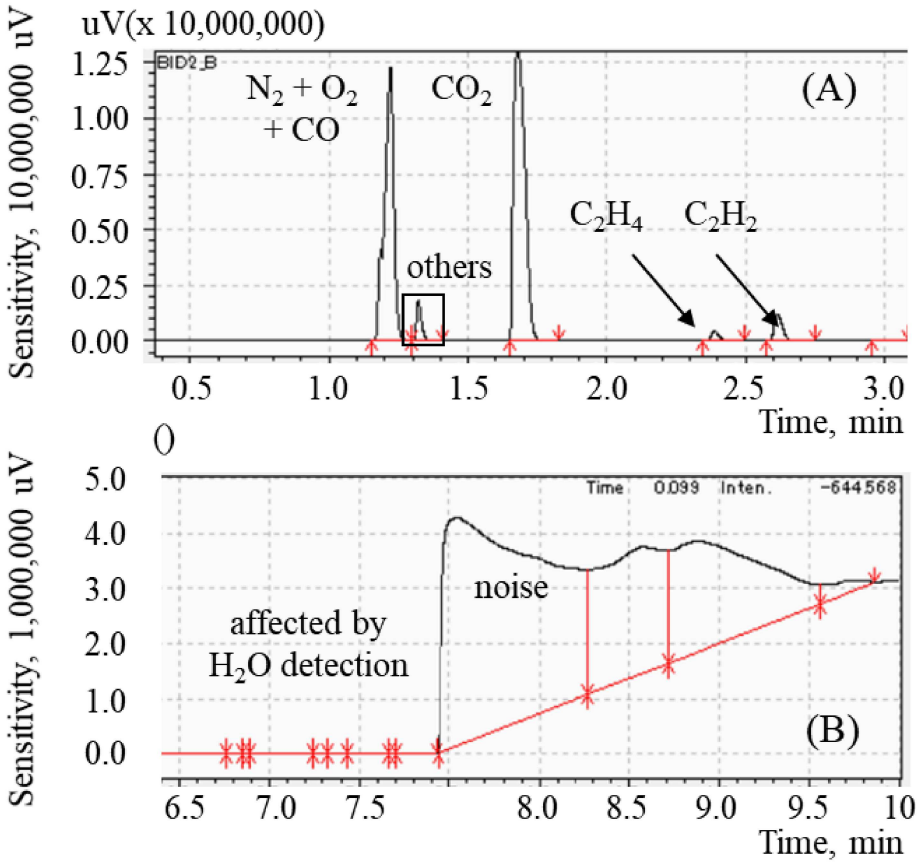

Fig. 5 - 3 (A) Typical signal of combustion product gas species detected by gas chromatography at 0.1 MPa with fuel porosity of 0.828 at gas collection distance h = 21.5 mm, and (B) detected noise due to presence of H_2O.

5.3 Chemical equilibrium calculation

The chemical equilibrium calculation is performed by CEA code with the prescribed mass fraction of the fuel and the oxidizer gases. We shall vary those values to fit to the experimentally-measured major gas species. For the fuel gases, according to the paper [119], main pyrolysis gases

of the polyethylene are to be methane (CH_4), ethylene (C_2H_4), and ethane (C_2H_6). For the oxidizer gases, the water vapor (H_2O) and oxygen (O_2) are chosen by assuming that pure H_2O_2 decomposes into the water vapor and oxygen as follows.

$$H_2O_2 \rightarrow H_2O + 0.5\ O_2 \qquad \text{Eq. 5 - 2}$$

For pure H_2O_2, the mass of the decomposed water vapor and oxygen shall be 18 g and 16 g, and both the mass fractions are 53 wt.% and 47 wt.%, respectively. Each mass fraction depending on the H_2O_2 concentration is estimated by multiplying the actual H_2O_2 concentration by the abovesaid mass fractions. For instance, when 80 wt.% H_2O_2 is used, the decomposed water vapor and oxygen are assumed to be 0.8 x 53 wt.% and 0.8 x 47 wt.%, respectively. In the CEA calculation, the effect of the H_2O_2 concentration will be also considered. The input data adopted in this work is summarized as follows.

Table 5 - 1 Input data for CEA calculation.

Oxidizer gases	$H_2O + O_2$
Fuel gases	CH_4, C_2H_4, C_2H_6
Pressure	0.1 MPa

5.4 Results and discussion: experimental results

5.4.1 One-dimensional profiles of CO_2 and H_2O concentration

In the chapter 4, it was proved that the burning event of the present specimen shall be progressed one-dimensionally. Following this fact, firstly, one-dimensional (1-D) CO_2 and H_2O (major gas species) concentration profiles measured as a function of the gas collection distance are presented to Fig. 5 - 4. The horizontal and vertical axes are the concentration [%] and the gas collection distance, h [mm], respectively. The dashed lines which are obtained from the squared least method are depicted for easy to confirm the data trend. Although the top surface location of the specimen moved during the gas collection are in a range between 1.5 mm and 1.8 mm under the conditions studied in this work, the gas collection distance (h), plotted in the figure, is the value when the gas collection is started.

As it is seen in Fig. 5 - 4, both the concentrations profiles are converged to almost the constant value. Taking into the account the general premixed combustion of the hydrocarbon fuel with oxygen, it is well-known that the CO_2 and H_2O concentrations as the product gas are converged to the constant [120]. With this regard, it is understood that the product gas of the present specimen reaches to the chemical equilibrium under the condition studied. With this respect, the prediction of the specific impulse by the CEA code is effective by inputting the potential combination of the

fuel (pyrolysis) gases, the oxidizer gases, and their mass fraction.

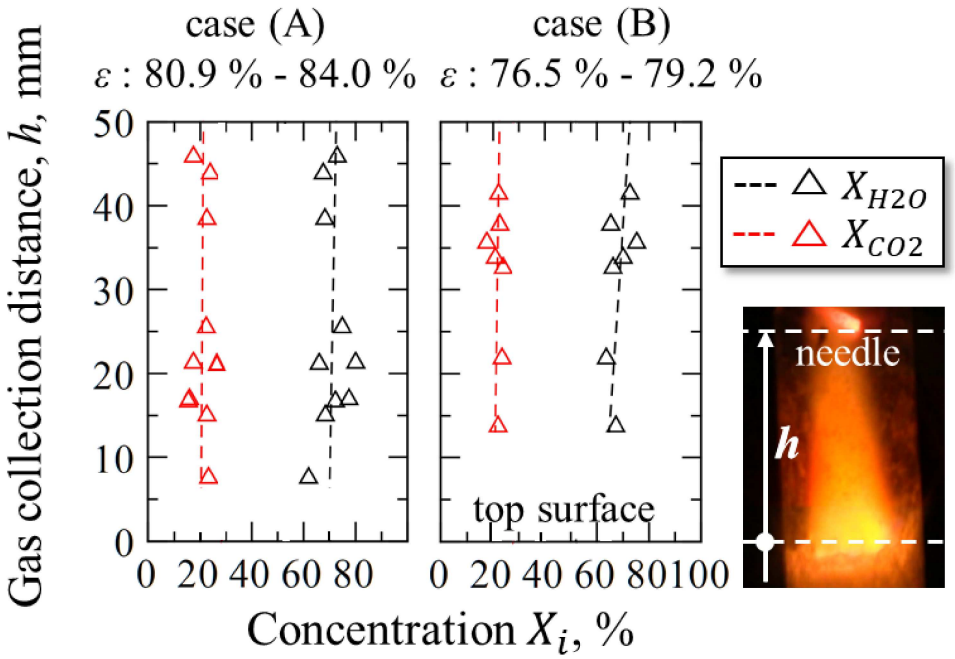

S

Fig. 5 - 4 Measured 1-D concentration profiles of CO_2 and H_2O under atmospheric pressure (0.1 MPa) and fuel porosity; case (A) 0.809 - 0.84 and case (B) 0.765 - 0.792.

5.4.2 Parametric estimation by CEA code (1): Effect of mass fraction of fuel gases on CO_2 and H_2O production

The CO_2 and H_2O concentrations computed by the CEA code are presented to Fig. 5 - 5. The input data of the calculation are summarized in Table 5 - 2. The equivalence ratios (φ) are chosen as 1.0 for the case (A) and 1.3 for the case (B), which corresponds to almost the fuel porosity range of the experiments. The horizontal and vertical axes are ratio of the mass fractions of ethylene (C_2H_4) – ethane (C_2H_6), which is defined in Eq. 5 - 3, and the concentration. Additionally,

the solid line represents the result obtained by 0 wt.% CH_4, and the dashed lines represent ones obtained by 25 wt.% and 50 wt.% CH_4, respectively. The CO_2 and H_2O concentration at the chemical equilibrium obtained from the experiments (value of the dashed lines in Fig. 5 - 4) are shown as well on the figure.

$$\alpha = \frac{C_2H_4\ (wt.\%)}{C_2H_4\ (wt.\%) + C_2H_6\ (wt.\%)} \qquad \text{Eq. 5 - 3}$$

Table 5 - 2 Condition for CEA calculation

Oxidizer gas	H_2O (vapor) + O_2 (50 wt.%: 50 wt.%)
Fuel gas	CH_4, C_2H_4, C_2H_6 (100 wt.% in total)
Pressure	0.1 MPa
equivalence ratio	1.0 for case (A), 1.3 for case (B)

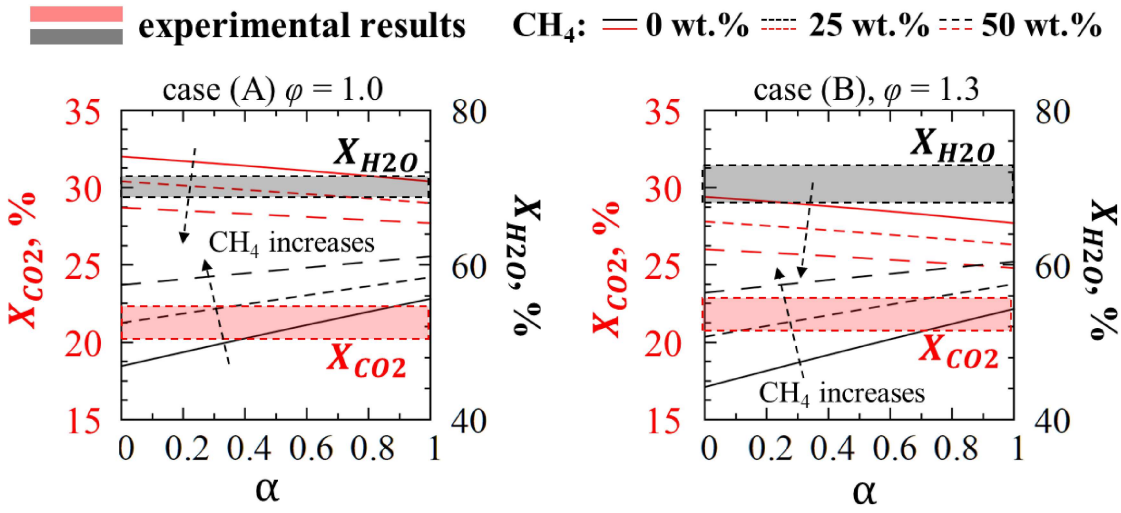

Fig. 5 - 5 Comparison between experimental result and CEA calculation result obtained under oxidizer gases of 50 wt.% H_2O and 50 wt.% O_2 and fuel gases of various α and CH_4.

It can be seen that the CO_2 concentration decreases as the ratio (a) increases, and the H_2O concentration is increased with the increase in the ratio a for both the case (A) and case (B). Additionally, it can be confirmed that the CO_2 concentration decreases, and the H_2O concentration increases, as the mass fraction of CH_4 increases. As compared to both the H_2O and CO_2 concentrations by experiments and the CEA calculation, it is obvious that there is large deference. Assuming that the experimental results are correct, this comparison result implies that the present input data for the CEA code are mistakenly selected. Therefore, the fuel gases, the oxidizer gases, and their mass fractions need to be changed to seek the potential combination of those that will match the experimentally obtained concentrations.

5.4.3 Parametric estimation by CEA code (2): Effect of mass fraction of oxidizer gases on CO_2 and H_2O production

In this work, H_2O_2 is enriched from 60 wt.% H_2O_2 with the methodology stated in Sec. 5.2, Suppose that the water in the solvent is not perfectly eliminated, the mass fraction of the decomposed water vapor (H_2O) is higher in comparison with that of 100 wt.% H_2O_2. Following this scenario, the mass fractions of the oxidizer gases are changed to 65 wt.% H_2O: 35 wt.% O_2, and its result under this condition (listed in Table 5 - 3) is given to Fig. 5 - 6. The axes, solid lines,

and dashed lines represent the same as Fig. 5 - 5.

Table 5 - 3 Input data for CEA calculation.

Oxidizer gas	H_2O (vapor) + O_2 (65 wt.%: 35 wt.%)
Fuel gas	CH_4, C_2H_4, C_2H_6 (100 wt.% in total)
Pressure	0.1 MPa
equivalence ratio	1.0 for case (A), 1.3 for case (B)

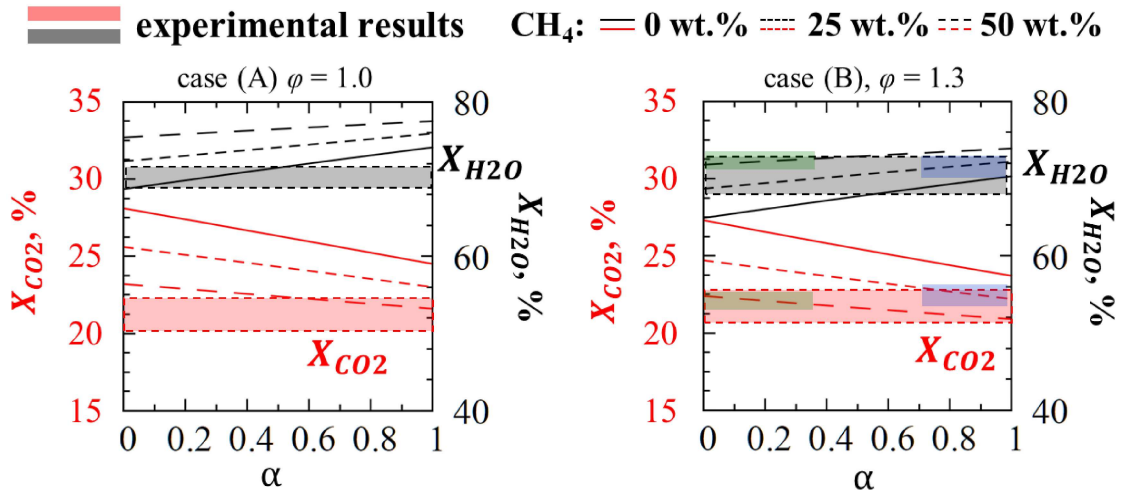

Fig. 5 - 6 Comparison between experimental result and CEA calculation result obtained under oxidizer gases of 65 wt.% H_2O and 35 wt.% O_2 and fuel gases of various α and CH_4.

It is observed that the trend of the CO_2 and H_2O concentrations exhibits the same as Fig. 5 - 5, and the CO_2 and H_2O concentrations obtained from the CEA calculation are found to approach to the experimental results as compared to Fig. 5 - 5 by increasing the mass fraction of water vapor. It can be also seen that the results of the CEA calculation match with the experimental results,

especially for 25 wt.% CH_4 and 50 wt.% CH_4 of the case (B). The ranges where the experimental results and the CEA calculation results match for both the CO_2 and H_2O concentrations are depicted in green and blue on Fig. 5 - 6. This finding reveals that the assumption of the fuel gases (CH_4, C_2H_4, and C_2H_6) are valid when distillation of H_2O_2 is insufficient. In the next section, the mass fraction of the fuel gases of CH_4, C_2H_4, and C_2H_6 for the green and blue region in the case (B) when the oxidizer gases 65 wt.% H_2O and 35 wt.% O_2 are adopted is discussed.

5.4.4 Pyrolysis gases and its mass fraction range

For the green region in Fig. 5 - 6, it is confirmed that the ratio of the mass fraction of ethylene (C_2H_4) – ethane (C_2H_6), α, is in a range between 0 – 0.4 with 50 wt.% CH_4, whereas α is 0.7 – 1 with 25 wt.% CH_4 for the blue region. Because the mass fractions of the fuel gases are accounted for 100 wt.% in total, the mass fraction of C_2H_4 and C_2H_6 share the rest of 50 wt.% (green region) and 75 wt.% (blue region), respectively. Therefore, a range of the mass fraction for C_2H_4 and C_2H_6 is determined as presented to Fig. 5 - 7. The horizontal and vertical axes on the figure are the mass fractions of C_2H_4 and C_2H_6, respectively.

The range of the mass fractions is varied between 0 – 20 wt.% C_2H_4 and 30 – 50 wt.% C_2H_6 for 50 wt.% CH_4 (the green region), whereas the range of the mass fraction is between 53 – 75 wt.%

C_2H_4 and 0 – 20 wt.% C_2H_6 for 25 wt.% CH_4 (the blue region). This result will help predicting the thrusting performance by the CEA code. With this methodology, the pyrolysis gases, the oxidizer gases, and the range of their mass fraction, released from the burning specimen could be predicted.

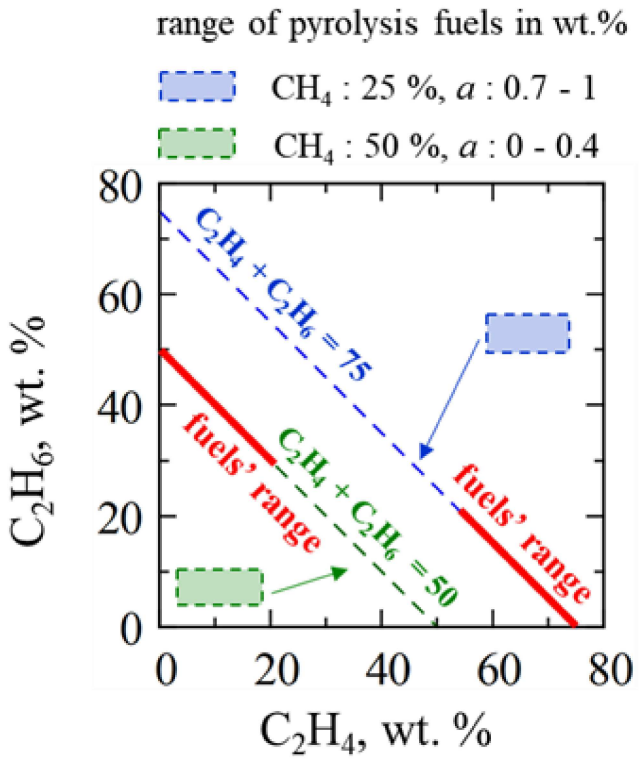

Fig. 5 - 7 Relationship between mass fractions of C_2H_4 and C_2H_6 under 50 wt.% CH_4 (green region) and 25 wt.% CH_4 (blue region).

5.4.5 Identification of the other product gases

The detected product gas species denoted as the “others” in Fig. 5 - 3 is unknown. Taking advantage of the prediction by the CEA code, the “others” is predicted. The predicted gas species except for CO_2 and H_2O computed by the CEA code are summarized in Table 5 - 4. Condition for the calculation is the same as case (A) listed in Table 5 - 3. It is seen that the detected product gas species except for CO_2 and H_2O are found to be small amount of CO, O_2, and OH (hydroxyl radical). As the chromatograph enables to examine the CO and O_2, as mentioned in Sec 5.2, it is suggested that the detected “others” would be the OH. Although the quantitative concentration of OH (X_{OH}) is still unknown, assuming that X_{OH} is 0.5 %, and modifying the H_2O concentration with Eq. 5 - 1 by taking into the account X_{OH}, the specific impulse will be estimated in the following section.

Table 5 - 4 Gas species detected by CEA calculation in order to predict “others” found in chromatograph presented to Fig. 3.

Oxidizer gas	H_2O (vapor) + O_2 (65 wt.%: 35 wt.%)
Fuel gas	CH_4, C_2H_4, C_2H_6 (100 wt.% in total)
Pressure	0.1 MPa
equivalence ratio	1.0 for case (A), 1.3 for case (B)

5.4.6 Expected specific impulse by the present thrusting system

Lastly, the specific impulse (I_{SP}, [s]) is estimated with the concentration of the end-product components for the case (A) and case (B) by the following equation. The concentration of the end-product component is defined as the concentration when the chemical equilibrium is reached, namely, the value at the dashed lines in Fig. 5 (experiment) and as the value computed by the CEA code.

$$I_{SP} = \frac{1}{g_0}\sqrt{\frac{2k}{k-1}\frac{R}{M_C}T_C\left[1-\left(\frac{p_e}{p_C}\right)^{\frac{k-1}{k}}\right]} \qquad \text{Eq. 5 - 4}$$

where g_0 [m/s^2], k [-], R [J/mol·K], M_C [kg/mol], T_C [K], p_e [Pa], and p_c [Pa] are the gravitational acceleration (9.81 m/s^2), the specific heat ratio, the universal gas constant (8.31 J/(mol·K)), the average molecular weight of the combustion gas, the burning temperature of the combustion gas, the nozzle exit pressure (0.1 MPa), and pressure near the burning surface, respectively. For the burning temperature (T_C), it was measured (1800 K at maximum) in the chapter 3 under almost the same experimental conditions conducted in this work. The molecular weight (M_C) and pressure (p_c) can be estimated as follows by assuming ideal gas,

$$M_C = \sum M_i X_i \qquad \text{Eq. 5 - 5}$$

$$p_c = \rho\frac{R}{M_C}T_C \qquad \text{Eq. 5 - 6}$$

where M_i [kg/mol] and ρ [kg/m^3] are the molecular weight of each product gas species and the density of the combustion gas. The density (ρ) and the specific heat ratio (k) are obtained by the CEA code. The average molecular weight (M_C) is firstly calculated based on the concentration at the dashed lines shown in Fig. 5 - 4, and the pressure (p_c) is determined accordingly.

Table 5 - 5 Molecular weight, and specific impulse obtained by experiments and CEA code calculated under 25 wt.% (CH_4), 60 wt.% (C_2H_4), and 15 wt.% (C_2H_6).

Symbol	case (A) φ = 1	case (B) φ = 1.3	Unit
M_C	24.1	24.4	g/mol
p_c	0.2 x 10^6	0.2 x 10^6	Pa
p_e	0.1 x 10^6		Pa
I_{SP} (experiment)	91.9	91.3	s
I_{SP} (CEA) 75 wt.% H_2O_2	94.7	94.8	s
I_{SP} (CEA) 90 wt.% H_2O_2	101	104	s
I_{SP} (CEA) 100 wt.% H_2O_2	102	106	s

The obtained molecular weight (M_C), pressure (p_c), the obtained specific impulse (I_{sp}), and the specific impulse computed by the CEA code under the conditions of the case (A) (φ = 1) and case (B) (φ = 1.3) are listed in Table 5 - 5. The input fuel gases and their mass fraction of the blue region are selected as 25 wt.% (CH_4), 60 wt.% (C_2H_4), and 15 wt.% (C_2H_6), respectively. The estimated specific impulse for case (A) and case (B) under various initial H_2O_2 concentrations in

the oxidizer are also summarized in Table 5 - 5. It is understood that the higher H_2O_2 concentration in the oxidizer gives better thrusting performance, however, its recovery is at most 10 %. Nevertheless, in case one prefers to have maximum performance in the present specimen, it is recommended to apply special methodologies such as the distillation at reduced pressure and freezing the solvent at the freezing temperature of the water [116] [121].

5.5 Concluding remarks of this chapter

The product gases of the burning polyethylene foam soaked with the enriched hydrogen peroxide (H_2O_2) at nitrogen-balanced 0.1 MPa ambient were studied to predict the thrusting performance of the present burning specimen. In the experiment, enriched H_2O_2 obtained through distilling procedure was used as the liquid oxidizer. The cylinder-shaped burning specimen embedded in the quartz tube was tested, and the steady end-burning regression was presented after the ignition at the top surface. One-dimensional (1-D) CO_2 and H_2O concentration profiles over the regression surface were measured experimentally by using a gas chromatography. Adopted porosity of the fuel form is the range of 0.765 – 0.84. It was found that the concentration profiles exhibited nearly flat, suggesting that the chemical equilibrium state has been reached satisfactory in the post-flame zone. The equilibrium calculation by the CEA code was then utilized in order to predict the exact combination of the pyrolysis gases, the oxidizer gases, their mass fraction, and the end gas components produced in this burning specimen and the specific impulse achievable by this burning specimen. The predicted mass fraction of oxygen shall be lower than that of pure H_2O_2, major pyrolysis gases components were found to be methane (CH4), ethylene (C_2H_4), and ethane (C_2H_6). A part of product gas species, which was not identified by the experiments, was found to be OH (hydroxyl radical). Potential specific impulse was estimated to

be in the range of 95 s to 106 s, depending on the initial H_2O_2 concentration. Using pure H_2O_2 was preferred to achieve the larger specific impulse of the present specimen.

Chapter 6

6 Concluding remarks of the dissertation

The objective in this dissertation is two folds as follows:

1) the fundamental burning characteristics of the specimen consisting of the porous combustible soaked in the liquid oxidizer are investigated.

2) the reason for the data scattering and the explosion-like burning, observed in the previous work by Nagata et al., is clarified.

3) the thrusting performance achievable in the present specimen is investigated.

In this dissertation, the comprehensive experimental and numerical investigations on the specimen, consisting of the polyethylene foam soaked in enriched hydrogen peroxide, as referred to the previous work by Nagata et al. in 1997, were conducted. In the experimental investigation, the experiments were carried out with the newly introduced chamber, which is filled with nitrogen, under pressures in a range between 0.1 MPa and 0.35 MPa in absolute pressure and fuel porosities in a range between 0.6 to 0.9. In the experimental investigations, the following findings on the fundamental burning characteristics of the tested specimen were obtained.

With the careful observation of the burning event and by carefully tracking the top surface (the burning surface) of the specimen by the image processing, (1) it was revealed that the top surface of the specimen moved downward at almost the steady regression rates, ranging between 1.6 mm/s and 3.2 mm/s, depending on the fuel porosity and pressure. (2) The direct temperature measurement trials by the thermocouple helped to know the thermal structure during the entire burning event, and (3) the regression of the specimen was found to be dominated by the premixed-like surface flame established close to the top surface of the specimen. Lastly, (4) the one-dimensionality of the burning process was proven by the simple thermal analysis. These findings played vital role in knowing the fundamental burning characteristics of the tested specimen which has been missing since the previous work by Nagata et al.

Utilizing the experimental findings, the one-dimensional burning model was then developed in this work, and the validity of the burning model was evaluated by the experimental results. The effect of the fuel porosity, pressure, type of the liquid oxidizer on the thermal structure during the burning event, on the potential regression rate, and on the pressure exponent were numerically predicted. In addition, considering the blow off limits of the premixed combustion in the gas-phase layer, the blow off limits and its effect of the imposed conditions were investigated in this work. The numerical findings revealed that the successive burning is widely achievable when

hydrogen peroxide is used as the liquid oxidizer, but it is only partially achievable when liquid oxygen is utilized. The tested range where Nagata et al. conducted might have been partially in the blow-off region, hence, local extinction (blow-off) and re-ignition may occur. It was found that, in the case when LOX is used, either very fuel rich or fuel lean condition needed to be selected to prevent any blow-off-driven fluctuation. This fact may support the data scattering and the explosion-like burning observed in the previous work reported by Nagata et al.

The product gases of the specimen at nitrogen-balanced 0.1 MPa ambient to predict the specific impulse of the present specimen were studied. In the experiments, we first measured 1-D CO_2 and H_2O concentration profiles over the regression surface by a gas chromatography under various fuel porosities 0.77 – 0.84. The concentration profiles exhibited nearly flat, suggesting that chemical equilibrium was reached satisfactory immediately after the regression surface. The equilibrium calculation was then utilized in order to predict optimal combination of pyrolysis gases, oxidizer gases, and their mass fraction, and estimate the other product gases potentially produced and thrusting performance achievable in this burning specimen. The expected specific impulse potentially achievable by the present burning specimen was estimated and found to be in the range of 95 s to 106 s, depending on the initial H_2O_2 concentration. This fact implied that using pure H_2O_2 was preferred to achieve the larger specific impulse of the present specimen.

Reference

[1] C. Cappelletti, S. Battistini and F. Graziani, "Small launch platforms for micro-satellites," Advances in Space Research, Vol. 62, (2018), pp. 3298-3304.

[2] T. Shimada, K. Kitagawa, M. Kanazaki, K. Chiba and M. Nakamiya, "Study of low-cost 100kg-satellite launcher using hybrid rocket engines," Conference paper for Space Propulsion, Colonge, Germany, (2014).

[3] E. Blanco, J. R. Behrens, B. A. Corbin, E. K. Green, A. J. Picard and A. Balakrishnan, "Global trends in small satellites," Institute for Defense Analyses, (2017), IDA PaperP-8638.

[4] T. Hunsaker, M. Bille and P. Kolodziejski, "Nanosat launch vehicles: A global perspective and business case," AIAA Space Conference and Exposition, San Diego, CA, (2013).

[5] T. Moretto and R. M. Robinson, "Small satellites for space weather research," Space Weather, Vol. 6, (2008), S05007.

[6] NASA, "NASA opens new cubesat opportunities for low-cost space exploration," 11th Aug. 2015. [Online]. Available: https://www.nasa.gov/press-release/nasa-opens-new-cubesat-opportunities-for-low-cost-space-exploration/. [Accessed 10th Oct. 2021].

[7] Nanosats Database, "ESTube-1," Nanosats Database, 8th Aug. 2021 (last modified). [Online]. [Accessed 10th Oct. 2021].

[8] R. H. Hamann, C. J. M. Verhoeven, A. A. Vaartjes and A. R. Bonnema, "Nanosatellites for microtechnology prequalification: the delfi program of delft university of technology," 6th Symposium on Small Satellites for Earth Observation, Berlin, Germany, (2007).

[9] R. Sandau, K. Brieß and M. D'Errico, "Small satellites for global coverage: Potential and limits," ISPRS Journal of Photogrammetry and Remote Sensing, Vol. 65, (2010), pp. 492-504.

[10] M. Komatsu and S. Nakasuka, "University of Tokyo nano datellite project "PRISM"," Transsactions of the Japan Society for Aeronautical and Space Sciences, Vol. 7, (2009), pp. 19-24.

[11] C. Yang, X. Hou and L. Wang, "Thermal design, analysis and comparison on three concepts of space solar power satellite," Acta Astronautica, Vol. 137, (2017), pp. 382-402.

[12] P. Jaffe, J. Hodkin, F. Harrington, C. Person, M. Nurnberger, B. Nguyen, S. LaCava, D. Scheiman, G. Stewart, A. Han, E. Hettwer and D. Rhoades, "Sandwich module prototype progress for space solar power," Acta Astronautica, Vol. 94, (2014), pp. 662-671.

[13] H. Heidt, J. Puig-Suari, A. S. Moore, S. Nakasuka and R. J. Twiggs, "CubeSat: A new generation of picosatellite for education and industry low-cost space experimentation," Proceedings of the 14th Annual/USU Conference on Small Satellites, Logan, USA, (2000).

[14] R. M. Millan, R. V. Steiger, M. Ariel, S. Bartalev, M. Borgeaud, S. Campagnola, J. C. Castillo-Rogez, R. Fléron, V. Gass, A. Gregorio, D. M. Klumpar, B. Lal, M. Macdonald, J. U. Park, V. S. Rao, K. Schilling, G. Stephens, A. M. Title and J. Wu, "Small satellites for space science: A COSPAR scientific roadmap," Advances in Space Research, Vol. 64, (2019), pp. 1466-1517.

[15] The European Space Agency, "History of the Ariane workhorse," The European Space Ag ency, [Online]. Available: https://www.esa.int/Enabling_Support/Space_Transportation/Hi story_of_the_Ariane_workhorse. [Accessed 8th Oct. 2021].

[16] NASA, "The space shuttle and its operations," NASA, [Online]. Available: https://www.nasa.gov/centers/johnson/pdf/584722main_Wings-ch3a-pgs53-73.pdf. [Accessed 8th Oct. 2021].

[17] Japan Aerospace Exploration Agency, "About H-IIA launch vehicle," Japan Aerospace Exploration Agency, [Online]. Available: https://global.jaxa.jp/projects/rockets/h2a/. [Accessed 8th Oct. 2021].

[18] Spacelight News + Media, "JAXA test fires H3 SRB-3 solid rocket booster, releases 360 video," March, (2020), URL: https://www.spaceflightnewsmedia.com/news/jaxa-mhi-srb3-solid-rocket-booster-test-360-video, access: 28th, Sep. (2021).

[19] A. J. P. van Kleef and B. A. Oving, "Affordable launch opportunities for small satellites," National Aerospace Laboratory, (2012), NLR-TP-2012-310.

[20] Z. Kang, Z. g. Wang, Q. Li and P. Cheng, "Review on pressure swirl injector in liquid rocket engine," Acta Astronautica, Vol. 145, (2018), pp. 174-198.

[21] S. Shioya, M. Kohga and T. Naya, "Burning characteristics of ammonium perchlorate-based composite propellant supplemented with diatomaceous earth," Combustion and Flame, Vol. 161, (2014), pp. 620-630.

[22] R. P. Fitzgerald and M. Q. Brewster, "Flame and surface structure of laminate propellants with coarse and fine ammonium perchlorate," Combustion and Flame, Vol. 136, (2004), pp. 313-326.

[23] A. Aziz, R. Mamat, W. K. W. Ali and M. R. M. Perang, "Review on typical ingredients for ammonium perchlorate based solid propellant," Applied Mechanics and Materials, Vol. 773-774, (2015), pp. 470-475.

[24] M. Zhu, X. Chen, C. Zhou, J. Xu, O. Musa and H. Xiang, "Experimental and numerical investigations on the decomposition and combustion characteristics of composite propellant with Mg/Al particles additives," Applied Thermal Engineering, Vol. 111 (2017), pp. 863-875.

[25] J. T. Essel, A. P. Nelson, L. B. Smilowitz, B. F. Henson, L. R. Merriman, D. Turnbaugh, C. Gray and K. B. Shermer, "Investigating the effect of chemical ingredient modifications on the slow cook-off violence of ammonium perchlorate solid propellants on the laboratory scale," Journal of Energitic Materials, Vol. 38, (2019), pp. 127-141.

[26] A. Davenas, G. Jacob, Y. Longevialle and C. Perut, "Energitic compounds for future space applications," Proceeding of the 2nd Internatinoal Conference on Green Propellants for Space Propulsion, Cagliari, Sardinia, Italy, (2004).

[27] S. Chaturvedi and P. N. Dave, "Review on thermal decomposition of ammonium nitrate," Journal of Energitic Materials, Vol. 31, (2013), pp. 1-26.

[28] R. Aggarwal, I. K. Patel and P. B. Sharma, "Green Propellant: A Study," International Journal of Latest Trends in Engineering and Technology, Vol. 6, (2015), pp. 83-87.

[29] N. Wingborg and M. Calabro, "Green solid propellants for launchers," Space Propulsion Conference, Rome, Italy, (2016), SP2016_3125163.

[30] A. Mazzetti, L. Merotto and G. Pinarello, "Paraffin-based hybrid rocket engines applications: A review and a market perspective," Acta Astronautica, Vol. 126, (2016), pp. 286-297.

[31] D. Pastrone, "Approaches to low fuel regression rate in hybrid rocket engines," International Journal of Aerospace Engineering, Vol. 2012, (2012), Article ID 649753.

[32] E. A. Alkuan and W. M. Alobaidi, "Experimental and theoretical research review of hybrid rocket motor techniques and applications," Advances in Aerospace Science and

Technology, Vol. 1, (2016), pp. 71-82.

[33] H. Nagata, S. Hagiwara, M. Wakita and T. Totani, "Optimal fuel grain design method for CAMUI type hybrid rocket," Proceedings of the 47th AIAA/ASME/SAE/ASEE Joint Propulsion Conference & Exhibit, San Diego, California, (2011), AIAA 2011-6105.

[34] T. Sakurai, S. Yuasa, H. Ando, K. Kitagawa and T. Shimada, "Performance and regression rate characteristics of 5-kN swirling-oxidizer-flow-type hybrid rocket," Journal of Propulsion and Power, Vol. 33, (2017), pp. 891-901.

[35] M. A. Karabeyoglu, G. Zilliac, B. J. Cantwell, S. DeZilwa and P. Castellucci, "Scale-up tests of high regression rate paraffin-based hybrid rocket fuels," Journal of Propulsion and Power, Vol. 20, (2012), pp. 1037-1045.

[36] T. V. Chelaru and F. Mingireanu, "Hybrid rocket engine, theoretical model and experiment," Acta Astronautica, Vol. 68, (2011), pp. 1891-1902.

[37] S. S. Wei, M. C. Lee, Y. H. Chien, T. H. Chou and J. S. Wu, "Experimental investigation of the effect of nozzle throat diameter on the performance of a hybrid rocket motor with swirling injection of high-concentration hydrogen peroxide," Acta Astronautica, Vol. 164, (2019), pp. 334-344.

[38] F. Piscitelli, G. Saccone, A. Gianvito, G. Cosentino and L. Mazzola, "Microcrystalline paraffin wax as fuel for hybrid rocket engine," Proceedings of the 6th European Conference for Aeronautics and Space Sciences, Krakow, Poland, (2015).

[39] S. Kang, D. Lee and E. Lee, "Design and performance evaluation of hybrid rocket using 95 wt % H2O2," Proceedings of the 52nd AIAA/SAE/ASEE Joint Propulsion Conference, Salt Lake City, Ut (2016), AIAA 2016-4864.

[40] B. Cantwell, A. Karabeyoglu and D. Altman, "Recent advances in hybrid propulsion," International Journal of Energetic Materials and Chemical Propulsion, Vol. 9, (2010), pp. 305-326.

[41] C. Oztan and V. Converstone, "Utilization of additive manufacturing in hybrid rocket technology: A review," Acta Astronautica, Vol. 180, (2021), pp. 130-140.

[42] M. Gieras and A Gorgeri, "Numerical modelling of the hybrid rocket engine performance," Propulsion and Power Research, Vol. 10, (2021), pp. 15-22.

[43] F. Barato, N. Bellomo and D. Pavarin, "Integrated approach for hybrid rocket technology

development," Acta Astronautica, Vol. 128, (2016), pp. 257-261.

[44] N. Tomita, K. Kitoh, K. Kohsetsu, K. Hasegawa and N. Maeda, "Fundamentals of Rocket Technology", CORONA PUBLISHING CO. LTD, 2015, pp. 46, in Japanese.

[45] K. Takahashi, K. Nakadai, M. Tanabe, T. Kuwahara and T. Shimada, "Combustion of aluminum particles nearv burning surface of composite propellant - Effects to temperature gradient-," Transactions of the Japan Society for Aeronautical and Space Sciences, Vol. 59, (2011), pp. 141-147.

[46] M. W. Beckstead, K. Puduppakkam, P. Thakre and V. Yang, "Modeling of combustion and ignition of solid-propellant ingredients," Progress in Energy and Combustion Science, Vol. 33, (2007), pp. 497-551.

[47] L. Xiao, X. Fan, J. Li, Z. Qin, X. Fu, W. Pang and Y. Wang, "Effect of Al content and particle size on the combustion of HMX-CMDB propellant," Combustion and Flame, Vol. 214, (2020), pp. 80-89.

[48] T. D. Hedman, L. J. Groven, K. Y. Cho, R. P. Lucht and S. F. Son, "The diffusion flame structure of an ammonium perchlorate based composite propellant at elevated pressures," Proceeding of the Combustion Institute, Vol. 34, (2013), pp. 649-656.

[49] V. V. Boldyrev, "Thermal decomposition of ammonium perchlorate," Thermochimica Acta, Vol. 443, (2006), pp. 1-36.

[50] M. W. Beckstead, "Solid propellant combustion mechanism and flame structure," Pure and Applied Chemistry, Vol. 65, (1993), pp. 297-307.

[51] M. K. Bharti and S. Chalia, "Depletion of stratospheric ozone by chlorinated exhaust of ammonium perchlorate based composite solid propellant formulations: A review," International Journal of Research in Advanced Engineering and Technology, Vol. 3, (2017), pp. 1-5.

[52] H. Belal, C. W. Han, I. E. Gunduz, V. Ortalan and S. F. Son, "Ignition and combustion behavior of mechanically activated Al–Mg particles in composite solid propellants," Combustion and Flame, Vol. 194, (2018), pp. 410-418.

[53] H. Habu and K. Hori, "The burning rate characteristics of magnalium (Mg/Al)-AP based solid propellant," Science and Technology of Energetic Materials, Vol. 67, (2006), pp. 187-192, in Japanese.

[54] G. Cican and A. D. Mitrache, "Rocket Solid Propellant Alternative Based on Ammonium Dinitramide," INCAS Bulletin, Vol. 9, (2017), pp. 17-24.

[55] S. Levi, D. Signoriello, A. Gabardi, M. Molinari, L. Galfetti, L. T. DeLuca, S. Cianfanelli and G. F. Klyakin, "Metalized solid rocket propellants based on AN/AP and PSAN/AP for access to space," Progress in Propulsion Physics, Vol. 1, (2009), pp. 97-108.

[56] G. Marxman and M. Gilbert, "Turbulent boundary layer combustion in the hybrid rocket," Symposium (International) on Combustion, Vol. 9, (1963), pp. 371-383.

[57] M. A. Karabeyoglu, B. J. Cantwell and D. Altman, "Development and testing of paraffin-based hybrid rocket fuels," Proceedings of the 37th Joint Propulsion Conference and Exhibit, Salt Lace City, Utah, (2001), AIAA 2001-4503.

[58] G. Zilliac and M. A. Karabeyoglu, "Hybrid rocket fuel regression rate data and modeling," Proceeding of the 42nd AIAA/ASME/SAE/ASEE Joint Propulsion Conference & Exhibit, Sacramento, California, (2006), AIAA 2006-4504.

[59] T.F. Milner and J. D. Herr, "Green rocket propulsion by reaction of Al and Mg powders and water," Proceedings of the 40th AIAA/ASME/SAE/ASEE Joint Propulsion Conference and Exhibit, Fort Lauderdalel, (2004), AIAA 2004-4037.

[60] Y. Funami and A. Takano, "Averaged regression rate of hybrid rocket fuel grain with a star fractal swirl port," The second Hybrid Rocket Symposium, (2019), HR-2019-001, in Japanese.

[61] S. Kim, J. Lee, G. Kim, J. Cho, H. Moon, H. Sung and J. Kim, "Combustion characteristics of the cylindrical multi-port grain for hybrid rocket motor," Proceedings of the 45th AIAA/ASME/SAE/ASEE Joint Propulsion Conference & Exhibit, Denver, Colorado, (2009), AIAA 2009-5112.

[62] L. Liu, X. He, Y. Wang, Z. Chen and Q. Guo, "Regression rate of paraffin-based fuels in hybrid rocket motor," Aerospace Science and Technology, Vol. 107, (2020), 106269.

[63] J. Y. Lestrade, J. Anthoine, A. J. Musker and A. Lecossais, "Experimental demonstration of an end-burning swirling flow hybrid rocket engine," Journal of Aerospace Science and Technology, Vol. 92, (2019), pp. 1-8.

[64] Y. Kawabata, A. Banno, Y. Wada, K. Ozawa, T. Shimada, N. Kato, K. Hori and R. Nagase, "Experimental investigation of fuel regression rate of low-melting-point thermoplastic

fuels in the altering-intensity swirling-oxidizer-flow-type hybrid rocket engine," Transaction of the Japan Society for Aeronautical and Space Science, Aerospace Technology Japan, Vol. 16, (2018), pp. 267-273.

[65] W. H. Knuth, M. J. Chiaverini, J. A. Sauer and D. J. Gramer, "Solid-fuel regression rate behavior of vortex hybrid rocket engine," Journal of Propulsion and Power, Vol. 18, (2002), pp. 600-609.

[66] E. E. Rice, D. J. Gramer, C. P. St. Clair and M. J. Chiaverini, "Mars ISRU CO/O2 hybrid engine development status," Proceedings of the 38th Aerospace Sciences Meeting and Exhibit, Reno, NV, (2003), AIAA 2000-1066.

[67] N. Tsujikado, M. Koshimae, R. Ishikawa, K. Kitahara and A. Ishihara, "Solid fuel grain design of 90% hydrogen peroxide/polyethylene solid fuel hybrid rocket engine," Proceedings of the 42nd AIAA/ASME/SAE/ASEE Joint Propulsion Conference & Exhibit, Sacramento, Califoria, (2006), AIAA 2006-4675.

[68] Y. Saito, T. Yokoi, L. Neumann, H. Yasukochi, K. Soeda, T. Totani, M. Wakita and H. Nagata, "Investigation of axial-injection end-burning hybrid rocket motor regression," Advances in Aircraft and Spacecraft Science, Vol. 4, (2017), pp. 281-296.

[69] L. Kamps and H. Nagata, "Tubular equivalent regression rate in hybrid rockets with complex geometries," Transaction of the Japan Society for Aeronautical and Space Sciences, Aerospace Technology Japan, Vol. 17, (2019), pp. 544-551.

[70] K. Ozawa and T. Shimada, "Theoretical prediction of regression rates in swirl-injection hybrid rocket engine," Progress in Propulsion Physics, Vol. 8, (2016), pp. 283-306.

[71] JAXA, "User's Manual Epsilon Launch Vehicle," July 2018. [Online]. Available: https://global.jaxa.jp/projects/rockets/epsilon/pdf/EpsilonUsersManual_e.pdf. [Accessed 13rd Oct. 2021].

[72] S. Venugopal, K.K. Rajesh and V. Ramanujachari, "Hybrid rocket technology," Defence Science Journal, Vol. 61, (2011), pp. 193-200.

[73] S. Yuasa, K. Yamamoto, H. Hachiya, K. Kitagawa and Y. Oowada, "Development of a small sounding hybrid rocket with a swirling-oxidizer-type engine," 37th Joint Propulsion Conference and Exhibit, Salt Lake City, UT, (2001), AIAA 2001-3537.

[74] J. Tsohas, B. Appel, A. Rettenmaier, M. Walker and S. Heister, "Development and launch

of the Purdue hybrid rocket technology demonstrator," Proceedings of the 45th AIAA/ASME/SAE/ASEE Joint Propulsion Conference & Exhibit, Denver, Colorado, (2009), AIAA 2009-4842.

[75] H. Nagata, T. Uematsu and K. Ito, "CAMUI type hybrid rocket as small scale ballisticflight testbed," Transactions of the Japan society aeronautical and space sciences, aerospace technology, Vol. 10, (2012), pp. 1-5.

[76] Taiki Aerospace News, No. 9, (2013), available online :https://www.town.taiki.hokkaido.jp/soshiki/kikaku/uchu/taiki-aerospace-news-H25.data/tasn9.pdf, in Japanese.

[77] M. Kobald, U. Fischer, K. Tomilin, A. Petrarolo and C. Schmierer, "Hybrid experimental rocket stuttgart: A low-cost technology demonstrator," Journal of Spacecraft and Rockets, Vol. 55, (2018), pp. 484-500.

[78] S. Nishino, T. Tateyama, Y. Funami and A. Takano, "Conceptual design and launch of hybrid rocket with star fractal swirl fuel grain," Proceedings of Space Transportation Symposium, Kanagawa Japan, (2019), STCP-2018-022, in Japanese.

[79] F. Heeg, L. Kilzer, R. Seitz and E. Stoll, "Design and test of a student hybrid rocket engine with an external carbon fiber composite structure," Aerospace, Vol. 7, (2020), aerospace7050057.

[80] S. Katharina, S. Andreas and L. Karsten, "The stern project - Hands on rockets science for university student," Conference: ESA PAC Symposium Visby, Sweden (2017).

[81] C. Hill, G. Doerksen, D. Stannard, W. S. Hinman, D. Quinn and C. Johansen, "Development and testing of a 4.4-kN paraffin-based hybrid rocket motor and test facility," 2018 Joint Propulsion Conference, Cincinnti Ohio (2018), AIAA 2018-4837.

[82] M, Kimura, Y. Wada, Y. Kawabata, N. Kato and K. Hori, "A study on the combustion efficiency of 5 kM thrsut class hybrid rocket motor with baffle plate," Proceedings of Space Transport Symposium, (2020), STCP-2020-006.

[83] H. Nagata, K. Okada, T. Sanada, T. Kato, R. Akiba, S. Satori and I. Kudo, "Combustion characteristics of fibrous fuels for dry towel hybrid rocket motor," The Journal of Space Technology and Science, Vol. 13, (1997), pp. 11-16.

[84] J. L. Sabourin, G. A. Risha, R. A. Yetter, S. F. Son and B. C. Tappan, "Combustion characteristics of nanoaluminum, liquid water, and hydrogen peroxide mixtures,"

Combustion and Flame, Vol. 154, (2008), pp. 587-600.

[85] H. Nagata, R. Akiba, N. Tanatsugu, M. Kohno, R. Yokota and S. Kayuta, "A Preliminary study of the wet towel hybrid rocket motor," Aeronautical and Space Sciences Japan. Vol. 45, (1997), pp. 365-370.

[86] D. S. Sundaram, V. Yang, Y. Huang, G. A. Risha, and R. A. Yetter, "Effects of particle size and pressure on combustion of nano-aluminum particles and liquid water," Combustion and Flame, Vol. 160, (2013), pp. 2251-2259.

[87] C. R. Zaseck, S. F. Son and T. L. Pourpointa, "Combustion of micron-aluminum and hydrogen peroxide propellants," Combustion and Flame, Vol. 160, (2013), pp. 184-190.

[88] "ImageJ," available online: https://imagej.nih.gov/ij/.

[89] USP technologies, "H2O2 decomposition volumes," [Online]. Available: https://www.h2o2.com/technical-library/physical-chemical-properties/thermodynamic-properties/default.aspx?pid=41&name=Decomposition-Volumes. [Accessed 19 Oct. 2021].

[90] USP technologies, "H2O2 Self-accelerated decomposition," [Online]. Available: https://www.h2o2.com/technical-library/physical-chemical-properties/thermodynamic-properties/default.aspx?pid=42&name=Self-Accelerated-Decomposition. [Accessed 18 Oct. 2021].

[91] L. L. McCrain and W. L. Roberts, "Measurements of the soot volume field in laminar diffusion flames at elevated pressures," Combustion and Flame, Vol. 140, (2005), pp. 60-69.

[92] G. P. Sutton and O. Biblarz, Rocket Propulsion Elements, Wley 9th edition (2017) 446-496.

[93] A. J. Sabadell, J. Wenograd and M. Summerfield, "Measurement of temperature profiles through solid-propellant flames using fine thermocouples," AIAA, Vol. 3, (1965), pp. 1580-1584.

[94] I. Aoki and N. Kubota, "Combustion wave structures of high- and low-energy double-base propellants," AIAA, Vol. 20, (1982), AIAA80-1165R.

[95] A. Ishihara, Y. Sakai, K. Konishi and E. Andoh, "Measurement of the burning surface temperature in ammonium perchlorate," Proceedings of the Combustion Institute, Vol. 28,

(2000), pp. 855-862.

[96] A. Ishihara, Y. Sakai, K. Konishi and E. Andoh, "Effect of pressure on the burning surface temperature of a polymeric fuel for a solid propellant," Proceedings of the Combustion Institute, Vol. 29, (2002), pp. 2873-2879.

[97] A. Ishihara, Y. Sakai, K. Konishi and E. Andoh, "Correlation between burning surface temperature and regression rate for polymethylmethacrylate," Proceedings of the Combustion Institute, Vol. 30, (2005), pp. 2123-2130.

[98] P. A. Giguère and I. D. Liu, "Kinetics of the thermal decomposition of hydrogen peroxide vapor," Canadian Journal of Chemistry, (1957), Number 4.

[99] L. DeLuca, F. Cozzi, G. Germinias, I. Ley and A. A. Zenin, "Combustion mechanism of an RDX-based composite propellant," Combustion and Flame, Vol. 118, (1999), pp. 248-261.

[100] M. Servieri, L. Galfetti, L. DeLuca, V. Y. Egorshev, B. N. Kondrikov and I. V. Grebenyuk, "Burning mechanism of a composite propellant," Proceedings of 33rd International Annual Conference of ICT: Energetic Materials Ignition, Combustion and Detonation, Karlsruhe, Germany, No. 7, (2002), pp. 1-14..

[101] M. Hertzberg and I. A. Zlochower, "Devolatilization wave structures and temperatures for the pyrolysis of polymethylmethacrylate, ammonium perchlorate, and coal at combustion level heat fluxes," Combustion and Flame, Vol. 84, (1991), pp. 15-37.

[102] L. Krishnamurthy and F. A. Williams, "Laminar combustion of polymethylmethacrylate in O2/N2 mixtures," Proceedings of Combustion Institute, Vol. 14, (1973), pp. 1151-1164.

[103] J. W. Park, O. K. Lim and W. J. You, "Effect of ignition heat source on design fire curve of polyethylene foam in a compartment fire," Case Studies in Thermal Engineering, Vol. 22, (2020), 100790.

[104] M. Thirumaleshwar, "Fundamentals of Heat and Mass Transfer," 1st edition, Pearson, (2006), pp. 453.

[105] M. A. Hitt and R. A. Frederick Jr., "Regression rate model predictions of an axial-injection end-burning hybrid motor," Journal of Propulsion and Power, Vol. 34, (2018), pp, 1-8.

[106] N. Gascoin, G. Fau, P. Gillard and A. Mangeot, "Experimental flash pyrolysis of high density polyethylene under hybrid propulsion conditions," Journal of Analytical and Applied Pyrolysis, Vol. 101, (2013), pp. 45-52.

[107] E. Magyari and A. Pantokratoras, "Note on the fffect of thermal radiation in the linearized rosseland approximation on the heat transfer characteristics of various boundary layer flows," International Communication in Heat and Mass Transfer, Vol. 38, (2011), pp. 554-556.

[108] S. Gordon and B. J. McBride, "Computer program for calculation of complex chemical equilibrium compositions and applications," Reference Publication 1311, NASA, (1996).

[109] B. W. Bush and F. E. Fendell, "Asymptotic analysis of laminar flame propagation for general lewis numbers," Combustion Science and Technology, Vol. 1, (1970), pp. 421-428.

[110] S. Kadowaki, "Asymptotic analysis on high-temperature premixed flames: instability of flame fronts under the constant-enthalpy conditions," Journal of Thermal Science and Technology, Vol. 5, (2010), pp. 1-10.

[111] G. B. Goodwin and E. S. Oran, "Premixed flame stability and transition to detonation in a supersonic combustor," Combustion and Flame, Vol. 197, (2018), pp. 145-160.

[112] R. Sangtyani, H. S. Saha, A. Kumar, A. Kumar and M. Gupta, "An alternative approach to improve burning rate characteristics and processing parameters of composite propellant," Combustion and Flame, Vol. 209, (2019), pp. 357-362.

[113] T. B. Y. Chen, A. C. Y. Yuen, B. Lin, L. Liu, A. L. P. Lo, Q. N. Chan, J. Zhang, S. C. P. Cheung and G.H. Yeoh, "Characterisation of pyrolysis kinetics and detailed gas species formations of engineering polymers via reactive molecular dynamics," Journal of Analytical and Applied Pyrolysis, Vol. 153 (2020), 104931.

[114] W. Kaminsky, "Recycling of polymers by pyrolysis," Journal de Physique IV Proceedings, EDP Sciences, Vol. 03 (1993) pp. C7-1543-C7-1552.

[115] P. Pędziwiatr, "Decomposition of hydrogen peroxide-kinetics and review of chosen catalysts," Acta Innovations, Vol. 26, (2018), pp. 45-52.

[116] A. H. Sulaymon, A. H. Al-Karabouli and S. I. Ghulam, "Concentration of hydrogen peroxide by batch distillation column," Iraqi Journal of Chemical and Petronium Engineering, 8, (2007), pp. 13-18.

[117] G. Rarata and P. Surmacz, "The safe preparation of HTP and concentrated H2O2 samples," Transactions of the Institute of Aviation, Vol. 217, (2011), pp. 116-124.

[118] E. Klemm, C. Mathivanan, T. Schwarz and S. Schirrmeister, "Evaporation of hydrogen

peroxide with a microstructured falling film," Chemical Engineering and Processing: Process Intensification, Vol. 50, (2011), pp. 1010-1016.

[119] F. J. Mastral, E. Esperanza, P. García and M. Juste, "Pyrolysis of high-density polyethylene in a fluidised bed reactor. Influence of the temperature and residence time," Journal of Analytical and Applied Pyrolysis, Vol. 63, (2002), pp. 1-15.

[120] P.H Bouma and L.P.H de Goey, "Premixed combustion on ceramic foam burners," Combustion and Flame, Vol. 119, (1999), pp. 133-143.

[121] E. J. Wernimont, M. C. Ventura, M. C. Grubelich, M. R. Vaughn and W. R. Escapule, "Low temperature operation of hydrogen peroxide gas generators: verification testing & possible applications," Proceeding of the 7th International Energy Conversion Engineering Conference, (2009), AIAA 2009-4617.

Appendixes

Appendix – A) Design of large volume chamber

Appendix – A – 1) Chamber thickness

In this work, pressure dependency on the fundamental burning characteristics of the present specimen was experimentally examined using the self-made chamber. Prior to the making of the chamber, the safety design of the chamber based on the maximum allowed pressure was firstly addressed for safety experiment. In this work, the maximum allowed pressure for the chamber is set to be 0.5 MPa in absolute pressure.

First, the chamber was designed to consists of plates. The thickness of the plates, which can resist the maximum allowed pressure (0.5 MPa), is determined. The thickness necessary to resist the pressure is calculated by the following equation. In this work, the rectangular-shaped chamber is designed as presented to Fig. A – 1 – 1. This is because this shape is easy to be made and enables us to equip the transparent quartz window for observation with the chamber. Although this equation is valid for the cylindrical-shaped chamber, and it is not suitable for the rectangular-shaped chamber, we judged that there should be no problem if a thickness sufficiently thicker than the thickness calculated by this equation is adopted.

$$t = \frac{PD}{2S\eta - 1.2P} + C \qquad \text{Eq. A – 1, 1}$$

where P [MPa] is the allowed pressure, D [m] is the diameter, S [MPa] is the allowed tensile force for the chamber material, η [-] is the joint efficiency, and C [m] is the corrosion allowance,

respectively. In this work, aluminum plates, which measures 15 mm of thickness, is employed for the chamber for ease of the making. Therefore, S can be decided as 230 MPa for A5052. Width or length of the chamber is designed to be 300 mm, so that D is decided as 300 mm. 0.2 of η is selected to make the thickness larger for safety. The calculated thickness is 0.3 mm under an assumption that C is zero. Therefore, thickness of the aluminum plate used in this work is large enough in comparison with the calculated thickness to resist the allowed pressure.

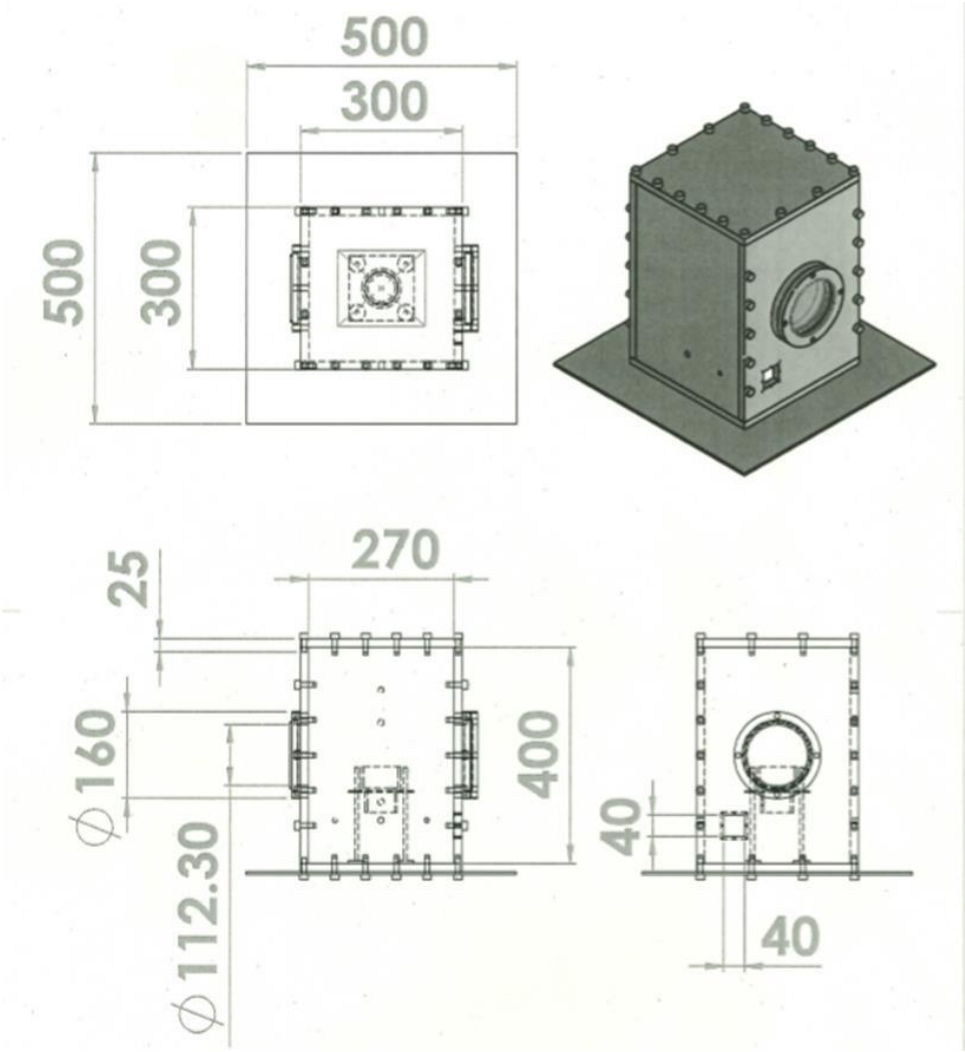

Fig. A - 1 - 1 Three dimension of self-made chamber used in this work.

Appendix – A – 2) Required diameter of bolts

Each aluminum plate is fixed with multiple bolts as shown in Fig. A – 2 – 1. When the internal pressure is applied to each aluminum plate, the aluminum plates are being fixed by the bolts, and thus the force by the internal pressure is applied to each bolt. For this reason, it is necessary to select suitable bolts to resist the force generated by the internal pressure. The top and bottom plates are each fixed by 16 bolts as shown in the above figure, and the front and back plates are each fixed by 18 bolts. The required diameter of each bolt to resist pressure up to 0.5 MPa is estimated here. **M10 Bolt**, which measures 9.026 mm in the effective diameter and 58 mm^2 in the effective area, made of SUS 304 is used for the chamber. The force applied to each plate plates are calculated as follows.

Force (F) applied to the top and bottom plates: 36.5 kN (at 0.5 MPa)

Force (F') applied to each bolt: 36.5 kN / 16 = 2.28 kN

Force (F) applied to the front and back plates: 54.0 kN (at 0.55 MPa)

Force (F') applied to each bolt: 54.0 kN / 18 = 3.0 kN

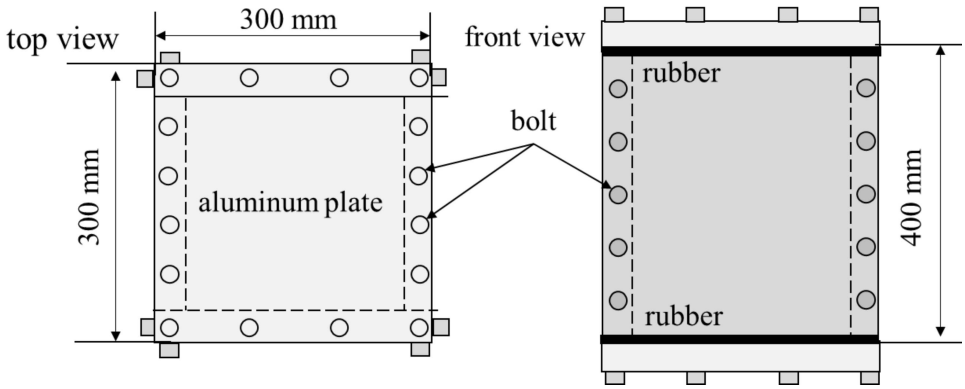

Fig. A – 2 – 1 Top view and front view of chamber, and number of bolts and location.

In addition, as shown in the following figure, tensile force and shear force are applied to each bolt and thread. Therefore, the bolt should resist up to 3.0 kN of the force. The force, which can be resisted with the bolt, is calculated as follows. Physical properties used in the calculation are listed in the following figure.

Tensile force

$$Tensile\ force = A \times yield\ stress \qquad \text{Eq. A – 2, 1}$$

Shear force

$$Shear\ force = A \times shear\ stress \qquad \text{Eq. A – 2, 2}$$

Shear force per a thread

$$= p \times d \times shear\ force \qquad \text{Eq. A – 2, 3}$$

where p [mm] is the pitch between the threads and d [mm] is effective diameter, respectively,

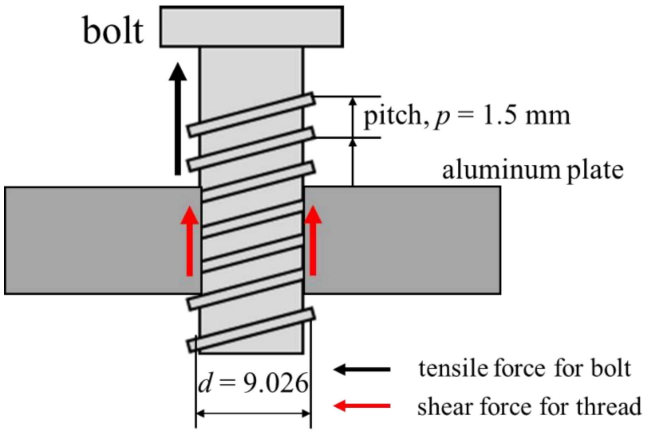

name	symbol	value	unit
yield stress	σ_y	98	[N/mm^2]
shear stress	τ	78	[N/mm^2]

Fig. A – 2 – 2 Shear force and tensile force, and its yield stress and shear stress of SUS304.

Based on the above relations, the allowed tensile force, the allowed shear force, and the allowed shear force per one thread are calculated as 5.684 kN, 4.524 kN, and 3.318 kN Recalling that the tensile force and the shear force applied to each bolt, when 0.5 MPa is applied, are 2.28 kN and 3.0 kN, hence, the bolt, which is M10, made of SUS304 is enough for resisting the allowed pressure (0.5 MPa).

Appendix – A – 3) Relief valve and acrylic plate for safety

Based on the maximum allowed pressure for the chamber, the maximum pressure were decided for the experiment. Even though the chamber is designed to resist up to the maximum allowd pressure, it should be necessary to consider additional matter for safety experiments. With this respect, a relief valve and a acrlic plate are equipped with to the chamber, as shown in the following figures.

Fig. A – 3 – 1 Relief valve and acrylic plate.

When pressure inside the chamber increases sharply, owing to unwanted burning behavior, and exceeds certain pressure, gas inside the chamber is released via the relief valve to outside. The certain pressure of the relief valve is selected as 0.4 MPa. In addition to the relief valve, an acrylic plate is equippted with to the chamber. If the relief valve fails to work properly, it would cause rupture of the chamber, and this acrylic plate plays important role in releasing the gas so as not to rupture the chamber. The acrlic plate is desgined to be broken at a slightly higher pressure than that of the relief valve (0.425 MPa). For this reason, the safety experimtns up to 0.4 MPa can be done with this chamber.

Appendix – B) Characteristics of hydrogen peroxide

Appendix – B – 1) History and decomposition reaction process of hydrogen peroxide

The use of hydrogen peroxide has a long history and can be traced back to 1930s. Hydrogen peroxide has been used for many applications to the aerospace propulsion and the power system because of excellent advantages, such as its high density, its monopropellant characteristics, its non-toxicity, and ease of handling. In recent years, there has been of renewed interests in the use of hydrogen peroxide as an oxidizer of the growing importance in using propellant low toxicity and enhanced versatility. Frequently called “rocket grade” hydrogen peroxide (RGHP) is highly concentrated hydrogen peroxide [Ref B, 1] and the RGHP has employed as the liquid oxidizer for many applications. Hydrogen peroxide exhibits a following reaction process decomposed

exothermically into the molecular oxygen and water (steam) when heated, and this decomposition reaction process is further accelerated by using a catalysis.

$$H_2O_2 \rightarrow H_2O + 0.5O_2 \qquad \text{Eq. B – 1, 1}$$

The decomposing temperature reaches above 1000 K, so that the rocket grade hydrogen peroxide is also used as hypergolic propellant. Furthermore, the exothermic reaction process with the high decomposing temperature (1000 K) is useful for automatic ignition either with continuous combustion in a bipropellant engine or with a solid fuel in the hybrid rocket.

Reference

[Ref B, 1] M. Ventura, E. Wernimont, S. Heister, and S. Yuan, Rocket grade hydrogen peroxide for use in propulsion and power devices – historical discussion of hazards, 43rd AIAA/ASME/SAE/ASEE Joint Propulsion Conference & Exhibit, Cincinnati, OH, (2007), AIAA 2007-5468

Appendix – B – 2) H_2O_2 concentration

The H_2O_2 concentration is quite important for the use of those applications. Hydrogen peroxide is high solubility in water, so that the H_2O_2 concentration can be adjusted by purified water. We can purchase the product of hydrogen peroxide diluted with the purified water (solvent) up to the concentration of 60 wt.% as the commercial availability. This percentage of the concentration is somehow a critical condition for safety use from a thermal balance of perspective.

A part of the purified water contained in hydrogen peroxide (< 100 wt.%) is firstly vaporized at 373

K while absorbing the latent heat of the vaporization (h_w) of the water. After completing vaporizing the water, the pure hydrogen peroxide is vaporized at higher temperature than the boiling temperature of the water (the latent heat of the vaporization of h_h).

The exothermic decomposition reaction with much of heat (h_e) is then initiated. The relationship between the latent heat of the vaporization and the exothermic heat by the decomposition reaction process, as a function of the H_2O_2 concentration is shown as follows.

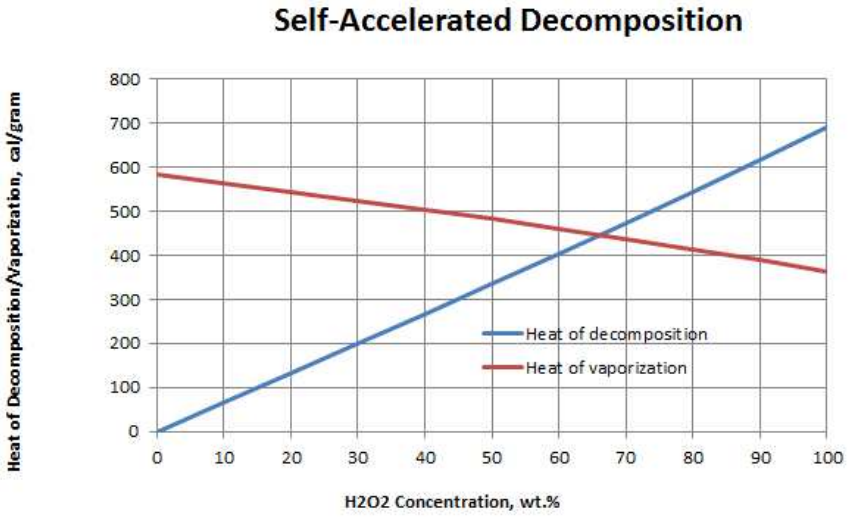

Fig. B – 2 – 1 Relationship of heat of vaporization and decomposition of hydrogen peroxide and H_2O_2 concentration [90].

As it is seen, when the H_2O_2 concentration is enriched up to 65 wt.%, the total latent heat of the vaporzation ($h_w + h_h$) becomes lower than the exothermic heat (h_g), leading to that continuous exothermic decomposition process occurs, and a lot of heat shall be released. For this reason, the comercially available hydrogen peroxide is distillated less 60 wt.% for safety use.

On the one hand, the oxygen liberation as a function of the H_2O_2 concentration is also shown

as a following figure. As is found, the oxygen liberation capacity is increased when the concentration of hydrogen peorxide is enriched further, together with the increase in the heat generated by the exothermic reaction process. This phenomenon lead to the intensified burning of the monopropellant and bipropellant (liquid rocket), so that the H_2O_2 concentration employed for the monopropellant and bipropllenat is enriched up to 90 wt.%, referring to as the rocket grade hydrogen peroxide.

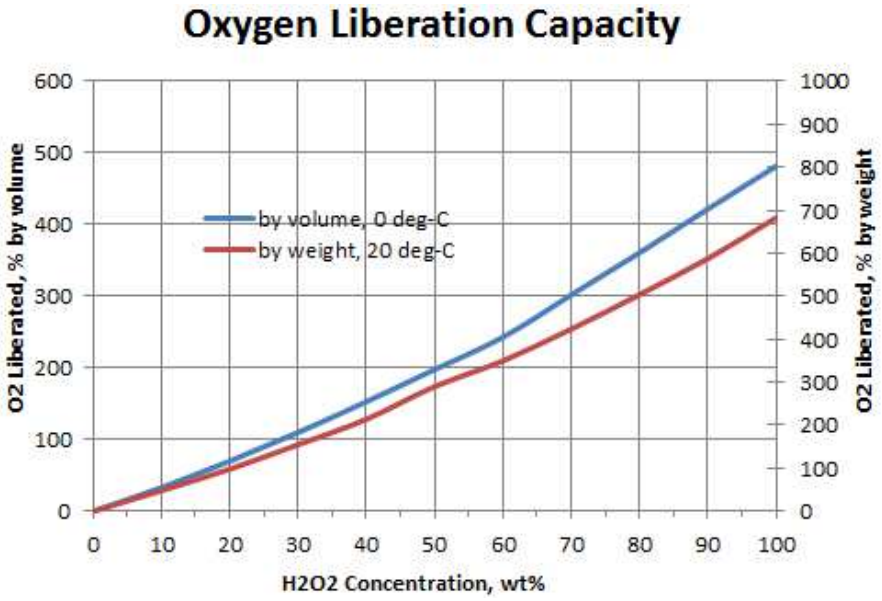

Fig. B – 2 – 2 Relationship of oxygen liberation capacity and H_2O_2 concentration [89].

Appendix – B – 3) Handling of hydrogen peroxide and distilling process

Appendix – B – 3 – 1) Handling of hydrogen peroxide

The high H_2O_2 concentration plays vital role in the propellant system. However, it is known that hydrogen peroxide shall initiate its decomposition reaction by externaol shock, heat, or impurity inclusion in the mixture of water-hydrogen peroxide. Since many applications using hydrogen peroxide is equipped with a tank to store, if an unwanted decomposition reaction is initiated by the external shock, heat, or the impurities, it pressurizes the tank, finally resuluting in a catastrophic damage to the sorroundings. Thus, careful handling of hydrogen peroxide is necessary for the safety use. The high concentration hydrogen peroxide can be stored safely if special engineered safety precautions and tight control of procedures are made, such as a cooling systen so as not to occur thermal runaway and ventilatiuon system of the gas generated by the decompositiuon process. In our laboratory, the original product (60 wt.% hydrogen peroxide) is carefully managed and stored in the highly closed chmaber as shown in the following figure.

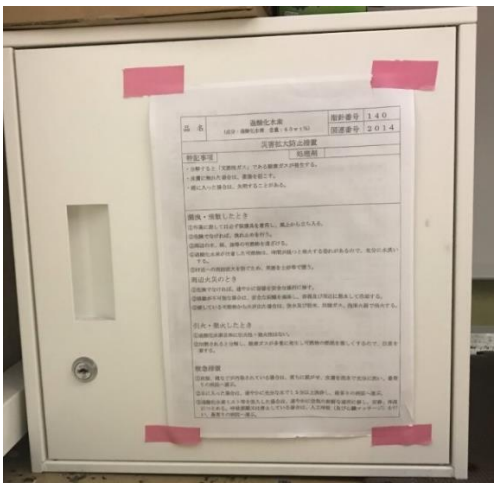

Fig. B – 3 – 1 highly closed chamber to store hydrogen peroxide.

Appendix – B – 3 – 2) Distilling process of H_2O_2 and vapor pressure

The distillation is a process whereby a mixture of liquids having different vapor pressures is separated into its components. At first one might think that this would be quite simple: if we have a solvent consisting of hydrogen peroxide (H_2O_2) that boils at 410 K (100 wt.%) and water with a boiling temperature of 373 K, all that would be necessary would be to heat the mixture to boiling temperature of the water; this would boil off all water, leaving pure liquid H_2O_2. However, these liquids will have substantial vapor pressures at all temperatures, not only at their boiling points.

In the present work, the commercially available solvent of H_2O_2 is distillated to enrich its concentration. Distilling procedure is to maintain the solvent at boiling temperature of the water at 0.1 MPa. Ideally, the distilled solvent shall reach 100 wt.% H_2O_2, however, it is not easy to have pure material because of unstable molecules. To determine its concentration of the solvent, there is a way measuring the density of the solvent. The density of the solvent is varied depending on its concentration and temperature as shown in the following figure. Hence, it is understood that the concentration of the solvent can be decided by measuring its density after the distillation.

As have stated in the Chapter 5, it was found that the precisely increasing the concentration would be hard to achieve. This is because the part of the H_2O_2 component in the solvent would be evaporated even left within the boiling temperature of the water (373 K). The evaporation rate of H_2O_2 shall be varied depending on its temperature, and its rate becomes higher as the temperature is high. Hence, H_2O_2 shall evaporate gradually even within the boiling temperature.

According to paper, it is highly recommended that the distilling procedure is conducted at reduced pressure (< 100 mm Hg). With this manner, the water component in the solvent can vaporized at the room temperature, and the evaporation rate of H_2O_2 can be inhibited, obtaining nearly pure H_2O_2.

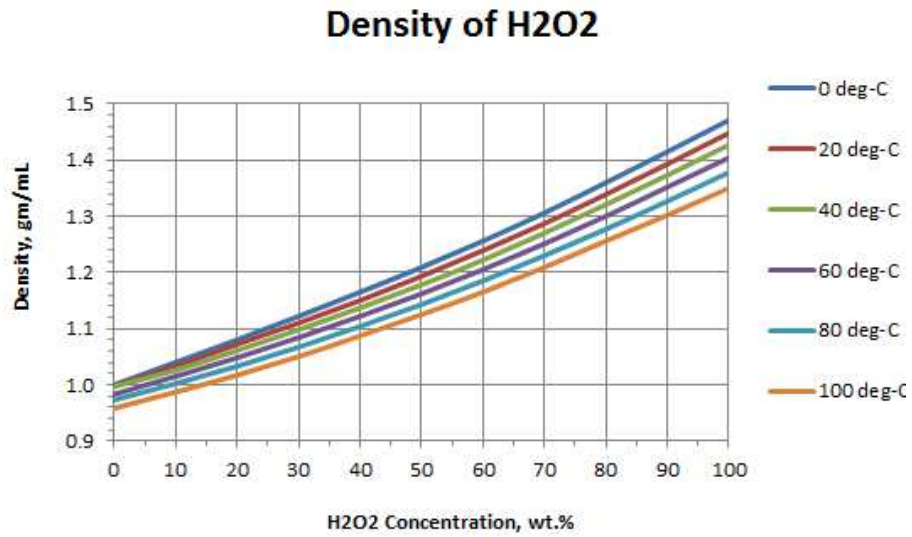

Fig. B – 3 – 2 – 1 Density of H_2O_2 solvent as a function of concentration and temperature.

As another methodology to concentrate the solvent, freezing the solvent at 273 K (freezing point of the water) is recommended. This is the methodology to utilize difference between the freezing temperature of the water and H_2O_2, as given as follows. It is clearly seen that there is large difference between freezing temperature in a range between pure H_2O_2 and pure water. Although only a slight difference of temperature at the point of the pure H_2O_2 and the pure water can be found in the following figure, this methodology is effective when the original solvent is around 50 wt.% with monitoring the temperature very carefully.

As mentioned, both the liquids (H_2O_2 and water) have substantial vapor pressure. The vapor pressure is the pressure of a vapor in contact with its liquid or solid form at a given temperature in a closed system. The vapor pressure is an indication of the liquid's evaporation rate. As the temperature of the liquid increases, the kinetic energy of the molecules also increases, thereby increasing the evaporation rate of the liquids.

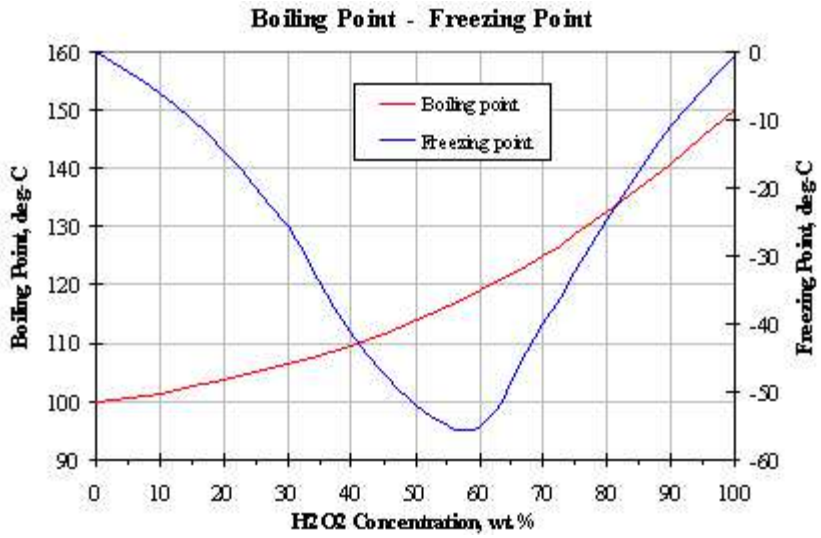

Fig. B – 3 – 2 – 2 Boiling temperature and freezing temperature of H_2O_2 solvent as a function of concentration.

Fig. B – 3 – 2 – 3 shows relationship among the concentration of the water-H_2O_2 solvent, its temperature, and the vapor pressure of the solvent. As shown here, it is seen that the vapor pressure is increased with the decrease in the H_2O_2 concentration and with increase in the temperature. It can be also seen that the vapor pressures at 373 K are 101 kPa (pure water, 0 wt.% H_2O_2) and 15 kPa (100 wt.% H_2O_2). The vapor pressure of the pure water is one order of

magnitude higher than that of the pure H_2O_2, showing that the evaporation rate of the water is larger than that of H_2O_2. It is indicated that the evaporation rate of both the liquids is much smaller under the reduced pressure, preventing the evaporation of both the liquids under their boiling temperatures. For this reason, the water component can be easily vaporized by the distillation at the reduced pressure and its boiling temperature (e.g., 3 kPa, 298 K), and the evaporation of H_2O_2 shall be inhibited.

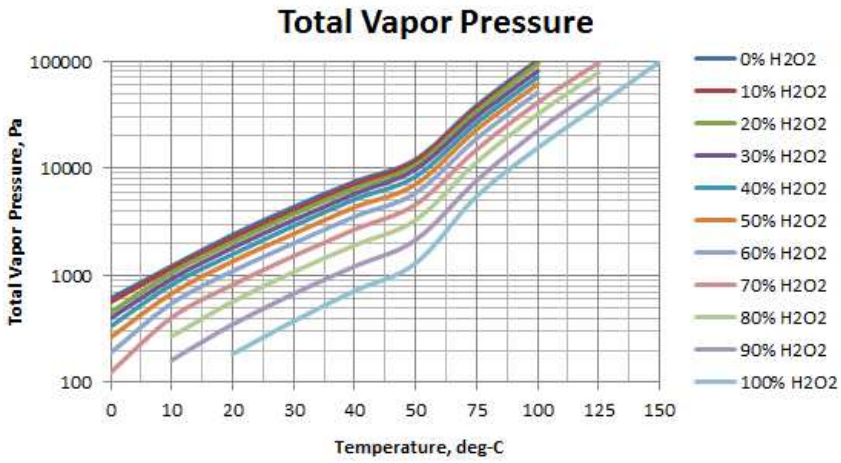

Fig. B – 3 – 2 – 3 Relationship between vapor pressure, temperature, and H_2O_2 concentration.

Appendix – C) Effect of other parameter on burning characteristics

C – 1) Effect of H_2O_2 concentration on regression rate: Experiments

Hydrogen peroxide is decomposed into the water vapor and the molecular oxygen by heated or catalysis, and its oxygen liberation capacity affects the burning characteristics. If the percentage of the H_2O_2 concentration is lower than 100 wt. %, ratio of the molecular oxygen liberated from the decomposition becomes lower. To investigate the effect of the H_2O_2 concentration on the

regression rate, experimental investigation as a function of the H_2O_2 concentration was conducted, prior to the main experiments shown in the Chapter 3.

The effect of the H_2O_2 concentration is presented to Fig. C – 1 – 1. The horizntal axis and the vetical axis represent the H_2O_2 concentration and the regression rate, respectively. Three-runs experiments are carried for each H_2O_2 concentration, and the error bars denoted on the figure is 95 % confident intervals to confirm the reproducibility. The experiments are conducted at nitrogen-balanced 0.1 MPa environment.

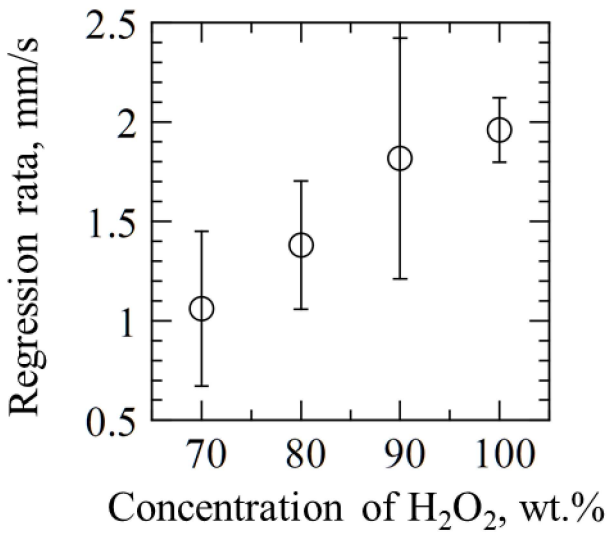

Fig. C – 1 – 1 Preliminary experiment: effect of H_2O_2 concentration on regression rate at standard pressure (0.1 MPa in absolute).

As it is seen, although the error bars are large, the average regression rate is increased with the increas in the H_2O_2 concentration. As mentioned, the heat generated from the exothermic reaction during the decomposition process is intensiied with the increase in the concentyration, and the oxygen liberation capacity increases as the concentration increases, leading to that the achievalble

burning temperature shall be higher. For this reason, heat to help promoting the regrssion of the specimen was intensified, resulting in that the faster regression rate could be achieved as the H_2O_2 concentration is increased. For the pupose of obtaining faster regression rate in this work, based on this results, the H_2O_2 concentration was enriched ideally up to 100 wt.%, and all the experimetns were conducted using the enriched hydrogen peroxide..

Appendix – C – 2) H_2O_2 concentration effect on regression rate: Prediction

As we have been known, the enriched hydrogen peroxide may trigger explosion, deflagration, and detonation, initiated by heat, external shock, and impurities inclusion because of the continuous exothermic reaction during the decomposition process [Ref C,1]. Once the exothermic reaction of the enriched hydrogen peroxide is activated, the heat is continuously released, and it will be uncontrollable and eventually cause unwanted accidents. In fact, explosion accidents of a container of hydrogen peroxide occurred, for instance, in Taiwan, Japan, and US [Ref C 2, 3]). According to an article, it was revealed that when hydrogen peroxide is enriched up to 90 wr% (90 wt% hydrogen peroxide diluted with 10 wt% water), it has possibility of the detonation due to the exothermic reaction [Ref C, 2]) For safety point of view, it is the desire to reduce the H_2O_2 concentration (< 90 wt%) to minimize the unwanted accident hazards, while achieving the comparable thrusting performance. To respond this issue, possibility of the present specimen employing the reduced concentration hydrogen peroxide (not pure) is discussed by comparing the

total mass flux of the AP-based composte solid propellant and the total mass flux of the present specimen employing the reduced concentration hydrogen peroxide.

Appendix – C – 2 – 1) Equivalence ratio vs fuel porosity and H_2O_2 concentration

A stoichiometric mass ratio (O/F_{th}) for complete combustion in the present specimen (fuel: C_2H_4, oxidizer: H_2O_2 diluted with H_2O) is determined from the following chemical reaction.

$$C_2H_4 + \frac{6}{a}[(1-a)H_2O + aH_2O_2] = 2CO_2 + \frac{2}{a}(a+3)H_2O \qquad \text{Eq. C – 2, 1}$$

where a is the H_2O_2 concentration on a mass basis. For instance, a = 0.8 when the concentration is chosen as 80 wt.%. Thus, if steady burning is achieved, the global equivalence ratio (φ) corresponding to the fuel porosity (ε) is given as follows.

$$\varphi = \frac{\left(\frac{O}{F}\right)_{th}}{\left(\frac{O}{F}\right)_{ex}} = \frac{\frac{v_O}{v_F}}{\frac{\varepsilon\rho_{eff\_L}}{(1-\varepsilon)\rho_S}} \qquad \text{Eq. C – 2, 2}$$

where (v_O/v_F) and effective density of the oxidizer (the solvent) ρ_{eff} are determined by the following relations.

$$\frac{v_O}{v_F} = \frac{\frac{6}{a}\left[(1-a)W_{H_2O} + aW_{H_2O_2}\right]}{W_{C_2H_4}} \qquad \text{Eq. C – 2, 3}$$

$$\rho_{eff} = (1-a)\rho_{H_2O} + a\rho_{H_2O_2} \qquad \text{Eq. C – 2, 3}$$

where ρ_{H_2O} [kg/m^3] is the density of water (1000) and $\rho_{H_2O_2}$ [kg/m^3] is the density of pure hydrogen peroxide (1450), respectively. The global equivalence ratios based on Eq. C – 2, 2 as a function the fuel porosity and the H_2O_2 concentration are depicted in Fig. C – 2 – 1. The stoichiometric condition of the fuel porosity to achieve the complete combustion (φ = 1) is chosen between ε = 0.82 and ε = 0.85, depending on the concentration. Fuel rich and lean conditions are determined accordingly. We define the range of fuel porosity between ε = 0.82 and ε = 0.85 as "optimal value" hereafter.

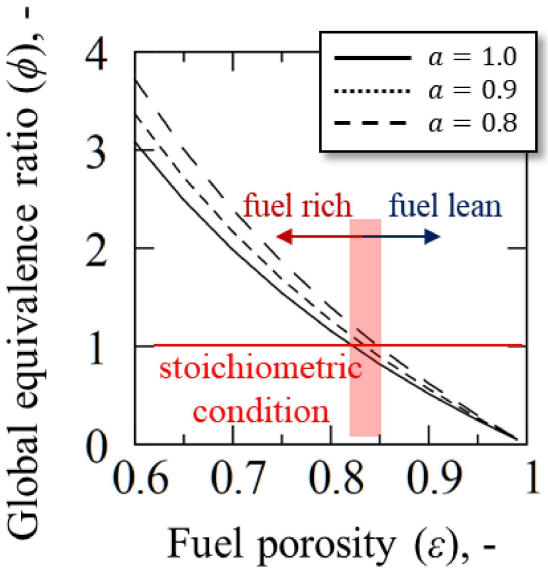

Fig. C – 2 – 1 Relationship between global equivalence (φ) ratio and fuel porosity (ε) as a function of concentration.

Appendix – C – 2 – 2) Effect of pressure and H_2O_2 concentration on total mass flux: Prediction

With the 1-D burning model developed in this work (Chapter 4), the effect of pressure and the H_2O_2 concentration on the total mass flux with a constant fuel porosity (ε = 0.8, φ = 1.2-1.4) is

presented in Fig. C – 2 – 2. The horizontal and vertical axes correspond to pressure and the total mass flux, respectively. For the case shown here, it is found that the total mass flux increases as pressure increases. This trend is similar to one found in the conventional AP-based composite solid propellant. In terms of the effect of the H_2O_2 concentration, it is clearly shown that the total mass flux is increased as the concentration increases.

Under the conditions studied in this work, the predicted total mass flux is varied in a range between 1.5 kg/(m^2·s) and 35 kg/(m^2·s), depending on pressure and the H_2O_2 concentration.

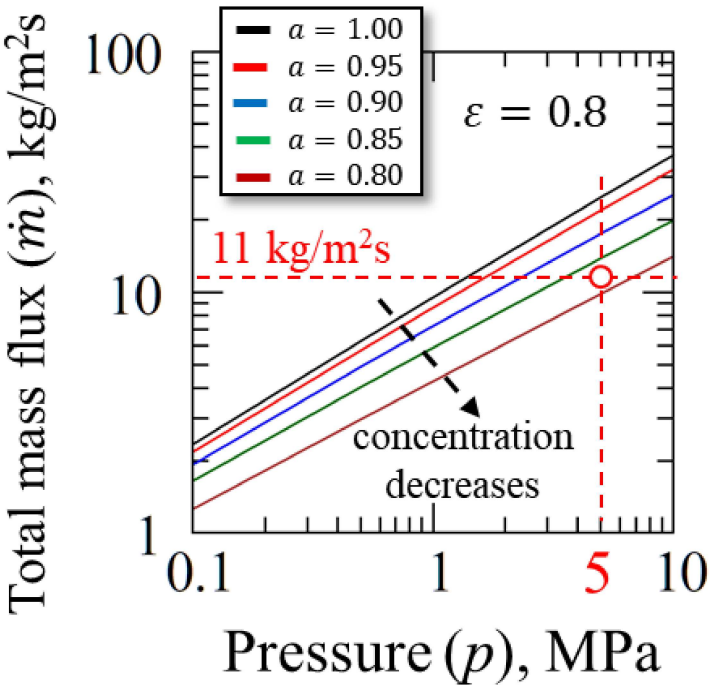

Fig. C – 2 – 2 Total mass flux as a function of pressure and H_2O_2 concentration with constant fuel porosity (ε = 0.8).

Assuming that the burning surface area is the same in both the specimen and the AP-based propellant, the same or higher total mass flux in the present specimen is the desire to obtain the

comparable thrusting performance to the AP-based composite solid propellant. Since the total mass flux of the AP-based composite solid propellant, consisting of ammonium perchlorate (68 wt.%), aluminum particles (18 wt.%), and hydroxyl-terminated polybutadiene, HTPB (14 wt.%), at 5 MPa, is reported as about 11 kg/(m^2·s) (shown with dashed lines in red on the figure [Ref C, 4]), it is proved that the present specimen has potential to obtain the same or higher mass flux at the same pressure. Furthermore, it is interesting to note that the H_2O_2 concentration is not always necessary to be enriched up to 100 wt.% (a = 1), and it can be rather decreased up to 85 wt.% (a = 0.85) as can see in the figure. As described, the enriched hydrogen peroxide has the possibility to have the detonation nature by the heat, the external shock, or the impurities. However, it is proven that it is not always necessary to enrich H_2O_2 concentration up to 100 wt.%, and potential risk by the detonation could be prevented while achieving comparable or more total mass flux to one achievable by the AP-based composite solid propellant.

Reference

[Ref. 1] Wu, D. and Qian, X.: Experimental Study on the Thermal Runaway of Hydrogen Peroxide with In-/organic Impurities by a Batch Reactor, Journal of Loss Prevention in the Process Industries, Vol. 51 (2018), pp.200-207.

[Ref. 2] Rarata, G and Smętek, J.: Explosives Based on Hydrogen Peroxide-A Historical Review and Novel Applications, Materiały Wysokoenergetyczne / High-Energetic Materials, Vol. 8 (2016), pp. 56-62.

[Ref. 3] Chi, C. Wu, S. Charpentier, J. I, Y. Shu, C.: Thermal Hazard Accident Investigation of Hydrogen Peroxide Mixing with Propanone Employing Calorimetric Approaches, Journal of Loss Prevention in the Process Industries, Vol. 25 (2012), pp. 142-147.

[Ref. 4] Tomita, N, Kitoh, K., Kohsetsu, K., Hasegawa, K. and Maeda, N.: Fundamentals of Rocket Technology, Corona Publishing Co. Ltd, Tokyo, 2015, pp. 58 (in Japanese).

Appendix – C – 2 – 3) Effect of fuel porosity and concentration on pressure exponents: Prediction

The pressure exponents obtained in the prediction, together with a typical range of pressure exponents of the AP-based composite solid propellant (the composition of the propellant is the same above) are shown in C – 2 – 3. The pressure exponents are calculated with the same manner shown in Chapter 4. The pressure exponent is obtained for various fuel porosities (ε: 0.7 - 0.9) and the H_2O_2 concentration (80 wt.% - 100 wt.%)

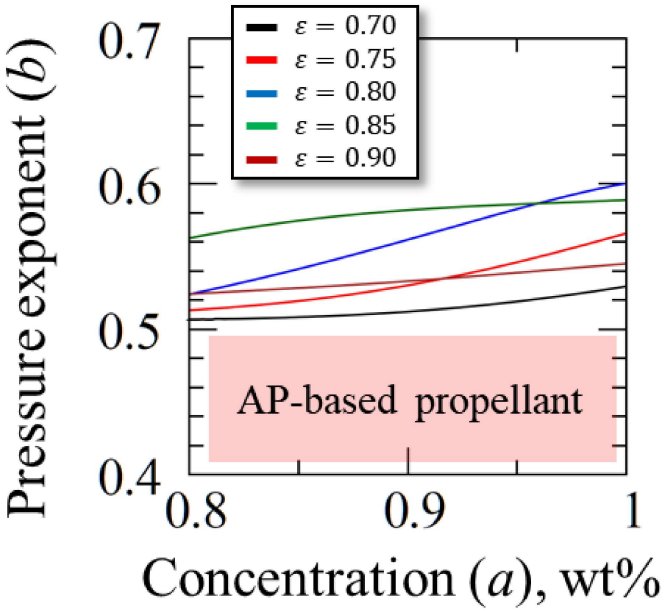

Fig. C – 2 – 3 Pressure exponents obtained in prediction as a function of fuel porosity and concentration, together with pressure exponent of AP- based composite solid propellant.

As found from the figure, it is seen that the pressure exponents are in a range between 0.52 and 0.6 and show an increasing trend as the H_2O_2 concentration increases. Additionally, the sensitivity of the fuel porosity to the pressure exponents is higher as the fuel porosity approaches to the

optimal value. Considering that the pressure exponents of the AP-based composite solid propellant are in a range between 0.4 and 0.5, it is found that the pressure exponents obtained in the present specimen is always shown above the one found in the AP-based composite solid propellant and shall be more pressure-sensitive in comparison with the AP-based composite solid propellant under conditions studied in this work. With this respect, more careful treatment on the pressure-coupled vibration (instability) in the combustion chamber shall be required than that of the compared with the AP-based composite solid propellant.

Appendix – C – 3) Effect of pore diameter

Appendix – C – 3 – 1) regression rate variation

Here, the effect of the pore diameter of the porous combustible on the burning characteristics is examined qualitatively. As described as follows, the pore diameter (D_P) is described as a function of permeability (K, m^2) and the fuel porosity (ε) [Ref C, 5] (Kozeny – Carman equation).

$$D_p = \frac{6(1-\varepsilon)}{\varepsilon}\sqrt{\frac{5K}{\varepsilon}} \qquad \text{Eq. C – 3, 1}$$

The permeability is defined as the state or quality of being permeable. From the above relation, the pore diameter, D_P, is determined by giving the permeability and the porosity. Assuming the porosity is constant value, and the pores inside the porous combustible are uniformly distributed, the pore diameter is determined by giving the permeability K into the above equation. The relationship between the permeability [m^2] and the pore diameter [μm], calculated from the above

relation is presented to Fig. C – 3 – 1 – 1. As it can be seen, the pore diameter increases for the case when the permeability is constant. In addition, the pore diameter is increased with the increase in the fuel porosity (K is constant). As the fuel porosity is defined as the ratio of the total pore volume (V_L) to the total volume (V), the pore diameter will be changed at the constant fuel porosity by altering the permeability.

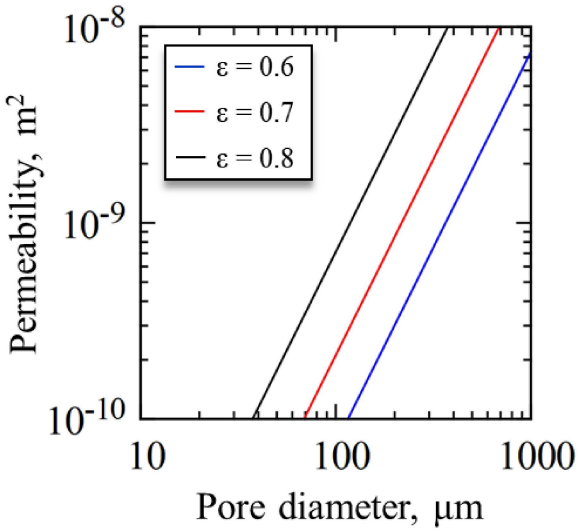

Fig. C - 3 - 1 - 1 Relationship among pore diameter (D_P), permeability (K), and porosity (ε).

When the pore diameter (D_P) is changed to be large, it is known that the pore-to-pore distance (D) increases as shown in Fig. C – 3 – 1 – 2. In this case, it is understood that fuel rich, or fuel richer, or stoichiometric zones will be emerged locally, as shown in Fig. C – 3 – 1 – 2. Hence, the regression rate will be varied as denoted in red, in such a case. This is remarkably appeared when the pore dimeter (D_P) and the pore-to-pore diameter (D) increase. Despite the same fuel porosity, the variation (amplitude) of the regression rate shall occur as the D and D_P become large, leading to local acceleration or deceleration. In this sense, the overall regression rate (average) shall not

be theoretically changed if the fuel porosity is constant, but it is considered that the steady burning would be hardly achieved in reality (experiment).

In our burning model, the following oxidizer to fuel mass ratio (*O/F*) has been adopted to predict the potential regression rate.

$$\frac{O}{F} = \frac{\varepsilon \rho_L}{(1-\varepsilon)\rho_S} \qquad \text{Eq. C – 3, 2}$$

Therefore, as stated, the regression will not be varied for the case when the fuel porosity remains constant. However, if the pore diameter is increased under the same fuel porosity, the pore-to-pore distance shall be increased. In this case, this locally ununiform pore distribution or ununiform porosity distribution would cause local acceleration or deceleration. For this reason, it is indicated that even if the same fuel porosity is, using the porous combustible with small pore diameter and small pore-to-pore distance would be important to ensure the validity of the above *O/F* relation and to inhibit the local acceleration and deceleration.

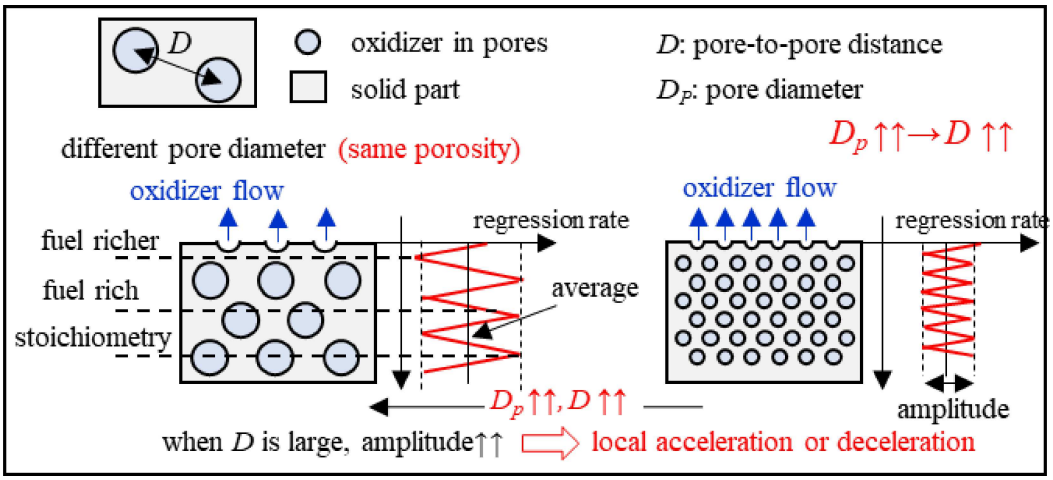

Fig. C - 3 - 1 - 2 Schematic illustration of different pore diameter (same porosity), pore-to-pore distance, and variation of regression rate.

Figure 3 – 1 – 3 shows the pressure dependency on potential regression rate obtained in the Chapter 4, together with considering the effect of the pore diameter. The shaded areas in blue and red represent the amplitude of the regression rate caused by the pore diameter as explained Fig. 3 – 1 – 2. Note that the shaded areas show qualitative range.

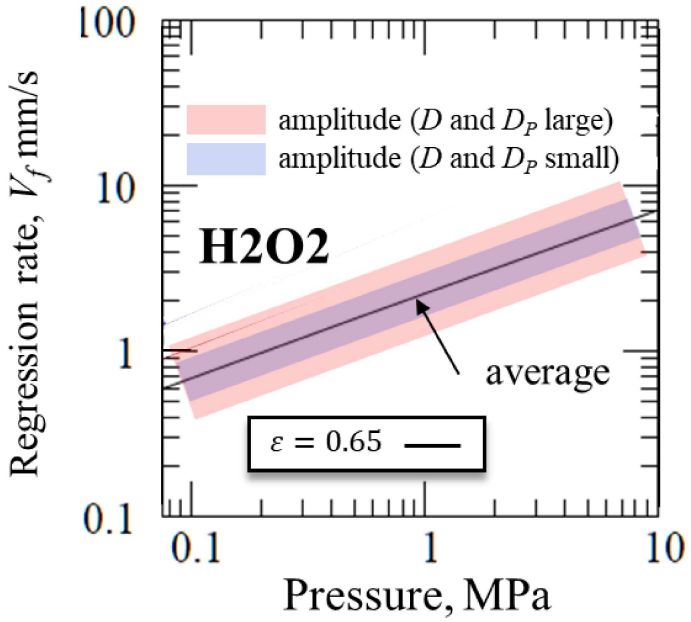

Fig. 3 – 1 – 3 Potential regression rates as a function of ambient pressure and fuel porosity, together with effect of pore diameter (D_P) and pore-to-pore diameter (D).

Appendix – C – 3 – 2) Pore diameter and quenching distance

In the temperature measurement reported in Chapter 3, it was indicated that the surface flame was established across the quenching distance (200 μm) between the top surface of the specimen and the flame edge as presented to Fig. C – 3 – 2 – 1. Assuming that the porous combustible with larger initial pore diameter is used, and then the flame edge becomes closer to the top surface, the flame can enter the pores, causing the breakdown of the 1-D combustion assumption and an

anomalous burning behavior, such as the backfire or flame spreading mode as shown in the following figure. In previous work by Nagata et al, they investigated the relationship between pore diameter and backfire (or flame spreading mode), which the flame enters the pores. It has been revealed that the flame could enter the pores easily when the initial pore diameter is large, leading to the backfire and causing transition from the 1-D combustion mode to flame spreading mode [Ref C, 6] [Ref C, 7]. For this reason, porous combustible with the small pore diameter plays vital role in inhibiting the anomalous combustion and breakdown of the 1-D combustion.

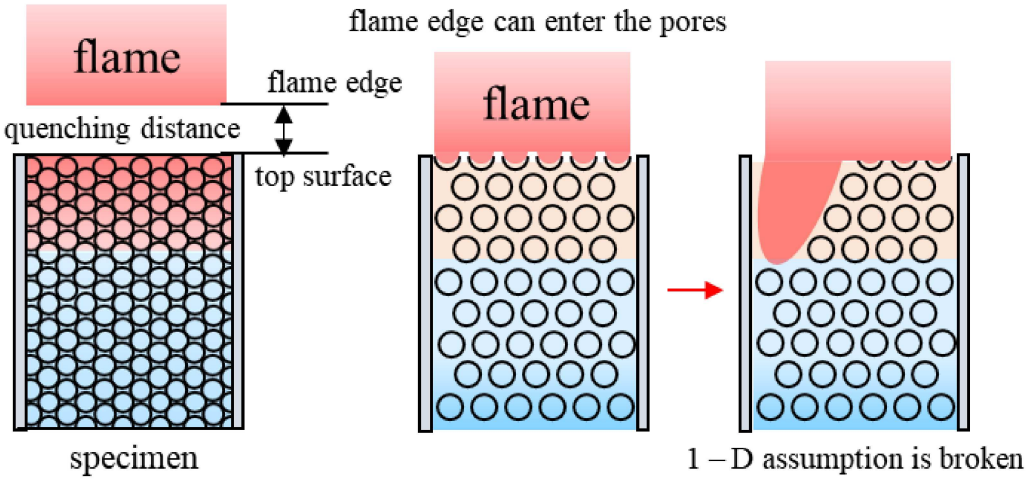

Fig. C - 3 - 2 - 1 Schematic illustration of backfire which is potentially occurred when initial pore diameter is increased.

Reference

[Ref C, 5] M. Kaviany: Principles of Heat Transfer in Porous Media, Springer, second edition, New York, 1995, pp. 33.

[Ref C, 6] T. Kato, N. Hashimoto, H. Nagata and I Kudo, A Preliminary Study of End-Burning Hybrid Rocket; Part 1 Combustion Stability, The Japan Society for Aeronautical and Space Sciences, (2001) pp. 33-39

[Ref C, 7] Y. Saito, Combustion Mechanisms of Axial-Injection End-Burning Hybrid Rockets, Hokkaido University Doctoral dissertation (2018) 98-100 (in Japanese).

Appendix – C – 3 – 3) Effect of pore distribution

Here, we would like to give an example of the unwanted burning behavior observed in our experiment. In the experiment conducted in the Chapter 3, the porous combustible is uniformly drilled to have uniform pore distribution inside the combustible. In this appendix we report importance of the uniform pore distribution to the burning characteristics form a viewpoint of our experimental observation..

As it can be seen in Fig. C – 3 – 3 – 1, the pore distribution is drilled to become ununiform intentionally in the experiment done in this appendix (the pore diameter : about 1 mm). The experiment is done with this specimen at 0.25 MPa under overall fuel porosity of 0.84, and a part of the observed burning behavior is presented to Fig. C – 3 – 3 – 1. After the forced ignition is made as usual, it is barely seen that the flame is established at the top surface of the specimen. However, after 4 s of the ignition, the flame attached to the top surface went towards inside the specimen rapidly and anomalous combustion (uncontrollable combustion) could be observed.

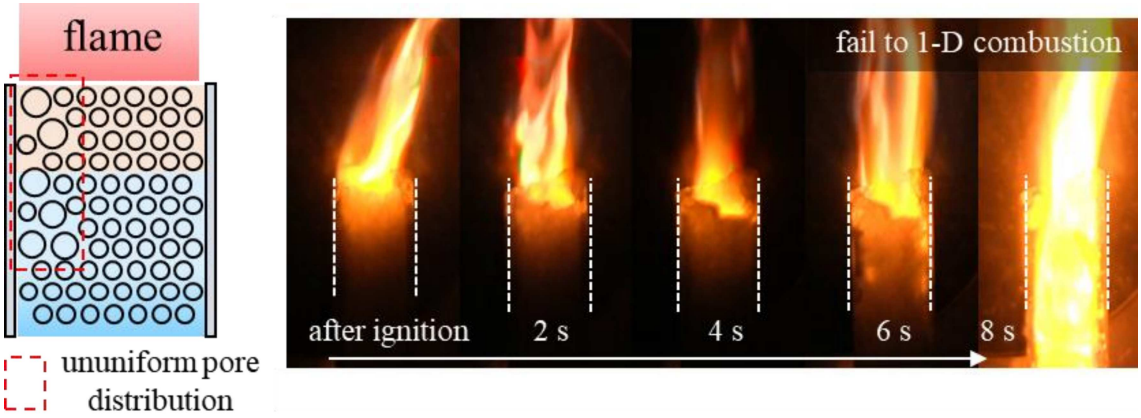

Fig. C - 3 - 4 - 1 Ununiform pore distribution and observed anomalous burning behavior at 0.25 MP under overall fuel porosity of 0.84.

If there is locally ununiform pore distribution and the larger pores. as presented in the figure, it would occur that the flame enters the pores, resulting in the anomalous combustion and causing the breakdown of the 1-D burning model assumed in the present work. In the present work, this phenomenon was frequently observed especially when the initial pressure and the fuel porosity are high. When pressure increases, kinetic time to react is decreased, leading to the thinner quenching distance and to that the flame is pushed onto the top surface of the specimen, This easily causes the flame enter the pores. In addition, in the case when the initial porosity is high, the flame can enter the pores easily. The result of the steady solution presented in the Chapter 4 must be valid only for the case when the burning event keeps progressing one-dimensionally. For the abovesaid reason, it was found that the porous combustible having the uniform pore distribution and the small pore diameter should be prepared to prevent the anomalous burning behavior, and it will lead to utilizing the prediction results indicated in the Chapter 4. Otherwise, the 1-D combustion would be hardly achieved.

Appendix – C – 4) Effect of concentration and density dependent index *n*

In the present work, the reaction index (n) is assumed to be unity. In this appendix, the effect of the reaction index on the potential regression rate and the blow off limit is examined.

Kadowaki et al. have investigated the burning characteristics of the premixed combustion for the case when the reaction index was parametrically changed [Ref C – 4, 1]. As referred to the

work by Kadowaki, the potential regression rate for the LOX case is examined as a function of the fuel porosity, the ambient pressure, and the reaction index (n), as presented to Fig. C – 4 – 1..

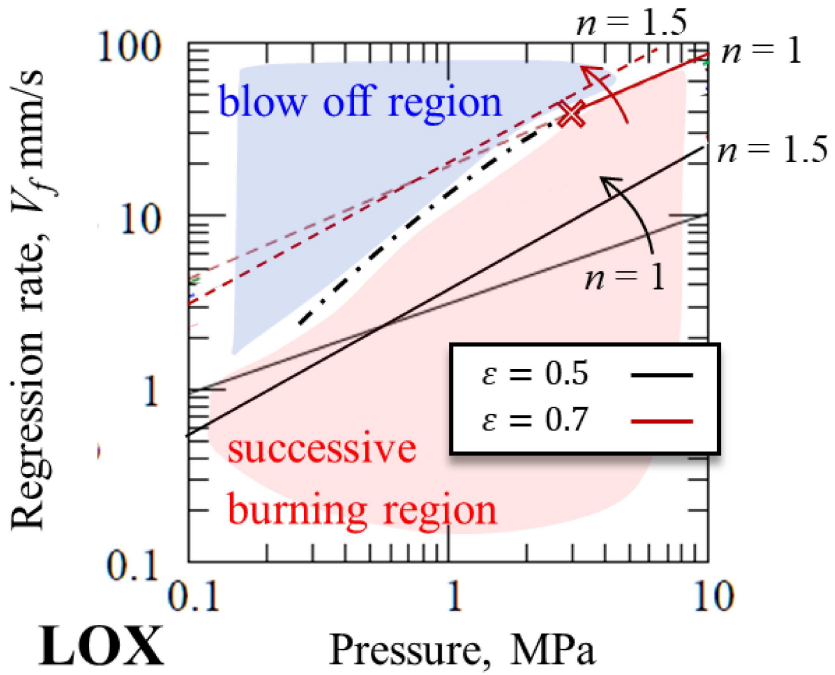

Fig. C - 4 - 1 Potential regression rate as a function of ambient pressure, fuel porosity, and reaction index (n = 1 and n = 1.5).

It is evident that the potential regression rate for n = 1 is higher than that of n = 1.5 in the pressure range up to 0.6 MPa. As it was found in the eigenvalue (Λ) relation stated in the Chapter 2, this is because the potential regression rate is proportional to the $(\rho Y)^n$. As the density of the gas mixture ejected from the specimen is proportional to the ambient pressure, and the density is less than unity below the certain pressure range, the potential regression rate for the case of n = 1.5 is slower in comparison with the case when the index (n) is unity. When the density exceeds the unity, we can find the transition point where the potential regression (n = 1.5) rate overlaps

one for the case of n = 1. Finally, it can be seen that the potential regression rate for the case of n = 1.5 becomes higher.

In terms of the blow off region and the successive-burning region, we found that both the region is strongly dependent on the reaction index (n), namely, the blow off region is widely found with the increase in the index, especially for the case of ε = 0.9. This is because the potential regression rate increases, and the spouting velocity (V_g) evolved from the top surface of the specimen exceeds the laminar burning velocity (V_{th}) as the index (n) increases. Therefore, it is revealed that the gradient of the relationship between the regression rate – pressure will be increased with the increase in the index.

Reference

[Ref C – 4, 1] Kadowaki et al., Asymptotic Analysis on High-temperature Premixed Flames; Instability of Flame Front under the Constant-enthalpy Conditions, Journal of Thermal Science and Technology, Vol. 10 (2010) pp. 1-10.

Appendix – D) Top surface detection by image processing (image J)

As we have stated in Chapter 3, the top surface of the specimen during the entire burning event was detected by the image processing software image J (a Java-based image processing program). We would like to show the prgoram code, written in this work, to detect the top surface as follows.

D – 1) Program code for the detection of the top surface

```
// Chose input and output directory
inputdirectory = getDirectory("Choose a input directory");
filelist = getFileList(inputdirectory);
outputdirectory = getDirectory("Choose a output directory");

// input the length for a pixel
defaultValue = 0;
pixcelLength = getNumber("Input Length of one pixel [mm/pixel]", defaultValue);
EndSurface=newArray(filelist.length);
run("Clear Results");
close("window Results");

// loop through all the images in the selected directory
for (i=0; i<filelist.length; i++) {
open(inputdirectory + filelist[i]);

// image processing program code (Otsu method)
```

```
//setTool("rectangle"); select rectangle

makeRectangle(714, 0, 564, 1080); select the rectangle range

run("Crop"); crop image based on the rectangle range

run("RGB Stack");

run("Stack to Images");

close("Green");

close("Blue");

selectWindow("Red");

run("Auto Threshold...", "method=Otsu white");

run("Median...", "radius=20");


// detection of top surface

h=getHeight();

w=getWidth();

EndSurface_y=runMacro("FindEndSurface", ""+h+" "+w+" "+pixcelLength);

EndSurface[i]=EndSurface_y;

run("Clear Results");

close("window Results");

close("window ROI Manager");


//save processed images

saveAs("Tiff", outputdirectory + filelist[i]);//

close();
```

```
}
// save location of top surface to CSV file
run("Clear Results");
for (i=0; i<filelist.length; i++) {
   setResult("EndSurface_y", i, EndSurface[i]);
}
saveAs("Results", outputdirectory + "End Suface.csv");
close("window Results");


// "FindEndSurface"
h=getHeight();
w=getWidth();
arg=getArgument();
s=split(arg);
h=s[0];
w=s[1];
pixcelLength=s[2];
EndSurface_y=0;
p=0;
for (j=0; j<=h; j++){
   for (i=0; i<=w; i++) {
      p=getPixel(i,j);
      if (p!=0){
```

```
            EndSurface_y=j;
            break;
        }
    }
}
EndSurface_y=EndSurface_y*pixcelLength;
return ""+EndSurface_y;
```

The abovementioned program ("FindEndSurface") code is schematically illustrated as a following figure. First, the original image during the burning event is cropped with selected rectangle range, and the original image is converted into the binarized images as follows.

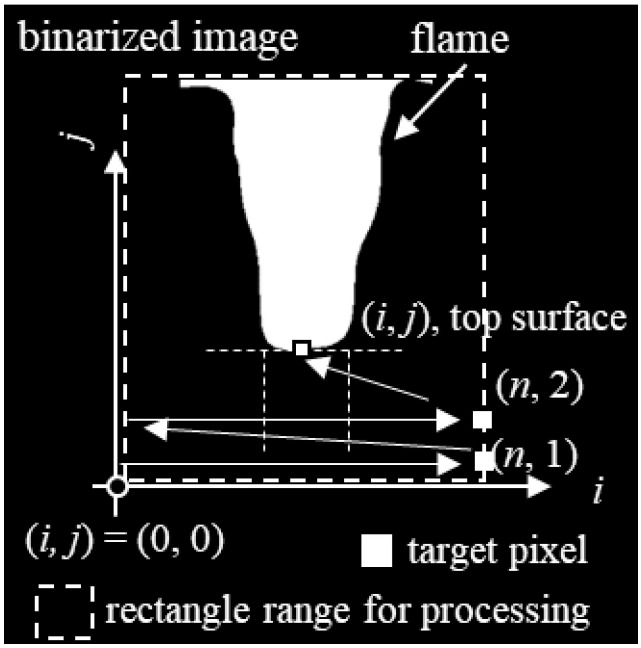

D – 1 – 1 Procedure of image processing to detect top surface location of specimen during burning event.

The selected rectangle range will be targeted for the image processing. The white area is identified as the flame area. In this program code, coordinates (i, j) are defined, and an origin of the coordinates are put on the lowest left of the rectangle range. Since the top surface of the specimen is assumed to be the lowest location of the white area, the detection of the lowest location of the flame is started from the origin. The detection is started at the origin, and a target pixel moves from (0, 0) towards (n, 0). If the white area corresponding to the flame is not detected, the target pixel moves to (0, 1) and then moves towards (n, 1). By repeating this method, the lowest location of the white area is detected.

Appendix – E) How to operate the gas chromatography

E – 1) How to operate the gas chromatography

The gas chromatography (GC2030, Shimadzu corporation) used in this work is shown in Fig. E – 1 – 1. The gas chromatography (GC) can analyze chemical composition contained either in liquid phase or gaseous phase by injecting sample (liquid or gas) into the GC. Here, procedure of the analysis with the GC is described.

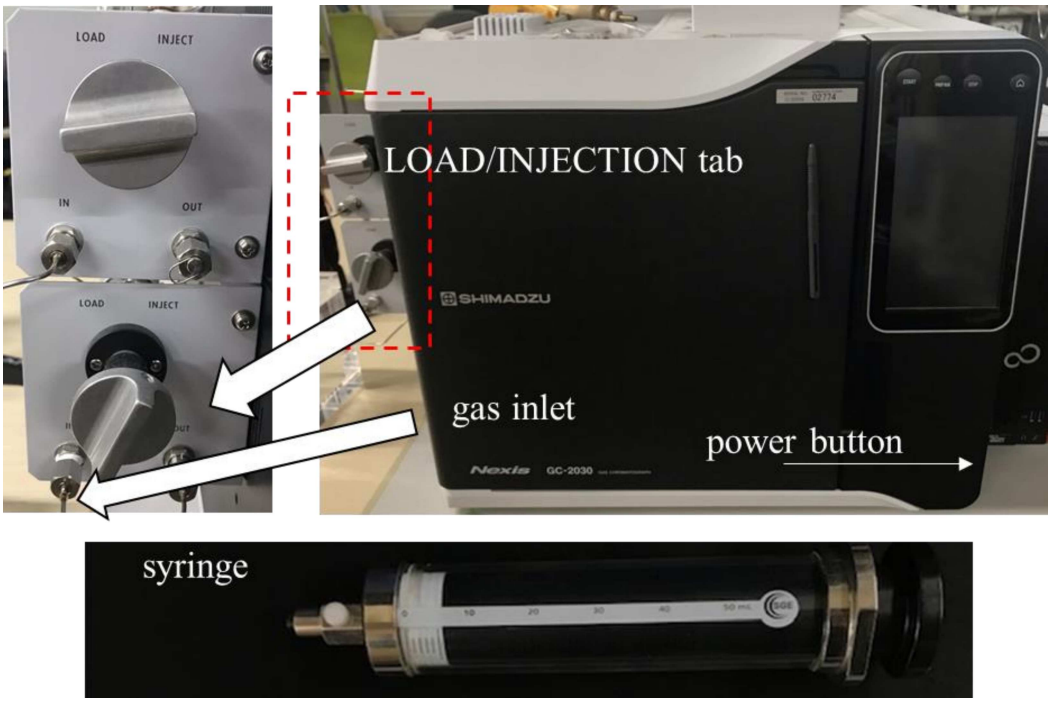

Fig. E – 1 – 1 Gas chromatography used in this work.

1. Open the regulator for carrier gas (helium is used) up to 0.5 MPa (secondary pressure) in gauge pressure.

2. Turn on the PC and the power button located at right side of the GC.

3. Open “LabSolutions” on PC and enter “OK” (ID: “Admin”, password is not required)

4. Select “2030” and push the button “GC kidou” on the LabSolutions.

5. Wait for about an hour (you can see “startup machi” on the LabSolutions)

6. After the LabSolutions says “GC junbityu”, turn on the button “laser” and “column”.

Please note that it is necessary to push these buttons repeatedly until the LabSolutions says “GC junbi-kanryo” (you will see green-labeled screen on the “GC junbi-kanryo)

7. Collect gas, which is targeted to be analyzed, by the syringe.

8. The syringe is then connected to the gas inlet of the GC.

8. At this moment, please make sure that both the LOAD/INJECT tab is set to be “LOAD”.

9. The gas collected is injected into the GC, and both the LOAD/INJECT tab is set to be “INJECT”

10. Push the button “analysis start” on the LabSolutions.

E – 2) How to determine the concentration of gas species

As have mentioned in Chapter 5, the concentration of the specific gas species can be determined by multiplying the pre-determined constant given to the specific gas species with the wavefront area which is detected by the chromatograph for the specific gas species. Thus, it is more important to know the pre-determined constant for each gas species. Here, we will explain a methodology for introducing the pre-determined constant.

As a first place, we will focus on deciding the pre-determined constant for ethylene (C_2H_4). The pre-determined constant is obtained by drawing s calibration curve for C_2H_4. To draw the

calibration curve for C_2H_4, it is necessary to have C_2H_4 standard gas whose the gas species and the concentration are known beforehand (Fig. E – 2 – 1 (top)). The gas species and its concentration of the standard gas are described as "C_2H_4, ethylene" and 99.5 %. The procedure to draw the calibration curve is as follows.

1. Inject the standard gas into a sampling bag.

2. Collect the standard gas by the syringe from the sampling bag.

3. Inject the collected standard gas into the gas chromatography.

4. Obtain the wavefront area corresponding to 99.5 wt.% of ethylene.

5. Plot the wavefront vs concentration as shown in Fig. E – 2 – 1 (bottom).

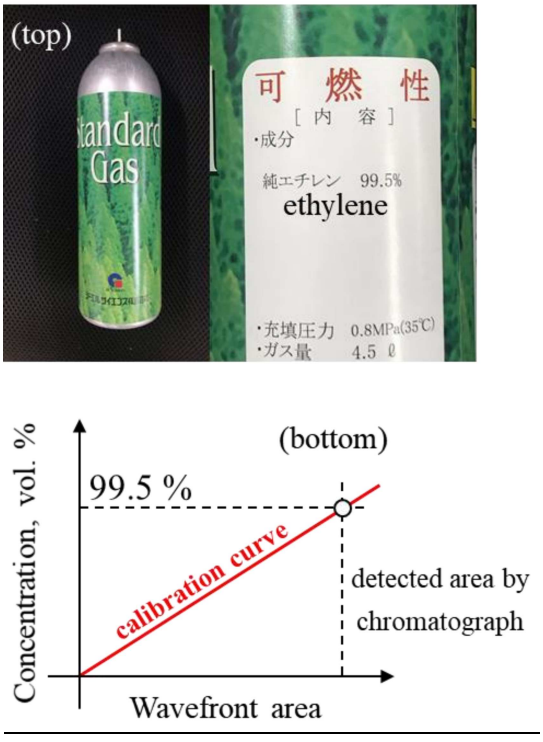

Fig. E – 2 – 1 (top) Standard gas (ethylene, 99.5 vol. %) (bottom) how to draw calibration curve.

As the relationship between the wavefront area and the concentration is regarded as linearity, the pre-determined constant is obtained from a gradient of the calibration curve.

Appendix – F) Reviewers' comments at defend (in Japanese)

Comments from Prof. Nagata

1. 端面燃焼式ハイブリッドロケットの圧力指数は 1 に近いが，本試験片での圧力指数はどれくらいか．なぜそのように大きく違いが生じるのか.

A – 1. 本試験片の圧力指数は，数値計算より過酸化水素を用いた場合で 0.51 – 0.6，液体酸素を用いた場合で 0.52 – 0.65 と予測されました．端面燃焼式ハイブリッドロケットは，多孔質状の固体燃料内部を気体酸化剤が流れるタイプのものであり拡散燃焼に近く，本試験片のようにあらかじめ液体酸化剤を湿潤させたものは予混合燃焼に近くなります．そのため，両者の燃焼形態は大きく異なり，このことが圧力指数に大きな違いが生じる理由と考えています．本試験片の燃焼は，従来のコンポジット型固体推進剤の燃焼に似ていることを考えると本試験片の圧力指数はコンポジット型固体推進剤の圧力指数（0.4 から 0.5 付近）に近くなると考えられます.

2. 過酸化水素の分解反応（発熱）が起きている箇所はどこか．発熱反応の影響は温度分布から見られるか．もし，見えない場合ではなぜか.

A – 2 純過酸化水素（気体）の分解率は，Fig. 1 のように約 670 K で 60 %，約 760 K で 100 % となります．このことを考えると，発熱反応は乾燥領域内部（領域 2）で徐々に起こり，予混合火炎領域（領域 3）で完結することになります.

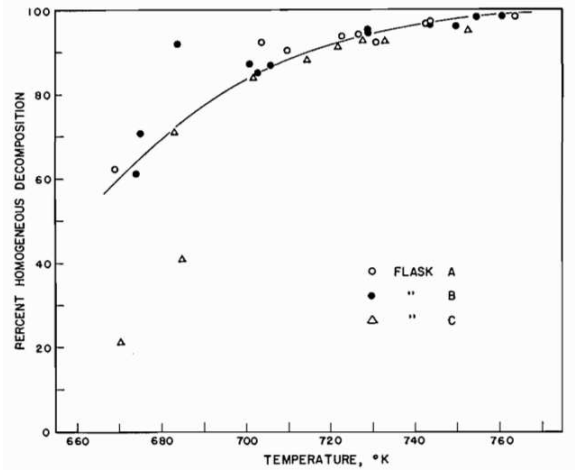

Fig. 1 純過酸化水素の分解率と温度の関係 [Ref 1].

純過酸化水素（気体）の分解による発熱とエチレンの燃焼熱は，それぞれ，98.1 kJ/mol（3.06 kJ/g），50.3 kJ/g であり，ポリエチレン発泡体がエチレンの重合体であると考えれば，

過酸化水素の分解による発熱量はエチレンの燃焼熱に比べて極めて小さいことがわかります（6 %程度）．このことを勘案すると，過酸化水素の分解反応による，予混合火炎領域（領域 3）の温度分布への影響は少ないと考えられます．また，上端面から乾燥領域内部へ流入する熱量に比べて，乾燥領域内で起こる分解反応による発熱量は極めて小さい（同様に 6 %程度）ことから，分解による発熱は温度分布に影響を与えていません．

[Ref 1] P. A. Giguère and I. D. Liu, Kinetics of the thermal decomposition of hydrogen peroxide vapor, Canadian Journal of Chemistry Vol. 35, 1957 pp. 283 - 293

3. 計測された火炎温度が断熱火炎温度よりも随分低いのか.

A – 3. 本審査会で示した温度分布は，生データであり，熱電対計測部の輻射熱損失を考慮していません．燃焼モデルの妥当性は，乾燥領域内部の温度分布で行っており，その温度領域（740 K 以下）では熱電対は赤熱せず（輻射損失の影響は小さい），妥当性評価に影響を与えないとして，輻射損失による補正は行っていません．一方で，輻射損失を考慮した場合の修正温度 T_m は Kaskan の補正式[Ref 2]を用いて求めることができます．

$$T_m = T + \frac{\varepsilon \sigma T^4 d}{2\lambda}$$

ここで，T [K]は熱電対指示温度（1500 K とする），ε [-]は計測部の放射率（コーティングされた白金の場合で 0.22 [Ref 3]），σ [W/(m^{2}K^4)]はステファンボルツマン定数（5.67 x 10^{-8}），d [m]は計測部直径（0.2 mm），そして λ [W/(mK)]は計測部周辺気体の熱伝導率（0.7，平衡計算で取得）とします．式中の”2”は，熱電対計測部を球体と仮定した場合の Nu となります．上記式で得られた修正温度は 1510 K となります．エチレンと純過酸化水素の断熱火炎温度は，平衡計算を用いて，同条件で 2500 K 程度であり，両者に大きな違いが生じています．この理由は，燃料ガスが純エチレンではないこと，熱電対素線側に熱伝導損失があること，完全断熱系でないこと，純過酸化水素（蒸留は不十分）ではないことに起因します．

[Ref 2] W. E. Kaskan, The dependence of flame temperature on mass burning velocity, Proceeding of the Combustion Institute, Vol. 6, 1957 pp. 134 – 143.

[Ref 3] Y. Nakamura et al., Feasibility study of temperature measurement in poor fire, Bulletin of Japan Association for Fire Science and Engineering Vol. 59, 2009 pp. 9 – 16.

Comments from Prof. Doi

1. 実験では，上端面より 1 mm 程度で火炎温度になっているが，そう考えると，解析で $x = \infty$ で T_∞ ではなくてよいのではないか．また温度が一定か，温度勾配が一定なのかどちらか.

A－1．質量流束 m_{dot} の解析解は，各領域の保存則と接続条件（$x = \infty$ で $T = T_\infty$ を含む）を用いて求めました．火炎温度となる位置（δ と定義）は質量流束 m_{dot}（厳密には噴出速度 V_g）や圧力に大きく依存することから，$x = \delta$ で $T = T_\infty$ の境界条件を与えると質量流束 m_{dot} の解析解を得るのが難しくなります．そのため，どの条件でも $x = \infty$ で $T = T_\infty$ としておくことで，燃焼モデルの単純化も含め，解析が容易になることからこのような接続条件を与えました．この接続条件を与えたときの，燃焼構造の解析解の具体例を Fig. 2 に示します．左の図が温度計測結果に近い解析条件となりますが，$x = \infty$ で $T = T_\infty$ の条件を与えた場合でも，火炎温度の位置は実験結果と多少異なるものの，そのオーダー（0.数 mm 程度）は実験結果と合っており，条件の与え方に妥当性があると考えらえられます．

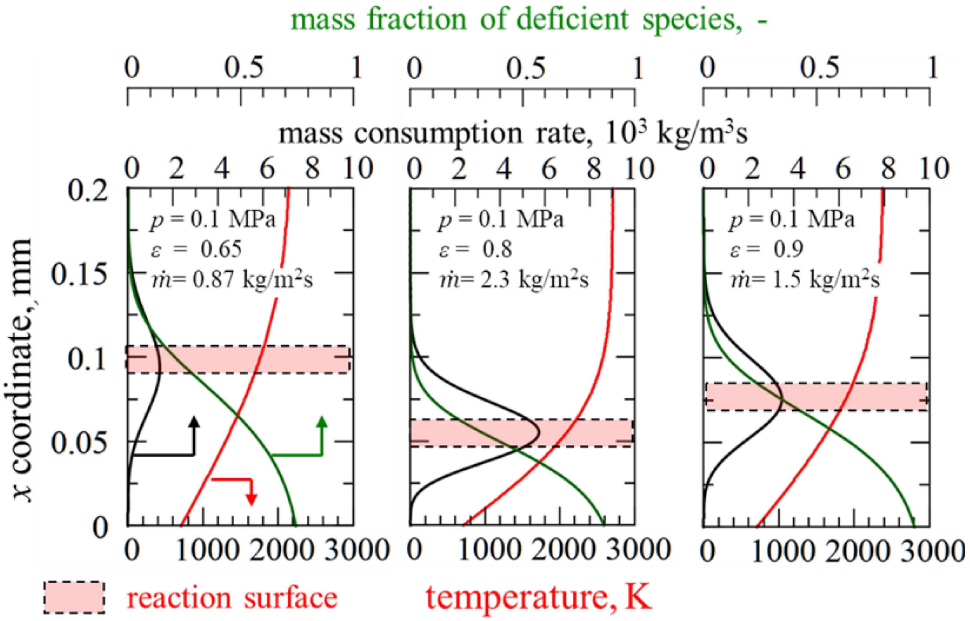

Fig. 2 燃焼構造の数値解析解.

試験片上端面での温度は一定としていますが，上端面の予混合火炎領域側の温度勾配は，Fig. 2 の燃焼構造のように変化します．これは，断熱火炎温度 T_∞ が解析条件によって変わるほか，予混合火炎領域での温度分布は質量流束 m_{dot} に応じて変化するためです．

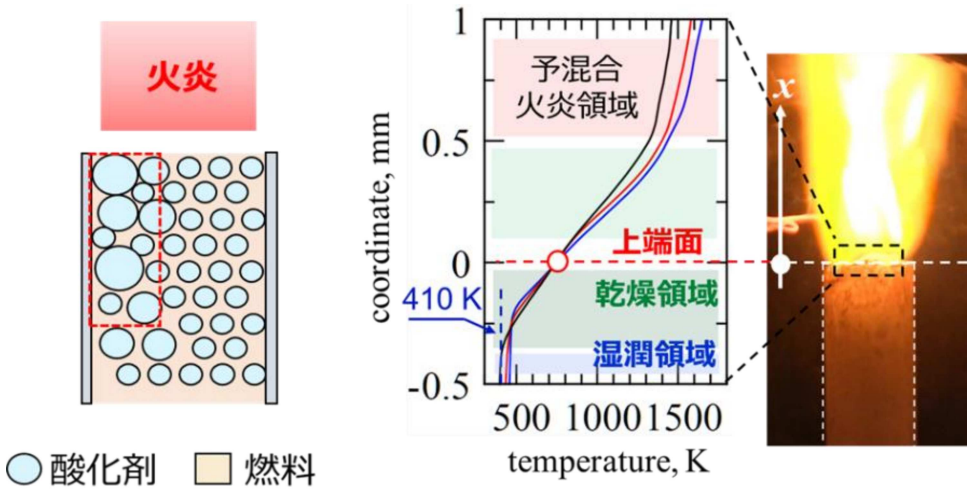

Fig. 3（左）空隙の大きさに偏りがある場合の試験片，（右）本研究で得られた燃焼構造.

Comments from Prof. Yanada

1. 局所的に空隙を大きさしたところでは，その大きさはどの程度か.

A – 1. Fig. 3（左）の赤破線の領域の空隙の大きさは 1 mm 程度であると考えています．Fig. 3（左）の赤破線の領域で火炎が潜り込むことから，空隙の大きさは消炎距離（試験片上端面から火炎の距離）よりも大きかったことが考えられます．消炎距離は，Fig. 3（右）の燃焼構造の調査結果より，1 mm 程度であることから，空隙の大きさは 1 mm 程度，またはそれ以上であることがわかります.

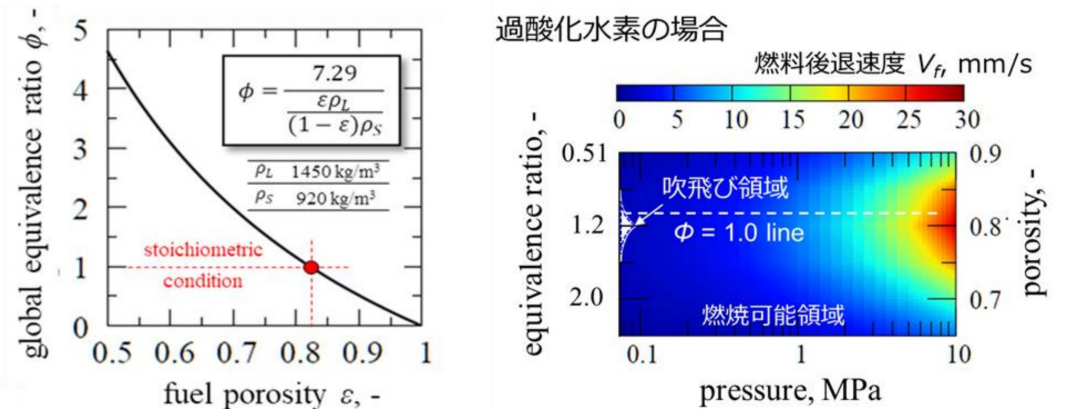

Fig. 4（左）空隙率と当量比の関係，（右）燃料後退速度の圧力と空隙率の関係.

2. 燃料後退速度は当量比 1 を境に対称となっているが，それはなぜか.

A – 2. Fig. 4（左）より，空隙率を変化させると，当量比が変化します．予混合燃焼において，Fig. 5 のように当量比が変化すると燃焼速度は変化し，当量比が 1 となる場合で最大値

を取ります．当量比が1以上，または1以下では燃焼速度は最大値から減少することから，Fig. 4（右）のように，当量比 1 を境に対称となっているように見えます．

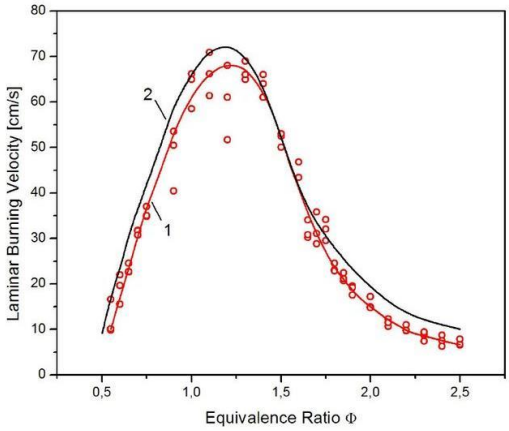

Fig. 5 当量比と層流燃焼速度の関係[Ref 4].

[Ref 4] A Gutkowski, Laminar burning velocity under quenching conditions for propane-air and ethylene-air flames, Archivum combustionis, 2006, pp. 1 - 11

3. 実際の推進剤内部で圧力制御は容易にできるか.

A – 3. 固体推進剤の場合，燃焼室内部を設定圧力まで加圧し燃焼を開始させます．初期圧力（着火前の燃焼室圧力）は加圧用ガスを用いて制御可能となります．固体推進剤では雰囲気圧力が決まれば，燃料後退速度が決まり，ミッションに応じた必要推力が設計段階で決定されます．そのため，燃焼中は，燃焼による圧力変動はあるものの，故意に圧力を変化させることはありません．

本研究で自作した燃焼室の耐圧力は 0.4 MPa 程度であり，それ以上の圧力場で燃焼試験は行えませんが，燃焼室を，（例えば）ステンレス製の円筒を用い，その厚みを大きくすればさらに高い圧力レンジで燃焼試験を行うことができます．

Comments from Associate prof. Matsuoka

1. 乾燥領域と湿潤領域の間の気液境界面も同様に燃料後退速度 V_f で移動すると思うが，どうか.

A – 1．すべての境界（試験片上端面と気液境界面）での質量流束は連続の式（質量流束 m_dot）を満たす必要があります．気液境界面では燃料成分はガス化せず，液体酸化剤のみの蒸発であるため，気液境界面での蒸発潜熱（接続条件の中身）では燃料後退速度 V_f ではなく，m_dot で記述する必要があります．

Comments from my supervisor (Prof. Nakamura)

1. 理論燃焼速度 V_{th} が噴出速度 V_g よりも大きくなると火炎が試験片上端面に追いつくことはあるのか．そのような現象はあり得るのか．

A－1．本研究では，理論燃焼速度 V_{th} と噴出速度 V_g を比較して，試験片上端面が加速するか否かを定性的に評価しました．過酸化水素の場合で V_{th} と V_g の差は小さく，試験片上端面の加速は起こりにくく，その一方で，液体酸素の場合ではその差が大きいため，加速は起こりやすいと考えます．

火炎が試験片上端面に追いつくかどうかは，試験片上端面と火炎の間の距離（消炎距離）をまた別に検討する必要があります．検討の例として，消炎距離は噴出速度 V_g [m/s]に予混合気体の拡散時間 [s]と予混合気体の反応時間 [s]の和（拡散時間＋反応時間）を乗ずることで求めることができます．消炎距離は，圧力に反比例し減少するため，圧力が高くなればなるほど，火炎は端面に近付くようになります．高い圧力になればなるほど，火炎が端面により近い領域で形成されるようになります．

Publication, conference, award, and research grant

Publications (peer review)

1. **D. Matsugi**, T. Matsuoka, and Y. Nakamura, Study of successive-burning characteristics of porous combustible soaked in liquid oxidizer, Combustion and Flame, Vol. 233, (2021), 111571.
2. **D. Matsugi**, Y. Hasebe, T. Yamazaki, T. Matsuoka, and Y. Nakamura, Experimental investigation of burning characteristics of porous combustible soaked in liquid oxidizer, Journal of Thermal Science and Technology, Vol. 16, (2021), pp. JTST0036
3. T. Matsuoka, T. Nishihara, **D. Matsugi**, D. Paul, K. Matsuyama, and Y. Nakamura, Necessary condition for measurement of heat flux sensor using a thermoelectric module, Fire Safety Journal, Vol. 125, (2021), 103427

International conferences (peer review)

1. **D. Matsugi** and Y. Nakamura, Study of Burning Characteristics of Porous Combustibles Soaked with a Liquid Oxidizer, 7th World Congress on Mechanical, Chemical, and Material Engineering (MCM'21), Virtual conference, 4th Aug. (2021), Session: Combustion, HTFF 124.
2. **D. Matsugi** and Y. Nakamura, Effect of Concentration of H_2O_2 on Burning Characteristics of H_2O_2-soaked Polyethylene Foam, 33rd International Symposium on Space Technology and Science (33rd ISTS), Virtual conference, 4th March. (2022), Session: Finalist Student Session 2.

Domestic conferences (no peer review)

1. S. Kawamura, **D. Matsugi**, T. Matsuoka, and Y. Nakamura, Study on combustion control of liquid fuel using porous media, The Japanese Society for Multiphase Flow, Fukuoka, Aug. (2019). P090, in Japanese.
2. **D. Matsugi**, T. Matsuoka, and Y. Nakamura, Study on end-burning characters of porous solid with liquid oxidizer, 57th Symposium (Japanese) on Combustion, Sapporo Hokkaido, Nov. (2019), Session: Propulsion I, B312, in Japanese

3. **D. Matsugi**, T. Yamazaki, T. Matsuoka, and Y. Nakamura, Study on potential Performance of propellant made by polyethylene foam soaked in hydrogen peroxide, Virtual conference, Nov. (2021), Session: Solid combustion I, C111, in Japanese.

Awards

1. **D. Matsugi** and Y. Nakamura, **Best Paper Award**: Study of Burning Characteristics of Porous Combustibles Soaked with a Liquid Oxidizer, 7th World Congress on Mechanical, Chemical, and Material Engineering (MCM'21), Online, Aug. (2021), Session: Combustion, HTFF 124.
2. **D. Matsugi** and Y. Nakamura, **JSASS** (Japan Society for Aeronautical and Space Science) **President Award**: Effect of Concentration of H_2O_2 on Burning Characteristics of H_2O_2-soaked Polyethylene Foam, 33rd International Symposium on Space Technology and Science (33rd ISTS), Online, March (2022), Session: Finalist Student Session 2.
3. **松木 大輝**，2021 年度豊橋技術科学大学学生表彰，2022 年 3 月 8 日

Research grants

1. **D. Matsugi** and Y. Nakamura, Experimental investigation of burning characteristic of porous combustible soaked in liquid oxidizer, Research Foundation for the Electrotechnology of Chubu, Publishing grant, Sep. (2021)
2. **松木 大輝**，中村 祐二，研究助成，コンポジット多孔質固体燃料によるハイブリッド型推進剤の高性能化，日東学術振興財団，2021 年 12 月–2023 年 12 月

Social activities

1. **松木 大輝**，東三河 SDGs Day 2019 発表者，2019 年9月 25 日，MUSASHi Innovation Lab CLUE
2. **松木 大輝**，小池誠一，豊橋技術科学大学 IGNITE セミナー“持続可能な社会を目指して ーSDGs の理論と実践”発表者，2019 年 10 月 24 日，豊橋技術科学大学附属図書館
3. **D. Matsugi**, Japan Seminar on Technology for Sustainability 2019 facilitator, July, 7 – 12,

2019, Fukushima National Institute of Technology,

4. **D. Matsugi**, International Seminar on Technology for Sustainability 2019 facilitator, Oct., 8 – 12, 2019, Thammasat University, Thailand.

Others

1. **D Matsugi**, T. Yamazaki, T. Matsuoka, and Y. Nakamura, “Effect of End Gases Produced by H_2O_2 Soaked Polyethylene Foam on Its Thrusting Performance, The proceeding of the Combustion Institute, (2022), Vancouver, Canada. (**under review**).